論文 / 著書情報
Article / Book Information

題目(和文)	吸着種領域モデル及び反応サイトイメージングによる固体酸化物型燃料電池多孔質電極における反応動力学に関する研究
Title(English)	Reaction Kinetics and Dynamics on Solid Oxide Fuel Cell Porous Electrodes through Species Territory Adsorption Model and Active Sites Imaging
著者(和文)	長澤剛
Author(English)	Tsuyoshi Nagasawa
出典(和文)	学位:博士(工学), 学位授与機関:東京工業大学, 報告番号:甲第10789号, 授与年月日:2018年3月26日, 学位の種別:課程博士, 審査員:花村 克悟,佐藤 勲,平井 秀一郎,山中 一郎,伏信 一慶
Citation(English)	Degree:Doctor (Engineering), Conferring organization: Tokyo Institute of Technology, Report number:甲第10789号, Conferred date:2018/3/26, Degree Type:Course doctor, Examiner:,,,,
学位種別(和文)	博士論文
Type(English)	Doctoral Thesis

Reaction Kinetics and Dynamics on Solid Oxide Fuel Cell Porous Electrodes through Species Territory Adsorption Model and Active Sites Imaging

by

Tsuyoshi Nagasawa

A dissertation submitted in partial fulfillment of the requirements for the degree Doctor of Philosophy in Mechanical Engineering

Supervised by Prof. Dr. Katsunori Hanamura

Tokyo Institute of Technology

March 2018

Abstract

Reaction Kinetics and Dynamics on Solid Oxide Fuel Cell Porous Electrodes through Species Territory Adsorption Model and Active Sites Imaging

by

Tsuyoshi Nagasawa

Department of Mechanical and Control Engineering

Tokyo Institute of Technology

Supervised by Prof. Dr. Katsunori Hanamura

The reaction kinetics and dynamics on solid oxide fuel cell porous electrodes were studied based on kinetic modeling and active sites imaging. The analytical model for hydrogen oxidation at anode, species territory adsorption model, was newly developed. Based on the model, explicit expression of anode overpotential could be obtained, which combines the overpotentials at low and high current density regions. The model was compared and discussed with experimental results of Ni/YSZ anodes. In addition, in order to visualize active sites of porous electrodes, a power generation equipment with a quench system by helium gas impinging jet was constructed. By using the equipment and oxygen isotope labeling, active sites of LSM/ScSZ cathode was visualized. The obtained ^{18}O mapping first imaged highly-distributed active sites in microstructure scale.

Table of Contents

Chapters

Chapter 1

Introduction

1.1 Background

The population growth and accelerated modernization in the world are followed by the increase in energy consumptions and greenhouse gas emissions. In order to reduce those consumptions/emissions, the development of energy conversion technology with higher efficiency is strongly required in modern society. Compared to the current combustion-based energy conversion technologies which are generally used for automotive engines or power plants, fuel cells offer higher energy conversion efficiency and lower greenhouse gas emissions. This feature is originated from the principle of fuel cells: chemical energy is directly converted to electricity, resulting that the efficiency is not limited by the Carnot cycle [1]. The absence of high-temperature combustion process and of open flame front is also followed by the elimination of harmful pollutants formations such as SO_x, NO_x, volatile organic carbon (VOC), and particulate matters (PM) [1]. Moreover, fuel cells are expected to play a central role of future energy system based on hydrogen, which can be produced from various energy sources such as fossil fuels or renewable energy [2].

Figure 1-1 summarizes the efficiency of fuel cells and other energy conversion devices with respect to system size. This figure was made based on several information collected from websites and literatures [2-14]. Generally, the efficiency of combustion-

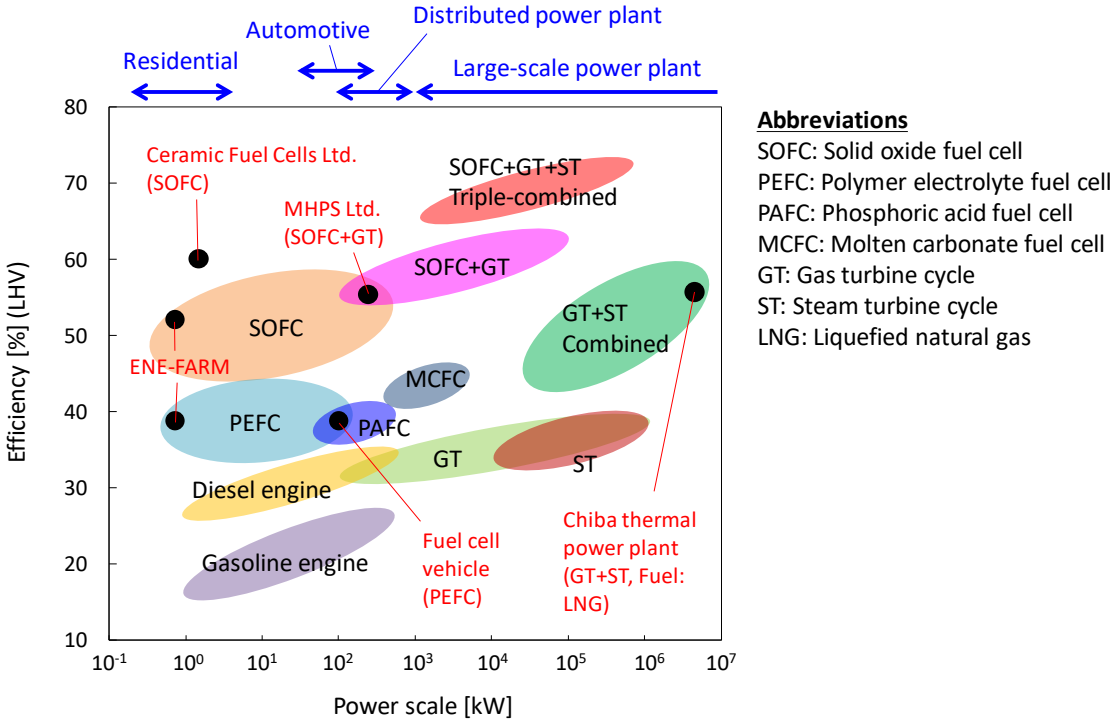

Figure 1-1. Efficiency of fuel cells and other energy conversion devices with respect to system size. The figure was made based on several sources [2-14].

based energy conversion increases with increasing the system size. In the case of heat engine, when the ratio of surface area to volume of the system decreases with increasing system size, the ratio of heat loss from surface to energy kept in its volume also decreases, resulting in the efficiency gain. For instance, the gas and steam turbines combined cycle in Chiba thermal power plant (Japan) shows the thermal efficiency of more than 55% at the system size of 10^6 kW scale [10]. On the other hand, the efficiency of fuel cells is, in principle, independent of power scale. Therefore, fuel cells have the advantage over heat engines especially at small system size ($< 10^3$ kW). In this scale, combustion-based technologies such as diesel or gasoline engines, or gas turbine cycle, show the efficiency of around 15 to 35% while fuel cells show 35 to 55% (LHV: lower heating value). This advantage has accelerated the development of fuel cell technologies for residential-scale

power generation system (1-5 kW), automotive power (~100 kW), and distributed power plant for smart grid energy system (100-1000 kW) as major applications (Fig. 1-1).

Fuel cells are generally categorized by their electrolyte material, such as phosphoric acid fuel cell (PAFC), molten carbonate fuel cell (MCFC), polymer electrolyte fuel cell (PEFC), and solid oxide fuel cell (SOFC). The main difference of those is operating temperature, which also determine the suitable applications. PAFC is typically operated at ~200 ℃ and possibly most-commercially developed fuel cells [2]. PAFC is mainly used for combined-heat-and-power (CHP) system in residences or buildings. PEFC can be applied for automotive power as well as stationary CHP system due to its low operating temperature (50-80 ℃). In Japan, the 1 kW-class residential CHP system with PEFC (ENE-FARM) was released in 2009 [7]. Moreover, the fuel cell vehicle (FCV) "MIRAI" with 100 kW-class PEFC has been commercialized by Toyota Motor Corporation in 2014 [8]. In contrast to PAFC or PEFC, MCFC and SOFC are typically operated at high-temperature range, ~650 ℃ and 700-1000 ℃, respectively. In addition to stationary CHP system for residences or buildings, these high-temperature fuel cells can be combined with heat engines such as gas or steam turbines. The combined system, which can give higher total thermal efficiency compared to individual utilization, is a promising candidate for distributed base-load power plants at 10^3 kW (MW) scale [1,2,11].

1.2 Solid oxide fuel cell (SOFC)

In this thesis, an SOFC is selected as a research object. The high operating temperature (700-1000 ℃) of SOFCs offers many advantages over other fuel cell technologies. First, SOFC gives highest conversion efficiency among all fuel cells as shown in Fig. 1-1. When hydrogen and oxygen is used as a fuel and oxidant, respectively,

maximum conversion efficiency of a fuel cell $\eta_{\max}$ is described as follows.

$$\eta_{\max} = \frac{\Delta G_f^{\circ}(\mathrm{H_2O})}{\Delta H_f^{\circ}(\mathrm{H_2O})} \tag{1.1}$$

Here, $\Delta G_f^{\circ}(\mathrm{H_2O})$ and $\Delta H_f^{\circ}(\mathrm{H_2O})$ represent the standard Gibbs free energy and enthalpy of H_2O formation, respectively. Although $\eta_{\max}$ decreases with increasing temperature, actual conversion efficiency of SOFCs is higher than that of low-temperature fuel cells such as PEFC or PAFC. This is because ion conductions and electrochemical reactions are generally enhanced at higher temperature, resulting that an internal resistance of a fuel cell decreases with increasing temperature [15]. Ceramic Fuel Cell Ltd. (Australia) has developed 1-2 kW class SOFC stack for residential units and achieved an electrical efficiency of 60%, which is extremely high for such a small power scale [11,12].

Second, precious metals such as Pt need not to be used as a catalyst for electrode reactions because the reaction rate is high enough at elevated temperature (~800 ℃), which is effective to reduce material costs. Third, in addition to hydrogen, various fuels such as hydrocarbon or biogas can be directly supplied to SOFCs because those fuels can be reformed to hydrogen on anode at high temperature. Subsequently, produced hydrogen is used for fuel cell reactions. Owing to the fuel flexibility, SOFCs can be operated with hydrocarbon-based fossil fuels such as natural gas. As a result, SOFC can be introduced on current hydrocarbon fuel infrastructure [16]. In other word, new hydrogen infrastructure needs not to be prepared for SOFCs, which is one of the biggest advantage over low-temperature fuel cells. Forth, high temperature exhaust heat generated in SOFC operation can be recovered and reused to further increase total thermal efficiency of the systems. As shown in Fig. 1-1, SOFC-gas turbine combined cycle and SOFC-gas turbine-steam turbine triple combined cycle can achieve electrical efficiency of 55-60% and 60-

70% (LHV), respectively [6].

In addition to above features originated form high operating temperature, design simplicity and flexibility of SOFCs, which are consisting of only solid components, is also advantages over other fuel cells. Two representative designs are planar and tubular types. Generally, the former shows higher performance and takes lower manufacturing cost while the later has higher mechanical strength and needs not to be sealed at high temperature to separate oxidant and fuel. Therefore, from a view point of the stability of stacks during long-term operation (several years), tubular design has the advantage [11].

Many advantages mentioned above have accelerated the development of SOFC technologies from components to systems, and the technology is currently in the early commercialization stage [17]. Several companies are conducting demonstration tests of SOFC operation, or have just started to sell SOFC power generation systems in the 2010's [11]. SOFCs with small power (less than ~10 kW) are generally applied to CHP systems

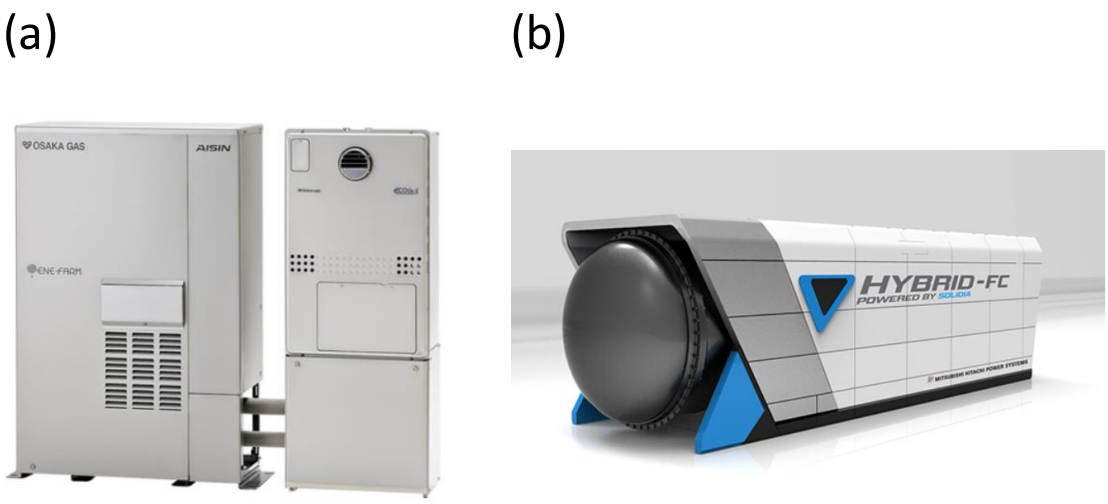

Figure 1-2. Commercialized SOFC products. (a) A 700 W SOFC combined heat and power (CHP) unit, ENE-FARM Type S [14]. (b) A 250 kW SOFC-micro gas turbine (MGT) hybrid system developed by Mitsubishi Hitachi Power Systems, Ltd. [18].

for residential buildings utilizing natural gas as a fuel. These CHP units have been developed by e.g. Ceramic Fuel Cell Ltd. (Australia), Hexis AG (Switzerland), and Osaka Gas in collaboration with Kyocera, Aisin, and Noritz (ENE-FARM Type S sold since 2012, Japan, shown in Fig.1-2(a) [14]). At present (2017), an electrical efficiency of the ENE-FARM Type S reaches 52% (LHV) [14]. Large scale (> ~100 kW) SOFC systems for distributed power generation have been also developed by e.g. Versa Power Systems (USA), Mitsubishi Hitachi Power Systems, Ltd. (MHPS, Japan), and Bloom Energy (USA). MHPS has commercialized 250 kW class SOFC-micro gas turbine (MGT) hybrid system with an electrical efficiency of 55% (LHV) in August 2017 as shown in Fig. 1-2(b) [6,18].

1.3 Principles and components of SOFC

SOFC generally consists of three main components, anode, electrolyte, and cathode. Figure1-3(a) shows the schematic of operated SOFC when hydrogen and oxygen is supplied at anode and cathode side, respectively. At the cathode, oxygen gas receives electrons from external circuit and becomes oxide ion. Generated oxide ion conducts through the electrolyte from the cathode to the anode. At the anode, water vapour is produced from hydrogen gas and oxide ion followed by the release of electrons to the external circuit, resulting in the production of electricity. The chemical equations at cathode and anode side are as follows.

$$\text{(Cathode)} \quad 1/2O_2 + 2e^- \rightarrow O^{2-} \tag{1.2}$$

$$\text{(Anode)} \quad H_2 + O^{2-} \rightarrow H_2O + 2e^- \tag{1.3}$$

As a result, total reaction in fuel cell operation is described as follows.

(Total) $1/2O_2 + H_2 \rightarrow H_2O$ (1.4)

The driving force of SOFC operation is equivalent to the oxygen partial pressure difference between two electrodes, and the electromotive force (EMF) of a cell is qualitatively expressed by Nernst Equation as follows.

$$\mathrm{EMF} = \Gamma \frac{RT}{4F} \ln\left[\frac{P_{O_2,\mathrm{cathode}}}{P_{O_2,\mathrm{anode}}}\right] \quad (1.5)$$

Here, Γ is the ionic transference number (ionic conductivity/total conductivity), T is operating temperature, F is Faraday constant, $P_{O_2,\mathrm{anode}}$ is oxygen partial pressure on the anode side, and $P_{O_2,\mathrm{cathode}}$ is on the cathode side. When no current passes through the cell, cell voltage corresponds to EMF (OCV: Open Circuit Voltage). Under cell operating conditions, cell voltage V decreases from EMF with increasing current density i due to the increase in several voltage losses as shown in Figure 1-4, and is described as follows.

$$V = \mathrm{EMF} - iR_{\mathrm{ohm}} - \eta_a - \eta_c \quad (1.6)$$

Here, iR_{ohm} shows an ohmic loss caused by conduction of ion and electron in the electrolyte, anode, and cathode. η_a and η_c shows anode and cathode overpotential, which is related to the electrochemical reactions and gas diffusions on each electrode. Each voltage loss should be reduced to increase power density of the cell.

Voltage losses mentioned above are strongly linked to the components of SOFCs. As an electrolyte, oxide materials with high oxide ionic conductivity at elevated temperature (600-1000 ºC) are used such as Y_2O_3-stabilized ZrO_2 (YSZ), Sc_2O_3-stabilized ZrO_2 (ScSZ), Gd_2O_3-doped CeO_2 (GDC), and Sm_2O_3-doped CeO_2 (SDC) [19]. Although ceria-based electrolyte shows higher oxide ion conductivity than those of zirconia-based ones, YSZ is the most practical electrolyte due to its high chemical

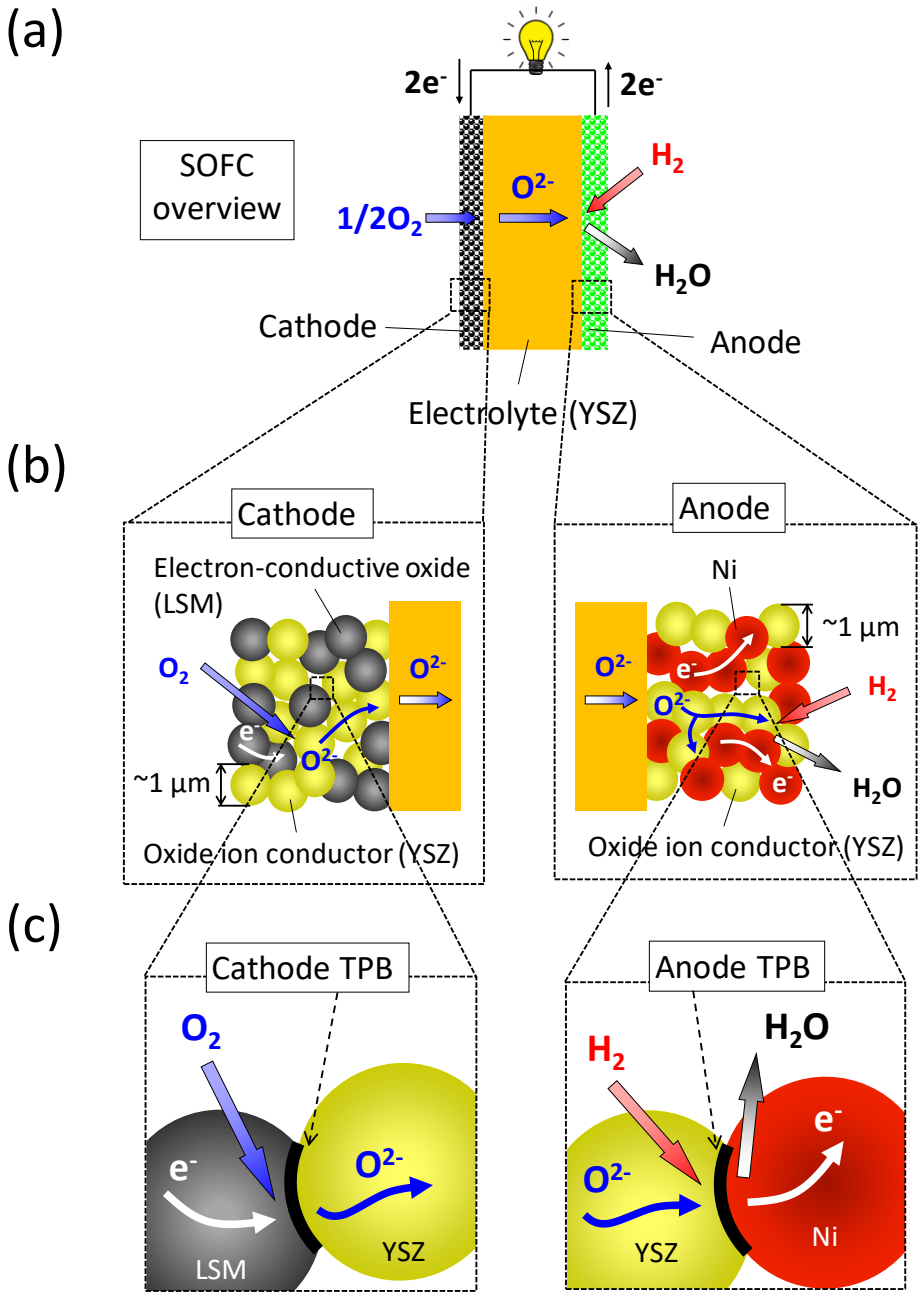

Figure 1-3. (a) Schematic of SOFC operated with hydrogen at anode and oxygen at cathode. (b) Schematics of porous composite cathode and Ni-cermet anode. (c) Enlarged views of electrodes particles near the triple phase boundary (TPB) in both anode and cathode.

stability and mechanical strength at elevated temperature in addition to the relatively low cost [11,19]. Figure 1-3(b) shows the detailed schematic of typical anode and cathode

used with YSZ electrolyte. Generally, porous composite electrodes are used for state-of-the-art SOFCs, such as Ni/YSZ for anodes or strontium-doped lanthanum manganite (LSM)/YSZ for cathodes [20,21]. These electrodes have micro/nano-scale complex structures consisting of electron conductors (Ni, LSM), oxide ion conductors (YSZ), and pore phases, where chemical species are transported and accompanied by electrochemical reactions. In these electrodes, electrochemical reaction is considered to occur at the triple phase boundary (TPB) of Ni/YSZ/gas phase for anode or LSM/YSZ/gas phase for cathode, as shown in Figure 1-3(c), because both anode and cathode reactions involve electrons, oxide ions, and gas species.

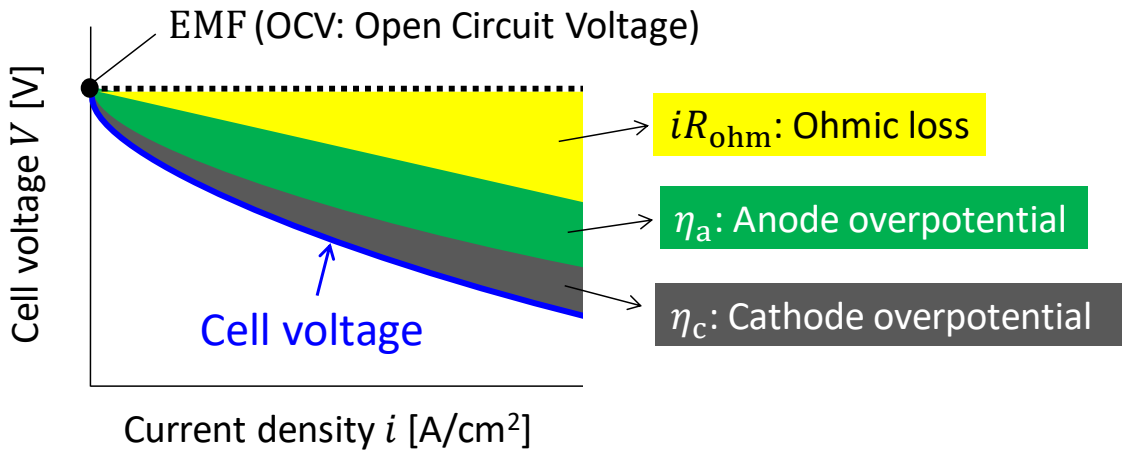

Figure 1-4. Terminal (cell) voltage of an SOFC with respect to current density. The voltage loss from OCV consists of ohmic loss, anode overpotential, and cathode overpotential.

1.4 Current status and challenges of SOFC

Intensive research and development on SOFCs has been conducted for more than 30 years, and the technology is currently in the early commercialization stage [17], as mentioned in section 1.2. For the widespread introduction of SOFC technologies to the

society, however, its material and system costs should be reduced and performance degradation issues during long-term operation need to be solved [22]. Lowering the operating temperature to intermediate range (600-800 ºC) is one of the major approach to overcome the former issues because cost-effective metallic materials can be used in this temperature range as an interconnect or other related components [16]. In order to achieve sufficient power density for practical applications, improvement of both electrolyte and electrodes performance at lower temperature is accelerated in SOFC field [16,22]. The latter issues, performance degradation, are originated from several factors such as sulfur poisoning [23,24], carbon deposition by hydrocarbon fuel [25-27], redox cycle [28,29], and Ni coarsening [30,31] on anode side or chromium poisoning [32,33], secondary phase formation between cathode and electrolyte [34,35], and segregation of strontium component [36,37] on cathode side. Intensive research and development for further understanding of these degradation mechanisms and improvement of SOFC durability has been conducted in recent days.

It is an inevitable and critical issue to enhance SOFC electrodes performance and stability in order to accomplish the operation at lower temperature and improvement of the lifetime for the widespread utilization. The performance of porous electrodes is dominated by following two phenomena; electrochemical reaction at the active sites and transport of gases, oxide ion, and electron in the porous structure. Moreover, degradation of electrodes performance mentioned above results from the change of active sites or transport paths of chemical species, which are blocked or reduced by deposited impurities, formed secondary phases, and microstructure changes through coarsening. Therefore, it is important to understand species transport phenomena coupled with electrochemical reactions proceeding inside porous electrodes precisely for further improvement of SOFC

performance and durability.

Species transport and electrochemical reactions in SOFC porous electrodes have been intensively investigated by numerical modeling and simulations [38-46]. Typical models based on effective medium theory make it possible to calculate averaged electric/ionic current distributions and to identify electrochemically active regions in composite electrodes [38-40]. In addition, numerical simulations of SOFC electrodes have been recently conducted based on actual microstructures obtained by a focused ion beam scanning electron microscope (FIB-SEM) [41-46]. In those simulations, gases, ions, and electron transport are solved by lattice Boltzmann method (LBM) [41,42], volume of fluid (VOF) method [43], finite element method (FEM) [44], sub-grid scale (SGS) method [45], or finite volume method (FVM) [46], and local three-dimensional distributions of ionic/electronic flows or electrical potential are provided. The development of those analysis and simulations can provide accurate description of transport phenomena inside SOFC electrodes. On the other hand, electrochemical reaction at the TPB has been mainly described by Butler-Volmer equation and exchange current density, which has been originally developed for reactions at interface between metal and liquid electrolyte [20]. In this scheme, all detailed reaction kinetics are lumped together into exchange current density, which is not established via phenomenological description but treated as fitting parameters [43] or given by empirical expressions [41,42,45,46]. For accurate prediction and physically-based interpretation of electrode performance, development of reliable electrochemical reaction model at the TPB based on elementary chemical reactions, such as adsorption of gas species, oxide ion migration, or surface reactions, are desired [45].

Several experimental studies have been also conducted to directly investigate

electrochemical reactions on SOFC electrodes. Oxygen chemical potential distributions of model (thin film) or porous cathodes were investigated at biased condition by microprobe oxygen sensor [47] or *in-situ* micro X-ray adsorption spectroscopy (XAS) [48,49]. Surface potential distribution of a cross section of the operated SOFC was detected by *in-situ* Kelvin force microscopy (KFM) [50]. In addition, atomic labeling using oxygen isotope has been introduced to visualize active reaction sites in thin film electrodes [51,52] or overall oxide ion flows in a practical SOFC [53]. However, experimental information about active reaction sites distribution or oxide ion paths in the microstructure of SOFC porous electrodes has not been reported so far. For validation of numerical results mentioned above, deeper understanding of species transport coupled with electrochemical reactions in the electrodes, and optimization of its microstructures, a visualization technique of active reaction sites and oxide ion paths in microstructure scale should be realized and developed.

1.5 Objectives and contents of thesis

For more accurate understanding and description of species transport phenomena coupled with electrochemical reactions proceeding inside SOFC, two main specific objectives toward construction of the detailed reaction kinetics and dynamics on porous electrodes are raised as the contents of current thesis below.

(i) Construction of analytical model for hydrogen oxidation in a TPB of SOFC anode based on elementary chemical reactions.

(ii) Development of visualization technique of active reaction sites and oxide ion paths in SOFC porous electrodes with microstructure scale.

In Chapter 1, background, principle, current status, and challenges of SOFC are

reviewed and summarized. In addition, the main specific targets of the thesis are raised and the structure of the thesis is explained. In Chapter 2, analytical model for hydrogen oxidation in an anode TPB, named as species territory adsorption model, is constructed based on elementary chemical reactions. It is shown that explicit expressions of current density and anode overpotential, and theoretical limit of current density can be derived from the model. In addition, the physical meaning of analytical results based on the model is discussed. In Chapter 3, the quantitative validation of species territory adsorption model is discussed. The dependence of anode overpotential on hydrogen partial pressure is experimentally investigated, which is compared to the model. All thermodynamic and kinetic parameters for the model are determined from referenced density functional theory (DFT)-database and careful fitting process between the analytical and experimental results. The analytical results are compared with several reported experimental results using Ni/YSZ cermet, and effective anode thickness predicted by the model is discussed. In Chapter 4, visualization technique of active reaction sites in SOFC porous electrodes with microstructure scale is developed. In order to quench a reaction, a SOFC power generation equipment with a nozzle for direct helium gas impinging jet to the cell is prepared. Using constructed quench system and oxygen isotope labeling, active sites of LSM/ScSZ composite cathode are visualized in microstructure scale. In Chapter 5, oxygen isotope exchange and quench experiment is conducted at 973 K. From the analysis of oxygen isotope diffusion profiles in YSZ electrolyte, quantitative oxide ion flux incorporated from a cathode/electrolyte interface to an electrolyte is estimated. Finally, the key findings and contributions in this study are summarized and future perspective is presented in Chapter 6.

References

[1] P. Singh, N.Q. Minh, *Int. J. Appl. Ceram. Technol.* 1 (1) (2004) 5–15.

[2] O.Z. Sharaf, M.F. Orhan, *Renew. Sust. Energ. Rev.* 32 (2014) 810–853.

[3] AIST website (http://www.aist.go.jp/aist_e/list/latest_research/2009/20091204/20091204.html).

[4] Shibaura Institute of Technology, Power & Energy Systems Lab. website (http://www.web.se.shibaura-it.ac.jp/kimi/study.php). (in Japanese)

[5] Ministry of Economy, Trade and Industry website, document "MHPS の燃料電池について" (http://www.meti.go.jp/committee/kenkyukai/energy_environment/jisedai_karyoku/pdf/003_01_00.pdf) (2015). (in Japanese)

[6] Fukuoka prefecture website, document "水素社会へ向けた MHPS における SOFC－マイクロガスタービンハイブリッドシステムの開発状況と今後の展開" (http://www.pref.fukuoka.lg.jp/uploaded/life/267507_52640768_misc.pdf) (2016). (in Japanese)

[7] Ministry of Economy, Trade and Industry website, document "家庭用燃料電池について" (http://www.meti.go.jp/committee/kenkyukai/energy/suiso_nenryodenchi/suiso_nenryodenchi_wg/pdf/002_01_00.pdf) (2014). (in Japanese)

[8] Toyota Motor Corporation website (http://toyota.jp/mirai/spec/). (in Japanese)

[9] Ministry of Economy, Trade and Industry, Agency for Natural Resources and Energy website, document "火力発電における論点" (http://www.enecho.meti.go.jp/committee/council/basic_policy_subcommittee/mitoshi/005/pdf/005_07.pdf) (2015). (in Japanese)

[10] TEPCO Fuel & Power, Inc. website (http://www.tepco.co.jp/fp/thermal-power/list/chiba.html). (in Japanese)

[11] S.C. Singhal, *WIREs Energy Environ.* 3 (2014) 179–194.

[12] R. Payne, J. Love, M. Kah, *ECS Transactions* 25 (2) (2009) 231–239.

[13] Panasonic Corporation website (https://panasonic.biz/appliance/FC/house_07.html). (in Japanese)

[14] AISIN SEIKI Co., Ltd. website (http://www.aisin.co.jp/cogene/enefarm.html). (in Japanese)

[15] 田川博章，固体酸化物燃料電池と地球環境，アグネ承風社 (1998). (in Japanese)

[16] E.D. Wachsman, K.T. Lee, *Science* 334 (2011) 935–939.

[17] N.Q. Minh, J. Mizusaki, S.C. Singhal, *ECS Transactions* 78 (1) (2017) 63–73.

[18] Mitsubishi Hitachi Power Systems, Ltd. website (http://www.mhps.com/jp/news/20170809.html). (in Japanese).

[19] K.C. Wincewicz, J.C. Cooper, *J. Power Sources* 140 (2005) 280–296.

[20] R.J. Gorte, J.M. Vohs, *Annu. Rev. Chem. Biomol. Eng.* 2 (2011) 9–30.

[21] J. Hanna, W.Y. Lee, Y. Shi, A.F. Ghoniem, *Prog. Energy Combust. Sci.* 40 (2014) 74–111.

[22] J.T.S. Irvine, P. Connor (Eds.), *Solid Oxide Fuel Cells: Facts and Figures*, Green Energy and Technology, Springer (2013).

[23] L. Yang, Z. Cheng, M. Liu, L. Wilson, *Energy. Environ. Sci.* 3 (2010) 1804–1809.

[24] D. Papurello, A. Lanzini, S. Fiorilli, F. Smeacetto, R. Singh, M. Santarelli, *Chem. Eng. J.* 283 (2016) 1224–1233.

[25] W. Wang, C. Su, Y. Wu, R. Ran, Z. Shao, Chem. Rev. 113 (2013) 8104–8151.

[26] K.S. Blinn, H. Abernathy, X. Li, M. Liu, L.A. Bottomley, M. Liu, *Energy. Environ. Sci.* 5 (2012) 7913–7917.

[27] H. Xu, Z. Dang, *Appl. Energy* 178 (2016) 294–307.

[28] H. Yokokawa, H. Tu, B. Iwanschitz, A. Mai, *J. Power Sources* 182 (2008) 400–412.

[29] T. Shimura, Z. Jiao, S. Hara, N. Shikazono, *J. Power Sources* 267 (2014) 58–68.

[30] F. Abdeljawad, B. Völker, R. Davis, R.M. McMeeking, M. Haataja, *J. Power Sources* 250 (2014) 319–331.

[31] J.S. Cronin, J.R. Wilson, S.A. Barnett, *J. Power Sources* 196 (2011) 2640–2643.

[32] E. Park, S. Taniguchi, T. Daio, J-T. Chou, K. Sasaki, *Solid State Ionics* 262 (2014) 421–427.

[33] K. Miyoshi, H. Iwai, M. Kishimoto, M. Saito, H. Yoshida, *J. Power Sources* 326 (2016) 331–340.

[34] S-Y. Park, J.H. Ahn, C-W. Jeong, C-W. Na, R-H. Song, J-H. Lee, *Int. J. Hydrog. Energy* 39 (2014) 12894–12903.

[35] F. Wang, M.E. Brito, K. Yamaji, D-H.Cho, M. Nishi, H. Kishimoto, T. Horita, H. Yokokawa, *Solid State Ionics* 262 (2014) 454–459.

[36] G.M. Rupp, A.K. Opitz, A. Nenning, A. Limbeck, J. Fleig, *Nat. Mater.* 16 (2017) 640–645.

[37] H. Ding, A.V. Virkar, M. Liu, F. Liu, *Phys. Chem. Chem. Phys.* 15 (2013) 489–496.

[38] P. Costamagna, P. Costa, V. Antonucci, *Electrochim. Acta* 43 (1998) 375–394.

[39] J. H. Nam, D. H. Jeon, *Electrochim. Acta* 51 (2006) 3446–3460.

[40] A. Banerjee, O. Deutschmann, *J. Catal.* 346 (2017) 30–49.

[41] N. Shikazono, D. Kanno, K. Matsuzaki, H. Teshima, S. Sumino, N. Kasagi, *J. Electrochem. Soc.* 157 (5) (2010) B665–B672.

[42] K. Matsuzaki, N. Shikazono, N. Kasagi, *J. Power Sources* 196 (2011) 3073–3082.

[43] P.R. Shearing, Q. Cai, J.I. Golbert, V. Yufit, C.S. Adjiman, N.P. Brandon, *J. Power Sources* 195 (2010) 4804–4810.

[44] T. Carraro, J. Joos, B. Rüger, A. Weber, E. I-Tiffée, *Electrochim. Acta* 77 (2012) 315–

325.

[45] M. Kishimoto, H. Iwai, M. Saito, H. Yoshida, *J. Electrochem. Soc.* 159 (3) (2012) B315–B323.

[46] K. Miyoshi, T. Miyamae, H. Iwai, M. Saito, M. Kishimoto, H. Yoshida, *J. Power Sources* 315 (2016) 63–69.

[47] T. Kawada, M. Sase, M. Kudo, K. Yashiro, K. Sato, J. Mizusaki, N. Sakai, T. Horita, K. Yamaji, H. Yokokawa, *Solid State Ionics* 177 (2006) 3081–3086.

[48] Y. Fujimaki, H. Watanabe, Y. Terada, T. Nakamura, K. Yashiro, S. Hashimoto, T. Kawada, K. Amezawa, *ECS Transactions* 57 (1) (2013) 1925–1932.

[49] K. Amezawa, Y. Fujimaki, T. Nakamura, K.D. Bagarinao, K. Yamaji, K. Nitta, Y. Terada, F. Iguchi, K. Yashiro, H. Yugami, T. Kawada, *ECS Transactions* 66 (2) (2015) 129–135.

[50] S.S. Nonnenmann, R. Kungas, J. Vohs, D.A. Bonnell, *ACS Nano* 7 (7) (2013) 6330–6336.

[51] T. Horita, K. Yamaji, N. Sakai, H. Yokokawa, T. Kawada, T. Kato, *Solid State Ionics* 127 (2000) 55–65.

[52] J. Fleig, A. Schintlmeister, A.K. Opitz, H. Hutter, *Scripta Mater.* 65 (2011) 78–83.

[53] T. Horita, T. Shimonosono, H. Kishimoto, K. Yamaji, M.E. Brito, Y. Hori, H. Yokokawa, *Electrochem. Solid-State Lett.* 13 (12) (2010) B135–B138.

Chapter 2

Species territory adsorption model for hydrogen oxidation in SOFC anode

2.1 Introduction

Porous composite electrodes such as Ni/YSZ, Ni/ScSZ, or Ni/GDC are widely used for state-of-the-art SOFC anode [1]. In these anodes, hydrogen oxidation is considered to occur mainly at the triple phase boundary (TPB) consisting of Ni, YSZ (ScSZ, GDC), and gas phases because hydrogen should be reacted with oxide ion accompanied with release of electrons [2,3]. For accurate prediction and physically-based interpretation of anode performance, clarifying the reaction mechanism at the TPB is indispensable and the development of reliable electrochemical reaction model based on elementary chemical reactions is desired. Various reaction mechanisms around the anode TPB have been proposed and discussed for past two decades [4-11]. Among these works, Ihara et al. regarded a Ni/YSZ/gas TPB as one dimensional line and proposed competitive adsorption mechanism among adsorbed species, i.e., H_{ad}, H_2O_{ad}, and O_{ad} on the TPB as shown in Figure 2-1 [7]. They assumed that the reaction rate is determined by surface reaction between H_{ad} and O_{ad} to produce H_2O_{ad} (Langmuir-Hinshelwood mechanism). Based on their model, the analytical expression of current density is derived as a function of oxygen activity in anode TPB, which could demonstrate experimental trends qualitatively.

On the other hand, some researches have recently shown that addition of perovskite

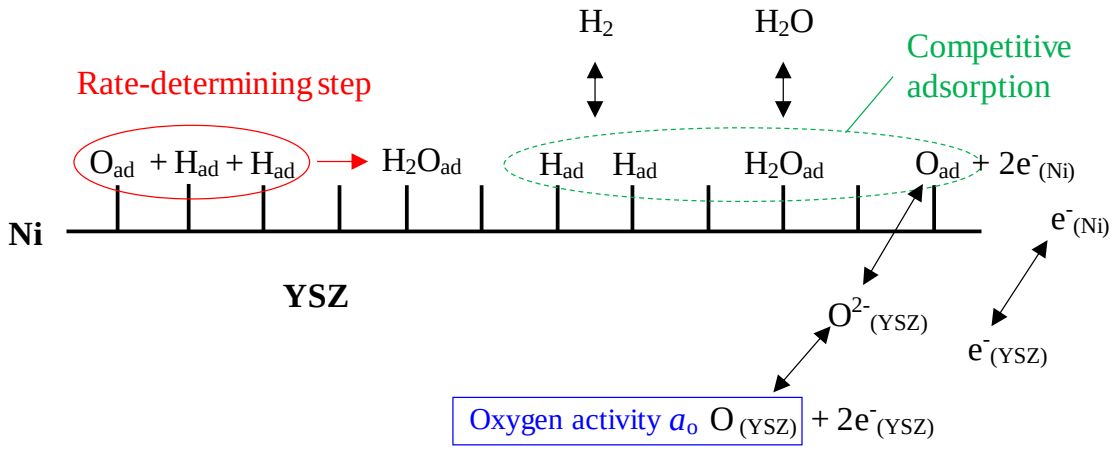

Figure 2-1. Schematic of competitive adsorption mechanism on Ni/YSZ anode proposed by Ihara et al [7].

proton conductors, such as $SrZr_{0.95}Y_{0.05}O_{3-x}$ (SZY) or $BaCe_{0.8}Y_{0.2}O_{3-x}$ (BCY) to Ni/YSZ or Ni/GDC cermet anodes is an effective way to improve anode electrochemical properties in hydrogen and hydrocarbon fuel [12-17]. Among them, it was shown that anode overpotential is reduced by adding BCY particles to Ni/GDC cermet anode [12]. In addition, thermal desorption spectroscopy (TDS) measurement disclosed that BCY adsorbs a significant amount of hydrogen [13]. Consequently, it was concluded that adsorbed hydrogen on BCY is supplied to Ni/GDC/gas TPB and the anodic reaction is enhanced as shown in Figure 2-2, resulting in the reduction of anode overpotential [13]. However, the above enhanced anodic reaction cannot be explained well by the competitive adsorption mechanism [7] because in this model, additionally supplied hydrogens from BCY adsorb on the TPB and fill the vacancy sites, resulting in a reduction of adsorbed oxygen, i.e., a decrease in reaction rate.

In a conventional cermet anode consisting of Ni and oxide ion conductor, hydrogen is mainly adsorbed onto the Ni surface, which has been confirmed by thermal desorption spectroscopy (TDS) measurement [13]. On the other hand, most of oxygen would be

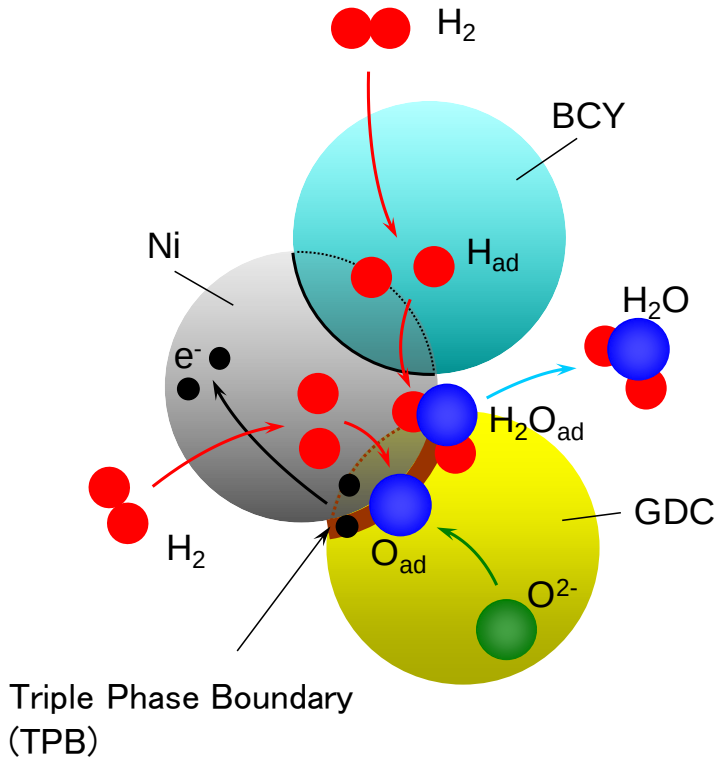

Figure 2-2. Schematic of the reaction mechanism for overpotential reduction in Ni/GDC-BCY anode [13].

adsorbed onto the surface of the oxide ion conductor around the TPB after the oxide ions released their electrons to the Ni bulk. Then, the adsorbed hydrogen reacts with the adsorbed oxygen at the TPB. Consequently, these species are adsorbed in a finite area around the TPB and do not necessarily occupy the same adsorption sites.

In this chapter, new analytical model for hydrogen oxidation in an anode TPB, named as species territory adsorption model, is constructed based on the Langmuir-type surface reaction between adsorbed hydrogen and oxygen, and on the other reactions at chemical equilibrium. The chemical species are assumed to be adsorbed in a finite surface area of Ni and oxide ion conductor around the TPB. First, explicit expressions of current density and anode overpotential, and theoretical limit of current density are derived based

on the model. Next, typical analytical results obtained by the model are shown, and the physical meanings of those are discussed.

2.2 Model construction

2.2.1 Assumptions

In this model, hydrogen oxidation at conventional cermet anode consisting of Ni and oxide ion conductor particles is considered. According to the percolation theory, to retain the network structure of each particle for conduction of ion or electron, the particle number concentration in the anode should be greater than 30% [18]. For simplicity, it is assumed that the particle size is uniform and the concentrations are the same. As a result, the unit structure of cermet anode consisting of Ni and oxide ion conductor can be considered as shown in Figure 2-3(a). Herein, the following assumptions are considered:

(i) The overall reaction rate is controlled by the surface reaction between the adsorbed hydrogen, H_{ad}, and the adsorbed oxygen, O_{ad}. The other reactions take place under chemical equilibrium conditions [equilibrium constants are expressed as K_i (i: each species)] because the reaction rates are much faster than the surface reactions.

(ii) Chemical species are adsorbed within finite areas, described as Area 1 and Area 2, on the surface of each material around the TPB.

(iii) H_2 molecules are adsorbed in Area 1, whereas H_2O molecules are adsorbed in Areas 1 and 2.

(iv) Adsorbed hydrogen, H_{ad}, can be moved between Areas 1 and 2.

(v) Adsorbed water, H_2O_{ad}, and oxygen, O_{ad}, can be moved between Areas 1 and 2.

Fig. 2-3(b) shows a schematic of the cross section of the TPB consisting of Ni, oxide ion conductor, and gas phases. The following assumption is considered:

(vi) In a reaction process from oxide ions in the conductor to adsorbed oxygen on Area 2, each reaction takes place under chemical equilibrium [7].

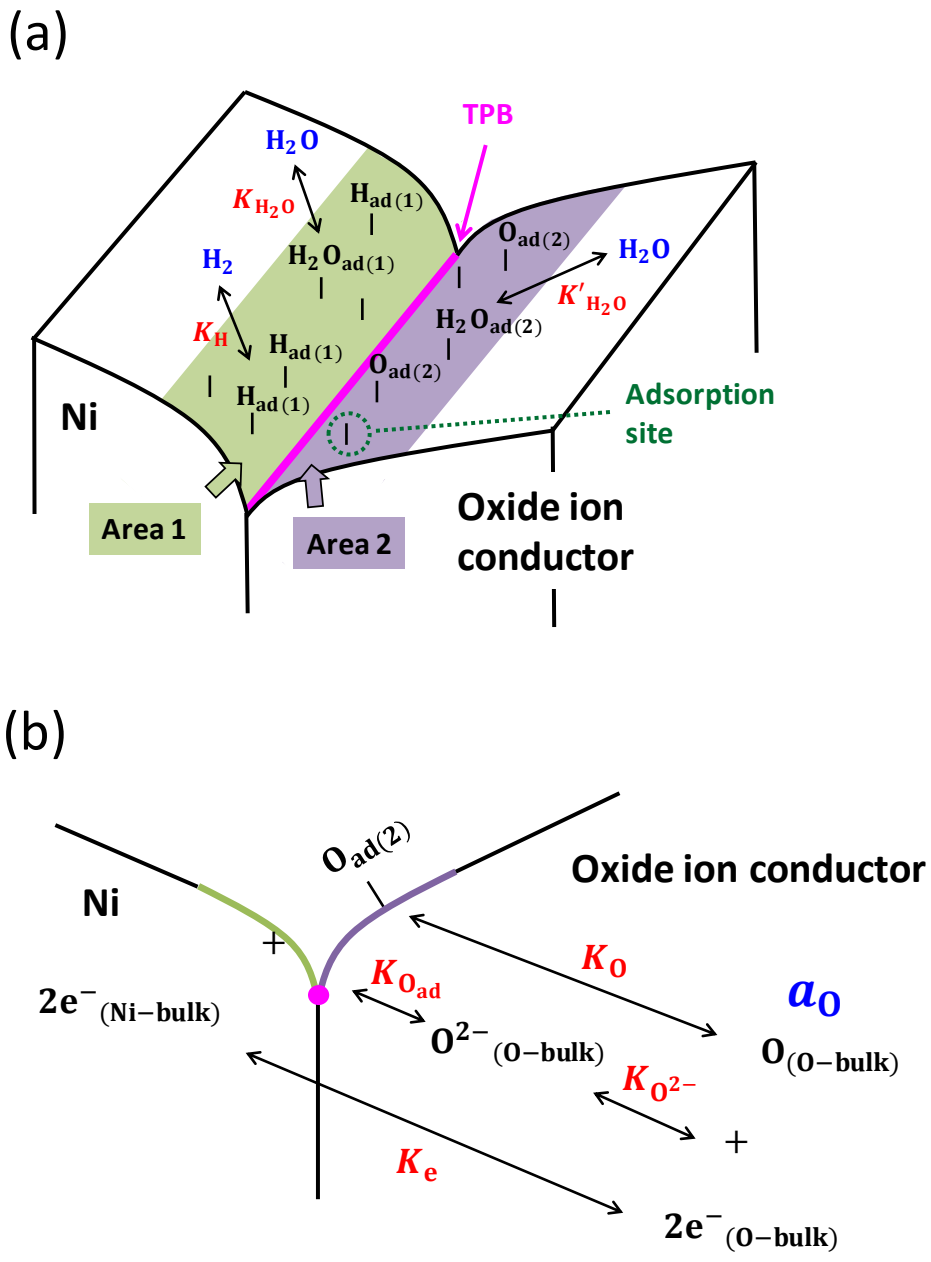

Figure 2-3. (a) Schematic of the TPB consisting of Ni and oxide ion conductor assumed in present model. (b) Schematic of the cross section of the interface between Ni and oxide ion conductor.

2.2.2 Reactions under chemical equilibrium

Based on the above assumptions for reactions under chemical equilibrium, the adsorption of H_2 and H_2O from the gas phase to Area 1 is described as follows:

$$H_2 + 2V_{ad(1)} \xleftrightarrow{K_H} 2H_{ad(1)} \tag{2.1}$$

$$H_2O + V_{ad(1)} \xleftrightarrow{K_{H_2O}} H_2O_{ad(1)} \tag{2.2}$$

Here, V represents adsorption sites on the surface and the subscript (1) denotes Area 1. Similarly, the adsorption of H_2O on Area 2 is expressed as follows:

$$H_2O + V_{ad(2)} \xleftrightarrow{K'_{H_2O}} H_2O_{ad(2)} \tag{2.3}$$

Adsorbed species, H_{ad}, O_{ad}, and H_2O_{ad} are assumed to be exchanged between Areas 1 and 2 through the following reactions:

$$H_{ad(1)} + V_{ad(2)} \xleftrightarrow{K_{H(ex12)}} H_{ad(2)} + V_{ad(1)} \tag{2.4}$$

$$O_{ad(2)} + V_{ad(1)} \xleftrightarrow{K_{O(ex12)}} O_{ad(1)} + V_{ad(2)} \tag{2.5}$$

$$H_2O_{ad(1)} + V_{ad(2)} \xleftrightarrow{K_{H_2O(ex12)}} H_2O_{ad(2)} + V_{ad(1)} \tag{2.6}$$

Reactions for the process from oxide ions in oxide ion conductor bulk to adsorbed oxygen on Area 2 are expressed as follows [7]:

$$O_{(O\text{-}bulk)} + 2e^-_{(O\text{-}bulk)} \xleftrightarrow{K_{O^{2-}}} O^{2-}_{(O\text{-}bulk)} \tag{2.7}$$

$$O_{(O\text{-}bulk)} + V_{ad(2)} \xleftrightarrow{K_O} O_{ad(2)} \tag{2.8}$$

$$O^{2-}_{(O\text{-}bulk)} + V_{ad(2)} \xleftrightarrow{K_{O_{ad}}} O_{ad(2)} + 2e^-_{(Ni\text{-}bulk)} \tag{2.9}$$

$$e^-_{(Ni\text{-}bulk)} \xleftrightarrow{K_e} e^-_{(O\text{-}bulk)} \tag{2.10}$$

Here, $O_{(O\text{-}bulk)}$ refers to oxygen atoms in the conductor bulk and corresponds to the oxygen activity, a_O, in experiments.

For H_{ad}, O_{ad}, and H_2O_{ad}, competitive adsorption should be assumed on Areas 1 and 2. The coverage of the adsorbed species i (i = H, O, H_2O, V) in Area k (k = 1, 2) is expressed by $\theta_{i(k)}$, which means the ratio of adsorbed species to all adsorption sites. On the surfaces of Areas 1 and 2, the summations of coverages should be both equal to unity as follows:

$$\theta_{\mathrm{H}(1)} + \theta_{\mathrm{O}(1)} + \theta_{\mathrm{H_2O}(1)} + \theta_{V(1)} = 1 \tag{2.11}$$

$$\theta_{\mathrm{H}(2)} + \theta_{\mathrm{O}(2)} + \theta_{\mathrm{H_2O}(2)} + \theta_{V(2)} = 1 \tag{2.12}$$

Using the coverages and partial pressure of molecules in the gas phase, the equilibrium constants of reactions (2.1), (2.2), (2.3), and (2.8) are described as follows:

$$K_{\mathrm{H}} = \frac{\theta_{\mathrm{H}(1)}{}^{2}}{P_{\mathrm{H_2}} \theta_{V(1)}{}^{2}} \tag{2.13}$$

$$K_{\mathrm{H_2O}} = \frac{\theta_{\mathrm{H_2O}(1)}}{P_{\mathrm{H_2O}} \theta_{V(1)}} \tag{2.14}$$

$$K'_{\mathrm{H_2O}} = \frac{\theta_{\mathrm{H_2O}(2)}}{P_{\mathrm{H_2O}} \theta_{V(2)}} \tag{2.15}$$

$$K_{\mathrm{O}} = \frac{\theta_{\mathrm{O}(2)}}{a_{\mathrm{O}} \theta_{V(2)}} \tag{2.16}$$

Here, $P_{\mathrm{H_2}}$ and $P_{\mathrm{H_2O}}$ are the partial pressures of hydrogen and water vapour, respectively. a_{O} expresses the oxygen activity in the oxide ion conductor bulk near the surface in Area 2. Moreover, the equilibrium constant, K_{O}, can be expressed using $K_{\mathrm{O^{2-}}}$, $K_{\mathrm{O_{ad}}}$, and K_{e} in reactions (2.7), (2.9), and (2.10) as follows

$$K_{\mathrm{O}} = K_{\mathrm{O^{2-}}} K_{\mathrm{O_{ad}}} K_{\mathrm{e}}{}^{2} \tag{2.17}$$

In addition, the equilibrium constants of reactions (2.4)–(2.6) are described as follows.

$$K_{\mathrm{H(ex12)}} = \frac{\theta_{\mathrm{H}(2)}\theta_{V(1)}}{\theta_{\mathrm{H}(1)}\theta_{V(2)}} \tag{2.18}$$

$$K_{\mathrm{O(ex12)}} = \frac{\theta_{\mathrm{O}(1)}\theta_{V(2)}}{\theta_{\mathrm{O}(2)}\theta_{V(1)}} \tag{2.19}$$

$$K_{\mathrm{H_2O(ex12)}} = \frac{\theta_{\mathrm{H_2O}(2)}\theta_{V(1)}}{\theta_{\mathrm{H_2O}(1)}\theta_{V(2)}} = \frac{K'_{\mathrm{H_2O}}}{K_{\mathrm{H_2O}}} \tag{2.20}$$

Here, Eq. (2.20) shows that $K_{\mathrm{H_2O(ex12)}}$ can be described by Eqs. (2.14) and (2.15).

Using Eqs. (2.11)–(2.20), all coverages in Areas 1 and 2, $\theta_{i(k)}$, can be solved and expressed explicitly as follows:

$$\theta_{V(1)} = \frac{1}{1+\sqrt{K_{\mathrm{H}}P_{\mathrm{H_2}}}+K_{\mathrm{O(ex12)}}K_{\mathrm{O}}a_{\mathrm{O}}+K_{\mathrm{H_2O}}P_{\mathrm{H_2O}}} \tag{2.21}$$

$$\theta_{\mathrm{H}(1)} = \frac{\sqrt{K_{\mathrm{H}}P_{\mathrm{H_2}}}}{1+\sqrt{K_{\mathrm{H}}P_{\mathrm{H_2}}}+K_{\mathrm{O(ex12)}}K_{\mathrm{O}}a_{\mathrm{O}}+K_{\mathrm{H_2O}}P_{\mathrm{H_2O}}} \tag{2.22}$$

$$\theta_{\mathrm{O}(1)} = \frac{K_{\mathrm{O(ex12)}}K_{\mathrm{O}}a_{\mathrm{O}}}{1+\sqrt{K_{\mathrm{H}}P_{\mathrm{H_2}}}+K_{\mathrm{O(ex12)}}K_{\mathrm{O}}a_{\mathrm{O}}+K_{\mathrm{H_2O}}P_{\mathrm{H_2O}}} \tag{2.23}$$

$$\theta_{\mathrm{H_2O}(1)} = \frac{K_{\mathrm{H_2O}}P_{\mathrm{H_2O}}}{1+\sqrt{K_{\mathrm{H}}P_{\mathrm{H_2}}}+K_{\mathrm{O(ex12)}}K_{\mathrm{O}}a_{\mathrm{O}}+K_{\mathrm{H_2O}}P_{\mathrm{H_2O}}} \tag{2.24}$$

$$\theta_{V(2)} = \frac{1}{1+K_{\mathrm{H(ex12)}}\sqrt{K_{\mathrm{H}}P_{\mathrm{H_2}}}+K_{\mathrm{O}}a_{\mathrm{O}}+K'_{\mathrm{H_2O}}P_{\mathrm{H_2O}}} \tag{2.25}$$

$$\theta_{\mathrm{H}(2)} = \frac{K_{\mathrm{H(ex12)}}\sqrt{K_{\mathrm{H}}P_{\mathrm{H_2}}}}{1+K_{\mathrm{H(ex12)}}\sqrt{K_{\mathrm{H}}P_{\mathrm{H_2}}}+K_{\mathrm{O}}a_{\mathrm{O}}+K'_{\mathrm{H_2O}}P_{\mathrm{H_2O}}} \tag{2.26}$$

$$\theta_{\mathrm{O}(2)} = \frac{K_{\mathrm{O}}a_{\mathrm{O}}}{1+K_{\mathrm{H(ex12)}}\sqrt{K_{\mathrm{H}}P_{\mathrm{H_2}}}+K_{\mathrm{O}}a_{\mathrm{O}}+K'_{\mathrm{H_2O}}P_{\mathrm{H_2O}}} \tag{2.27}$$

$$\theta_{H_2O(2)} = \frac{K'_{H_2O} P_{H_2O}}{1 + K_{H(ex12)} \sqrt{K_H P_{H_2}} + K_O a_O + K'_{H_2O} P_{H_2O}} \tag{2.28}$$

The details of derivation are shown in Appendix A.

2.2.3 Reaction rate controlled by the surface reaction in Areas 1 and 2

Based on assumption (i), the overall reaction rate is controlled by the surface reaction between H_{ad} and O_{ad} to produce H_2O_{ad} (Langmuir-type reaction). In this case, ten combinations of reactions can be considered as shown in Table 2-1. For instance, in the case of reaction (I) in Table 2-1, two adsorbed hydrogens, H_{ad}, in Area 1 react with O_{ad} in Area 2 to produce H_2O_{ad} in Area 1, and the adsorption sites, V_{ad}, in Areas 1 and 2 are simultaneously produced as follows:

$$2H_{ad(1)} + O_{ad(2)} \underset{k_{cI}}{\overset{k_{aI}}{\rightleftarrows}} H_2O_{ad(1)} + V_{ad(1)} + V_{ad(2)} \tag{2.29}$$

Here, k_{aI} and k_{cI} are the rate constants of anodic and cathodic reactions in reaction (I). The rate constants k_{aj} and k_{cj} for reaction j $(= I - X)$ [A/cm^2] include factors of the surface reaction rate and the length of the TPB as follows:

Table 2-1. Combination of the surface reaction in the anode; 1 and 2 represent Areas 1 and 2, respectively.

Reaction no.	H_{ad}	H_{ad}	O_{ad}	↔	H_2O_{ad}	V_{ad}	V_{ad}
(I)	1	1	2	↔	1	1	2
(II)	1	1	2	↔	2	1	1
(III)	1	1	1	↔	1	1	1
(IV)	2	2	1	↔	1	2	2
(V)	2	2	1	↔	2	1	2
(VI)	2	2	2	↔	2	2	2
(VII)	1	2	1	↔	1	1	2
(VIII)	1	2	1	↔	2	1	1
(IX)	1	2	2	↔	1	2	2
(X)	1	2	2	↔	2	1	2

$$k_{a(c)j} = zFl_{\mathrm{TPB}}k'_{a(c)j} \tag{2.30}$$

Herein, a valence z (=2), Faraday constant F [C/mol], length of the TPB per unit area l_{TPB} [cm/cm^2], and rate constant per unit TPB length $k'_{a(c)j}$ [mol/(s•cm)] are used, where l_{TPB} is calculated by the anode thickness t [μm], and the TPB density ρ_{TPB} [μm/μm^3] ($l_{TPB} = t\rho_{\mathrm{TPB}} \times 10^4$).

The net current density generated by reaction (I), i_I, is described as the difference between the anodic current density, i_{aI}, and the cathodic current density, i_{cI}, as shown in Eq. (2.31). Each current density is described by the reaction rate constants and the coverages of adsorbed species.

$$i_I = i_{aI} - i_{cI} = k_{aI}\theta_{\mathrm{H}(1)}{}^2\theta_{\mathrm{O}(2)} - k_{cI}\theta_{\mathrm{H_2O}(1)}\theta_{V(1)}\theta_{V(2)} \tag{2.31}$$

Similarly, i_j for $j = II - X$ is described as Eqs. (2.32)–(2.40), respectively.

$$i_{II} = i_{aII} - i_{cII} = k_{aII}\theta_{\mathrm{H}(1)}{}^2\theta_{\mathrm{O}(2)} - k_{cII}\theta_{\mathrm{H_2O}(2)}\theta_{V(1)}{}^2 \tag{2.32}$$

$$i_{III} = i_{aIII} - i_{cIII} = k_{aIII}\theta_{\mathrm{H}(1)}{}^2\theta_{\mathrm{O}(1)} - k_{cIII}\theta_{\mathrm{H_2O}(1)}\theta_{V(1)}{}^2 \tag{2.33}$$

$$i_{IV} = i_{aIV} - i_{cIV} = k_{aIV}\theta_{\mathrm{H}(2)}{}^2\theta_{\mathrm{O}(1)} - k_{cIV}\theta_{\mathrm{H_2O}(1)}\theta_{V(2)}{}^2 \tag{2.34}$$

$$i_V = i_{aV} - i_{cV} = k_{aV}\theta_{\mathrm{H}(2)}{}^2\theta_{\mathrm{O}(1)} - k_{cV}\theta_{\mathrm{H_2O}(2)}\theta_{V(1)}\theta_{V(2)} \tag{2.35}$$

$$i_{VI} = i_{aVI} - i_{cVI} = k_{aVI}\theta_{\mathrm{H}(2)}{}^2\theta_{\mathrm{O}(2)} - k_{cVI}\theta_{\mathrm{H_2O}(2)}\theta_{V(2)}{}^2 \tag{2.36}$$

$$i_{VII} = i_{aVII} - i_{cVII} = k_{aVII}\theta_{\mathrm{H}(1)}\theta_{\mathrm{H}(2)}\theta_{\mathrm{O}(1)} - k_{cVII}\theta_{\mathrm{H_2O}(1)}\theta_{V(1)}\theta_{V(2)} \tag{2.37}$$

$$i_{VIII} = i_{aVIII} - i_{cVIII} = k_{aVIII}\theta_{\mathrm{H}(1)}\theta_{\mathrm{H}(2)}\theta_{\mathrm{O}(1)} - k_{cVIII}\theta_{\mathrm{H_2O}(2)}\theta_{V(1)}{}^2 \tag{2.38}$$

$$i_{IX} = i_{aIX} - i_{cIX} = k_{aIX}\theta_{\mathrm{H}(1)}\theta_{\mathrm{H}(2)}\theta_{\mathrm{O}(2)} - k_{cIX}\theta_{\mathrm{H_2O}(1)}\theta_{V(2)}{}^2 \tag{2.39}$$

$$i_X = i_{aX} - i_{cX} = k_{aX}\theta_{\mathrm{H}(1)}\theta_{\mathrm{H}(2)}\theta_{\mathrm{O}(2)} - k_{cX}\theta_{\mathrm{H_2O}(2)}\theta_{V(1)}\theta_{V(2)} \tag{2.40}$$

As a result, the total current density, i_{total}, is expressed by the summation of current densities i_j ($j = I, II, \cdots, X$) for each reaction from (I) to (X) in Table 2-1 [summation of Eqs. (2.31)–(2.40)].

$$i_{\mathrm{total}} = \sum_{j=I}^{X} i_j \tag{2.41}$$

2.2.4 Competitive adsorption model and species territory adsorption model

The equilibrium constants for the exchange of species, $K_{\mathrm{H(ex12)}}$, $K_{\mathrm{O(ex12)}}$, and $K_{\mathrm{H_2O(ex12)}}$ can be assumed to be a value from 0 to unity, and these values correspond to the distribution of coverage of adsorbed species as shown in Figure 2-4.

When $K_{\mathrm{H(ex12)}} = K_{\mathrm{O(ex12)}} = K_{\mathrm{H_2O(ex12)}} = 1$, the coverage for each species in Areas 1 and 2 are the same, i.e., $\theta_{i(1)} = \theta_{i(2)}$ (i = H, O, H_2O, V) in Eqs. (2.11), (2.12), and (2.18)–(2.20). As a result, this model is mathematically reduced to that of the conventional competitive adsorption at the TPB [7].

On the other hand, there is no mutual migration of adsorbed hydrogen and oxygen when $K_{\mathrm{H(ex12)}} = K_{\mathrm{O(ex12)}} = 0$. As a result, hydrogen can only be adsorbed in Area 1 and oxygen only in Area 2; that is, $\theta_{\mathrm{O(1)}} = \theta_{\mathrm{H(2)}} = 0$. As a result, only surface reactions (I) and (II) among the combinations listed in Table 2-1 would be dominant in this model. We defined this model as the "species territory adsorption model".

For any values of $K_{\mathrm{H(ex12)}}$ and $K_{\mathrm{O(ex12)}}$ between 0 and unity, hydrogen and oxygen can be assumed to be adsorbed on both surfaces in Areas 1 and 2. In this case, even if the hydrogen coverage in Area 1 reaches unity, hydrogen will migrate and be continuously adsorbed in Area 2 with a uniform coverage. Similarly, even if the coverage of oxygen in Area 2 reaches unity, oxygen will migrate and be continuously adsorbed in Area 1. The migration of adsorbed species is described by the equilibrium constants for

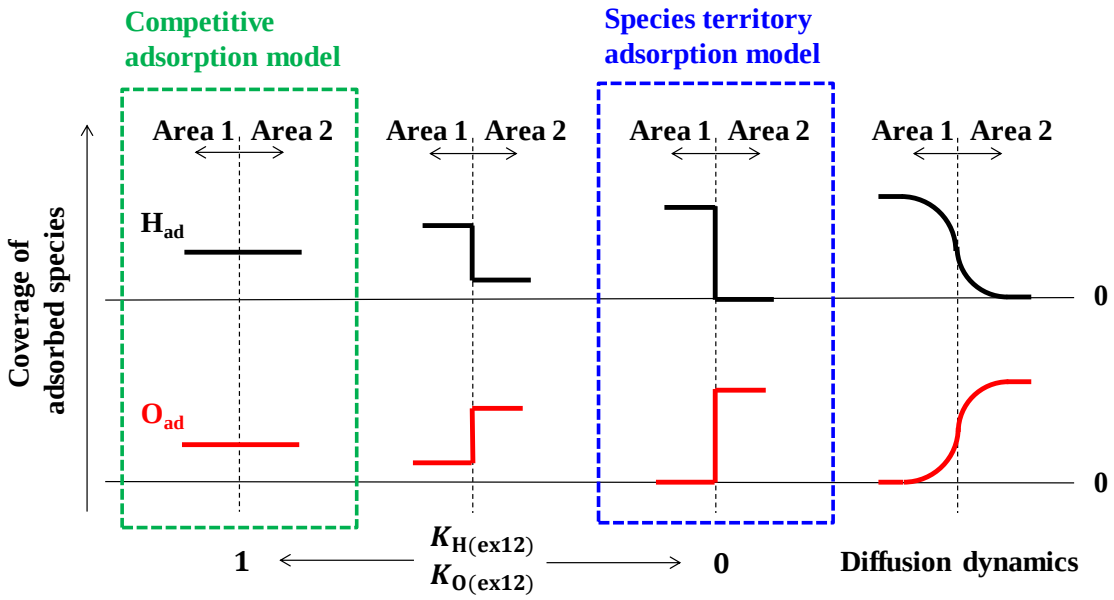

Figure 2-4. Relationship between the coverage of the adsorbed species near the TPB between Areas 1 and 2 and the equilibrium constants for species exchanges. Schematic for practical diffusion dynamics is also shown.

exchange instead of the diffusion coefficients in practical dynamics, as shown in Fig. 2-4.

To discuss the physical meaning of $K_{\mathrm{H(ex12)}}$ and $K_{\mathrm{O(ex12)}}$, the effect of those values on variations of the current density with respect to the oxygen activity, a_{O}, was investigated based on Eq. (2.41) as shown in Figure 2-5. In order to focus on the mutual migration of adsorbed hydrogen and oxygen between Areas 1 and 2, $K_{\mathrm{H_2O(ex12)}}$ was fixed to unity ($K_{\mathrm{H_2O}} = K'_{\mathrm{H_2O}}$), and $K_{\mathrm{H(ex12)}}$ and $K_{\mathrm{O(ex12)}}$ were varied from zero to unity. The assumed parameters for the calculation of Eq. (2.41) are shown in Table 2-2. Here, all equilibrium constants and reaction rate constants, k_{aj} and k_{cj}, for $j = I, II$ are the same as those used for comparison between analytical and experimental results of Ni/YSZ in Chapter 3.

When $\left(K_{\mathrm{H(ex12)}}, K_{\mathrm{O(ex12)}}\right) = (0,0)$, the current density is kept constant in the range

of $a_{\mathrm{O}} \geq 10^{-7}$, as shown in Fig. 2-5. This indicates that the coverage of oxygen in Area 2 reaches unity.

On the other hand, when $\left(K_{\mathrm{H(ex12)}}, K_{\mathrm{O(ex12)}}\right) = (0,1)$, the current density is slightly higher than that of the case of $\left(K_{\mathrm{H(ex12)}}, K_{\mathrm{O(ex12)}}\right) = (0,0)$ in the range of $2 \times 10^{-11} \leq a_{\mathrm{O}} \leq 10^{-9}$. This is because reaction (III) in Table 1 takes place through migration of the adsorbed oxygen from Area 2 to Area 1. However, in the range of $a_{\mathrm{O}} \geq 4 \times 10^{-9}$, the current density drastically decreases with increasing oxygen activity

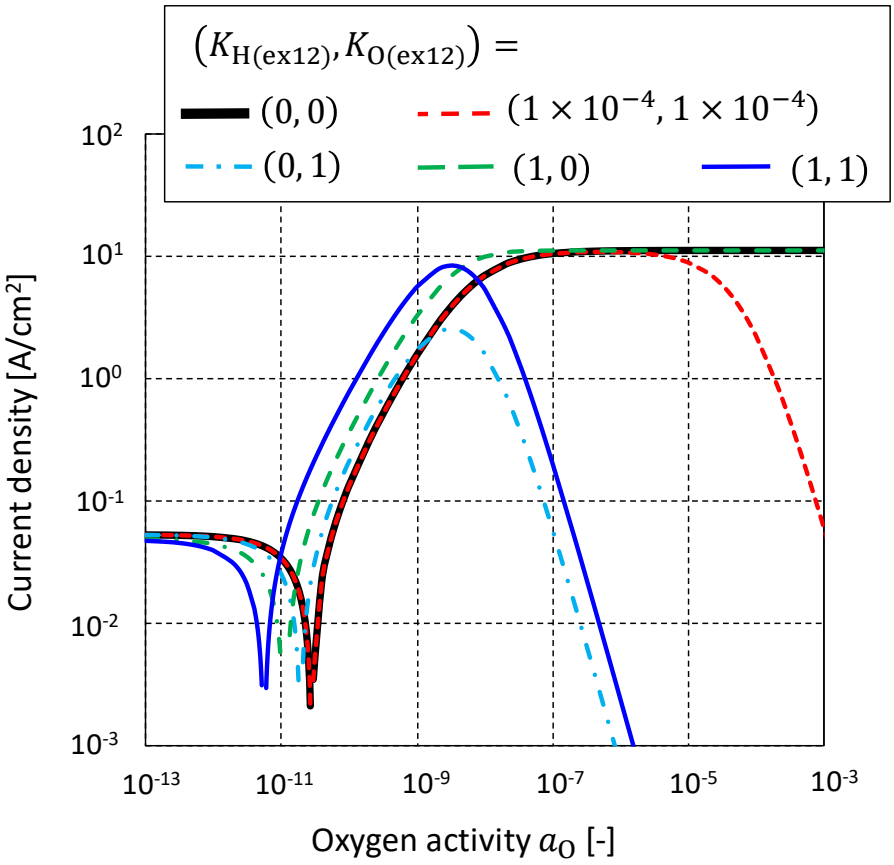

Figure 2-5. The effect of equilibrium constants for species exchange between Areas 1 and 2 ($K_{\mathrm{H(ex12)}}$ and $K_{\mathrm{O(ex12)}}$) on varieties of current density with oxygen activity, a_{O}. $K_{\mathrm{H_2O(ex12)}}$ is fixed to unity ($K_{\mathrm{H_2O}} = K'_{\mathrm{H_2O}}$). The analytical results were calculated by Eq. (2.41) assuming parameters listed in Table 2-2.

Table 2-2. Assumed partial pressures of H_2 and H_2O, equilibrium constants, and reaction rate constants for the calculation of Figure 2-5. All equilibrium constants and reaction rate constants, k_{aj} and k_{cj}, for $j = I, II$ are the same as those used for comparison between analytical and experimental results of Ni/YSZ in Chapter 3.

Parameter	Value
T [K]	1073
$\Delta G^{\circ}_{f}(\mathrm{H_2O})$ [kJ/mol]]	-377.372
$P_{\mathrm{H_2}}$ at anode [atm]	0.97
$P_{\mathrm{H_2O}}$ at anode [atm]	0.03
K_{H} [/atm]	5.5×10^{-3}
K_{O} [-]	1.66×10^{8}
$K_{\mathrm{H_2O}}$ [/atm]	3.47×10^{-4}
$K'_{\mathrm{H_2O}}$ [/atm]	3.47×10^{-4}
k_{aj} $(j = I, II)$ [A/cm^2]	1.23×10^{3}
k_{cj} $(j = I, II)$ [A/cm^2]	2.11×10^{3}
k_{aj} $(j = III - X)$ [A/cm^2]	1.23×10^{3}
k_{cj} $(j = III - X)$ [A/cm^2]	2.0×10^{2}

because the coverage of the adsorbed hydrogen decreases with increasing coverage of oxygen in Area 1.

Similarly, when $\left(K_{\mathrm{H(ex12)}}, K_{\mathrm{O(ex12)}}\right) = (1,0)$, the current density becomes higher than that of the case of $\left(K_{\mathrm{H(ex12)}}, K_{\mathrm{O(ex12)}}\right) = (0,0)$ in the range of $10^{-11} \leq a_{\mathrm{O}} \leq 10^{-7}$ through reactions (VI), (IX), and (X) in Table 2-1, which relate to migration of the adsorbed hydrogen into Area 2. On the other hand, the current density is constant in the range of $a_{\mathrm{O}} \geq 10^{-7}$, similar to the case of $\left(K_{\mathrm{H(ex12)}}, K_{\mathrm{O(ex12)}}\right) = (0,0)$ because the oxygen coverage reaches unity, i.e., the adsorbed hydrogen in Area 2 is completely

replaced by adsorbed oxygen.

In the case of $\left(K_{\mathrm{H(ex12)}}, K_{\mathrm{O(ex12)}}\right) = (1,1)$, which is the conventional competitive adsorption model [7], the current density increases with increasing oxygen activity in the range of $10^{-11} \leq a_{\mathrm{O}} \leq 10^{-9}$ as compared to the case of $\left(K_{\mathrm{H(ex12)}}, K_{\mathrm{O(ex12)}}\right) = (0,0)$ because all reactions in Table 1 take place. However, similar to the case of $\left(K_{\mathrm{H(ex12)}}, K_{\mathrm{O(ex12)}}\right) = (0,1)$, the current density drastically decreases with increasing oxygen activity in the range of $a_{\mathrm{O}} \geq 4 \times 10^{-9}$.

Ni-patterned electrodes on YSZ with well-defined TPB geometry were developed to investigate the mechanism of hydrogen oxidation by Mizusaki et al. [19], Bieberle et al. [5], and Boer [20]. All of their works indicated that hydrogen oxidation mainly occurs at the Ni-YSZ-gas TPB. Additionally, the TDS measurement [13] disclosed that hydrogen is mainly adsorbed onto the Ni surface in Ni/GDC or Ni/YSZ cermet anodes. Moreover, recent first-principle calculations [21,22] predicted that the hydrogen oxidation reaction in a Ni/YSZ anode occurs at the interface between Ni and YSZ, not on the surface of Ni or YSZ. Based on the above prior works, it can be assumed that surface reactions (I) and (II) in Table 2-1 are the dominant reactions. Consequently, the equilibrium constants for the exchange of adsorbed hydrogen and oxygen can be assumed to be much smaller than unity. For example, Fig. 2-5 also shows a result for $\left(K_{\mathrm{H(ex12)}}, K_{\mathrm{O(ex12)}}\right) = (1 \times 10^{-4}, 1 \times 10^{-4})$. The current density corresponds to that for $\left(K_{\mathrm{H(ex12)}}, K_{\mathrm{O(ex12)}}\right) = (0,0)$ in the range of $a_{\mathrm{O}} \leq 4 \times 10^{-6}$, whereas in the range of $a_{\mathrm{O}} \geq 4 \times 10^{-6}$, the current density decreases with increasing oxygen activity. Consequently, the modified model proposed here is useful for a wide range of oxygen activities up to a high value where the coverage of the species reaches unity.

The current density in the case of $\left(K_{\mathrm{H(ex12)}}, K_{\mathrm{O(ex12)}}\right) = (1 \times 10^{-4}, 1 \times 10^{-4})$

corresponds to that in the case of $\left(K_{\mathrm{H(ex12)}}, K_{\mathrm{O(ex12)}}\right) = (0,0)$ for a wide range of oxygen activities. Therefore, for simplicity, the assumption of $\left(K_{\mathrm{H(ex12)}}, K_{\mathrm{O(ex12)}}\right) = (0,0)$, that is, the species territory adsorption model, will be used in the following discussion.

2.2.5 Explicit expression of anode overpotential with current density

As mentioned above, it can be assumed that reactions (I) and (II) in Table 2-1 will be dominant. As a result, the current density described in Eq. (2.41) can be reduced as follows:

$$\begin{aligned} i_{\mathrm{total}} &\cong i_I + i_{II} \\ &= \left(i_{aI} - i_{cI}\right) + \left(i_{aII} - i_{cII}\right) \\ &= \left(k_{aI} + k_{aII}\right)\theta_{\mathrm{H}(1)}{}^2\theta_{\mathrm{O}(2)} - k_{cI}\theta_{\mathrm{H_2O}(1)}\theta_{V(1)}\theta_{V(2)} - k_{cII}\theta_{\mathrm{H_2O}(2)}\theta_{V(1)}{}^2 \\ &= \frac{\left(k_{aI} + k_{aII}\right)K_{\mathrm{H}}P_{\mathrm{H_2}}K_{\mathrm{O}}a_{\mathrm{O}} - \left(k_{cI}K_{\mathrm{H_2O}}P_{\mathrm{H_2O}} + k_{cII}K'_{\mathrm{H_2O}}P_{\mathrm{H_2O}}\right)}{\left(1 + \sqrt{K_{\mathrm{H}}P_{\mathrm{H_2}}} + K_{\mathrm{O(ex12)}}K_{\mathrm{O}}a_{\mathrm{O}} + K_{\mathrm{H_2O}}P_{\mathrm{H_2O}}\right)^2\left(1 + K_{\mathrm{H(ex12)}}\sqrt{K_{\mathrm{H}}P_{\mathrm{H_2}}} + K_{\mathrm{O}}a_{\mathrm{O}} + K'_{\mathrm{H_2O}}P_{\mathrm{H_2O}}\right)} \end{aligned} \tag{2.42}$$

Herein, the terms multiplied by $K_{\mathrm{H(ex12)}}$ and $K_{\mathrm{O(ex12)}}$ can be neglected based on the discussion in the previous section 2.2.4. As a result, Eq. (2.41) can be reduced to the following:

$$i = \frac{\left(k_{aI} + k_{aII}\right)K_{\mathrm{H}}P_{\mathrm{H_2}}K_{\mathrm{O}}a_{\mathrm{O}} - \left(k_{cI}K_{\mathrm{H_2O}}P_{\mathrm{H_2O}} + k_{cII}K'_{\mathrm{H_2O}}P_{\mathrm{H_2O}}\right)}{\left(1 + \sqrt{K_{\mathrm{H}}P_{\mathrm{H_2}}} + K_{\mathrm{H_2O}}P_{\mathrm{H_2O}}\right)^2\left(1 + K_{\mathrm{O}}a_{\mathrm{O}} + K'_{\mathrm{H_2O}}P_{\mathrm{H_2O}}\right)} \tag{2.43}$$

Because Eq. (2.43) is a linear equation of oxygen activity, a_{O}, the explicit expression of a_{O} can be obtained as shown in Eq. (2.44). (On the other and, the expression of current density by the conventional competitive adsorption model is a cubic polynomial of a_{O} [7], and it is difficult to solve for a_{O}.)

$$a_{\mathrm{O}} = \frac{\left(1 + K'_{\mathrm{H_2O}} P_{\mathrm{H_2O}}\right) i + C_2}{K_{\mathrm{O}} \left(C_1 - i\right)} \tag{2.44}$$

Here, C_1 and C_2 are described as follows:

$$C_1 = \frac{\left(k_{aI} + k_{aII}\right) K_{\mathrm{H}} P_{\mathrm{H_2}}}{\left(1 + \sqrt{K_{\mathrm{H}} P_{\mathrm{H_2}}} + K_{\mathrm{H_2O}} P_{\mathrm{H_2O}}\right)^2} \tag{2.45}$$

$$C_2 = \frac{k_{cI} K_{\mathrm{H_2O}} P_{\mathrm{H_2O}} + k_{cII} K'_{\mathrm{H_2O}} P_{\mathrm{H_2O}}}{\left(1 + \sqrt{K_{\mathrm{H}} P_{\mathrm{H_2}}} + K_{\mathrm{H_2O}} P_{\mathrm{H_2O}}\right)^2} \tag{2.46}$$

The oxygen activity, a_{O}, in the oxide ion conductor bulk near Area 2 is related to the anode potential, E_a, as follows:

$$E_a = \frac{RT}{2F} \ln\left[\frac{a_{\mathrm{O}}}{a_{\mathrm{O(CR)}}}\right] \tag{2.47}$$

where F is the Faraday constant, R is the gas constant, T is the absolute temperature, and $a_{\mathrm{O(CR)}}$ is the oxygen activity of reference electrode at the cathode side (CR). The details of Eq. (2.47) are shown in Appendix B. Here, the oxygen is assumed to be in equilibrium with the outer gas phase at the CR. Then, $a_{\mathrm{O(CR)}}$ is described as follows [23].

$$a_{\mathrm{O(CR)}} = a_{\mathrm{O}}(\mathrm{g}) = P_{\mathrm{O_2}}{}^{1/2} \tag{2.48}$$

where $a_{\mathrm{O}}(\mathrm{g})$ is the oxygen activity of the outer gas phase and $P_{\mathrm{O_2}}$ is the oxygen partial pressure at the cathode side. As a result, substitution of Eqs. (2.44) and (2.48) into Eq. (2.47) gives following equation:

$$E_a = \frac{RT}{2F} \ln\left[\frac{\left(1 + K'_{\mathrm{H_2O}} P_{\mathrm{H_2O}}\right) i + C_2}{K_{\mathrm{O}} \left(C_1 - i\right)}\right] - \frac{RT}{4F} \ln\left[P_{\mathrm{O_2}}\right] \tag{2.49}$$

Figure 2-6(a) shows a schematic of the electrolyte-supported single cell discussed here [7,12]. On both the anode side and the cathode side, working and reference electrodes are prepared. Figure 2-6(b) shows the electrical potential of each electrode under the

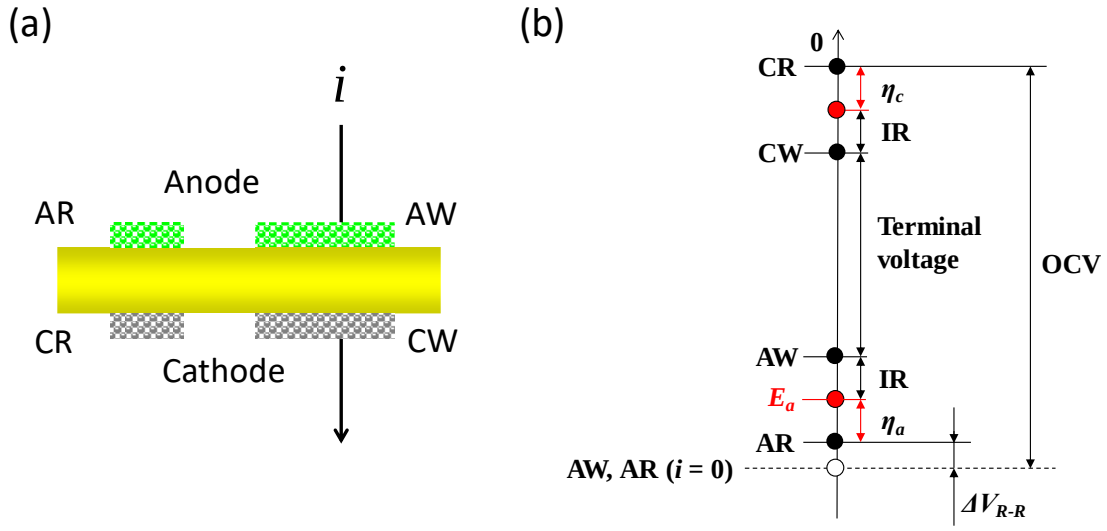

Figure 2-6. (a) Schematic of SOFC single cell with working and reference electrodes. (b) Electrical potential of each electrode under the condition that current density, i, is applied between anode working (AW) and cathode working (CW) when the electrical potential of cathode reference (CR) is set to zero.

condition that current density i is applied between anode working (AW) and cathode working (CW) when the electrical potential of cathode reference (CR) is set to zero. From Fig. 2-6(b), the anode overpotential, η_a, is described as the sum of the anode potential, E_a, and the voltage between CR and the anode reference (AR), V_{R-R} [7]. In addition, we can define the decrease in the electromotive force as ΔV_{R-R}, which is a result of the change in the fuel composite condition followed by a DC current between the anode and cathode working electrodes. As a result, the anode overpotential is described as follows:

$$\eta_a = E_a + V_{R-R} = E_a + \left(OCV - \Delta V_{R-R}\right) \tag{2.50}$$

Here OCV is the open circuit voltage, which is described in H_2-H_2O atmosphere at the anode side (P_{H_2}, P_{H_2O}) and O_2 at the cathode side (P_{O_2}) as follows [24].

$$OCV = -\frac{\Delta G_f^{\circ}(H_2O)}{4F} - \frac{RT}{2F}\ln\left[\frac{P_{H_2O}}{P_{H_2}}\right] + \frac{RT}{4F}\ln\left[P_{O_2}\right] \tag{2.51}$$

where $\Delta G_f^{\circ}(\mathrm{H_2O})$ is the standard Gibbs free energy of formation of H_2O. In addition, we assume that ΔV_{R-R} is negligibly small [12]. By substituting E_a in Eq. (2.49) and OCV in Eq. (2.51) into Eq. (2.50), the anode overpotential can be described as a function of the current density for given partial pressures of H_2 and H_2O at the anode side:

$$\eta_a = \frac{RT}{2F}\ln\left[\frac{\left(1+K'_{\mathrm{H_2O}}P_{\mathrm{H_2O}}\right)i+C_2}{K_{\mathrm{O}}\left(C_1-i\right)}\right]-\frac{\Delta G_f^{\circ}(\mathrm{H_2O})}{4F}-\frac{RT}{2F}\ln\left[\frac{P_{\mathrm{H_2O}}}{P_{\mathrm{H_2}}}\right] \tag{2.52}$$

Here, C_1 and C_1 are given by Eqs. (2.45) and (2.46), respectively. As shown in Eq. (2.52), anode overpotential is independent of $P_{\mathrm{O_2}}$ at the cathode side.

As shown above, the analytical expression of anode overpotential with current density could be directly obtained based on the species territory adsorption model. Generally, the anode overpotential in a region of low current density is proportional to $\ln i$, whereas in a region of high current density, it is proportional to $[1/(i_{\mathrm{limit}}-i)]$; herein, i_{limit} is the limiting current density [25]. These two terms, which are conventionally expressed independently, are combined in the kernel of the logarithmic function, as shown in Eq. (2.52).

2.3 Analytical results based on the model

2.3.1 Typical curves of current density and anode overpotential

Figure 2-7(a) and (b) show typical curves of current density as a function of oxygen activity, $i(a_{\mathrm{O}})$, calculated by Eq. (2.43), and of anode overpotential as a function of current density, $\eta_a(i)$, by Eq. (2.52). The assumed parameters for the calculation of Eq. (2.43) and (2.52) are shown in Table 2-3. All equilibrium constants and reaction rate constants are the same as those used for comparison between analytical and experimental results of Ni/YSZ in Chapter 3. The partial pressures of hydrogen and water vapor, $P_{\mathrm{H_2}}$

and P_{H_2O}, were fixed at 0.57 and 0.03 atm, respectively.

In Fig. 6(a), the cathodic and anodic currents are dominant in the ranges of $a_O \leq 3.5 \times 10^{-11}$ and $a_O \geq 3.5 \times 10^{-11}$, respectively. When the anodic current is dominant ($a_O \geq 3.5 \times 10^{-11}$), the current density is initially proportional to a_O, that is, the gradient of i with respect to a_O is almost unity (this region is defined as Region I in the figure). As a_O increases, the gradient of i with a_O becomes smaller than unity and the current density asymptotes to a constant value (this region is defined as Region II). As mentioned in section 2.2.4, this means that the coverage of oxygen in Area 2 ($\theta_{O(2)}$) approaches unity. In other words, the current density approaches a limiting value, i_{limit}, when $K_O a_O$ approaches infinity. Using Eq. (2.43), i_{limit} can be described as follows:

$$\begin{aligned} i_{limit} &= \lim_{K_O a_O \to \infty} \frac{\left(k_{aI} + k_{aII}\right) K_H P_{H_2} K_O a_O - \left(k_{cI} K_{H_2O} P_{H_2O} + k_{cII} K'_{H_2O} P_{H_2O}\right)}{\left(1 + \sqrt{K_H P_{H_2}} + K_{H_2O} P_{H_2O}\right)^2 \left(1 + K_O a_O + K'_{H_2O} P_{H_2O}\right)} \\ &= \frac{\left(k_{aI} + k_{aII}\right) K_H P_{H_2}}{\left(1 + \sqrt{K_H P_{H_2}} + K_{H_2O} P_{H_2O}\right)^2} \\ &= \left(k_{aI} + k_{aII}\right) \theta_{H(1)}{}^2 \\ &= C_1 \end{aligned} \tag{2.53}$$

From Eq. (2.53), it is disclosed that i_{limit} is equal to C_1 in Eq. (2.45) and is determined by the rate constants k_{aI} and k_{aII} and the coverage of adsorbed hydrogen in Area 1 [$\theta_{H(1)}$; in Eq. (2.22), $K_{H(ex12)}$ and $K_{O(ex12)}$ are zero]. Similarly, the model proposed by Williford and Chick illustrated that the coverage of oxygen at the TPB reaches unity as the current density approaches the limiting value [8].

In Fig. 2-7(b), it is shown that the anode overpotential is proportional to $\ln i$ in the range of $i \leq 5.7$ A/cm^2 (Region I), whereas it drastically increases in the range of $i \geq 5.7$ A/cm^2 (Region II) because the term $[1/(C_1 - i)]$ in Eq. (2.52) diverges when the current density approaches the limiting value, $i_{limit}(= C_1)$. The drastic increase of anode

overpotential, as shown in Region II of Fig. 2-7(b), is generally called a concentration overpotential, which is conventionally explained by gas diffusion in a porous electrode [25-29]. On the other hand, based on the reaction model discussed here, the limit of

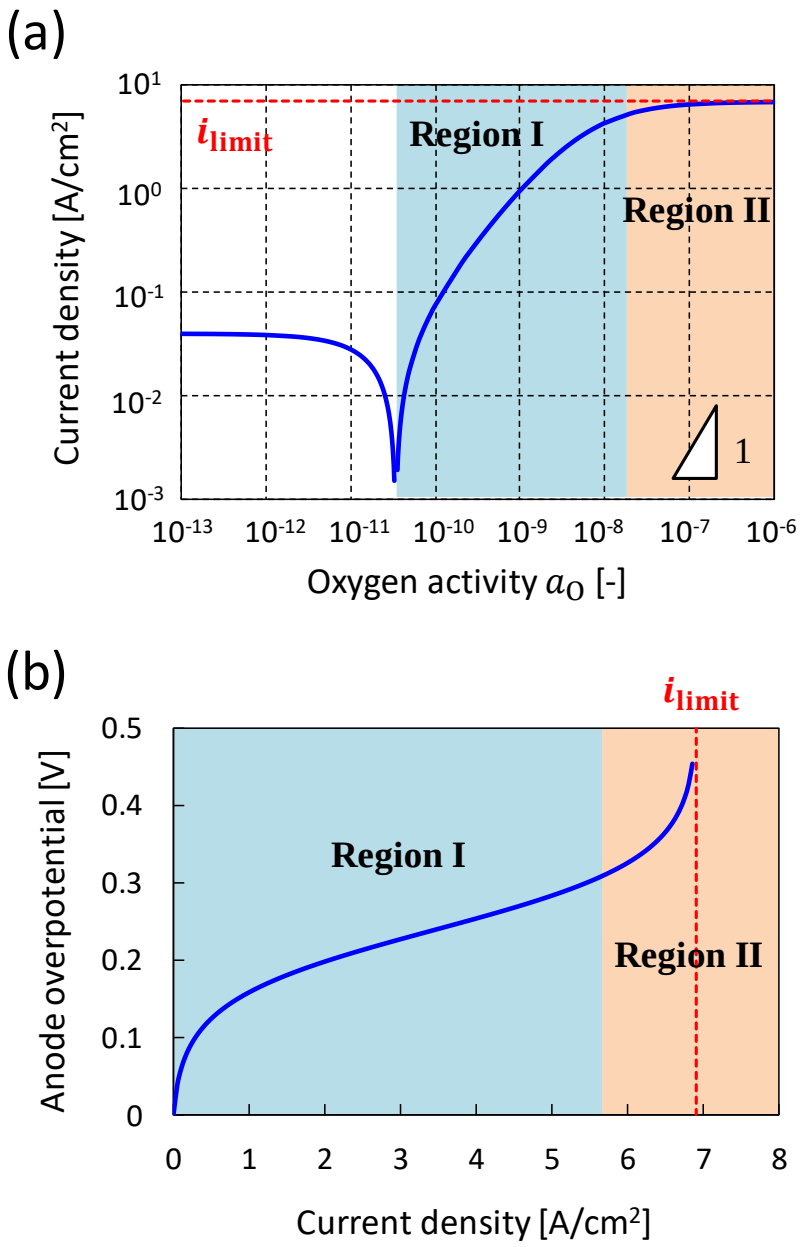

Figure 2-7. Typical curve of (a) current density as a function of oxygen activity by Eq. (2.43) and (b) anode overpotential as a function of current density by Eq. (2.52). The parameters listed in Table 2-3 were used for the calculation.

Table 2-3. Assumed partial pressures of H_2 and H_2O, equilibrium constants, and reaction rate constants for the calculation of Figures 2-7 and 2-8. All equilibrium constants and reaction rate constants are the same as those used for comparison between analytical and experimental results of Ni/YSZ in Chapter 3.

Parameter	Value
T [K]	1073
$\Delta G^{\circ}_{f}(\mathrm{H_2O})$ [kJ/mol]]	-377.372
$P_{\mathrm{H_2}}$ at anode [atm]	0.57
$P_{\mathrm{H_2O}}$ at anode [atm]	0.03
K_{H} [/atm]	5.5×10^{-3}
K_{O} [-]	1.66×10^{8}
$K_{\mathrm{H_2O}}$ [/atm]	3.47×10^{-4}
$K'_{\mathrm{H_2O}}$ [/atm]	3.47×10^{-4}
k_{aj} $(j = I, II)$ [A/cm^2]	1.23×10^{3}
k_{cj} $(j = I, II)$ [A/cm^2]	2.11×10^{3}

current density and concentration overpotential is determined not by gas diffusion coefficient in a porous anode but by the maximum coverage of the adsorbed species at the TPB. Similarly, Williford and his coworkers have proposed a model in which the concentration polarization is controlled by competitive adsorption and surface diffusion near the TPB, and their model was in good agreement with experimental results [30]. In addition, some researchers have mentioned that surface processes, such as competitive adsorption and/or surface diffusion near the TPB, strongly affect the performance of anodes [8,31,32]. The validity of the reaction model proposed here is discussed based on a comparison between analytical and experimental results in Chapter 3.

2.3.2 Coverages of adsorbed species on Areas 1 and 2

Figure 2-8 shows coverages of adsorbed species on Areas 1 and 2 as a function of oxygen activity a_{O} calculated by Eqs. (2.21)–(2.28) with the parameters listed in Table 2-3. In Eqs. (2.21)–(2.28), $K_{\mathrm{H(ex12)}}$ and $K_{\mathrm{O(ex12)}}$ are set to zero. The analytical result of current density with oxygen activity is also shown in Fig. 2-8. As shown in this figure, coverages on Ni ($\theta_{\mathrm{H}(1)}, \theta_{\mathrm{H_2O}(1)}, \theta_{V(1)}$) are constant against oxygen activity because oxygen atom adsorbs only on the oxide ion conductor surface and does not occupy adsorption site on Ni surface in this model. While vacancy site is dominant, $\theta_{\mathrm{H}(1)}$ is less than 0.1 and $\theta_{\mathrm{H_2O}(1)}$ is much smaller than all other coverage on Ni. This trend corresponds to some results predicted by other models [9,10,33]. In the case of oxide ion conductor surface (Area 2), while coverage of oxygen atom ($\theta_{\mathrm{O}(2)}$) increases with a_{O} and approaches unity, $\theta_{\mathrm{H_2O}(2)}$ and $\theta_{V(2)}$ decrease because adsorbed oxygen and water occupy adsorption sites on Area 2 competitively.

In Region I, the low-current-density area ($i \leq 5.7$ A/cm^2), the coverage of adsorbed oxygen is of the same order as that of adsorbed hydrogen (for example, at $a_{\mathrm{O}} = 4.0 \times 10^{-10}$ and $i = 0.39$ A/cm^2, $\theta_{\mathrm{H}(1)} = 5.3 \times 10^{-2}$ and $\theta_{\mathrm{O}(2)} = 6.2 \times 10^{-2}$). Therefore, the amount of excess adsorbed oxygen that is not consumed by adsorbed hydrogen is small, and $\theta_{\mathrm{O}(2)}$ is kept to a value less than unity. Schematic of the TPB corresponding to Region I is shown in Figure 2-9(a).

In Region II, the high-current-density area ($i \geq 5.7$ A/cm^2), the amount of adsorbed oxygen is quite large as compared to that of adsorbed hydrogen (for example, at $a_{\mathrm{O}} = 3.0 \times 10^{-8}$ and $i = 5.8$ A/cm^2, $\theta_{\mathrm{H}(1)} = 5.3 \times 10^{-2}$ and $\theta_{\mathrm{O}(2)} = 8.3 \times 10^{-1}$), the situation corresponding to which is shown in Figure 2-9(b). In other words, the amount of adsorbed hydrogen is not sufficient to consume the adsorbed oxygen. As a result,

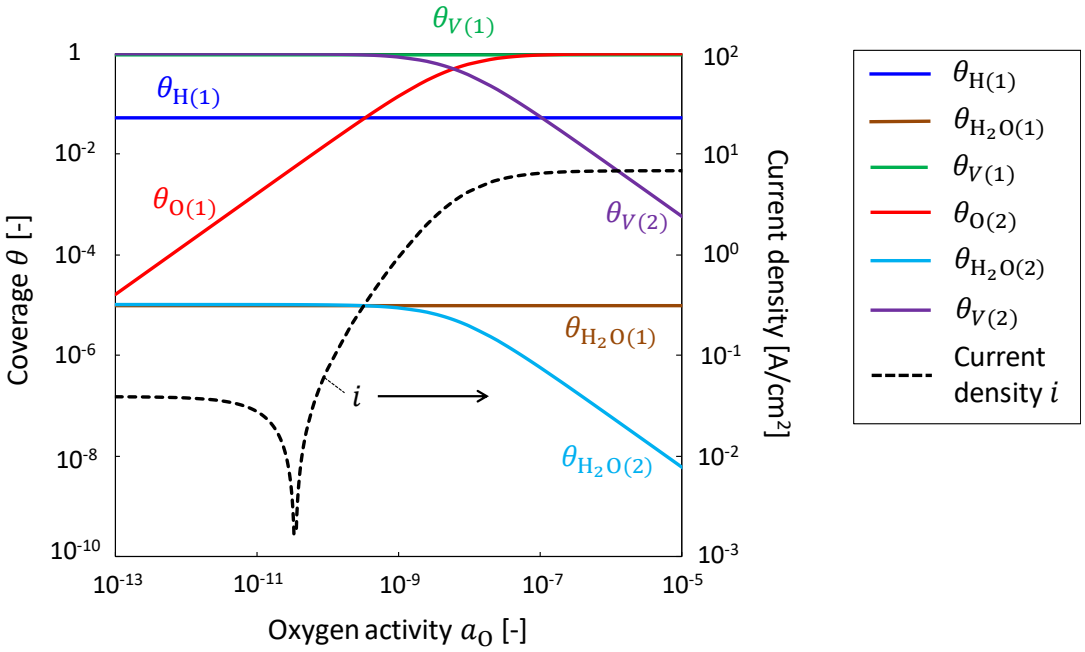

Figure 2-8. Calculated coverages of adsorbed species on the anode as a function of oxygen activity. Subscript 1 and 2 represents Area 1 (Ni surface) and Area 2 (oxide ion conductor surface), respectively. The analytical result of current density with oxygen activity is also shown by dotted line. The parameters listed in Table 2-3 were used for the calculation.

excess adsorbed oxygen occupies the vacancy sites in Area 2, and the coverage of oxygen in Area 2 ($\theta_{\mathrm{O}(2)}$) approaches unity, which is followed by the limiting current density, i_{limit}.

As discussed above, the change and limitation of current density can be explained by the change of coverages of adsorbed species in the species territory adsorption model because the reaction rate [current density, Eq. (2.42)] is determined by the coverages. In addition, each coverage in Area 1 or 2 is assumed to be uniform, in other words, surface diffusion rate of adsorbed species to the TPB is infinity as described in Fig. 2-4. As a result, the effective width of Area 1 or 2 from the TPB line does not affect the current density in this model.

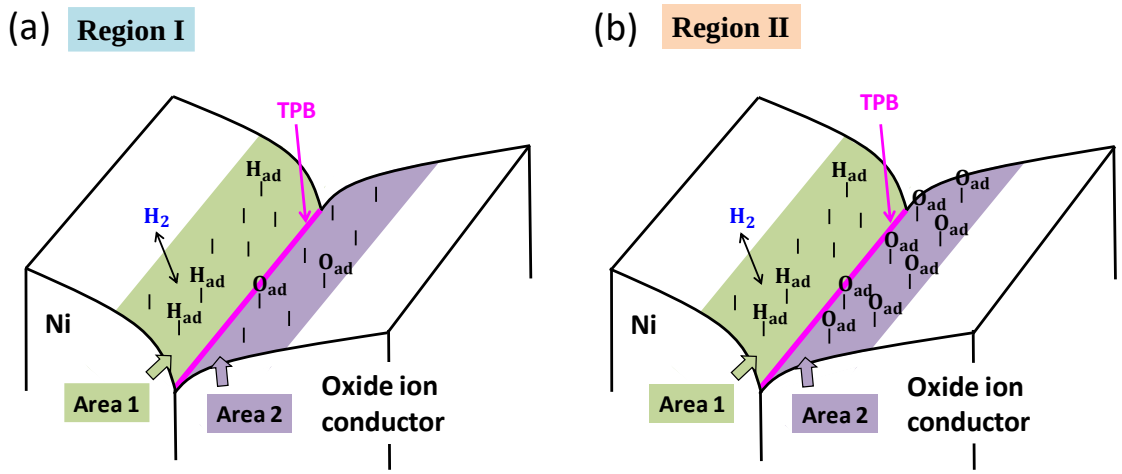

Figure 2-9. Schematic of the TPB corresponding to (a) Region I (low-current-density area) and (b) Region II (high-current-density area).

2.4 Summary

New analytical model for hydrogen oxidation in the TPB of Ni/oxide ion conductor cermet anode of SOFC, named as species territory adsorption model, was constructed. It was assumed that the chemical species could be adsorbed within a finite narrow area on Ni or oxide ion conductor around the TPB. The reaction rate in the anode was controlled by the surface reaction between the adsorbed hydrogen and adsorbed oxygen; all other reactions took place under chemical equilibrium. Based on the reaction model, analytical expressions of the current density with respect to oxygen activity and the anode overpotential with respect to current density could be obtained. The latter could combine the anode overpotential at low- and high-current-density regions, which were conventionally expressed independently. Moreover, it was clarified that the current density asymptotes the limiting value as the oxygen coverage around the TPB approaches unity. The theoretical limitation of current density given here is determined by the rate constants of surface reactions and the coverage of adsorbed hydrogen on Ni.

References

[1] N. Mahato, A. Banerjee, A. Gupta, S. Omar, K. Balani, *Prog. Mater. Sci.* 72 (2015) 141–337.

[2] W.G. Bessler, M. Vogler, H. Störmer, D. Gerthsen, A. Utz, A. Weber, E. I-Tiffée, *Phys. Chem. Chem. Phys.* 12 (2010) 13888–13903.

[3] B.S. Prakash, S.S. Kumar, S.T. Aruna, *Renew. Sust. Energ. Rev.* 36 (2014) 149–179.

[4] J. Mizusaki, H. Tagawa, T. Saito, T. Yamamura, K. Kamitani, K. Hirano, S. Ehara, T. Takagi, T. Hikita, M. Ippommatsu, S. Nakagawa, K. Hashimoto, *Solid State Ionics* 70/71 (1994) 52–58.

[5] A. Bieberle, L.P. Meier, L.J. Gauckler, *J. Electrochem. Soc.* 148, 6 (2001) A646–A656.

[6] C. Wen, R. Kato, H. Fukunaga, H. Ishitani, K. Yamada, *J. Electrochem. Soc.* 147, 6 (2000) 2076–2080.

[7] M. Ihara, T. Kusano, C. Yokoyama, *J. Electrochem. Soc.* 148, 3 (2001) A209–A219.

[8] R.E. Williford, L.A. Chick, *Surf. Sci.* 547 (2003) 421–437.

[9] M. Vogler, A. B-Hütter, L. Gauckler, J. Warnatz, W.G. Bessler, *J. Electrochem. Soc.* 156, 5 (2009) B663–B672.

[10] D.G. Goodwin, H. Zhu, A.M. Colclasure, R.J. Kee, *J. Electrochem. Soc.* 156, 9 (2009) B1004–B1021.

[11] W. Yao, E. Croiset, *J. Power Sources* 248 (2014) 777–788.

[12] S. Yano, S. Nakamura, S. Hasegawa, M. Ihara, K. Hanamura, *J. Therm. Sci. Tech-Jpn.* 4(3) (2009) 431–436.

[13] K. Masuda, M. Ihara, K. Hanamura, *Mech. Eng. J.* 1(3) (2014) Paper No. 14-00017.

[14] T. Nagasawa, D. Chen, S.Y. Lai, M. Liu, K. Hanamura, *J. Power Sources* 324 (2016) 282–287.

[15] Y. Jin, H. Saito, K. Yamahara, M. Ihara, *Electrochem. Solid-State Lett.* 12(2) (2009) B8–B10.

[16] Y. Jin, H. Yasutake, K. Yamahara, M. Ihara, *J. Electrochem. Soc.* 157(1) (2010) B130–B134.

[17] Y. Jin, H. Yasutake, K. Yamahara, M. Ihara, *Chem. Eng. Sci.* 65 (2010) 597–602.

[18] M.J. Powell, *Phys. Rev. B* 20(10) (1979) 4194–4198.

[19] J. Mizusaki, H. Tagawa, T. Saito, K. Kamitani, T. Yamamura, K. Hirano, S. Ehara, T. Takagi, T. Hikita, M. Ippommatsu, S. Nakagawa, K. Hashimoto, *J. Electrochem. Soc.* 141(8) (1994) 2129–2134.

[20] B. de Boer, *Ph.D. Thesis*, University of Twente, The Netherlands (1998).

[21] M. Shishkin, T. Ziegler, *J. Phys. Chem. C* 114 (2010) 11209–11214.

[22] C.S. Cucinotta, M. Bernasconi, M. Parrinello, *Phys. Rev. Lett.* 107 (2011) 206103.

[23] J. Mizusaki, K. Amano, S. Yamauchi, K. Fueki, *Solid State Ionics* 22 (1987) 313–322.

[24] 田川博章，固体酸化物燃料電池と地球環境，アグネ承風社 (1998). (in Japanese)

[25] S. Kakac, A. Pramuanjaroenkij, X.Y. Zhou, *Int. J. Hydrogen Energ.* 32 (2007) 761–786.

[26] H. Yakabe, M. Hishinuma, M. Uratani, Y. Matsuzaki, I. Yasuda, *J. Power Sources* 86 (2000) 423–431.

[27] R. Suwanwarangkul, E. Croiset , M.W. Fowler, P.L. Douglas, E. Entchev, M.A. Douglas, *J. Power Sources* 122 (2003) 9–18.

[28] J.W. Kim, A.V. Virkar, K.Z. Fung, K. Mehta, S.C. Singhal, *J. Electrochem. Soc.* 146 (1999) 69–78.

[29] A.S. Joshi, K.N. Grew, A.A. Peracchio, W.K.S. Chiu, *J. Power Sources* 164 (2007) 631–638.

[30] R.E. Williford, L.A. Chick, G.D. Maupin, S.P. Simner, J.W. Stevenson, *J. Electrochem. Soc.* 150(8) (2003) A1067–A1072.

[31] Y. Shi, N. Cai, C. Li, *J. Power Sources* 164 (2007) 639–648.

[32] V.P. Zhdanov, *Phys. Rev. E* 67 (2003) 042601.

[33] W.G. Bessler, J. Warnatz, D.G. Goodwin, *Solid State Ionics* 177 (2007) 3371–3383.

Chapter 3

Comprehensive analysis of Ni/YSZ anode using species territory adsorption model

3.1 Introduction

As an anode material for SOFCs, a cermet electrode consisting of Ni and YSZ is widely used because of its high catalytic activity for hydrogen oxidation and of high chemical stability at elevated temperature [1-3]. The hydrogen oxidation at the Ni-YSZ-gas TPB is one of the key processes in SOFC operation, and numerous efforts have been made to understand its mechanism from the view point of experimental [4-8], numerical [9-15], or analytical [16,17] approaches. Among them, detailed electrochemical reaction models based on elementary chemical reactions have been presented by Vogler et al. [9] or Goodwin et al. [10] to explain the experimental results of Ni-patterned anode on YSZ substrate [7,8], which has well-defined TPB geometry. These models include adsorption/desorption of the gas-phase species, surface reactions and diffusions of adsorbed species, and charge transfer processes at the TPB.

Although such multi-step elementary kinetic approaches are useful to investigate detailed reaction mechanism, it is difficult to combine with numerical simulations at anode microstructure because it requires high computational power and many unknown parameters. The number of needed parameters such as quantities of state, activation energy, or frequency factor increases with the number of assumed elementary reactions.

Some of those are roughly estimated, taken from different studies, or obtained from fitting to a limited data set. Therefore, generality and reliability of reaction model and parameters are still questionable [18,19].

On the other hand, some research groups have recently developed computational studies of anode reaction based on density functional theory (DFT) in order to investigate detailed reaction mechanism and obtain reliable kinetic parameters [12-15,19]. Those studies essentially do not include any assumption or fitting parameter, however, it is difficult to predict macroscopic electrochemical properties such as current density, overpotential, or impedance spectra from DFT calculations directly.

In contrast to above numerical studies, the analytical model constructed in Chapter 2 (species territory adsorption model) gives simple explicit expressions of current density as a function of oxygen activity, and anode overpotential as a function of current density. This simple model enables to predict current density or anode overpotential with a small number of parameters compared to multi-step reaction models reported previously [9,10]. In order to discuss the validation of the species territory adsorption model quantitatively, the identification of reliable kinetic/thermodynamic parameters and the comparison with experimental results are needed.

In this chapter, the model parameters for Ni/YSZ anode are determined through the comparison with several experimental results and the introduction of referenced kinetic and thermodynamic parameters by DFT calculations. First, the dependence of anode overpotential on hydrogen partial pressure is experimentally measured using an electrolyte-supported single cell with a Ni/YSZ anode. Next, the combination of referenced DFT-database and fitting to the measured and reported [17,20] experimental results gives all reaction parameters. This makes it possible to estimate effective anode

thickness based on the model. Finally, the analytical results are compared with several reported experimental results [17,21-25] of Ni/YSZ cermet anodes, and the quantitative validation of the model and estimated effective anode thickness are discussed.

3.2 Experimental section

3.2.1 Cell fabrication and microstructure characterization

In the current study, an electrolyte-supported button cell with a Ni/YSZ anode and a LSM/ScSZ cathode was fabricated for the power generation experiment. For the electrolyte, a YSZ (8 mol% Y_2O_3-stabilized ZrO_2) disk with a diameter of 20 μm and thickness of 300 μm was used. To manufacture the anode, a mixture of NiO, YSZ (NiO:YSZ=66:34 wt.%, corresponds to Ni:YSZ=50:50 vol.%), α-terpineol, and ethyl cellulose was prepared and coated onto one side of the disk. The disk was dried at 90 ℃ for 12 h and sintered at 1300 ℃ for 4 h in an ambient atmosphere. The cathode was fabricated using a composite powder of LSM ($La_{0.85}Sr_{0.15}MnO_3$) and ScSZ (10 mol%

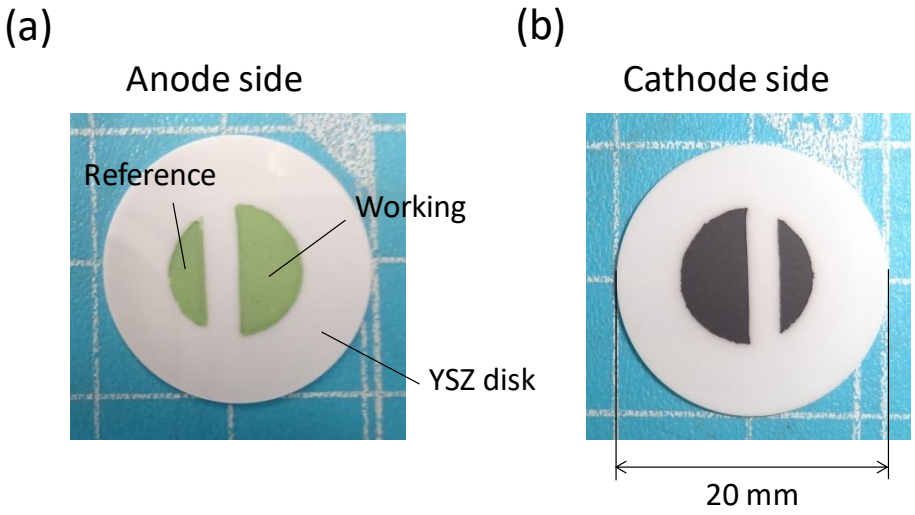

Figure 3-1. Pictures of (a) anode and (b) cathode side of the single cell used in the power generation experiment.

Sc_2O_3-1 mol% CeO_2-ZrO_2) at a weight ratio of 80:20, and the same admixture for the anode paste was used. The paste was coated onto the other side, dried at 90 ℃ for 12 h, and sintered at 1200 ℃ for 4 h in an ambient atmosphere. Both the anode and cathode were separated into two parts to prepare reference electrodes, as shown in Figure 3-1. The thickness of the fabricated anode and cathode were about 20 μm and 6 μm, respectively.

The microstructure of the anode was investigated by SEM as shown in Figure 3-2. Before taking the SEM image, the anode was reduced at 1073 K in hydrogen atmosphere.

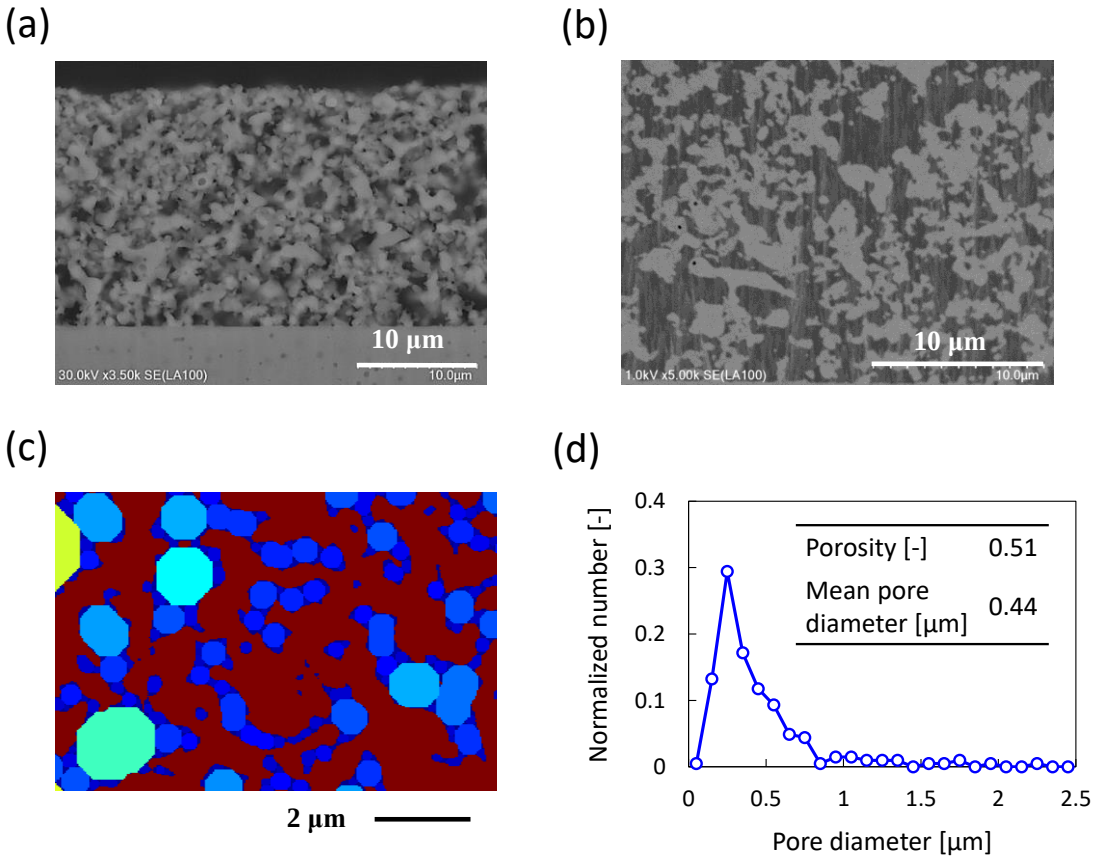

Figure 3-2. (a) SEM image of the cross section of Ni/YSZ anode taken at an acceleration voltage at 30 kV. (b) SEM image taken at 1.0 kV. White and black region correspond to anode material and pore phase, respectively. (c) Circle approximated image of the pore structure of Ni/YSZ anode. (d) Pore size distribution of Ni/YSZ anode obtained by an approximation that circles are inscribed to pores in the binarized image. Porosity and mean pore diameter of the anode is also shown.

Then, the sample was infiltrated with an epoxy resin, and the cross-section of the anode was polished by a cross section polisher in order to obtain a smooth surface. The SEM images of cross section of the anode were taken at an acceleration voltage of 30 kV (Fig.3-2(a)) and 1.0 kV (Fig.3-2(b)). In Fig. 3-2(b), white and black part shows the material and epoxy resin (correspond to pore), respectively. The binarized images of Fig. 3-2(b) gives the porosity of anode, 0.51, which is close to the value of Ni/YSZ (Ni:YSZ=50:50 vol.%) measured by FIB-SEM, 0.49 [26]. The pore size distribution was obtained by an approximation that circles are inscribed to pores in the binarized image [27], which is shown as Fig. 3-2(c). Fig. 3-2(d) shows the pore size distribution of Ni/YSZ anode. From this analysis, mean pore diameter of the anode, 0.44 μm, was obtained.

3.2.2 Experimental setup of fuel cell operation

Figure 3-3(a) shows a schematic of a flow line for the power generation experiment. A mixture of humid, gaseous H_2 and Ar was introduced into the anode side. The total flow rate of the mixture was fixed at 200 mL/min. The partial pressure of hydrogen was controlled by the flow rate of gaseous H_2 and Ar. The humidity was controlled by H_2O produced via oxidation of H_2 through mixing with 1~3% O_2 gas. On the other hand, pure oxygen was introduced on the cathode side with a flow rate of 60 mL/min. The operating temperature was fixed at 1073 K throughout the experiment by using an electric furnace.

Figure 3-3(b) shows the detailed schematic of the single cell during power generation. The single cell was pressed by ceramic tubes of double tube structure. The cell was fixed with outer ceramic pipes using glass seal. Gold and platinum mesh attached to top of inner ceramics tubes were used as a current collector, and these meshes were contacted with the anode and the cathode surfaces, respectively. Pt wires attached to each

mesh are used for electrochemical measurements. Prior to the power generation experiment, the anode was reduced in 3%-humidified hydrogen atmosphere at 1073 K for 1 h.

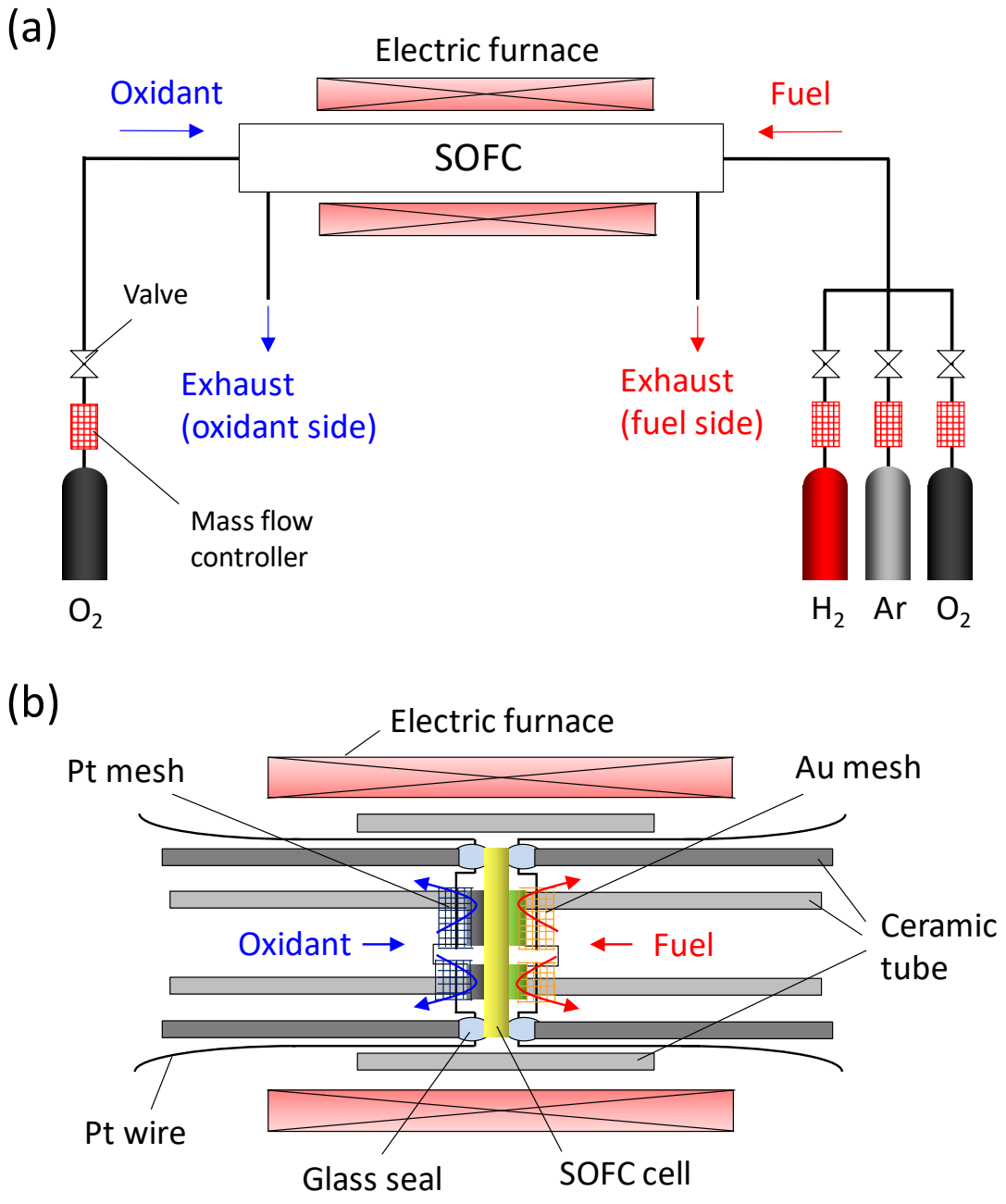

Figure 3-3. (a) Schematic of a flow line for the SOFC power generation experiment. (b) Detailed schematic of the single cell during power generation.

3.2.3 Electrochemical measurements

In this experiment, I-V characteristics and electrochemical impedance were measured at 1073 K under four atmospheric conditions of anode side: $(P_{H_2}, P_{H_2O}) = (0.97,0.03)$, $(0.07,0.03)$, $(0.02,0.03)$, and $(0.015,0.01)$ atm. The effective electrode area of the single cell used here was 0.368 cm^2. The I-V curves in each condition are summarized in Appendix C. Observed OCV at $(P_{H_2}, P_{H_2O}) = (0.97,0.03)$, $(0.07,0.03)$, $(0.02,0.03)$, and $(0.015,0.01)$ atm were 1.12 (theory: 1.14), 0.991 (1.02), 0.914 (0.959), and 0.918 (0.997), respectively. Although measured OCV are 1.8~7.9 % lower than theoretical ones, the magnitude trend toward atmospheric condition is consistent with the

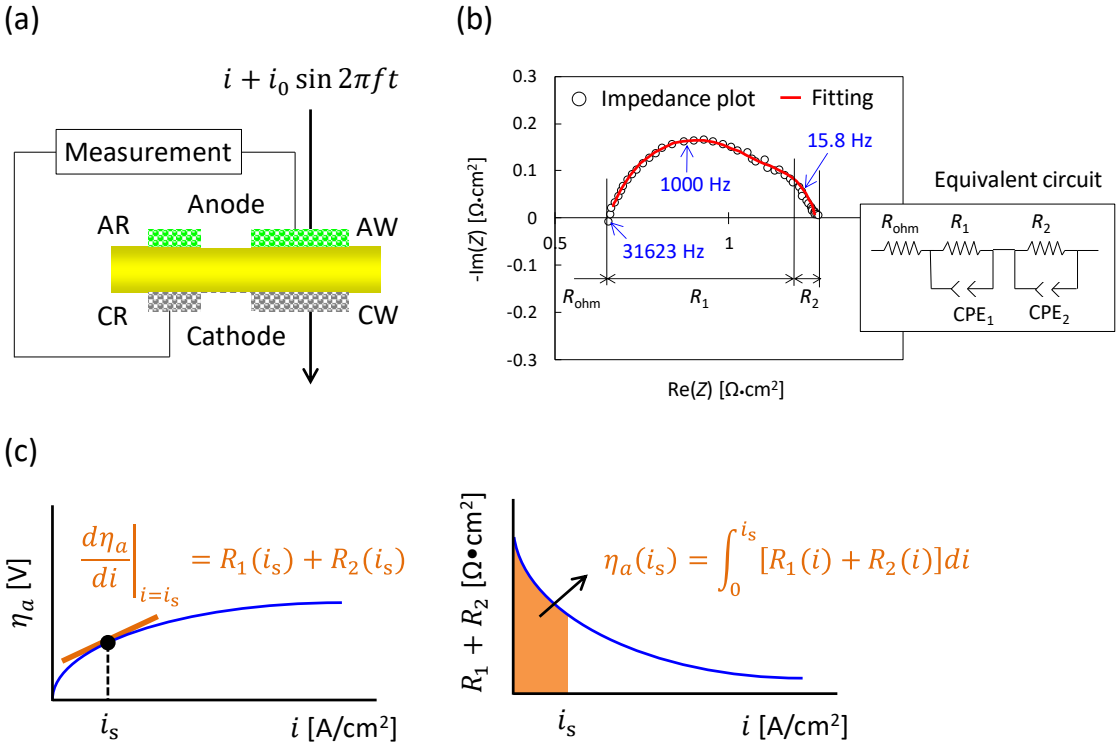

Figure 3-4. (a) Electrical circuit used to measure alternating current impedance. (b) Impedance spectra and fitting curve of Ni/YSZ anode at OCV under $(P_{H_2}, P_{H_2O}) = (0.97,0.03)$ atm. The equivalent circuit for the fitting process is also shown. (c) The mathematical relationship between anode overpotential and polarization resistance R_1 and R_2. i_s indicates certain (arbitrary) current density.

theory. The electrochemical impedance spectra between anode working (AW) and cathode reference (CR) were acquired by applying alternating current $i + i_0 \sin 2\pi ft$ at i = 0 (OCV), 0.082, 0.16, and 0.24 A/cm^2 as shown in Figure 3-4(a). Here, the amplitude i_0 was 20 mA and the frequency f was swept from 10^6 to 10^{-2} Hz. Figure 3-4(b) shows the electrochemical impedance spectra (Cole-Cole plots) at OCV under $\left(P_{\mathrm{H_2}}, P_{\mathrm{H_2O}}\right) = (0.97, 0.03)$ atm. The spectra consist of two arcs around f = 1000 and 15.8 Hz, and fitting process using equivalent circuit shown in Fig. 3-4(b) gives the values of polarization resistances R_1 (high frequency range) and R_2 (low frequency range). In the fitting process, ohmic resistance (R_{ohm}) was fixed to the initiation point of high-frequency arc. All impedance spectra, fitting curves, and obtained R_{ohm}, R_1, and R_2 are summarized in Appendix C.

Since the sum of polarization resistances $(R_1 + R_2)$ corresponds to the gradient of the anode overoptential to current density $(d\eta_a/di)$ [28], the anode overpotential $\eta_a(i)$ was calculated using following expression:

$$\eta_a(i_s) = \int_0^{i_s} \left[R_1(i) + R_2(i)\right] di \tag{3.1}$$

where i_s indicates certain (arbitrary) current density. The relationship between anode overpotential and polarization resistance $(R_1 + R_2)$ is illustrated in Figure 3-4(c).

Experimental oxygen activity a_{O} was calculated using following expression:

$$a_{\mathrm{O}} = \exp\left(\frac{2FE_a}{RT}\right) \tag{3.2}$$

Here, anode potential E_a was calculated using η_a obtained from Eq. (3.1) and experimentally-observed OCV value as follows.

$$E_a = \eta_a - OCV \tag{3.3}$$

3.3 Basic formulas and related parameters of the model

The basic formulas of the species territory adsorption model and related thermodynamic/kinetic parameters are summarized in this section. Figure 3-5 shows a schematic of the TPB consisting of Ni, YSZ, and gas phases. Area 1 and 2 are assumed finite area on Ni and YSZ which contribute to species adsorption, respectively. All chemical reactions considered in the model are listed in Table 3-1. As mentioned in Chapter 2, hydrogen and oxygen are assumed to be adsorbed mainly on the surface areas of Area 1 and 2, respectively. Dissociative adsorption of hydrogen molecule on Ni surface is well-known phenomena, however, oxygen migration from YSZ bulk to its surface is not well understood [29]. As shown in Fig. 3-5, an oxygen atom supplied from YSZ bulk has a possibility to be adsorbed on (i) YSZ surface or (ii) interface between Ni and YSZ.

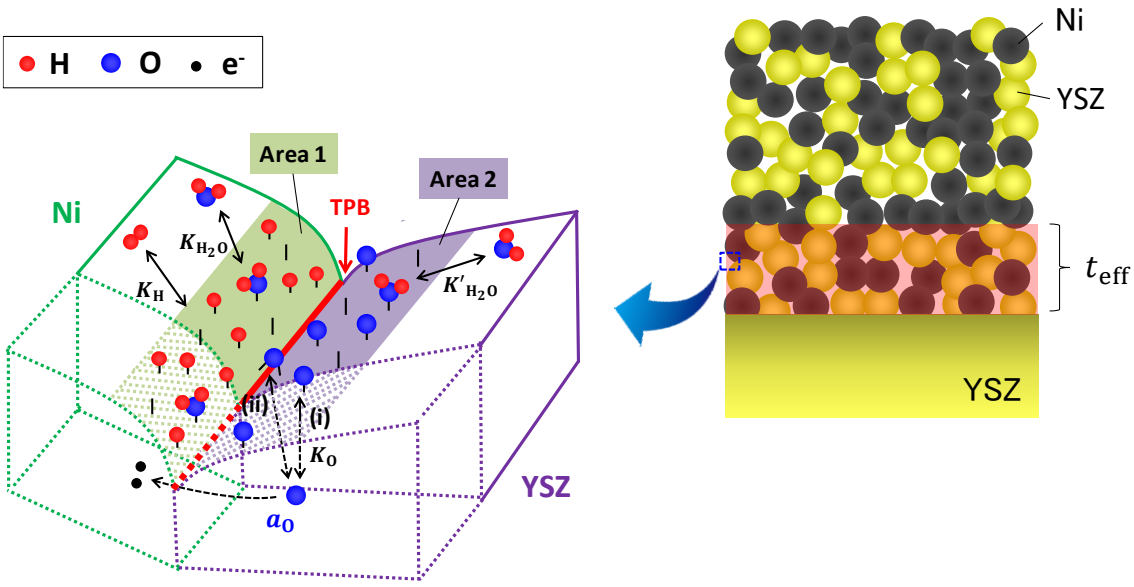

Figure 3-5. Schematics of the TPB consisting of Ni, YSZ, and gas phases and of the concept of an effective anode thickness t_{eff}. Area 1 and 2 are assumed finite area on Ni and YSZ which contribute to species adsorption, respectively. Two possible paths for oxygen migration (i) and (ii) are shown.

Table 3-1. Chemical reactions considered in the model and thermodynamic/kinetic parameters (physical quantities of state, frequency factor, and activation energy) used for the calculation of analytical results. V_{ad} represents surface vacancy site. Subscript ad(1) and ad(2) means Area 1 (Ni surface) and Area 2 (YSZ surface), respectively.

Reaction	Assumption	K, k	ΔH [kJ/mol]	ΔS [J/(mol•K)]	A [mol/(s•cm)]	E_{act} [eV]
$\mathrm{H_2} + 2V_{\mathrm{ad}(1)} \leftrightarrow 2\mathrm{H}_{\mathrm{ad}(1)}$	Equilibrium	K_{H}	-92[a]	-129[a]	–	–
$\mathrm{H_2O} + V_{\mathrm{ad}(1)} \leftrightarrow \mathrm{H_2O}_{\mathrm{ad}(1)}$	Equilibrium	$K_{\mathrm{H_2O}}$	-18[a]	-83[a]	–	–
$\mathrm{H_2O} + V_{\mathrm{ad}(2)} \leftrightarrow \mathrm{H_2O}_{\mathrm{ad}(2)}$	Equilibrium	$K'_{\mathrm{H_2O}}$	-18[b]	-83[b]	–	–
$\mathrm{O}_{(\mathrm{YSZ})} + V_{\mathrm{ad}(2)} \leftrightarrow \mathrm{O}_{\mathrm{ad}(2)}$	Equilibrium	K_{O}	-171[c]	-2[c]	–	–
$2\mathrm{H}_{\mathrm{ad}(1)} + \mathrm{O}_{\mathrm{ad}(2)} \rightarrow \mathrm{H_2O}_{\mathrm{ad}(1)} + V_{\mathrm{ad}(1)} + V_{\mathrm{ad}(2)}$ and $2\mathrm{H}_{\mathrm{ad}(1)} + \mathrm{O}_{\mathrm{ad}(2)} \rightarrow \mathrm{H_2O}_{\mathrm{ad}(2)} + 2V_{\mathrm{ad}(1)}$	Rate-determining step	k_{aI} and k_{aII}	–	–	1.03×10^{-2}[d]	1.02[e]

a) Parameters for steam methane reforming on Ni(111) surface obtained from DFT calculations [30].
b) Assumed to be the same as the parameters on Ni(111) surface.
c) Obtained from fitting to the current and reported [17] experimental results of Ni/YSZ cermet anodes.
d) Obtained from fitting to the experimental result of Ni-patterned anode [20].
e) Parameters for surface reaction between $\mathrm{H_{ad}}$ and $\mathrm{O_{ad}}$, or $\mathrm{H_{ad}}$ and $\mathrm{OH_{ad}}$ on Ni(111) surface obtained from DFT calculations [19].

In the case (i), oxygen atom forms chemical bond to only YSZ surface while it forms to both YSZ and Ni surface in the case (ii). The favored adsorption site for oxygen atom is discussed based on the comparison between the model and experiments later.

In this model, current density i [A/cm^2] is described as a function of oxygen activity a_{O} in the YSZ bulk near the TPB, as follows.

$$i = \frac{\left(k_{aI} + k_{aII}\right) K_{\mathrm{H}} P_{\mathrm{H_2}} K_{\mathrm{O}} a_{\mathrm{O}} - \left(k_{cI} K_{\mathrm{H_2O}} P_{\mathrm{H_2O}} + k_{cII} K'_{\mathrm{H_2O}} P_{\mathrm{H_2O}}\right)}{\left(1 + \sqrt{K_{\mathrm{H}} P_{\mathrm{H_2}}} + K_{\mathrm{H_2O}} P_{\mathrm{H_2O}}\right)^2 \left(1 + K_{\mathrm{O}} a_{\mathrm{O}} + K'_{\mathrm{H_2O}} P_{\mathrm{H_2O}}\right)} \tag{3.4}$$

In addition to this, the analytical expression of anode overpotential η_a [V] is described explicitly as a function of current density i as follows:

$$\eta_a = \frac{RT}{2F} \ln\left[\frac{\left(1 + K'_{\mathrm{H_2O}} P_{\mathrm{H_2O}}\right) i + C_2}{K_{\mathrm{O}}\left(C_1 - i\right)}\right] - \frac{\Delta G_f^{\circ}(\mathrm{H_2O})}{4F} - \frac{RT}{2F} \ln\left[\frac{P_{\mathrm{H_2O}}}{P_{\mathrm{H_2}}}\right] \tag{3.5}$$

where C_1 and C_2 are given by Eqs. (3.6) and (3.7), respectively.

$$C_1 = \frac{\left(k_{aI} + k_{aII}\right) K_{\mathrm{H}} P_{\mathrm{H}_2}}{\left(1 + \sqrt{K_{\mathrm{H}} P_{\mathrm{H}_2}} + K_{\mathrm{H_2O}} P_{\mathrm{H_2O}}\right)^2} = i_{\mathrm{limit}} = \left(k_{aI} + k_{aII}\right) \theta_{\mathrm{H(1)}}{}^2 \tag{3.6}$$

$$C_2 = \frac{k_{cI} K_{\mathrm{H_2O}} P_{\mathrm{H_2O}} + k_{cII} K'_{\mathrm{H_2O}} P_{\mathrm{H_2O}}}{\left(1 + \sqrt{K_{\mathrm{H}} P_{\mathrm{H}_2}} + K_{\mathrm{H_2O}} P_{\mathrm{H_2O}}\right)^2} \tag{3.7}$$

Here C_1 corresponds to limiting current density i_{limit}, which is determined by the coverage of adsorbed hydrogen in Area 1, $\theta_{\mathrm{H(1)}}$, not by gas diffusion coefficient in a porous anode in this model, as discussed in Chapter 2. In Eqs. (3.4)–(3.7), P_{H_2} and $P_{\mathrm{H_2O}}$ are partial pressure [atm] of hydrogen and water vapor at the anode side, respectively. R is the gas constant [J/(K•mol)] and T is the absolute temperature [K]. K_i and K'_i (i = species) express equilibrium constants, and are determined by van't Hoff equation as follows.

$$K = \exp\left(-\frac{\Delta G}{RT}\right) = \exp\left[-\frac{\left(\Delta H - T\Delta S\right)}{RT}\right] \tag{3.8}$$

Here, ΔG, ΔH, and ΔS represent a change of Gibbs free energy, enthalpy, and entropy, respectively. k_{iI} and k_{iII} ($i = a$: anodic reaction, $i = c$: cathodic reaction) represents reaction rate constants for the rate-determining step of this model described in Table 3-1. The anodic reaction rate constant is determined by Arrhenius-type expression as follows.

$$k_{aI} = k_{aII} = zF\rho_{\mathrm{TPB}} t_{\mathrm{eff}} k'_a = zF\rho_{\mathrm{TPB}} t_{\mathrm{eff}} A \exp\left(-\frac{E_{act}}{RT}\right) \tag{3.9}$$

Herein, z shows a valence $(= 2)$, F the Faraday constant [C/mol], ρ_{TPB} the TPB density per unit volume [cm/cm^3], t_{eff} the electrochemically effective anode thickness [cm], k'_a the anodic reaction rate constant per unit TPB length [mol/(s•cm)], A the frequency factor per unit TPB length [mol/(s•cm)], and E_{act} [J/mol] the activation energy. For simplicity, it is assumed that all TPB located in an area within certain distance (t_{eff}) from an anode/electrolyte interface contributes electrochemical reaction uniformly

while the reaction does not occur in other area as shown in Fig. 3-5. The cathodic reaction rate constant is determined to satisfy the condition of $\eta_a = 0$ at $i = 0$, that is,

$$k_{cI} = k_{cII} = \frac{2k_{aI}K_{\mathrm{O}}K_{\mathrm{H}}}{K_{\mathrm{H_2O}} + K'_{\mathrm{H_2O}}} \cdot \exp\left[\frac{\Delta G_f^{\circ}(\mathrm{H_2O})}{2RT}\right] \tag{3.10}$$

3.4 Identification of parameters for Ni/YSZ anode

3.4.1 Quantities of state and activation energy predicted by DFT

In order to calculate current density or anode overpotential based on Eq. (3.4) or (3.5), quantities of state, such as ΔH and ΔS, for adsorption equilibrium and kinetic parameters in reaction rate constants, such as A and E_{act}, for surface reactions described in Table 3-1 are required. However, it's difficult to obtain these parameters experimentally due to the complexities of the heterogeneous reactions on the surface and a short life time of reaction intermediates at high temperature. Therefore, some of these quantities or parameters are referred from calculated results based on density function theory (DFT) [19,30]. The quantities of state and kinetic parameters used for the calculation of analytical results are listed in Table 3-1. In this table, subscripts ad(1) and ad(2) represent Area 1 (Ni) and 2 (YSZ) in Fig. 3-5, respectively. Recently, a comprehensive DFT calculation for nickel-catalyzed steam methane reforming (SMR) on Ni(111) has been conducted by Blaylock et al. [30]. In their work, ΔH and ΔS for 36 elementary reactions of SMR on Ni(111) are presented. Here, ΔH and ΔS for H_2 and H_2O adsorption reactions on Ni are referred from their work.

In addition to this, activation energy for surface reaction between H_{ad} and O_{ad}, or H_{ad} and OH_{ad} on Ni(111) predicted by DFT has been presented by several groups, which is summarized in literature [19]. In the case of $O_{ad} + H_{ad} \rightarrow OH_{ad}$, a range and averaged

value of the reported activation energies are 0.79-1.06 eV and 0.95 eV, respectively. In the case of $OH_{ad} + H_{ad} \rightarrow H_2O_{ad}$, those are 0.87-1.23 eV and 1.09 eV, respectively. Here, the value of 1.02 eV which is an arithmetic average of 0.95 and 1.09 is used for E_{act} in Eq. (3.9). In contrast to abundant information on Ni, thermodynamic and kinetic data sets on YSZ are insufficient or not well established [9,10]. Unlike the well-defined atomic structure of Ni, YSZ atomic structure varies according to concentrations and positions of Zr, Y, O, and oxygen vacancy, which strongly affect surface reactivity and bulk property of YSZ predicted by DFT [31]. In the current work, ΔH and ΔS for H_2O adsorption on YSZ surface were assumed to be the same as those on Ni(111) surface. This assumption should not be a problem because the results depend very weakly on these values in this model, which will be discussed in section 3.5. Finally, four unknown parameters, ΔH and ΔS between oxygen atom adsorbed on YSZ surface and in its bulk (described as $\Delta H_{O(2)}$ and $\Delta S_{O(2)}$, respectively), effective anode thickness t_{eff}, and frequency factor A in Eq. (3.9) are remained. Determination process of these values are presented in the following section.

3.4.2 Parameters identified through fitting to the experimental results

$\Delta H_{O(2)}$ and $\Delta S_{O(2)}$ are determined through fitting to experimental results measured in this study (section 3.2) and reported by Ihara et al. [17]. In the calculation of analytical results, P_{H_2} and P_{H_2O} inside the porous anode are needed. The variation of H_2 concentration at anode/electrolyte interface from bulk gas composition ΔC_{H_2} [mol/m^3] can be roughly estimated by Fick's first law as follows [32]:

$$\Delta C_{H_2} = \frac{-ti}{2FD_{\text{eff}}} \tag{3.11}$$

where t is the anode thickness [= 20 μm from Fig. 3-2(a)], i the current density [A/m^2],

and D_{eff} the effective diffusivity in porous media [m^2/s]. In the case of H_2-H_2O system, D_{eff} is described as follows [33].

$$D_{\mathrm{eff}} = \frac{\varepsilon}{\tau} D_{\mathrm{H_2-H_2O}} = \frac{\varepsilon}{\tau} \times 4.28 \times 10^{-4} \times \frac{T^{1.75}}{P_{\mathrm{total}}} \tag{3.12}$$

Here, ε is the porosity [= 0.51 from Fig. 3-2(d)], τ the tortuosity factor (= 1.96 from the FIB-SEM observation by Iwai et al [26]), and P_{total} the total pressure (= 1.013×10^5 Pa). Even in the condition of highest fuel utilization of 15.7 % (0.24 A/cm^2 at $P_{\mathrm{H_2}} = 0.02$ atm), the estimated decrease in H_2 concentration at the anode/electrolyte interface compared to anode surface is less than 0.13 %. Therefore, $P_{\mathrm{H_2}}$ and $P_{\mathrm{H_2O}}$ inside the porous anode are set to the same as supplied gas compositions in this study.

The fitting results of Eq. (3.4) or (3.5) to the experimental results of this study and Ihara et al. [17] are shown in Figures 3-6 and 3-7, respectively. In experiments at low $P_{\mathrm{H_2}}$, the region where current density reaches or asymptotes to limiting current density (i_{limit}) can be observed as shown in ($P_{\mathrm{H_2}}$, $P_{\mathrm{H_2O}}$) = (0.02, 0.03) and (0.015, 0.01) atm in Fig. 3-6 or ($P_{\mathrm{H_2}}$, $P_{\mathrm{H_2O}}$) = (0.05, 0.01) atm in Fig. 3-7(a). In the model proposed here, i_{limit} corresponds to C_1 in Eq. (3.6) and is a function of the product of t_{eff} and A ($t_{\mathrm{eff}}A$) while independent of $\Delta H_{\mathrm{O(2)}}$ and $\Delta S_{\mathrm{O(2)}}$. The comparison between Eq. (3.6) and experimentally-observed i_{limit} gives unique value of the product $t_{\mathrm{eff}}A$ for an anode in this study and Ref. [17], respectively. Here, $t_{\mathrm{eff}}A$ is different for each reference because t_{eff} should depend on an anode microstructure used in each experiment, especially YSZ network [4]. The identification of $t_{\mathrm{eff}}A$ is followed by that of $\Delta H_{\mathrm{O(2)}}$ and $\Delta S_{\mathrm{O(2)}}$, which are determined to achieve a best fit to all experimental results presented in Figs. 3-6 and 3-7. From a comparison between degrees of freedom of $O_{ad(2)}$ and $O_{(YSZ)}$, $\Delta S_{\mathrm{O(2)}}$ should be a negative value because $O_{ad(2)}$ can move two-dimensionally while $O_{(YSZ)}$ can

three-dimensionally. Under this constraint condition, $\Delta H_{O(2)} = -171$ kJ/mol and $\Delta S_{O(2)} = -2$ J/(mol•K) are obtained by fitting with experimental data sets.

The fitting of the model to Ni-patterned anode experiments gives a value of frequency factor A precisely. Figure 3-8 shows the fitting result of the model to Ni-patterned anode experiment by B.de. Boer [20]. Here, $\Delta H_{O(2)}$ and $\Delta S_{O(2)}$ are fixed to the same values obtained above, that is, -171 kJ/mol and -2 J/(mol•K) respectively. As a result, $A = 1.03 \times 10^{-2}$ mol/(s•cm) is obtained from a fitting of Eq. (3.5) to experimental results. Based on the value of A, $t_{\text{eff}} = 1.50$ μm for this study and 1.79 μm for Ref. [17] were obtained from fitted value of the product $t_{\text{eff}}A$.

3.4.3 Estimation of effective anode thickness for reported Ni/YSZ experiments

From a comparison between Eq. (3.5) and experimentally-observed anode overpotential in various references, t_{eff} of each experiment can be estimated because all other unknown parameters, $\Delta H_{O(2)}$, $\Delta S_{O(2)}$, and A, have been already identified. Here, experimental results of four Ni/YSZ anodes reported previously [21-25] are compared with present model, and each t_{eff} is estimated. The fitting results of the model to experiments are shown in Figures 3-9 for Ref. [21], 3-10 for [22], 3-11 for [23], and 3-12 for [24,25]. The ρ_{TPB} and estimated effective anode thickness t_{eff} of all experiments referred in this chapter are summarized in Table 3-2. Values of ρ_{TPB} of the anode used in this study and Ref. [17] are estimated by weight ratio of NiO and YSZ based on the data sets corrected by a FIB-SEM [34]. For other four experiments [21-25], measured value by the FIB-SEM is presented. From Table 3-2, the value of t_{eff} has a range from 1.12 to 2.39 μm in six Ni/YSZ anodes. The obtained fitting results and estimated t_{eff} are discussed in the following section 3.5.

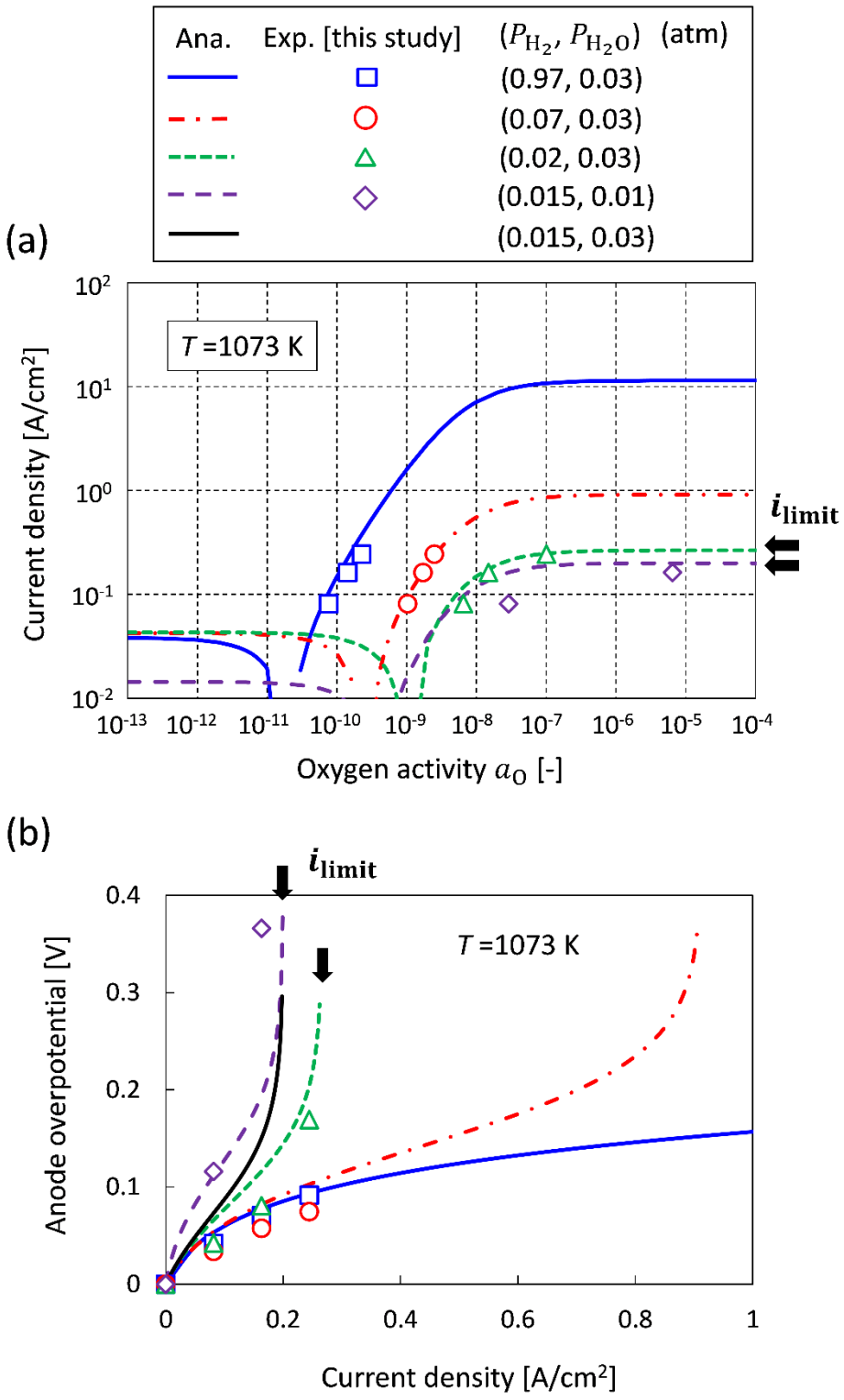

Figure 3-6. Fitting of the model to Ni/YSZ anode experiments in this study to determine the product $t_{\mathrm{eff}}A$, $\Delta H_{O(2)}$, and $\Delta S_{O(2)}$. Analytical results in (a) and (b) are obtained by Eq. (3.4) and (3.5), respectively. The dependence of (a) current density or (b) anode overpotential on hydrogen partial pressure are shown.

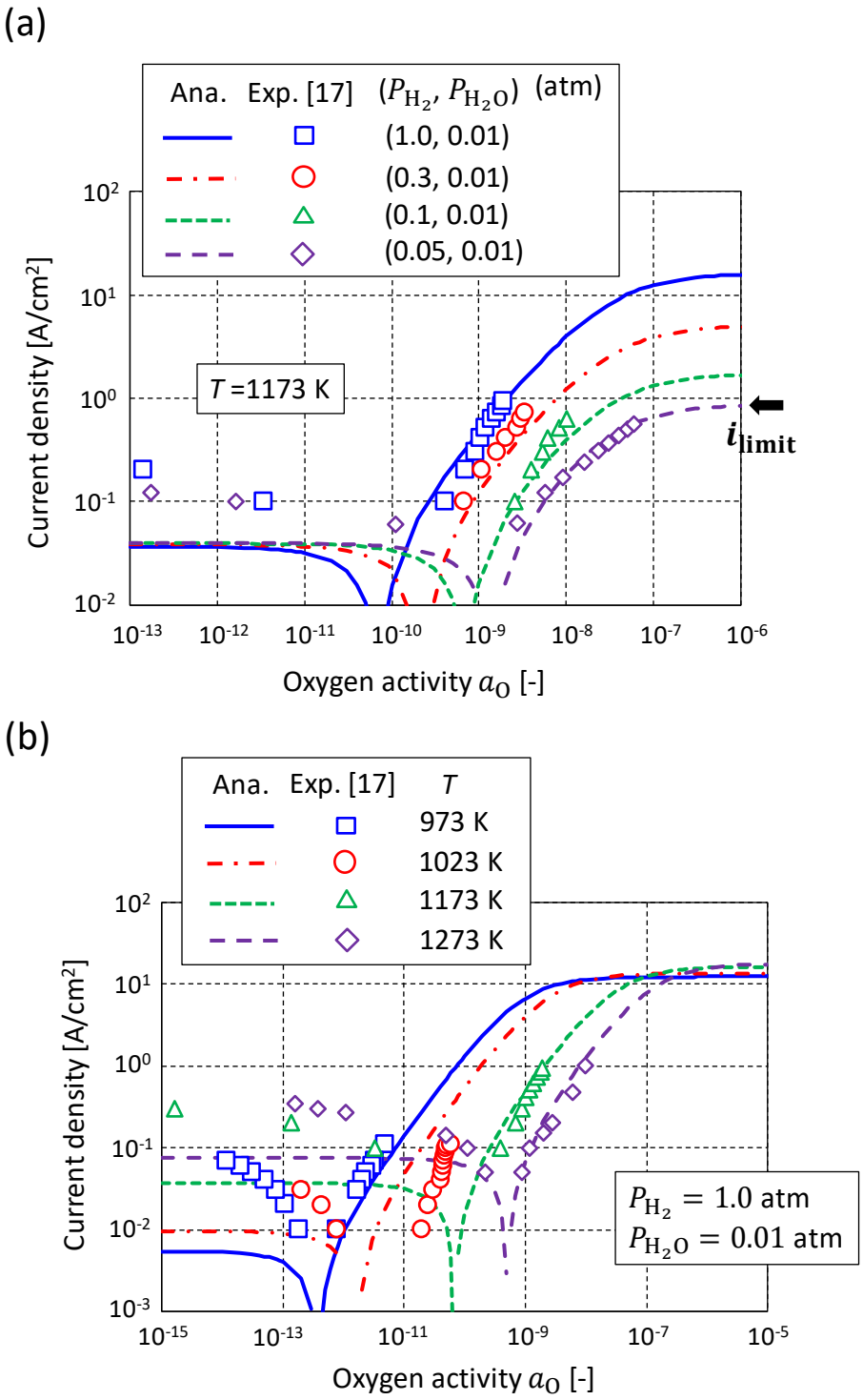

Figure 3-7. Fitting curves of Eq. (3.4) to Ni/YSZ anode experiments by Ihara et al. [17] to determine the product $t_{\mathrm{eff}}A$, $\Delta H_{\mathrm{O}(2)}$, and $\Delta S_{\mathrm{O}(2)}$. (a) and (b) shows the dependence of current density on hydrogen partial pressure and temperature, respectively.

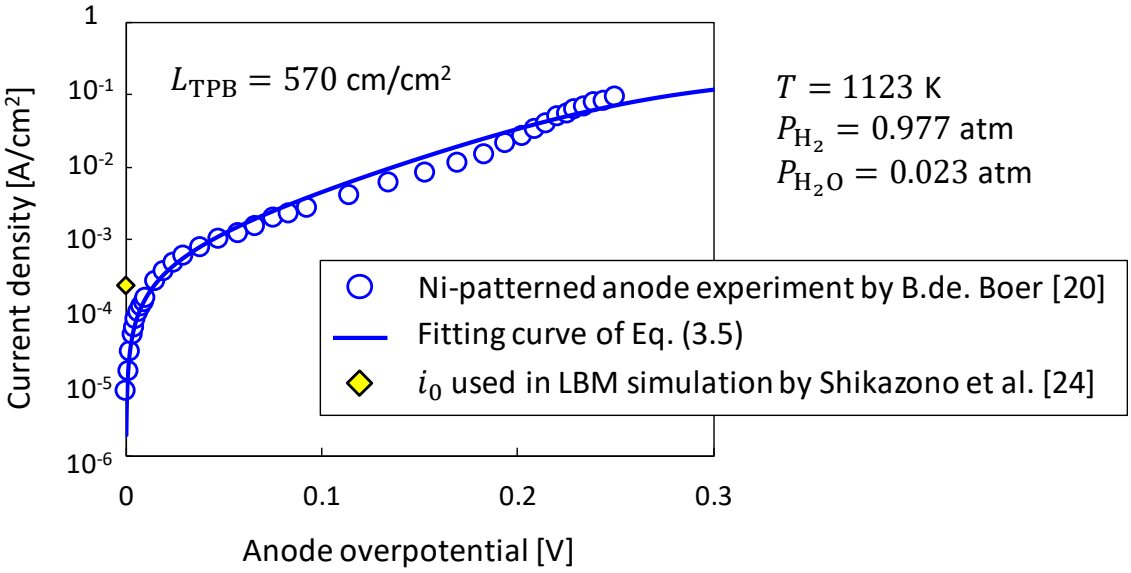

Figure 3-8. Fitting curve of Eq. (3.5) to Ni-patterned anode experiment by B.de Boer [20] to determine a frequency factor A for hydrogen oxidation. Exchange current density used in LBM simulation by Shikazono et al. [24] is also shown.

Table 3-2. Experimental data sets of Ni/YSZ cermet anode used for the comparison with analytical results and estimated effective anode thickness.

Experiment	Electrode	ρ_{TPB} [μm/μm³]	t_{eff} [μm]	Condition
This study	Ni/YSZ cermet NiO 66 wt%	2.58[a]	1.50	$T = 1073$ K $P_{\mathrm{H_2}} = 0.015 - 0.97$ atm $P_{\mathrm{H_2O}} = 0.01 - 0.03$ atm
Ihara et al. [17]	Ni/YSZ cermet NiO 60 wt%	2.66[a]	1.79	$T = 973 - 1273$ K $P_{\mathrm{H_2}} = 0.05 - 1$ atm $P_{\mathrm{H_2O}} = 0.01$ atm
Kishimoto et al. [21]	Ni/YSZ cermet Ni 50 vol%	2.49[b]	1.35	$T = 1073 - 1273$ K $P_{\mathrm{H_2}} = 0.8 - 0.97$ atm $P_{\mathrm{H_2O}} = 0.03 - 0.2$ atm
Matsui et al. [22]	Ni/YSZ cermet Ni 50 vol%	2.49[b]	2.39	$T = 1273$ K $P_{\mathrm{H_2}} = 0.6 - 0.97$ atm $P_{\mathrm{H_2O}} = 0.03 - 0.4$ atm
Kanno et al. [23]	Ni/YSZ cermet NiO 60 vol%	2.11[b]	1.12	$T = 1023 - 1123$ K $P_{\mathrm{H_2}} = 0.8 - 0.97$ atm $P_{\mathrm{H_2O}} = 0.03 - 0.2$ atm
Shikazono et al. [24] and Kishimoto et al. [25]	Ni/YSZ cermet Ni 50 vol%	2.556[b] (active TPB: 56.8 % [26])	2.24 (3.95 based on active TPB)	$T = 1273$ K $P_{\mathrm{H_2}} = 0.9 - 0.988$ atm $P_{\mathrm{H_2O}} = 0.012 - 0.1$ atm

a) Estimated by weight ratio of NiO and YSZ based on the data sets corrected by FIB-SEM [34].
b) Measured value by FIB-SEM.

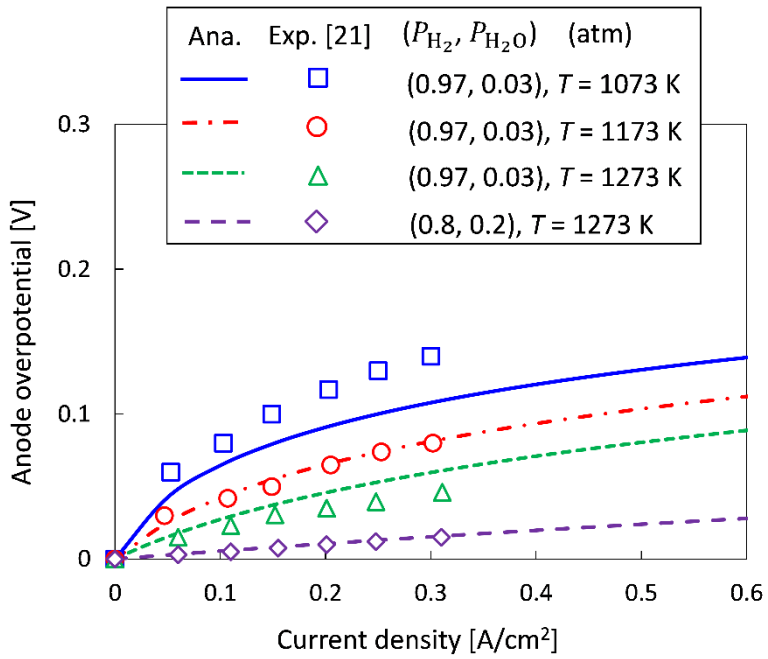

Figure 3-9. Fitting curves of Eq. (3.5) to Ni/YSZ anode experiments by Kishimoto et al. [21] to determine t_{eff}. Parameters in Table 3-1 are used for calculation of analytical results. The dependence of anode overpotential on temperature is shown.

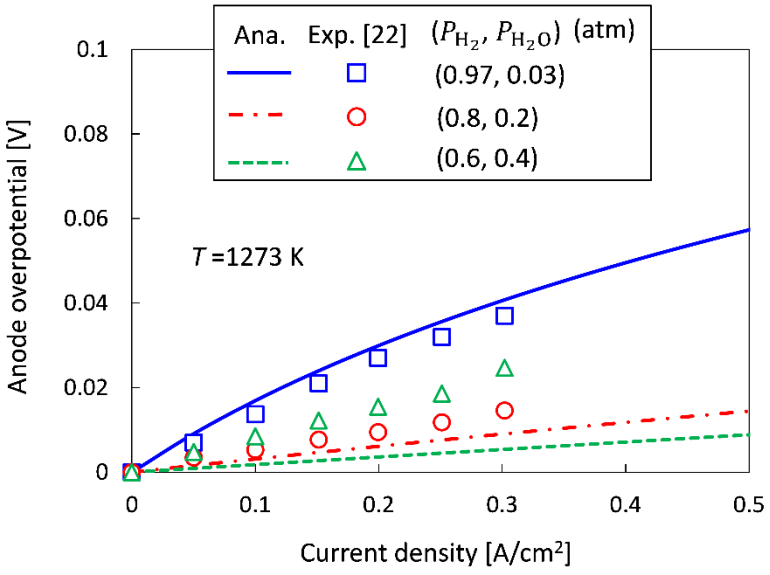

Figure 3-10. Fitting curves of Eq. (3.5) to Ni/YSZ anode experiments by Matsui et al. [22] to determine t_{eff}. Parameters in Table 3-1 are used for calculation of analytical results. The dependence of anode overpotential on steam partial pressure at 1273 K is shown.

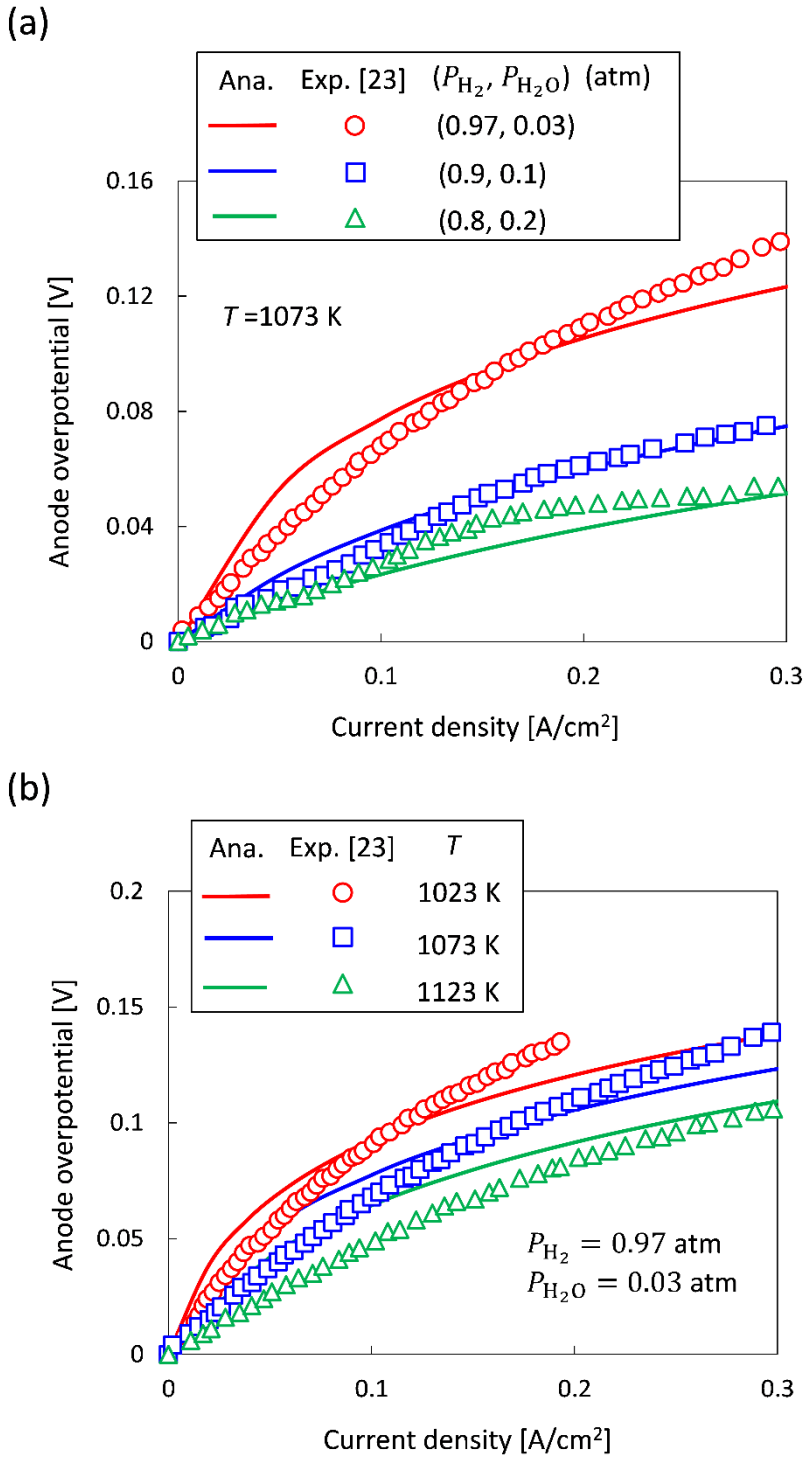

Figure 3-11. Fitting curves of Eq. (3.5) to Ni/YSZ anode experiments by Kanno et al. [23] to determine t_{eff}. Parameters in Table 3-1 are used for calculation of analytical results. The dependences of anode overpotential on (a) steam partial pressure at 1073 K and (b) temperature at (P_{H_2}, P_{H_2O}) = (0.97, 0.03) atm are shown.

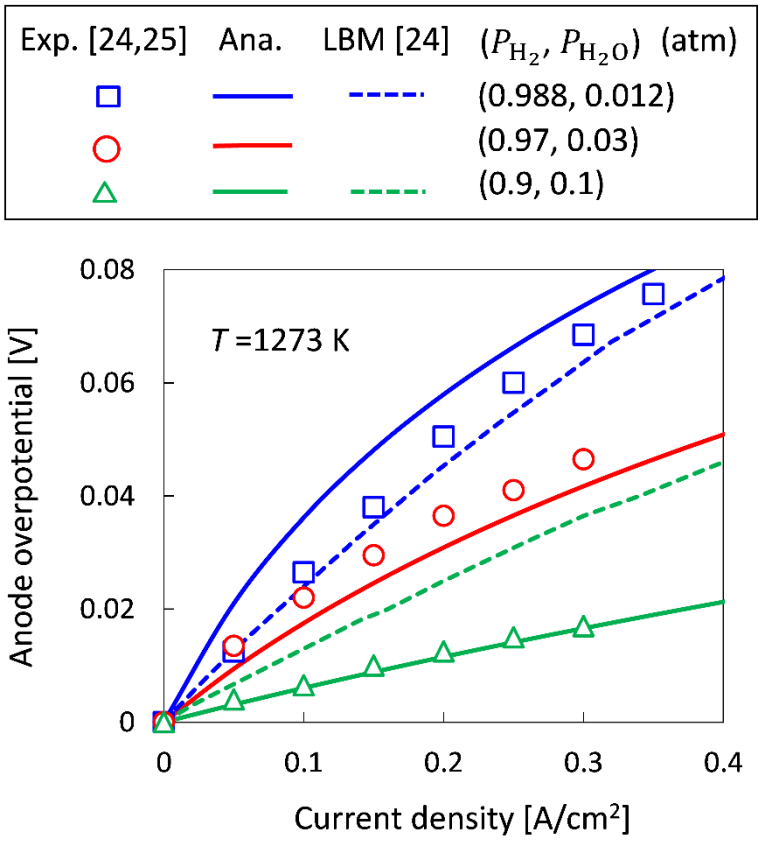

Figure 3-12. Fitting curves of Eq. (3.5) to Ni/YSZ anode experiments from Refs. [24,25] to determine t_{eff}. Parameters in Table 3-1 are used for calculation of analytical results. The dependence of anode overpotential on steam partial pressure at 1273 K is shown. Dashed lines show anode overpotential calculated in LBM simulation by Shikazono et al. [24].

3.5 Discussions

3.5.1 Dependence on fuel compositions and temperature

The dependences of current density with oxygen activity $i(a_{\text{O}})$ [Eq. (3.4)] and anode overpotential with current density $\eta_a(i)$ [Eq. (3.5)] on hydrogen partial pressure, steam partial pressure, and temperature are discussed based on obtained fitting results.

As shown in Figs. 3-6(a) and 3-7(a), as the hydrogen partial pressure P_{H_2} decreases, both the experimental and the analytical current densities shift in the direction of higher

oxygen activity on the horizontal axis. That is, in order to obtain the same current density, a higher oxygen activity is required. In Eq. (3.6), it is clear that the value of i_{limit} decreases with decreasing $P_{\mathrm{H_2}}$. Following the decrease in i_{limit}, the current density, $i(a_{\mathrm{O}})$, shifts in the direction of higher oxygen activity on the horizontal axis. In the case of $P_{\mathrm{H_2}} \leq 0.05$ atm in Figs. 3-6(a) and 3-7(a), the experimental current densities asymptote i_{limit} with increasing oxygen activity a_{O}, which are in good agreement with analytical results based on the model.

From the analytical and experimental results under the conditions of ($P_{\mathrm{H_2}}$, $P_{\mathrm{H_2O}}$) = (0.97, 0.03), (0.07, 0.03), and (0.02, 0.03) atm in Fig. 3-6(b), it is clear that the anode overpotential is not strongly affected by $P_{\mathrm{H_2}}$ in the low-current-density range ($i \leq 0.1$ A/cm^2). In the case of ($P_{\mathrm{H_2}}$, $P_{\mathrm{H_2O}}$) = (0.015, 0.01) atm, the anode overpotential around 0.1 A/cm^2 is higher than those for the other three fuel composites. Moreover, in the case of ($P_{\mathrm{H_2}}$, $P_{\mathrm{H_2O}}$) = (0.015, 0.03) atm, the calculated anode overpotential around 0.1 A/cm^2 is relatively close to the anode overpotentials of ($P_{\mathrm{H_2}}$, $P_{\mathrm{H_2O}}$) = (0.97, 0.03), (0.07, 0.03), and (0.02, 0.03) atm. Therefore, the increase in overpotential around 0.1 A/cm^2 of ($P_{\mathrm{H_2}}$, $P_{\mathrm{H_2O}}$) = (0.015, 0.01) atm is a result of the decrease in humidity from 0.03 to 0.01 atm. On the other hand, the anode overpotential increases drastically as the current density approaches the limiting current density (=C_1) in Eq. (3.6), as discussed in Chapter 2. In the case of ($P_{\mathrm{H_2}}$, $P_{\mathrm{H_2O}}$) = (0.02, 0.03) and (0.015, 0.01) atm, i_{limit} based on Eq. (3.6) is 0.27 and 0.20 A/cm^2, respectively. At the region where the current density approaches these values, the experimental plots follows the analytical trends. Wen et al. [16] investigated the dependence of the anode overpotential of a Ni/YSZ cermet anode on a fuel composition, which clarified that an anode overpotential is independent of hydrogen concentration while decreases with increasing humidity in hydrogen fuel. Their results

show the same trend as the present analytical and experimental results in the low-current-density range ($i \leq 0.1$ A/cm^2).

In order to discuss the P_{H_2} and P_{H_2O} dependence of anode overpotential, the calculated variations Δ of anode overpotential [Eq. (3.5)], 1st term, and 2nd + 3rd terms of Eq. (3.5) from standard condition at 1073 K and 0.1 A/cm^2 are shown as a function of P_{H_2} and P_{H_2O} in Figures 3-13(a) and (b), respectively. The standard condition is set to $P_{H_2} = 0.97$ atm for Fig. 3-13 (a) and $P_{H_2O} = 0.01$ atm for Fig. 3-13(b). From Fig. 3-13(a), the incremental of 1st term and decrement of 2nd + 3rd terms due to the decrease in P_{H_2} are balanced, which results in the constant η_a over a wide range of P_{H_2}. On the

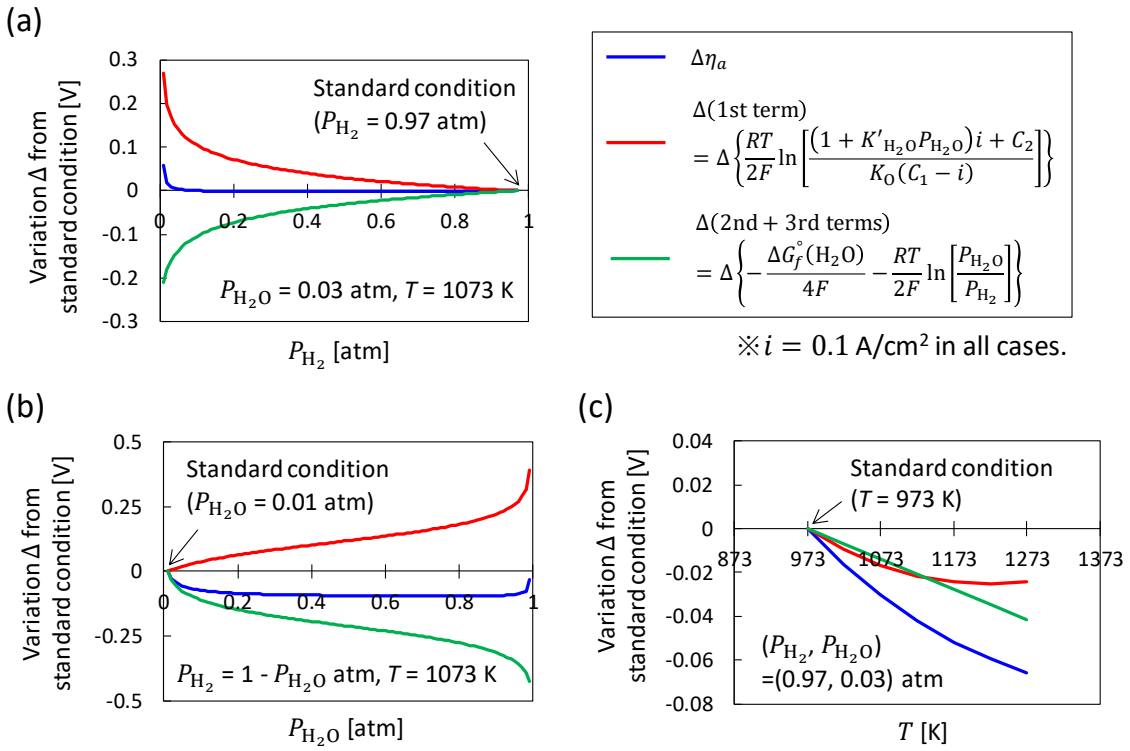

Figure 3-13. Calculated variations Δ of anode overpotential [Eq. (3.5)], 1st term, and 2nd + 3rd terms of Eq. (3.5) from standard condition as a function of (a) P_{H_2}, (b) P_{H_2O}, and (c) T. The standard condition of (a), (b), and (c) is $P_{H_2} = 0.97$ atm, $P_{H_2O} = 0.01$ atm, and T = 973 K, respectively. Current density is fixed to 0.1 A/cm^2 in all cases, and other calculated conditions are denoted in each graph.

other hand, the incremental of 1st term is smaller than the decrement of 2nd + 3rd terms due to the increase in $P_{\mathrm{H_2O}}$. Consequently η_a decreases with increasing $P_{\mathrm{H_2O}}$, as shown in Fig. 3-13(b). The fitting results in Figs. 3-6(b), 3-9, 3-10, 3-11(a), and 3-12 shows that the model represents the $P_{\mathrm{H_2O}}$ dependence of η_a well in the range of $0.01 \leq P_{\mathrm{H_2O}} \leq 0.2$ atm. At high humidity ($P_{\mathrm{H_2O}} = 0.2 - 0.4$ atm) in Fig. 3-10, however, the model predicts that the anode overpotential becomes lower with increasing humidity, which does not agree with experimental trend. One possible explanation of this disagreement is the surface oxidation of Ni caused by increased equilibrium $P_{\mathrm{O_2}}$ with humidity at anode side as mentioned previously [35].

The temperature dependence of $i(a_{\mathrm{O}})$ and $\eta_a(i)$ can be also discussed based on the model. Fig. 3-7(b) discloses that as the temperature increases, the analytical current densities shift toward high oxygen activity on the horizontal axis. This trend is in good agreement with experimental results by Ihara et al. [17]. The shift in the direction of the high oxygen activity mainly results from the change of K_{O}. In this model, the terms of K_{O} and a_{O} always appear as a product, $K_{\mathrm{O}}a_{\mathrm{O}}$, as shown in Eqs. (2.21)–(2.28). In addition, K_{O} decreases with increasing temperature through Eq. (3.8), which results in the shift of $i(a_{\mathrm{O}})$ in the direction of high oxygen activity on the horizontal axis. On the other hand, analytical curves in Fig. 3-7(b) also indicate that temperature does not strongly affect i_{limit} [Eq. (3.6)]. This is because the coverage of adsorbed hydrogen in Area 1, $\theta_{\mathrm{H(1)}}$, decreases with increasing temperature, while anodic reaction rate constants, k_{aI} and k_{aII} increase through Arrhenius-type expression [Eq. (3.9)].

As shown in Figs. 3-9 and 3-11(b), the analytical results of anode overpotential decrease with increasing temperature, which agrees well with the experimental results. The calculated variations Δ of anode overpotential [Eq. (3.5)], 1st term, and 2nd + 3rd

terms of Eq. (3.5) from standard condition ($T = 973$ K) at 0.1 A/cm^2 are shown as a function of T in Figures 3-13(c). From this figure, both 1st term and 2nd + 3rd terms decrease with increasing temperature, which is followed by the decrease in anode overpotential.

3.5.2 Effective anode thickness

Figure 3-14 summarizes effective anode thickness estimated by present model with respect to temperature, which is replotted from Table 3-2. From Fig. 3-14, a general trend is seen in six anodes: t_{eff} increases with temperature. As Miyawaki et al. pointed out [36], effective anode thickness is dominated by the balance between electrochemical reaction rate at the TPB and oxide ion conductivity in the YSZ phase, both of which increase with temperature. Fig. 3-14 indicates that when temperature increases, the enhancement of oxide ion conductivity is larger than that of electrochemical reaction rate, resulting in an increase in the effective anode thickness. The same trend was reported in the numerical simulation by Miyawaki et al. [36].

Although the trend of increased t_{eff} with temperature is observed in Fig. 3-14, quantitative discussion of t_{eff} is still difficult because it strongly depends on frequency factor A, that is, what kind of Ni-patterned anode experiment is selected as a basic data. Here, the analytical results based on our model are compared with LBM simulation by Shikazono et al. [24]. This is because in their work, exchange current density per unit TPB length for Butler-Volmer equation were obtained from Ni-patterned anode experiment by B.de Boer [20], which is the same one used in this study as shown in Fig. 3-8. In addition, active TPB ratio, 56.8%, is also presented in their microstructure [26], which has continuous networks of Ni from TPB to current collector, of YSZ to electrolyte,

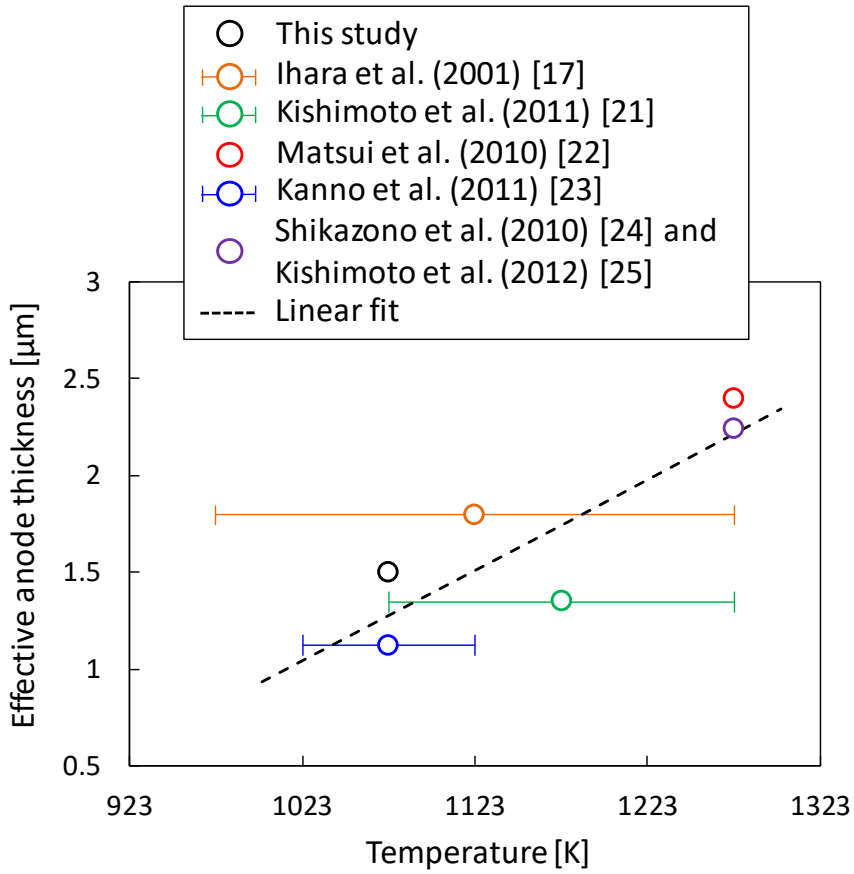

Figure 3-14. Correlation between temperature and effective anode thickness estimated by the fitting of present model to experimental results. Error bar shows the temperature range and plot represents the average temperature in each experiment. The data is replotted from Table 3-2.

and of pore to inlet gas phase. This can lead to quantitatively more precise value of t_{eff}, 3.95µm. The comparison of anode overpotentials at 1273 K obtained by experiments [24,25], current model, and LBM simulation from Shikazono et al [24] is shown in Fig. 3-12. The LBM simulation overestimates the anode overpotential at a high humidity (10% H_2O). The same trends are observed in other simulations at practical anode microstructure [21,23,25]. In those works, it was mentioned that the dependence of exchange current density on gas compositions assumed in the simulations possibly causes the discrepancy. On the other hand, dependence on steam partial pressure is well reproduced by the present

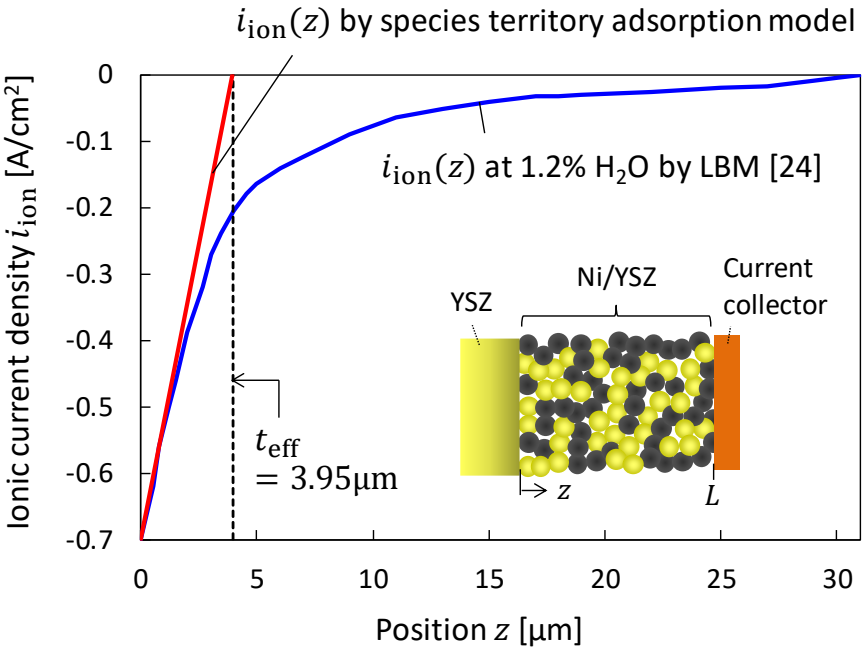

Figure 3-15. Ionic current density distributions at 1273 K in anode thickness direction z, $i_{\mathrm{ion}}(z)$, estimated by the model and calculated by the LBM simulation [24]. The distribution by the model is based on the assumption that all active TPBs at $z \leq t_{\mathrm{eff}}$ contributes electrochemical reaction uniformly while the reaction does not occur in other area.

model. As shown here, if the same Ni-patterned anode experiment is selected as a basic data, the present model can predict more precise dependence of anode overpotential on steam partial pressure than that by Butler-Volmer equation with empirical exchange current density.

Figure 3-15 shows ionic current density distributions at 1273 K in anode thickness direction z, $i_{\mathrm{ion}}(z)$, estimated by the model and calculated by the LBM at 1.2% H_2O [24]. Under the condition, experimental results are in good agreement with those predicted by LBM simulations in Fig. 3-12. Here, $i_{\mathrm{ion}}(z)$ estimated by the model is linear because the distribution is based on the assumption that all active TPBs at $z \leq t_{\mathrm{eff}}$ ($= 3.95\mu m$) contributes electrochemical reaction uniformly while the reaction does not

occur in other area. In Fig. 3-15, the LBM result is consistent with the linear profile by present model at $z \leq 1.5$ μm. On the other hand, $|i_{\mathrm{ion}}(z)|$ by the LBM is larger than that by present model at $z \geq 1.5$ μm. This indicates that in the LBM, all active TPBs at $z \leq 1.5$ μm uniformly contribute electrochemical reaction while the reaction at $z \geq 1.5$ μm is not uniform. In order to predict an non-uniform ionic current density distribution in porous anode, numerical simulation, such as LBM, needs to be conducted instead of evaluation of t_{eff} through fitting. The above discussion indicates that the introduction of present model into numerical simulation instead of Butler-Volmer equation can give more accurate prediction of anode polarization. One proposed scheme is as follows. At first, oxygen chemical potential distribution $\mu_{\mathrm{O}}(\boldsymbol{r})$ is calculated by numerical simulation [24, 37]. Here, $\boldsymbol{r}$ shows a position vector in an electrode. Then, a local oxygen activity $a_{\mathrm{O}}(\boldsymbol{r})$ in an electrode is obtained as follows [38]

$$a_{\mathrm{O}}(\boldsymbol{r}) = \exp\left[\frac{\mu_{\mathrm{O}}(\boldsymbol{r}) - \mu_{\mathrm{O}}^{\circ}}{RT}\right] \tag{3.13}$$

where μ_{O}^{0} is μ_{O} of 1 atm O_2 gas. Finally, local charge-transfer current density $i(\boldsymbol{r})$ [A/cm^3] is obtained from $a_{\mathrm{O}}(\boldsymbol{r})$ and Eq. (3.4) divided by t_{eff}.

3.5.3 Sensitivity analysis

In this section, the effect of $\theta_{\mathrm{H_2O(2)}}$ and $\theta_{\mathrm{O(2)}}$ on calculated anode overpotential was discussed through a sensitivity analysis because ΔH and ΔS for H_2O adsorption on YSZ (described as $\Delta H_{\mathrm{H_2O(2)}}$ and $\Delta S_{\mathrm{H_2O(2)}}$, respectively) were assumed to be the same as those on the Ni(111) surface, and for O adsorption on YSZ ($\Delta H_{\mathrm{O(2)}}$ and $\Delta S_{\mathrm{O(2)}}$) were determined through the fitting to the experimental results, as shown in Section 3.4. The effect $\Delta H_{\mathrm{H_2O(2)}}$ and $\Delta H_{\mathrm{O(2)}}$ values on anode overpotential and coverages adsorbed

species on YSZ ($\theta_{O(2)}$, $\theta_{H_2O(2)}$, $\theta_{V(2)}$) were investigated under the condition of (P_{H_2}, P_{H_2O}) = (0.97, 0.03) atm at 1073 K.

Figure 3-16(a) shows the analytical results of anode overpotential with current density at $\Delta H_{H_2O(2)}$ = 100, -18, and -100 kJ/mol. Anode overpotential does not vary when $\Delta H_{H_2O(2)}$ is increased from -18 to 100. On the other hand, anode overpotential

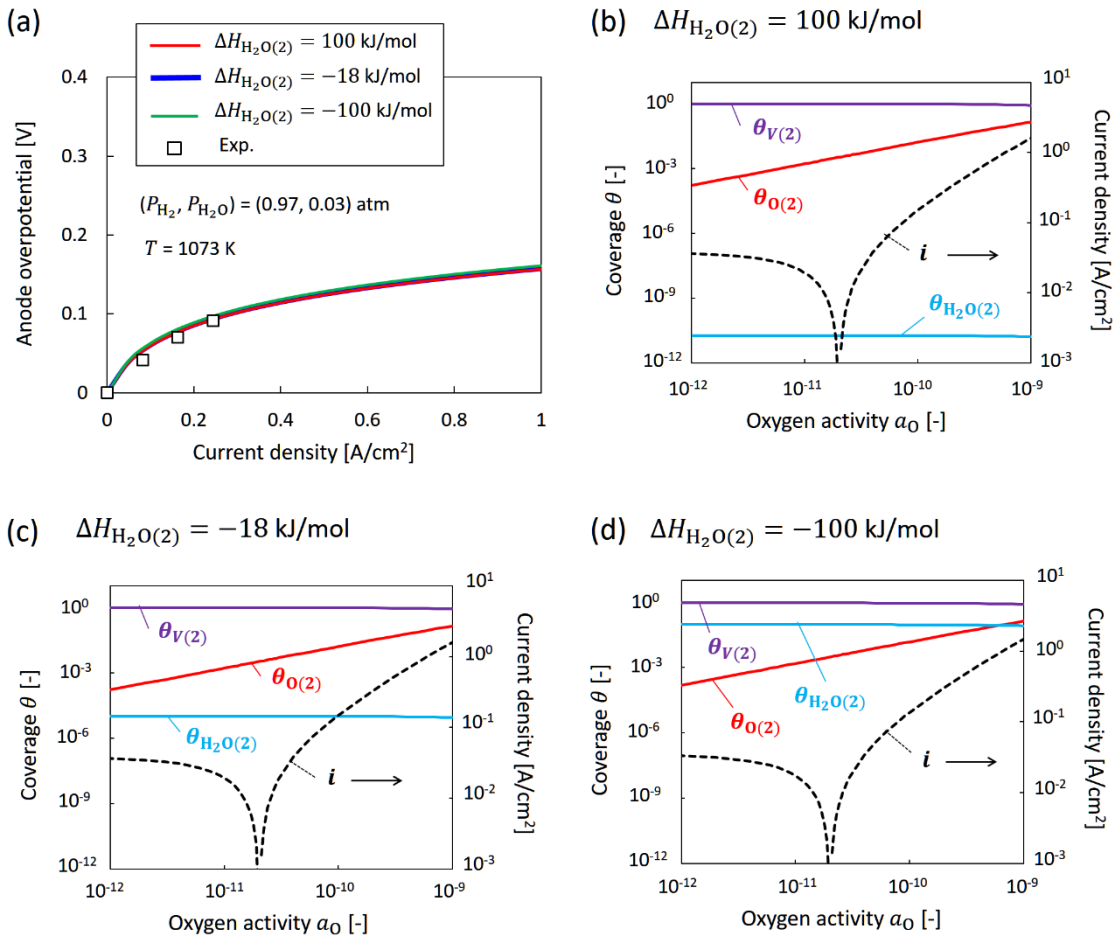

Figure 3-16. (a) Analytical results of anode overpotential with current density at $\Delta H_{H_2O(2)}$ = 100, -18, and -100 kJ/mol under the conditions of (P_{H_2}, P_{H_2O}) = (0.97, 0.03) atm and T = 1073 K. Experimental result is the same as in Fig. 3-6(b). (b)-(d) The corresponding calculated coverages of adsorbed species on YSZ as a function of oxygen activity at (b) $\Delta H_{H_2O(2)}$ = 100, (c) -18, and (d) -100 kJ/mol. The analytical result of current density with oxygen activity is also shown by dotted line.

slightly increases when $\Delta H_{H_2O(2)}$ is decreased from -18 to -100. Figures 3-16(b)–(d) show the coverages of adsorbed species on YSZ and the current density as a function of a_O at $\Delta H_{H_2O(2)}$ = 100, -18, and -100 kJ/mol, respectively. Even though $\theta_{H_2O(2)}$ increases from 10^{-11} to 10^{-1} with decreasing enthalpy $\Delta H_{H_2O(2)}$ from 100 to -100 kJ/mol, both any other coverage on YSZ and the current density do not change significantly. As

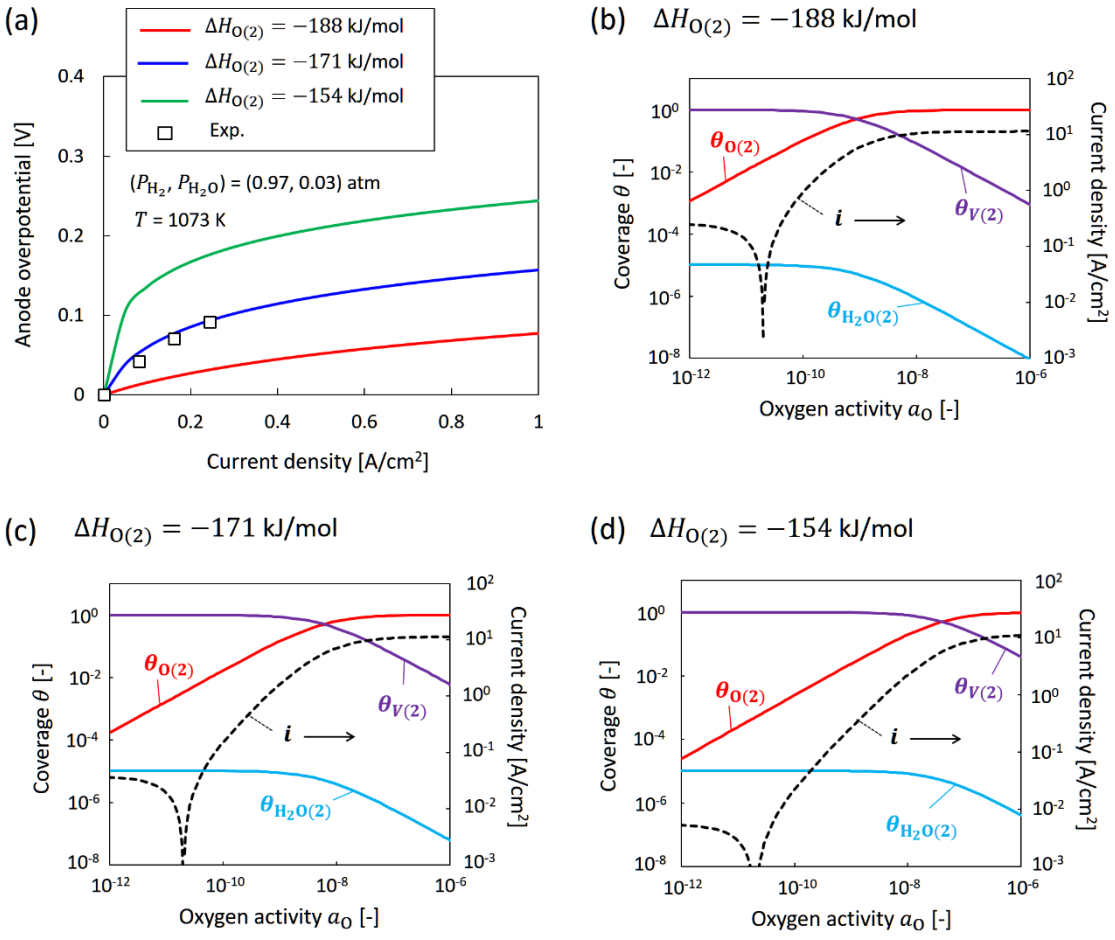

Figure 3-17. (a) Analytical results of anode overpotential with current density at $\Delta H_{O(2)}$ = -188, -171, and -154 kJ/mol under the conditions of (P_{H_2}, P_{H_2O}) = (0.97, 0.03) atm and T = 1073 K. Experimental result is the same as in Fig. 3-6(b). (b)-(d) The corresponding calculated coverages of adsorbed species on YSZ as a function of oxygen activity at (b) $\Delta H_{O(2)}$ = -188, (c) -171, and (d) -154 kJ/mol. The analytical result of current density with oxygen activity is also shown by dotted line.

vacancy site is dominant on YSZ, an increase in coverage $\theta_{H_2O(2)}$ does not affect $\theta_{O(2)}$, resulting in the weak impact of $\Delta H_{H_2O(2)}$ or $\theta_{H_2O(2)}$ on anode overpotential and current density.

The impact of $\Delta H_{O(2)}$ on the analytical results of anode overpotential is shown in Figure 3-17(a). From this figure, it is disclosed that only 10% change of $\Delta H_{O(2)}$ from the fitted value (from -171 to -188 or -154 kJ/mol) causes 2-3 times variation of anode overpotential. Figures 3-17(b)–(d) show the coverages of adsorbed species on YSZ and the current density as a function of a_O at $\Delta H_{O(2)}$ = -188, -171, and -154 kJ/mol, respectively. As $\Delta H_{O(2)}$ increases from -188 to -154 kJ/mol, $\theta_{O(2)}$ decreases in two orders of magnitude, resulting in one order of magnitude decrease of current density. As shown in Eq. (2.42), anodic current is proportional to $\theta_{O(2)}$ while independent of $\theta_{H_2O(2)}$ in this model. Therefore, anode overpotential and current density are strongly affected by $\Delta H_{O(2)}$ and almost independent of $\Delta H_{H_2O(2)}$ at the region where anodic current is dominant, as shown in Figs. 3-16 and 3-17.

3.5.4 Insights into oxygen migration process

At the end of this chapter, an oxygen migration process is discussed based on the model. From the fitting process in the section 3.4, $\Delta H_{O(2)}$ should be a large negative value; -171 kJ/mol. This means that oxygen migration from YSZ bulk to its surface near the TPB is an exothermic reaction. Similar trend was reported in DFT study by Cucinotta et al. [13]. Their calculation indicates that by filling the vacancy at Ni/YSZ interface with oxygen atom migrated from YSZ bulk, the potential energy of the reaction system decreases by about 81.9 kJ/mol. Although this energy gap is smaller than fitted $\Delta H_{O(2)}$ value obtained here, qualitative trend is consistent.

Alternatively, it could be interpreted that an oxygen atom supplied from YSZ bulk is adsorbed on the interface between Ni and YSZ as shown in path (ii) of Fig. 3-5 since the standard enthalpy of formation of NiO, -239.7 kJ/mol [39] is relatively close to the fitted $\Delta H_{O(2)}$. The large negative value of $\Delta H_{O(2)}$ is possibly attributed to the enthalpy of chemical bond formation between oxygen atom and Ni surface. Most of recent DFT calculations of hydrogen oxidation at Ni/YSZ anode [12-15] concluded that energetically favored path involves the reaction between hydrogen atom on Ni and oxygen atom bound to both Ni and YSZ, which is consistent with reaction path (ii) of Fig. 3-5.

As discussed in the sensitivity analysis in Fig. 3-17, parameters related to the oxygen migration process and the oxygen coverage on YSZ have a great impact on current density and anode overpotential. This result indicates that the dynamics of oxygen atom in the bulk and on the surface near the TPB, which is discussed here, is a key process for the enhancement of fuel oxidations and the improvement of anode performance. In order to understand the reaction mechanism of hydrogen oxidation at the anode and obtain new guidelines for the advanced SOFC anode design with higher electrochemical performance, precise dynamics of oxygen atom near the TPB should be further investigated and clarified.

3.6 Summary

The quantitative validation of the species territory adsorption model for Ni/YSZ anode was discussed based on the comparison to measured and reported experimental results. By introducing referenced thermodynamic and kinetic parameters predicted by DFT calculations, the model can predict anode overpotential using unknown values of quantities of state for oxygen migration process in YSZ near a TPB, frequency factor for

hydrogen oxidation, and effective anode thickness. The former two were determined through careful fitting process between the model and experimental results of Ni/YSZ cermet and Ni-patterned anodes. This makes it possible to estimate effective anode thickness based on the model. The estimated effective thicknesses for six Ni/YSZ anodes used in this study and several references show positive correlation with temperature. In addition, the comparison between results obtained by proposed model and by a published numerical simulation indicates that if the same Ni-patterned anode experiment is selected as a basic data, the present model can predict more precise dependence of anode overpotential on steam partial pressure than that by Butler-Volmer equation with empirical exchange current density. This suggests that the introduction of present model into numerical simulation instead of Butler-Volmer equation can give more accurate prediction of anode polarization. Moreover, the sensitivity analysis showed that the model parameters related to the oxygen migration process and the oxygen coverage on YSZ have a great impact on current density and anode overpotential. This result indicates that the dynamics of oxygen atom in the bulk and on the surface near the TPB is a key process for the enhancement of fuel oxidations and the improvement of anode performance.

References

[1] J. Hanna, W.Y. Lee, Y. Shi, A.F. Ghoniem, *Prog. Energy Combust. Sci.* 40 (2014) 74–111.

[2] R.J. Gorte, J.M. Vohs, *Annu. Rev. Chem. Biomol. Eng.* 2 (2011) 9–30.

[3] A. Atkinson, S. Barnett, R.J. Gorte, J.T.S. Irvine, A.J. Mcevoy, M. Mogensen, S.C. Singhal, J. Vohs, *Nat. Mater.* 3 (2004) 17–27.

[4] M. Brown, S. Primdahl, M. Mogensen, *J. Electrochem. Soc.* 147 (2) (2000) 475–485.

[5] S.P. Jiang, S.P.S. Badwal, *J. Electrochem. Soc.* 144 (11) (1997) 3777–3784.

[6] J. Mizusaki, H. Tagawa, T. Saito, K. Kamitani, T. Yamamura, K. Hirano, S. Ehara, T. Takagi, T. Hikita, M. Ippommatsu, S. Nakagawa, K. Hashimoto, *J. Electrochem. Soc.* 141 (8) (1994) 2129–2134.

[7] J. Mizusaki, H. Tagawa, T. Saito, T. Yamamura, K. Kamitani, K. Hirano, S. Ehara, T. Takagi, T. Hikita, M. Ippommatsu, S. Nakagawa, K. Hashimoto, *Solid State Ionics* 70/71 (1994) 52–58.

[8] A. Bieberle, L.P. Meier, L.J. Gauckler, *J. Electrochem. Soc.* 148 (6) (2001) A646–A656.

[9] M. Vogler, A. B-Hütter, L. Gauckler, J. Warnatz, W.G. Bessler, *J. Electrochem. Soc.* 156 (5) (2009) B663–B672.

[10] D.G. Goodwin, H. Zhu, A.M. Colclasure, R.J. Kee, *J. Electrochem. Soc.* 156 (9) (2009) B1004–B1021.

[11] W. Yao, E. Croiset, *J. Power Sources* 248 (2014) 777–788.

[12] M. Shishkin, T. Ziegler, *J. Phys. Chem. C* 114 (2010) 11209–11214.

[13] C.S. Cucinotta, M. Bernasconi, M. Parrinello, *Phys, Rev. Lett.* 107 (2011) 206103.

[14] S.C. Ammal, A. Heyden, *J. Phys. Chem. Lett.* 3 (2012) 2767–2772.

[15] S. Liu, T. Ishimoto, D.S. Monder, M. Koyama, *J. Phys. Chem. C* 119 (2015) 27603–27608.

[16] C. Wen, R. Kato, H. Fukunaga, H. Ishitani, K. Yamada, *J. Electrochem. Soc.* 147 (6) (2000) 2076–2080.

[17] M. Ihara, T Kusano, C. Yokoyama, *J. Electrochem. Soc.* 148 (3) (2001) A209–A219.

[18] D. Mogensen, J.-D. Grunwaldt, P.V. Hendriksen, K. Dam-Johansen, J.U. Nielsen, *J. Power Sources* 196 (2011) 25–38.

[19] S. Liu, T. Ishimoto, M. Koyama, *Appl. Surf. Sci.* 333 (2015) 86–91.

[20] B.de Boer, *Ph.D. Thesis*, University of Twente, The Netherlands (1998).

[21] M. Kishimoto, H. Iwai, M. Saito, H. Yoshida, *J. Power Sources* 196 (2011) 4555–4563.

[22] T. Matsui, R. Kishida, J.Y. Kim, H. Muroyama, K. Eguchi, *J. Electrochem. Soc.* 157 (5) (2010) B776–B781.

[23] D. Kanno, N. Shikazono, N. Takagi, K. Matsuzaki, N. Kasagi, *Electrochimica Acta* 56 (2011) 4015–4021.

[24] N. Shikazono, D. Kanno, K. Matsuzaki, H. Teshima, S. Sumino, N. Kasagi, *J. Electrochem. Soc.* 157 (5) (2010) B665–B672.

[25] M. Kishimoto, H. Iwai, M. Saito, H. Yoshida, *J. Electrochem. Soc.* 159 (3) (2012) B315–B323.

[26] H. Iwai, N. Shikazono, T. Matsui, H. Teshima, M. Kishimoto, R. Kishida, D. Hayashi, K. Matsuzaki, D. Kanno, M. Saito, H. Muroyama, K. Eguchi, N. Kasagi, H. Yoshida, *J. Power Sources* 195 (2010) 955–961.

[27] S. Uemura, D. Fukabori, S. Tsushima, S. Hirai, *Transactions of the JSME, Ser. B* 78 (785) (2012) 74–82 (in Japanese).

[28] E. Siebert, A. Hammoucha, M. Kleitz, *Electrochim. Acta* 40 (11) (1995) 1741–1753.

[29] M. Shishkin, T. Ziegler, *J. Phys. Chem. C* 113 (2009) 21667–21678.

[30] D.W. Blaylock, T. Ogura, W.H. Green, G.J.O. Beran, *J. Phys. Chem. C* 113 (2009) 4898–4908.

[31] M. Shishkin, T. Ziegler, *Phys. Chem. Chem. Phys.* 16 (2014) 1798–1808.

[32] S. Primdahl, M. Mogensen, *J. Electrochem. Soc.* 146 (8) (1999) 2827–2833.

[33] J.H. Nam, D.H. Jeon, *Electrochim. Acta* 51 (2006) 3446–3460.

[34] J.R. Wilson, J.S. Cronin, S.A. Barnett, *Scr. Mater.* 65 (2011) 67–72.

[35] K. Eguchi, Y. Kunisa, K. Adachi, H. Arai, *J. Electrochem. Soc.* 143 (11) (1996) 3699–3703.

[36] K. Miyawaki, M. Kishimoto, H. Iwai, M. Saito, H. Yoshida, *J. Power Sources* 267 (2014) 503–514.

[37] K. Matsuzaki, N. Shikazono, N. Kasagi, *J. Power Sources* 196 (2011) 3073–3082.

[38] J. Mizusaki, K. Amano, S. Yamauchi, K. Fueki, *Solid State Ionics* 22 (1987) 313–322

[39] S. Seki (Ed.), Kagaku Binran-Kiso II, second ed. Handbook of Chemistry-basic II (1975) pp. 962, Maruzen, Tokyo (in Japanese).

Chapter 4

Imaging of microstructure-scaled active sites in porous composite cathode

4.1 Introduction

Porous composite electrodes are widely used for state-of-the-art SOFCs, such as Ni/YSZ for anodes or LSM/YSZ for cathodes. These electrodes have micro/nano-scale complex structures consisting of electron conductors, oxide ion conductors, and pore phases, where chemical species are transported and accompanied by electrochemical reactions at the TPB. The distributions of active reaction sites and the transport paths of ions and electrons greatly affect the electrode performance, which has been intensively investigated by numerical modeling and simulations [1-5]. However, experimental information about active reaction site distribution or oxide ion paths in the microstructure of the composite electrode has not been reported so far. Imaging active sites in composite electrodes can verify numerical results and attain new guidelines to optimize its microstructures for further improvement of SOFC performance and stability. In addition, oxygen migration process near the reaction site has not been well understood [6] though the process strongly affects electrochemical performance of an anode, as discussed in Chapter 3. Tracking oxide ion paths near the TPB of composite electrodes can give valuable information related to the detailed reaction mechanisms. Therefore, an imaging technique of active sites and oxide ion flows in porous composite electrodes should be

realized and developed in microstructure scale.

Atomic labeling using oxygen isotope is a powerful tool to visualize active sites and oxide ion flows in SOFC materials, which has been mainly applied to thin film electrodes with well-defined geometries at low temperatures (573-973 K) to clearly distinguish oxygen incorporation sites from other parts [7-9]. Oxygen isotope exchange using Pt electrode on YSZ electrolyte under cathodic polarization was conducted at 973 K by Kawada et al. [7], showing that Pt/YSZ/gas TPBs are active sites. In the case of LSM/YSZ system, Horita et al. [8] showed that both TPB and LSM bulk paths are active. In addition, effective TPB width of Pt thin film cathode on YSZ was investigated at about 600 K by Fleig et al. [9]. In the case of composite electrodes operated at a practical temperature (~1073 K), however, it seems hard to identify active sites in the zirconia phase because the incorporated isotope diffuses quickly into the whole area of YSZ or ScSZ, forming a micron/submicron-scaled percolation structure and resulting in a uniform concentration of ^{18}O. Although overall oxide ion flows from cathode to anode sides in a practical SOFC was visualized using a ^{18}O labeling by Horita et al. [10], active reaction sites have not been observed in an electrode particle scale so far.

In this study, the LSM/ScSZ porous cathode is selected as a target for active sites imaging. Although lanthanum cobaltite and ferrite cathodes, such as $(La,Sr)CoO_3$ (LSC) or $(La,Sr)(Co,Fe)O_3$ (LSCF), are more active for oxygen reduction, LSM-based cathodes are the most practical because LSM is more thermodynamically stable than mixed conductors containing cobalt or iron [5,11,12]. In addition, a thermal expansion match between LSM and YSZ makes it easier to fabricate a wide variety of cathode microstructures and cell geometries [12]. In the LSM/ScSZ (YSZ) system, both the TPB between the LSM-ScSZ and gas phases, and the double phase boundary (DPB) between

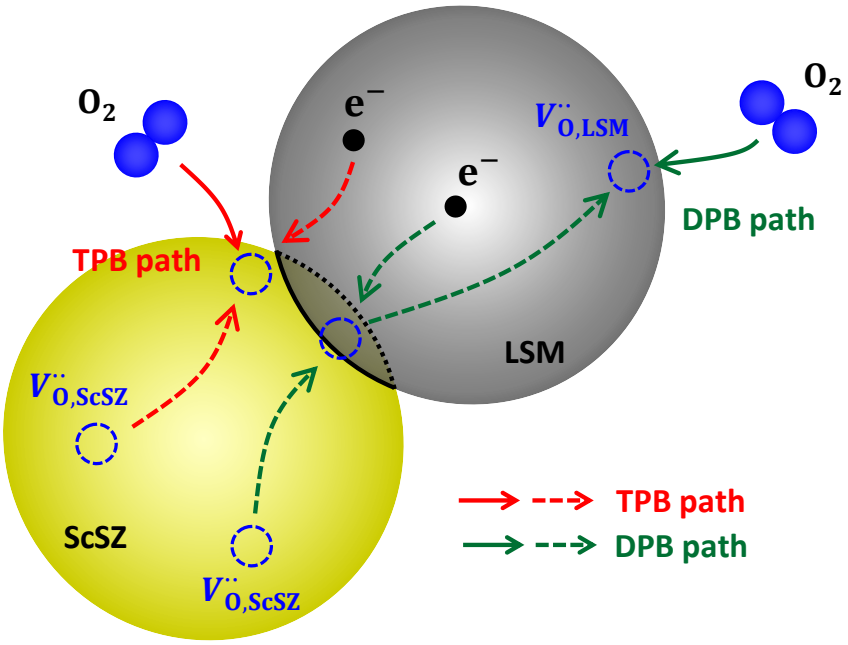

Figure 4-1. Two oxygen reduction pathways at the LSM/ScSZ cathode [15]. Oxygen atoms are incorporated from the gas phases into the ScSZ bulk in the TPB path while into the LSM bulk in the DPB path.

the LSM and gas phases work as active sites for oxygen reduction [13-16]. Figure 4-1 shows a schematic of two oxygen reduction pathways in the LSM/ScSZ system given in kinetic study of oxygen vacancy formation of LSM by Jiang et al. [15]. At a low current density, oxygen reduction mainly proceeds at the TPB denoted by a TPB path.

$$\frac{1}{2}O_2 + 2e^- + V_{O,ScSZ}^{\bullet\bullet} \rightarrow O_{O,ScSZ}^{\times} \tag{4.1}$$

Here, $V_{O,ScSZ}^{\bullet\bullet}$ and $O_{O,ScSZ}^{\times}$ represent an oxygen vacancy and O^{2-} in the ScSZ bulk, respectively. At a high current density, the remaining electrons are provided to the interface between LSM and ScSZ because not all the electrons can be consumed at the TPB. This is followed by the partial reduction of Mn^{3+} to Mn^{2+} accompanied by the generation of oxygen vacancies in the LSM bulk, as follows:

$$O_{O,LSM}^{\times} + 2e^- + V_{O,ScSZ}^{\bullet\bullet} + 2Mn^{\bullet} \rightarrow O_{O,ScSZ}^{\times} + V_{O,LSM}^{\bullet\bullet} + 2Mn^{\times} \tag{4.2}$$

Here, $O^{\times}_{O,LSM}$ and $V^{\cdot\cdot}_{O,LSM}$ show the oxide ion, O^{2-}, and an oxygen vacancy in the LSM bulk, respectively. Moreover, $Mn^{\cdot}$ represents a normal Mn^{3+} ion, while $Mn^{\times}$ represents a reduced state, e.g. Mn^{2+}. The generated oxygen vacancy diffuses to the LSM surface and recombines with oxygen gas (DPB path in Fig. 1) with the re-oxidation of Mn^{2+} to Mn^{3+}, as follows:

$$\frac{1}{2}O_2 + V^{\cdot\cdot}_{O,LSM} + 2Mn^{\times} \rightarrow O^{\times}_{O,LSM} + 2Mn^{\cdot} \quad (4.3)$$

This means that with an increasing charge transfer current, oxygen reduction sites are expanded from a TPB to a DPB, and oxygen diffusion is promoted into the LSM bulk. Indeed, the enhanced ^{18}O diffusion into the LSM bulk with increasing cathodic polarization has been confirmed by several isotope exchange experiments using thin film cathodes [13,17]. The oxygen tracer diffusion coefficient of LSM is seven orders of magnitude smaller than that of ScSZ [18,19]; thus, the oxygen isotope incorporated into LSM diffuses only about 10 nm during 1 min annealing in $^{18}O_2$ at 1073 K, and is expected to remain inside the same particle (the concentration of ^{18}O depends strongly on the activity of oxygen reduction). Consequently, the isotope oxygen inside the LSM works as an active site 'detector'.

In this chapter, visualization technique of active reaction sites in SOFC porous electrodes with microstructure scale is developed. In order to quench a reaction, a SOFC power generation equipment with a nozzle for direct helium gas impinging jet to the cell is prepared, and its cooling performance is evaluated. Using constructed quench system and oxygen isotope labeling, active sites for oxygen reduction reaction in LSM/ScSZ porous cathode are visualized in microstructure scale. An electrolyte-supported cell is operated in $^{18}O_2$ at 1073 K and subsequently quenched to a room temperature. Then, the ^{18}O distribution in cross section of the cathode is obtained by secondary ion mass

spectroscopy (SIMS) with a spatial resolution of 50 nm. Finally, the active sites distribution is discussed based on the obtained ^{18}O concentration images.

4.2 Experimental section

4.2.1 Power generation equipment with quench system

In order to quench a reaction in a SOFC cell during isotope exchange experiment, a power generation equipment with a nozzle for a helium impinging jet was prepared. As shown in Figure 4-2(a), the flow system includes $^{18}O_2$ supply and recirculation lines at cathode side and helium lines at both anode and cathode sides. 4-way and 6-way valves are used to change gas atmospheres quickly for anode and cathode sides, respectively. The $^{18}O_2$ recirculation line is used when long-time (> 3 min) $^{18}O_2$ anneal is needed in an experiment. Figure 4-2(b) shows a details of the quench system. Inside an electric furnace, a single cell is fixed with ceramic tubes using a glass seal. A Pt wire attached to the cell is used for electrochemical measurement. Inside the ceramic tubes, nozzles with a diameter of 1 mm, which are covered by a water cooling jacket and a thermal insulator, are set at both anode and cathode sides. In this equipment, an inside of the nozzle can be kept at a room temperature while the SOFC cell is operated at 1073 K (The detailed thermal design of the developed quench system is presented in Appendix D). The operated cell is abruptly cooled by supplying helium gas of 10 L/min, which is equivalent to a flow velocity of 213 m/s at an outlet of the nozzle. The impinging jet and high thermal conductivity of He, which is one order of magnitude larger than that of typical gases such as Air, N_2, or Ar [20], enhance a heat transfer, resulting in a high cooling rate. A photograph of the nozzle is shown in Figure 4-2(c). The cooling performance of the equipment was experimentally evaluated and discussed. The details of the experiment are

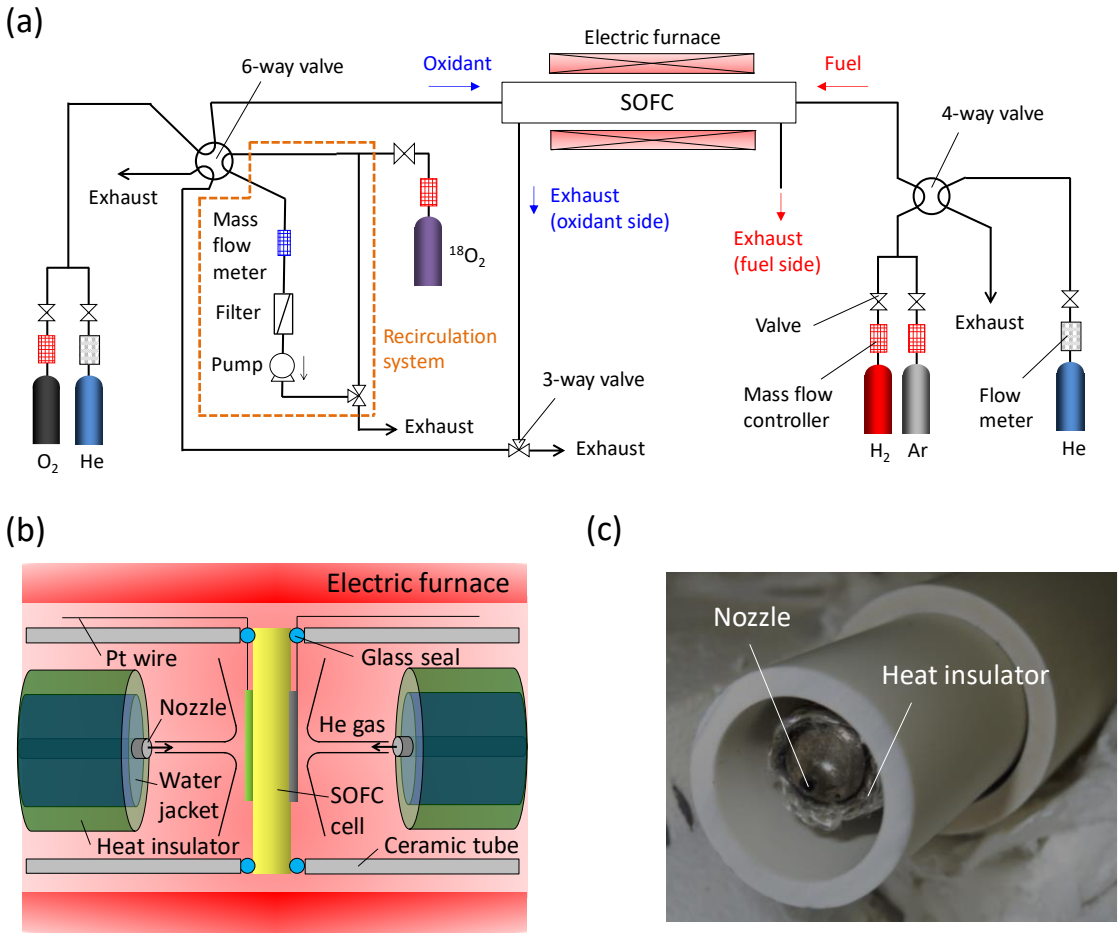

Figure 4-2. Power generation equipment with quench system for isotope exchange experiment. (a) Schematic of a flow line for the SOFC power generation experiment in $^{18}O_2$ atmosphere. The system is equipped with a $^{18}O_2$ recirculation pump and He flow line. (b) Detailed schematic of the quench system inside electric furnace. A nozzle for helium impinging jet is covered by water cooling jacket and heat insulator. (c) Photograph of the nozzle for quenching.

presented with the results and discussion in section 4.3.

4.2.2 Cell fabrication

As shown in Figure 4-3(a), an electrolyte-supported cell was used in this work. For the electrolyte, a YSZ (8 mol% Y_2O_3-stabilized ZrO_2) disk with a diameter of 20 mm and thickness of 300 μm was used. To manufacture the anode, a mixture of NiO, YSZ (weight

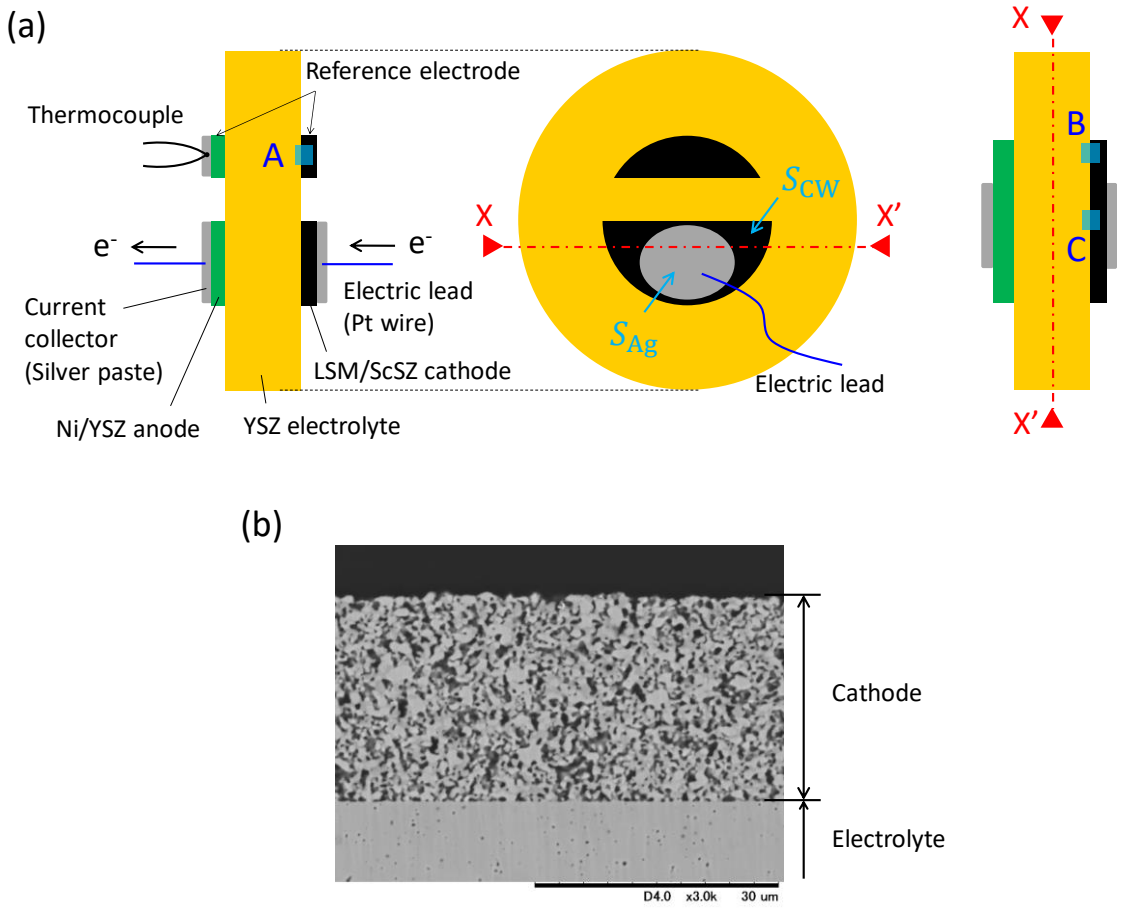

Figure 4-3. (a) Electrolyte-supported cell with working and reference electrodes used in this study. SIMS images were obtained from sections A, B, and C. In the middle figure, area of cathode working and attached current collector (silver paste) is described by S_{CW} and S_{Ag}, respectively. (b) SEM image of the cross section of LSM/ScSZ cathode.

ratio of NiO:YSZ=66:34), α-terpineol, ethyl cellulose, a dispersant, and a plasticizer was prepared and coated onto one side of the disk. The disk was dried at 90 ℃ for 12 h and sintered at 1300 ℃ for 4 h in an ambient atmosphere. The cathode was fabricated using a composite powder of LSM ($La_{0.8}Sr_{0.2}MnO_{3-\delta}$) and ScSZ (10 mol% Sc_2O_3-1 mol% CeO_2-ZrO_2) at a weight ratio of 50:50, and the same admixture for the anode paste was used. The paste was coated onto the other side, dried at 90 ℃ for 12 h, and sintered at 1200 ℃

for 4 h in an ambient atmosphere. Both the anode and cathode were separated into two parts to prepare reference electrodes, as shown in Fig. 4-3(a). The thicknesses of the fabricated anode and cathode were about 20 μm and 25 μm, respectively. The SEM image of the cross section of the cathode is shown in Figure 4-3(b). Pt wire was attached to working electrodes as an electric lead using a current collector of silver paste (Heraeus, C8728). In the middle of Fig. 4-3(a), area of cathode working and attached current collector (silver paste) is described by S_{CW} and S_{Ag}, respectively. The electrode area covered by a current collector was about 50 % ($S_{\mathrm{Ag}}/S_{\mathrm{CW}} = 0.5$) in this study. A K-type thermocouple was also attached to the anode reference using silver paste to monitor the cell temperature.

4.2.3 Power generation in $^{18}O_2$ and quench experiment

Initially, the cell was operated in 50% H_2 and 50% Ar for the anode side and in 100% normal O_2 for the cathode side at 1073 K for 10 min under a constant current density of 0.14 A/cm^2. Then, the normal O_2 was switched to $^{18}O_2$ (>97.5%, Center of Molecular Research), and the cell was operated for 3 min. Finally, the cell was abruptly quenched to a room temperature by the helium impinging jet of 10 L/min at both anode and cathode sides. Since fuel and oxidant were also supplied through water-cooled nozzles in this experiment, high flow rate causes a decrease in temperature during fuel cell operation. Therefore, the total flow rate of each side was fixed to relatively low value, 30 mL/min. The amount of supplied H_2 and O_2 seems to be sufficient for the power generation because fuel and oxygen utilization during operation at 0.14 A/cm^2 is 2.3 % and 0.6 %, respectively.

4.2.4 SIMS analysis

The ^{18}O distribution in a cross section of the quenched cathode was obtained by secondary ion mass spectroscopy (SIMS) with a spatial resolution of 50 nm (CAMECA, NanoSIMS 50L). Before the SIMS analysis, pores of the sample were infiltrated with an epoxy resin; then, the cross section of the cathode was polished using a cross section polisher (JEOL, SM-09010CP) to obtain a smooth surface. A focused Cs^+ primary ion beam (beam diameter: ca. 100 nm) was scanned on the polished surfaces and secondary ions were detected by a double-focusing magnetic sector mass spectrometer. Here, the distributions of four secondary ions ($^{16}O^-$, $^{18}O^-$, $^{55}Mn^{16}O^-$, and $^{90}Zr^{16}O^-$) were analysed.

4.3 Results and discussion

4.3.1 Evaluation of cooling performance

Cooling performance of the developed system was evaluated using two YSZ disks as shown in Figure 4-4(a). A K-type thermocouple with a diameter of 0.127 mm was fixed between two YSZ electrolyte disks using silica glue. This sample was set to the equipment described in Fig. 4-2(b), a temperature was monitored during a quenching, and the results were compared with an analytical solution of heat conduction equation. YSZ plane wall with a thickness of 600 μm was assumed for the calculation of heat conduction as shown in Figure 4-4(b). Both surfaces of the wall were cooled by a helium impinging jet, and the temperature change of the center (point A) was calculated based on both local Nusselt number at stagnation point, Nu_{max}, and average Nusselt number in the region with a diameter of 20 mm, Nu_{ave}. Nu_{max} is calculated as follows [21].

$$Nu_{max} = 5.97 Pr^{0.5} Re_D^{0.5} \left(H/D\right)^{-0.1} \tag{4.4}$$

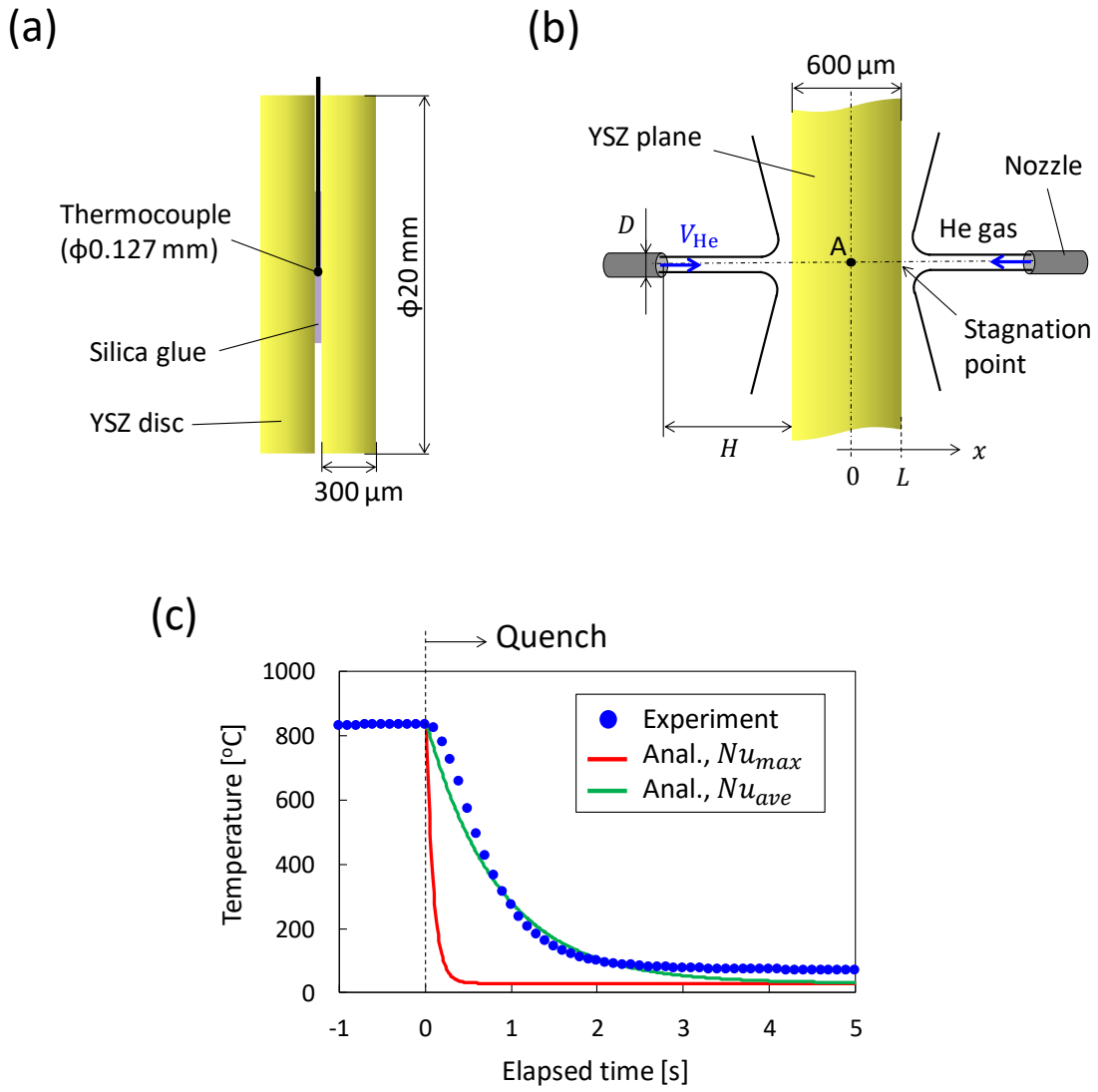

Figure 4-4. Evaluation of cooling performance. (a) Thermocouple between two YSZ electrolytes attached by silica glue for temperature measurement. (b) Assumed geometry for calculation of heat conduction equation. V_{He} is a flow velocity of ejected helium. (c) Experimental and analytical results of temperature change at the center of electrolyte [point A in (b)] during quenching using He impinging jet. Two analytical results based on average and local Nusselt number are shown.

Here, H is a distance between the nozzle and wall (= 12 mm), and D is a diameter of the nozzle (= 1 mm). Re_D is calculated by the representative length D and the velocity of ejected helium V_{He} (= 213 m/s). Nu_{ave} is obtained by following formula [21].

$$Nu_{ave} = \frac{D}{r} \cdot \frac{1 - 1.1\frac{D}{r}}{1 + 0.1\left(\frac{H}{D} - 6\right)\frac{D}{r}} \cdot 2Re_D^{0.5}\left(1 + \frac{Re_D^{0.55}}{200}\right)^{0.5} \cdot Pr^{0.42} \quad (4.5)$$

where r is a radius of the region for the average (=10 mm). As a result, $Nu_{max} = 160$ and $Nu_{ave} = 6.77$ are obtained. Analytical lines in Figure 4-4(c) are exact solutions of 1-dimensional unsteady-state heat conduction equation for plane wall under the boundary condition of the third kind with above Nusselt numbers [22].

In the experiment, one side of the sample was exposed to 50% H_2-50% Ar and another to pure O_2 at 830 ℃ for a few minutes, subsequently the sample was cooled to a room temperature by changing the gas to helium of 10 L/min. Fig. 4-4(c) shows experimental and analytical results of temperature change during quenching. At $t = 0$ sec., gas atmosphere was quickly changed to helium. As shown in Fig. 4-4(c), the temperature of YSZ electrolyte could be decreased from 830 to 150 ºC within 1.5 sec., which was in good agreement with analytical results based on the average Nusselt number Nu_{ave}. The cooling rate obtained here (1.5 sec.) is much faster than the previous ones (ca. 20 sec. ~ several minutes) by blowing inert gas to a wall of a reactor tube [7,8,13,17]. The analytical results based on Nu_{max} predict that it takes only 0.2 sec. to decrease the temperature from 830 to 150 ºC, which is much faster than experimental results.

Based on the obtained temperature profiles in Fig. 4-4(c), diffusion length of oxygen atom during quenching was estimated. As shown in Figure 4-5(a), 1-dimensional semi-infinite solid of YSZ is assumed and relative ^{18}O concentration profile is obtained by solving a diffusion equation numerically. Before the quench, ^{18}O is assumed to exist only near the TPB ($x = 0$), which is denoted by 'Initial' in Figure 4-5(b). There is no ^{18}O flux at $x = 0$ and an oxygen diffusivity in YSZ bulk D_{bulk} [m^2/s] at each temperature is calculated by

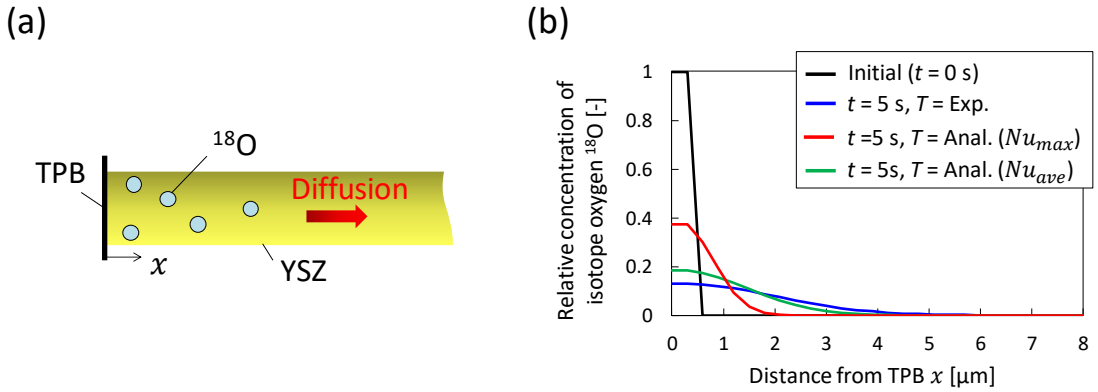

Figure 4-5. (a) Schematic of ^{18}O diffusion in 1-dimensional semi-infinite solid of YSZ. (b) Numerical results of relative ^{18}O concentration profile in YSZ bulk in 5 sec. after quench has been started.

following experimental relation [23].

$$D_{\text{bulk}} = 8.0\times10^{-7}\exp\left(-1.11\text{eV}/k_{\text{B}}T\right) \tag{4.6}$$

Fig. 4-5(b) shows ^{18}O concentration profile (t = 5 sec.) after the sample is cooled enough in Fig. 4-4(c). Based on the experimental temperature profile, ^{18}O diffuses maximum 4 μm from TPB and an obvious concentration difference is observed between locations at x = 0 and 2-3 μm. This indicates that the quench can suppress ^{18}O diffusion length within a scale of 2-3 YSZ particles with diameter of 1 μm. Fig. 4-5(b) also indicates that quenching with Nu_{max} can give an obvious ^{18}O concentration difference between locations at x = 0 and 1 μm.

4.3.2 Electrochemical performance and monitored temperature

First, the initial I-V characteristics and electrochemical impedance of the cell used in the isotope exchange were measured at 1073 K, as shown in Figures 4-6(a) and (b), respectively. The impedance spectra were measured between anode working and cathode working at 0.14 A/cm^2. The cell showed a maximum power density (P_{max}) of 0.085

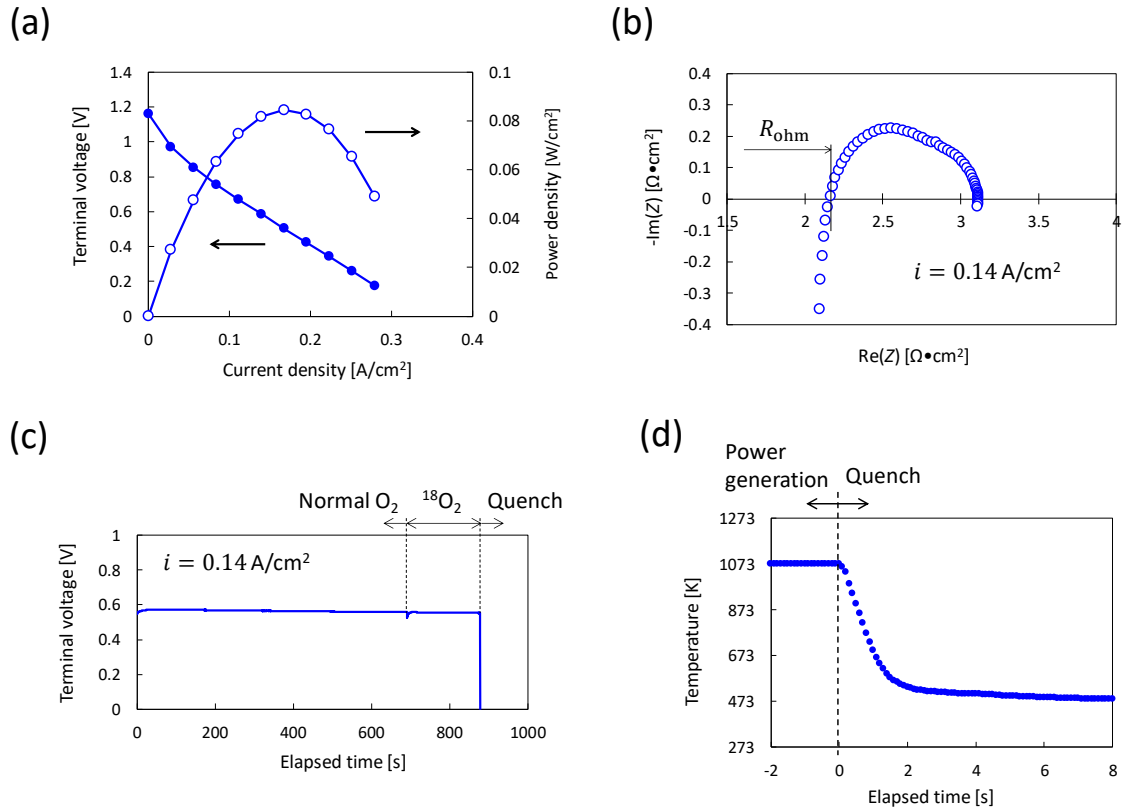

Figure 4-6. (a) Initial performance of the cell used in the isotope exchange at 1073 K. Mixture of 50% H_2 – 50% Ar and pure oxygen were supplied as a fuel and oxidant, respectively. (b) Impedance spectra at 0.14 A/cm^2 measured between anode working and cathode working. (c) Terminal voltage versus elapsed time with a constant current density of 0.14 A/cm^2. (d) Temperature change of the cell during quenching measured by the thermocouple in Fig. 4-3(a).

W/cm^2 and overall ohmic resistance (R_{ohm}) of 2.16 Ω•cm^2, which is larger than the value estimated for R_{ohm} from the ionic conductivity [24] and thickness of the YSZ electrolyte (1.50 Ω•cm^2). This comes from the small contact area between the electrode and current collector [25], and is discussed later. While a constant current density of 0.14 A/cm^2 was applied, the cell showed an almost stable terminal voltage of about 0.56 V until quenching reaction as shown in Figure 4-6(c). In the quenching process, the temperature of the cell measured by the thermocouple in Fig. 4-3(a) decreased from 1073 K to 673 K in 1 sec.,

as shown in Figure 4-6(d). This rapid cooling makes it possible to keep the electrode in an operational state by suppressing the diffusion length of the oxide ion within about 3 μm in ScSZ [19] and 1 nm in LSM [18]. The cooling rate observed here was a little bit smaller than the rate in the quench performance test [Fig. 4-4(c)], which maybe resulted from the difference of the position of thermocouples in Figs. 4-3(a) and 4-4(a).

4.3.3 Secondary ion mappings

In this study, SIMS images at the interface between the cathode and electrolyte were taken from different three sections A, B, and C in Fig. 4-3(a). Section A is a part of cathode reference and represents OCV (non-biased) condition while both sections B and C are placed in cathode working (biased condition). Since several studies suggested an inhomogeneous current density distribution induced by non-uniform contact between cathode and current collector [25,26], SIMS images at section B (biased, far area from current collector) and C (biased, directly under the contact area of the current collector) were collected here. Figures 4-7, 4-8, and 4-9 show the secondary ion mappings at sections A, B, and C, respectively. In these figures, (a) shows a phase mapping of LSM and zirconia based on the intensity of $Mn^{16}O^-$ and $Zr^{16}O^-$, and (b) shows an ^{18}O concentration ($= c_{18O}$) mapping represented by $I(^{18}O^-)/[I(^{16}O^-) + I(^{18}O^-)]$. Here, $I(^{16}O^-)$ and $I(^{18}O^-)$ indicate the SIMS signal intensity of each ion. Obtained c_{18O} value means a ratio of the number of ^{18}O atom to the total number of oxygen atom in arbitrary volume. Prior to the calculation of c_{18O} image, binarization processing is performed on the $^{16}O^-$ image to remove all signal from pore phases. From the phase mapping images, the LSM, zirconia (ScSZ, YSZ), and pore phases can be distinguished clearly in microstructure scale.

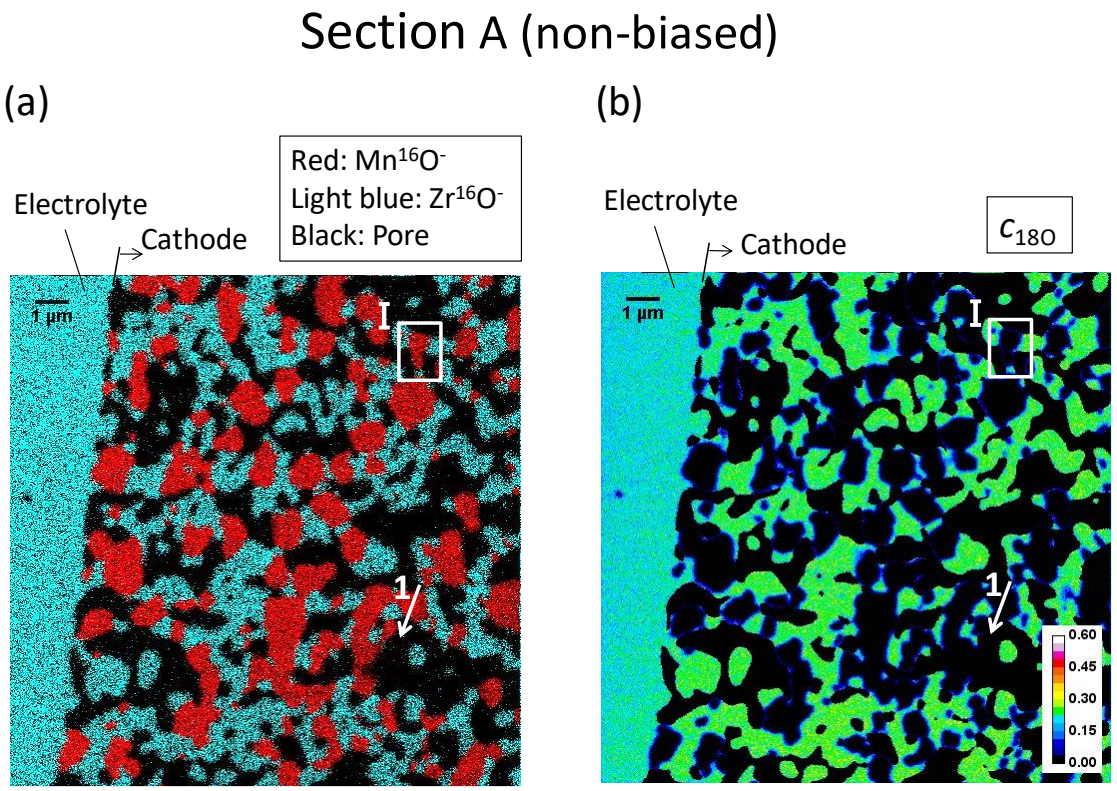

Figure 4-7. Secondary ion mappings of the interface between the LSM/ScSZ cathode and YSZ electrolyte obtained from section A (non-biased) in Fig. 4-3(a). (a) Phase mapping of each material. Red and light blue represent $Mn^{16}O^-$ (LSM) and $Zr^{16}O^-$ (ScSZ, YSZ), respectively. The black regions show the pore phases. (b) Oxygen isotope concentration ($= c_{18O}$) mapping represented by $I(^{18}O^-)/[I(^{16}O^-) + I(^{18}O^-)]$.

As shown in Fig. 4-7(b), ^{18}O is uniformly distributed in the ScSZ phase with $c_{18O} \approx 0.25$, while an almost natural value of $c_{18O} = 0.002$ is observed inside the LSM bulk under no current condition. ^{18}O exchanges with lattice oxygen of ScSZ surface (surface exchange) and diffuses to inside ScSZ bulk (tracer diffusion) under non-biased condition while does not diffuse to inside LSM bulk due to a low oxygen tracer diffusivity of LSM [18].

In SIMS image at section B shown in Fig. 4-8(b), ^{18}O is distributed only inside the ScSZ bulk with $c_{18O} \approx 0.25$ as in the case with non-biased condition (section A) though

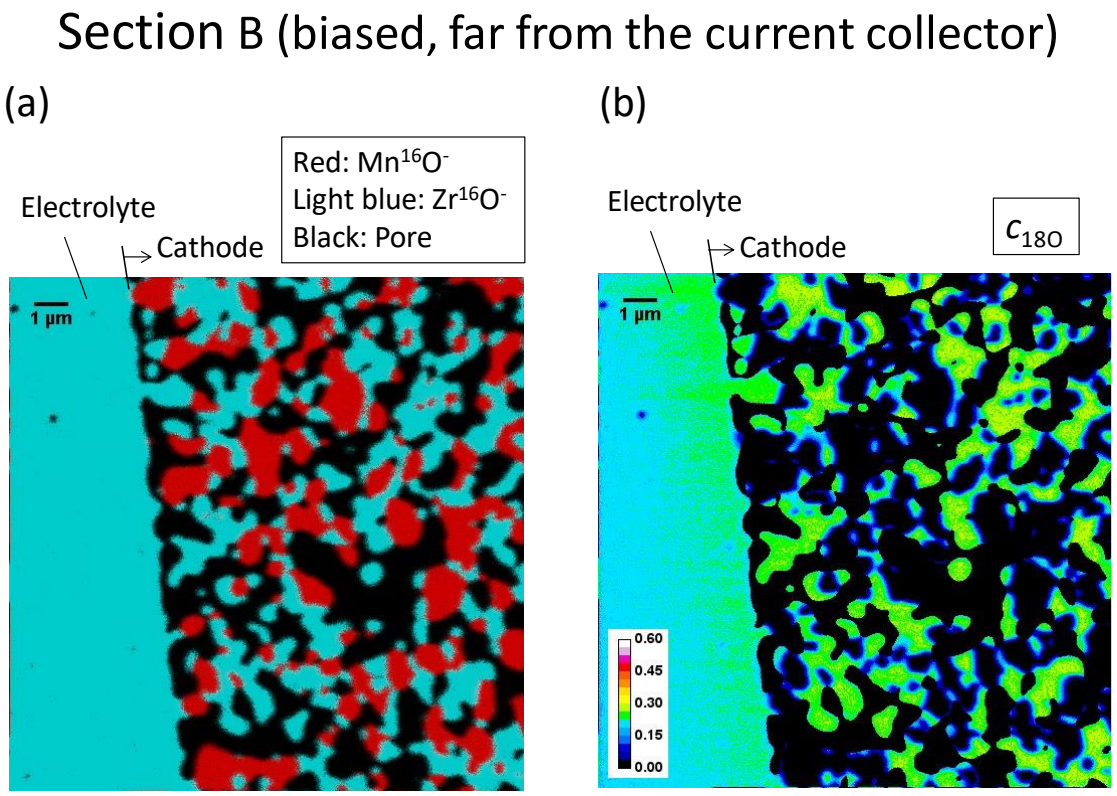

Figure 4-8. Secondary ion mappings of the interface between the LSM/ScSZ cathode and YSZ electrolyte obtained from section B (0.14 A/cm^2-biased, far area from the current collector) in Fig. 4-3(a). (a) Phase mapping of each material. Red and light blue represent $Mn^{16}O^-$ (LSM) and $Zr^{16}O^-$ (ScSZ, YSZ), respectively. The black regions show the pore phases. (b) Oxygen isotope concentration ($= c_{18O}$) mapping represented by $I(^{18}O^-)/[I(^{16}O^-) + I(^{18}O^-)]$.

section B is a part of cathode working. This means that a cathode area far from a current collector is almost inactive. The correlation between this result and electrochemical impedance spectra is discussed in section 4.3.4.

At section C shown in Fig. 4-9(c), an almost uniform ^{18}O distribution in ScSZ with a considerably higher $c_{18O} \approx 0.55$ compared to that in section A or B is observed. By supplying a current, the ^{18}O concentration in ScSZ becomes higher because of incorporated oxygen by the electrochemical reaction. However, the TPB where ^{18}O is

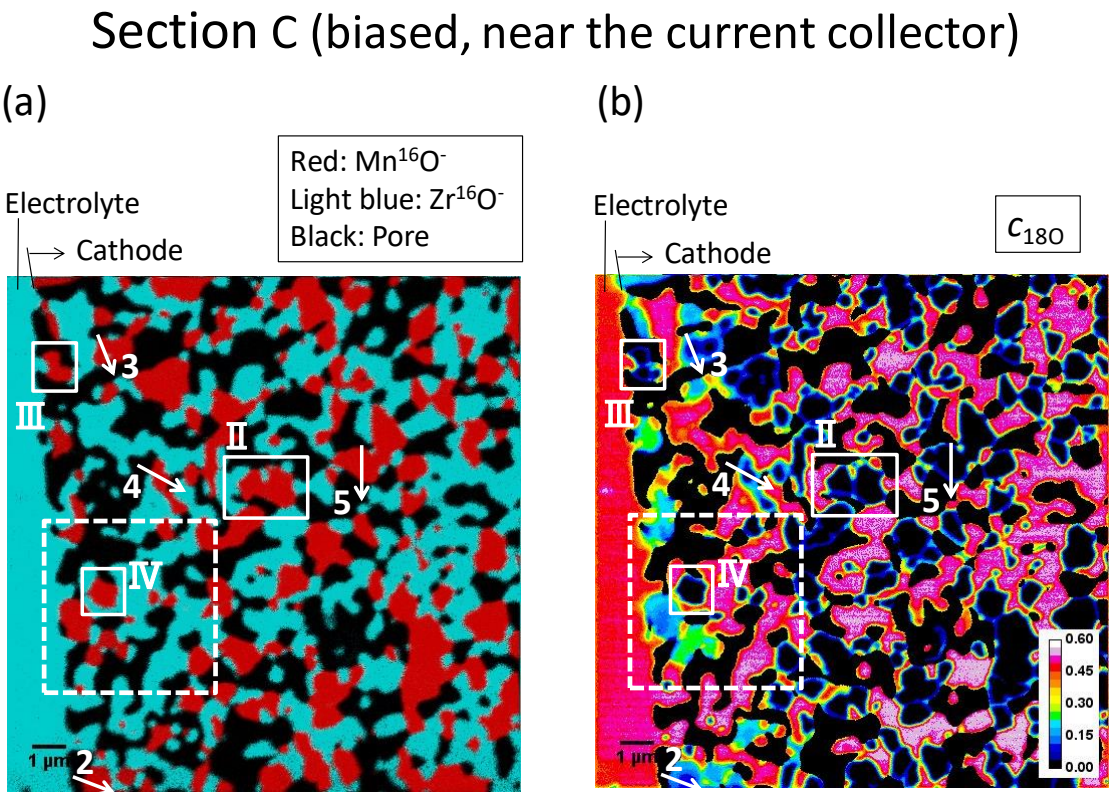

Figure 4-9. Secondary ion mappings of the interface between the LSM/ScSZ cathode and YSZ electrolyte obtained from section C (0.14 A/cm^2-biased, directly under the contact area of the current collector) in Fig. 4-3(a). (a) Phase mapping of each material. Red and light blue represent $Mn^{16}O^-$ (LSM) and $Zr^{16}O^-$ (ScSZ, YSZ), respectively. The black regions show the pore phases. (b) Oxygen isotope concentration ($= c_{18O}$) mapping represented by $I(^{18}O^-)/[I(^{16}O^-) + I(^{18}O^-)]$. The high resolution images in Fig. 4-12 were taken at the area surrounded by dashed lines.

incorporated could not be distinguished because of the fast tracer diffusion inside ScSZ [19]. In contrast, we can observe a non-uniform ^{18}O concentration image inside the LSM at section C, and the details are discussed in section 4.3.5.

4.3.4 Effect of contact area between cathode and current collector

As shown in Fig. 4-8(b), the SIMS image at section B indicates that the area far from the current collector is not active. In order to explore this result, the effect of a contact

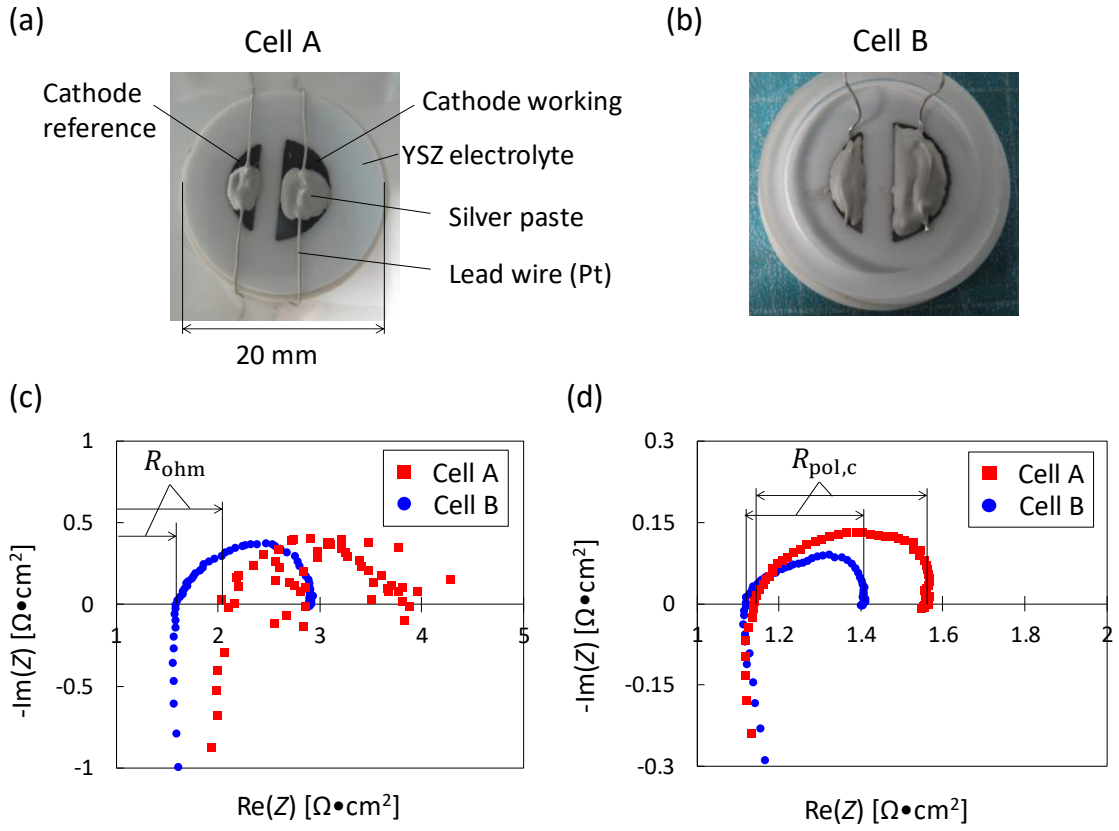

Figure 4-10. (a,b) Photographs of cathode side of (a) cell A and (b) cell B used in power generation experiment to investigate the effect of contact area between cathode and current collector on the electrochemical performance. (c,d) Impedance spectra of cell A and B under OCV condition at 1073 K measured between (c) anode working and cathode working and (d) cathode working and cathode reference.

area between cathode and current collector on the electrochemical performance was investigated using conventional power generation equipment shown in Fig. 3-3 in Chapter 3. The same single cells as used in the isotope exchange experiment were prepared. The electrochemical measurements were conducted at 1073 K. As a fuel and oxidant, 3%-humidified hydrogen and pure oxygen were supplied, respectively. Total flow rate of anode and cathode side is 200 mL/min and 60 mL/min, respectively. Current was collected by pressing Au mesh for anode side, and by attaching Ag paste for cathode side. In this experiment, the impedance spectra of two cells, cell A and B, with different ratio

Table 4-1. The effect of contact area between cathode and current collector on overall ohmic resistance and cathode polarization resistance under OCV condition at 1073 K.

Cell	Raito of cathode area covered by current collector (Ag paste), S_{Ag}/S_{CW} [%]	Overall ohmic resistance R_{ohm} [Ω•cm^2]	Cathode polarization resistance $R_{pol,c}$ [Ω•cm^2]
Cell A	76.5	2.04	0.43
Cell B	89.3	1.59	0.30

of cathode area covered by Ag paste (S_{Ag}/S_{CW}) were collected. Photographs of two cells are shown in Figures 4-10(a) and (b). The overall ohmic resistance R_{ohm} was obtained from impedance spectra at OCV measured between anode working and cathode working as shown in Figure 4-10(c), and the cathode polarization resistance $R_{pol,c}$ was measured between cathode working and cathode reference in Figure 4-10(d). S_{Ag}/S_{CW}, R_{ohm}, and $R_{pol,c}$ of two cells are summarized in Table 4-1.

From Table 4-1, both R_{ohm} and $R_{pol,c}$ decrease with increasing S_{Ag}/S_{CW}. In the case of cell B ($S_{Ag}/S_{CW} = 89.3\%$), measured $R_{ohm} = 1.59$ Ω•cm^2 is relatively close to the estimated value of 300μm-thickness YSZ, 1.5 Ω•cm^2 [24]. These results indicate that a cathode area far from a current collector does not contribute to the electrochemical reaction and oxide ion/electron conduction, which support the SIMS observation results in Fig. 4-8. Several former works also show that cathode polarization increases with decreasing a contact area between cathode and current collector [25,26].

4.3.5 Line profile analysis of ^{18}O concentration mappings

As shown in Fig. 4-9(b), the non-uniform distribution of ^{18}O concentration was observed inside the LSM at section C. c_{18O} profiles inside several LSM particles denoted by lines 2 to 5 in Fig. 4-9 are shown in Figure 4-11. As a comparison, a c_{18O} profile of the LSM at OCV condition, which is indicated by line 1 in Fig. 4-7, is also

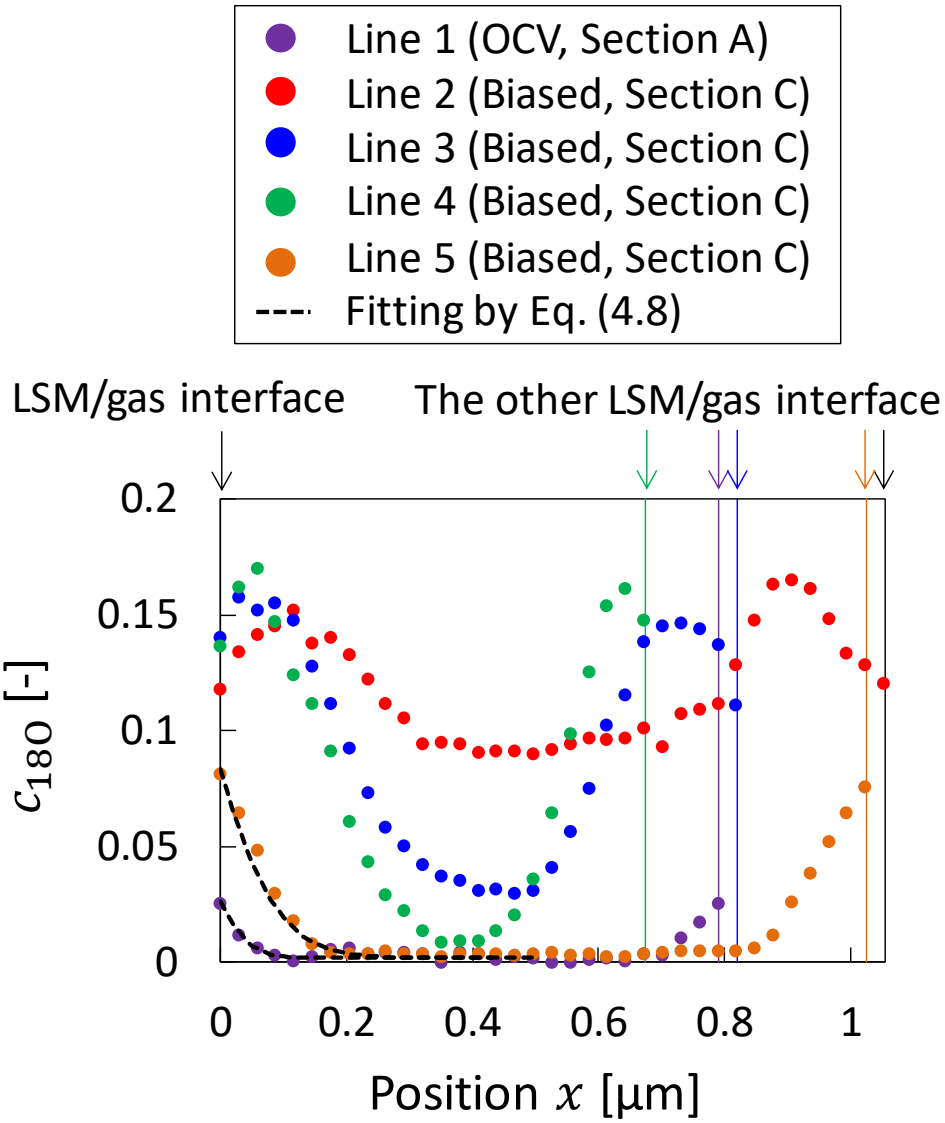

Figure 4-11. c_{18O} line profiles inside LSM particles denoted by line 1 in Fig. 4-7 and lines 2 to 5 in Fig. 4-9. Positive direction in position x corresponds to each arrow direction in Figs. 4-7 and 4-9. Fitting curves of Eq. (4.8) to the profiles of line 1 and 5 are also shown.

shown. From Fig. 4-11, typical monotonically decreasing diffusion profiles are observed in line 1 and 5. On the other hand, c_{18O} profiles near the cathode/electrolyte interface (lines 2 to 4) have a maximum value inside a LSM bulk, not at a surface. This can be clearly observed in high-resolution SIMS images shown in Figure 4-12. Fig. 4-12 was

taken at the area surrounded by dashed lines in Fig. 4-9 with a beam diameter of ca. 50 nm. The phase mapping and ^{18}O concentration are not exactly corresponds to that in Fig. 4-9 because the measured plane in Fig. 4-12 was deeper than that of Fig. 4-9. The original surface in Fig. 4-9 was a little bit removed by high-intensity primary ions, which was emitted by changing the SIMS equipment from low to high-resolution modes. LSM particles denoted by circles in Fig. 4-12 show higher c_{18O} inside the bulk than that on

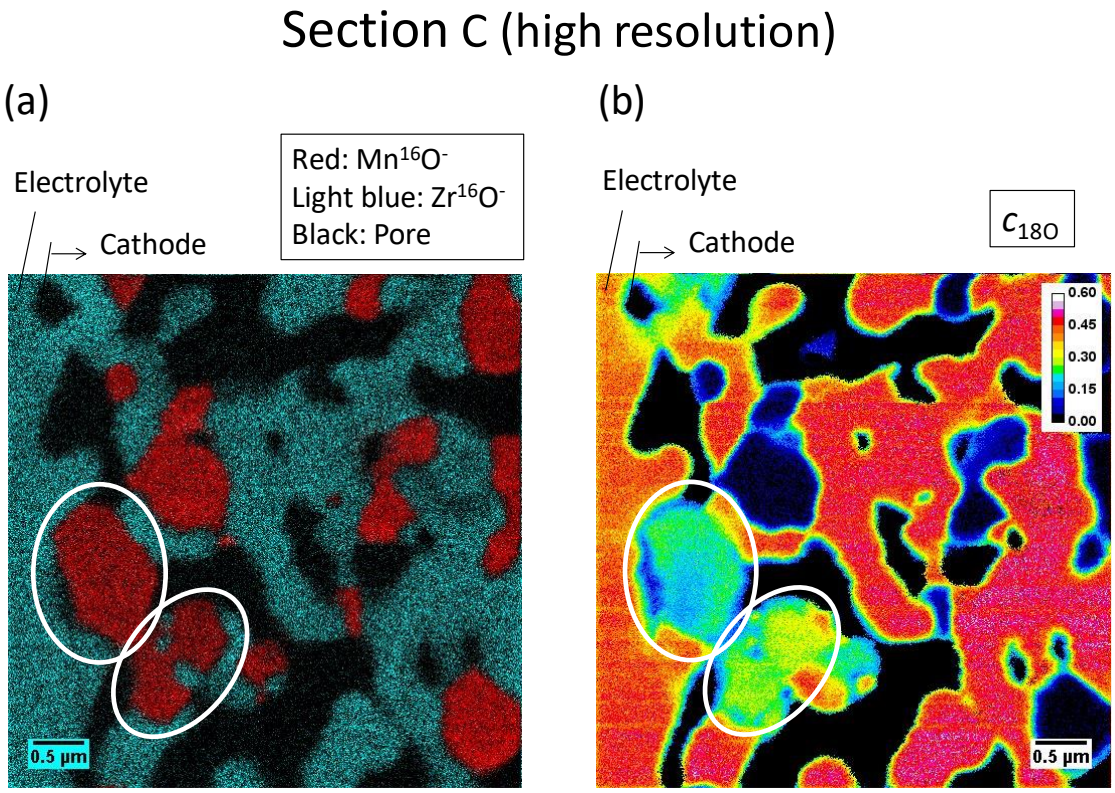

Figure 4-12. High-resolution secondary ion mappings of the interface between the LSM/ScSZ cathode and YSZ electrolyte obtained from the area surrounded by dashed lines in Fig. 4-9. (a) Phase mapping of each material. Red and light blue represent $Mn^{16}O^-$ (LSM) and $Zr^{16}O^-$ (ScSZ, YSZ), respectively. The black regions show the pore phases. (b) Oxygen isotope concentration ($= c_{18O}$) mapping represented by $I(^{18}O^-)/[I(^{16}O^-) + I(^{18}O^-)]$. The measured plane is deeper than that of Fig. 4-9 because the original surface was a little bit removed by high-intensity primary ions, which was emitted by changing the SIMS equipment from low to high-resolution modes.

the surfaces. Such a “uphill” diffusion profile under cathodically-biased condition has been recently reported in oxygen isotope exchange experiment using a LSM thin film on a YSZ electrolyte by Huber et al. [17,27]. In their work, an uphill diffusion profile results from a combination of oxygen vacancy concentration distribution induced by polarization and fast grain boundary diffusion in the LSM layer. It was also shown that this uphill diffusion profile appears and enhanced at higher overpotential [17,27]. In Fig. 4-9(b), uphill diffusion profiles are observed at the region where distance from electrolyte/cathode interface (d) is shorter than 3.8 μm, indicating that local overpotentials are higher and charge transfer reactions are more enhanced at the region of d < 3.8 μm than those at other regions. This result qualitatively shows that reaction sites near the cathode/electrolyte interface are more electrochemically active than those at other regions. Some previous study showed that cathode polarization resistance decreases with increasing LSM/YSZ layer thickness t at t < ~ 2-6 μm while becomes constant value at t > ~ 2-6 μm [28,29], indicating the existence of active regions near the cathode/electrolyte interface. In addition, several numerical simulations [2,4,5,30] showed that local charge transfer current densities increase when the position approaches from cathode top surface to cathode/electrolyte interface. These works are qualitatively consistent with the SIMS result obtained here. This is the first experimental work to visualize active sites in an SOFC porous electrode in microstructure scale.

In the OCV (section A) and the region at d > 3.8 μm of section C, c_{18O} profiles in LSM particles can be analysed by assuming diffusion in a semi-infinite media because c_{18O} drops to an almost natural value, 0.002, around the center of each particle as shown in lines 1 and 5 in Fig. 4-11. At the gas/LSM interface, the rate of isotope exchange is assumed to be proportional to the isotope concentration difference between gas and solid

phases. This boundary condition is descried as follows

$$-D^* \left.\frac{\partial c_{18O}}{\partial x}\right|_{x=0} = k^* \left(c_{18O}^{g} - c_{18O}^{s}\right) \tag{4.7}$$

where D^* is the oxygen tracer diffusion coefficient, k^* is the surface exchange coefficient, c_{18O}^{s} is the ^{18}O fraction at the surface, and c_{18O}^{g} (= 97.5 %) is the isotope enrichment of the gas. The analytical solution of 1-dimentional diffusion equation for a semi-infinite media under the boundary condition (4.7) is given as follows [31].

$$\frac{c_{18O} - c_{18O}^{bg}}{c_{18O}^{g} - c_{18O}^{bg}} = \mathrm{erfc}\left[\frac{x}{2\sqrt{D^* t}}\right] - \exp\left(\frac{k^* x}{D^*} + \frac{k^{*2} t}{D^*}\right) \times \mathrm{erfc}\left[\frac{x}{2\sqrt{D^* t}} + k^* \sqrt{\frac{t}{D^*}}\right] \tag{4.8}$$

Here, c_{18O}^{bg} (= 0.2 %) is the natural isotope background level of ^{18}O and t (= 188 s) is the time of the isotope anneal. c_{18O} profiles can be well fitted to Eq. (4.8) as shown in lines 1 and 5 of Fig. 4-11, and D^* and k^* values can be determined.

Both in the case of section A and C, D^* and k^* are determined at 15 measured points and plotted against d as shown in Figures 4-13(a) and (b). Here d is defined as a relative position of each point (LSM/gas interface at each measured line profile) from electrolyte/cathode interface. All measured points, an example of fitted graph, and obtained D^* and k^* values are shown in Appendix E. At the OCV, averaged $D^* = 1.21 \times 10^{-13}$ cm^2/s is within the range of reported order of magnitude of D^* in LSM bulk at 1073 K, 10^{-15} to 10^{-13} cm^2/s [18,32,33]. Averaged $k^* = 1.17 \times 10^{-9}$ cm/s obtained here is relatively close to 2.67×10^{-9} cm/s by Fearn et al. [33]. From Figs. 4-13(a) and (b), both averaged D^* (3.24×10^{-13} cm^2/s) and k^* (5.91×10^{-9} cm/s) at section C are clearly higher than those at section A, indicating that under biased condition, both LSM bulk diffusion and surface exchange reaction are enhanced compared to non-biased condition. The enhanced k^* under biased condition also seems to be attributed to the increased oxygen vacancies in LSM, as is the case with enhanced D^* mentioned in Fig. 4-1. Previous

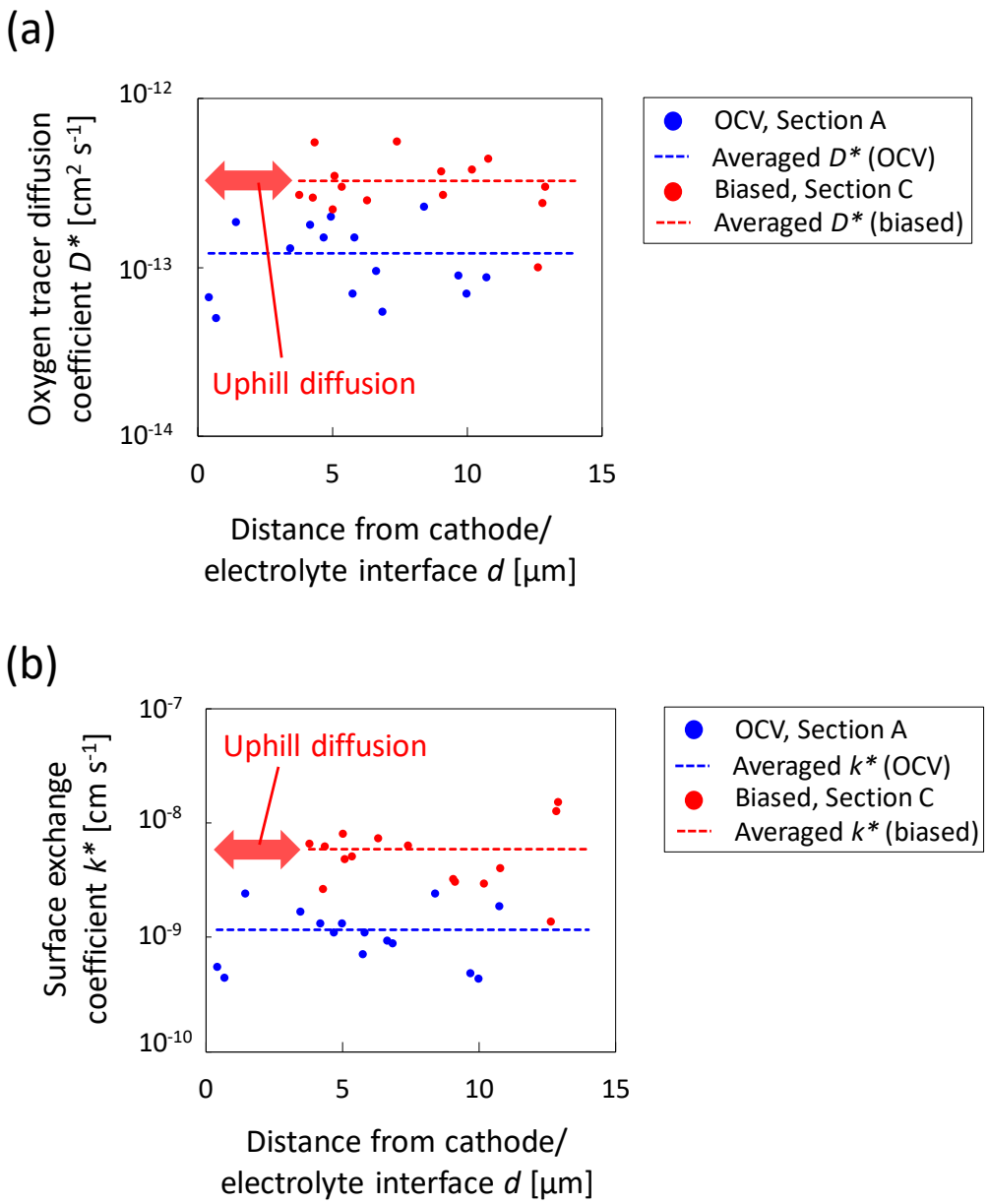

Figure 4-13. (a) Oxygen tracer diffusion coefficient D^* and (b) surface exchange coefficient k^* of LSM particles are plotted against distance from cathode/electrolyte interface (d) in the case of sections A and C. Each averaged value of 15 measured points is also shown. For section C, D^* and k^* are not obtained at $d < 3.8$ µm as uphill diffusion profiles are observed in this region.

experimental and numerical studies [34,35] pointed out that a higher oxygen vacancy concentration in cathode materials such as LSM or LSCF resulted in a higher surface

exchange rate (higher k^*) because the reaction seems to occur at the surface oxygen vacancy. In this case, increased bulk and surface oxygen vacancies of LSM induced by overpotential are followed by the enhanced D^* and k^*, respectively. In this experimental condition, however, obvious dependence of D^* and k^* on d was not observed in the range of $3.8 < d < 13$ μm at section C.

4.3.6 Grain boundary diffusion and inactive LSM particles

Some other valuable information related to the oxygen transport mechanism and/or active site distribution can be also obtained from the SIMS signal in several LSM particles. Figures 4-14(a) and (b) show magnified phase and c_{18O} mappings of LSM particles denoted by spot I in Fig. 4-7 (OCV) and spot II in Fig. 4-9 (biased), respectively. Grain boundary diffusion inside LSM bulk is observed in these spots, and the line profile of both spots (Figure 4-14(c)) indicate that grain boundary diffusion is enhanced at biased condition (spot II) compared to at OCV (spot I). In addition, LSM particles in spots III and IV at Fig. 4-9 show no ^{18}O diffusion inside their bulk though these locations are close to the electrolyte/cathode interface. This means that these particles are inactive (or at least less active) than others, which possibly results from an insufficient network of LSM particles in the microstructure. The reported 3D-microstructure analysis by FIB-SEM [36] shows that in the conventional LSM-YSZ composite (LSM:YSZ = 50:50 wt%), the pore and YSZ phase networks are entirely connected (> 99 vol%), while 10-20 vol% of the LSM particles are isolated. The combination of active sites imaging conducted here and 3D-microstructure observations by FIB-SEM can give further understanding of the phenomena inside the LSM/ScSZ porous cathode.

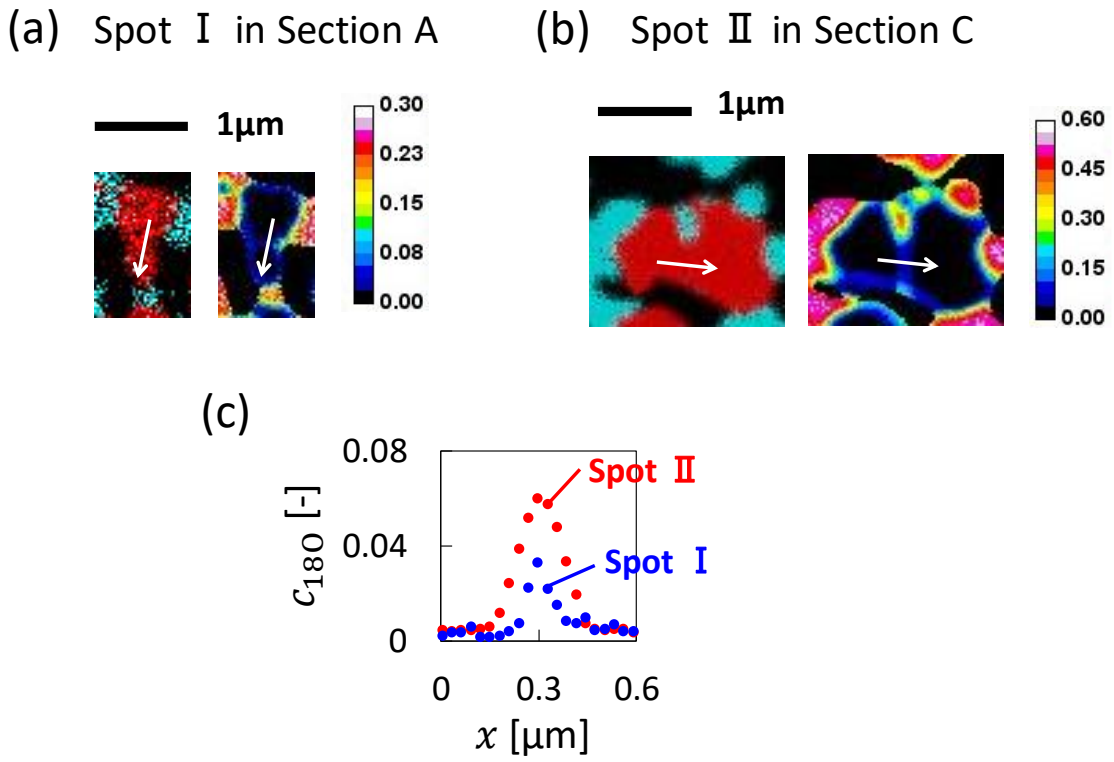

Figure 4-14. Grain boundary diffusion in LSM. (a,b) Magnified phase and c_{18O} mappings of LSM particles denoted by (a) spot I in Fig. 4-7 (OCV) and (b) spot II in Fig. 4-9 (biased). (c) c_{18O} line profiles denoted by arrows in (a) and (b)

4.4 Summary

Imaging technique of active reaction sites in SOFC porous electrodes was developed in microstructure scale. A power generation equipment with a nozzle for direct helium gas impinging jet to the cell was newly prepared to quench an SOFC reaction. The quench performance test showed that the temperature of YSZ electrolyte could be decreased from 830 to 150 ºC within 1.5 sec, which was in good agreement with analytical results based on the average Nusselt number of impinging jet heat transfer. Using constructed quench system and oxygen isotope labeling, active sites for oxygen reduction reaction in LSM/ScSZ porous cathode were visualized. From the ^{18}O concentration mappings of the

quenched cathode obtained by SIMS, it was disclosed that cathode area far from a current collector does not contribute to the electrochemical reaction and oxide ion/electron conduction. This result was also supported by the dependence of electrochemical performance on contact area between cathode and Ag paste current collector. In addition, the expansion of the oxygen reduction sites from a TPB to a DPB enables us to identify those positions in electrode particle scale by slow oxygen tracer diffusion in the LSM bulk. Enhanced ^{18}O concentration and uphill diffusion profiles inside LSM observed only near the cathode/electrolyte interface indicates that reaction sites near the cathode/electrolyte interface are more electrochemically active than those at other regions. This is the first experimental work to visualize active sites in an SOFC porous electrode in microstructure scale. Finally, an oxygen tracer diffusion coefficient and a surface exchange coefficient of each LSM particle were quantified from c_{18O} line profiles, which were enhanced at current-biased condition compared to those at OCV.

References

[1] P. Costamagna, P. Costa, V. Antonucci, *Electrochim. Acta* 43 (1998) 375–394.

[2] J. H. Nam, D. H. Jeon, *Electrochim. Acta* 51 (2006) 3446–3460.

[3] N. Shikazono, D. Kanno, K. Matsuzaki, H. Teshima, S. Sumino, N. Kasagi, *J. Electrochem. Soc.* 157 (2010) B665–B672.

[4] K. Miyoshi, T. Miyamae, H. Iwai, M. Saito, M. Kishimoto, H. Yoshida, *J. Power Sources* 315 (2016) 63–39.

[5] A. Banerjee, O. Deutschmann, *J. Catal.* 346 (2017) 30–49.

[6] M. Shishkin, T. Ziegler, *J. Phys. Chem. C* 113 (2009) 21667–21678.

[7] T. Kawada, T. Horita, N. Sakai, H. Yokokawa, M. Dokiya, J. Mizusaki, *Solid State Ionics* 131 (2000) 199–210.

[8] T. Horita, K. Yamaji, N. Sakai, Y. Xiong, T. Kato, H. Yokokawa, T. Kawada, *J. Power Sources* 106 (2002) 224–230.

[9] J. Fleig, A. Schintlmeister, A.K. Opitz, H. Hutter, *Scripta Mater.* 65 (2011) 78–83.

[10] T. Horita, T. Shimonosono, H. Kishimoto, K. Yamaji, M.E. Brito, Y. Hori, H. Yokokawa, *Electrochem. Solid-State Lett.* 13 (12) (2010) B135–B138.

[11] C. Sun, R. Hui, J. Roller, *J. Solid State Electrochem.* 14 (2010) 1125–1144.

[12] S.B. Adler, *Chem. Rev.* 104 (2004) 4791–4843.

[13] T. Horita, K. Yamaji, N. Sakai, H. Yokokawa, T. Kawada, T. Kato, *Solid State Ionics* 127 (2000) 55–65.

[14] A.K. Opitz, M. Kubicek, S. Huber, T. Huber, G. Holzlechner, H. Hutter, J. Fleig, *J. Mater. Res.* 28 (2013) 2085–2105.

[15] Y. Jiang, S. Wang, Y. Zhang, J. Yan, W. Li, *J. Electrochem. Soc.* 145 (1998) 373–378.

[16] R. Radhakrishnan, A.V. Virkar, S.C. Singhal, *J. Electrochem. Soc.* 152 (2005) A210–

A218.

[17] T.M. Huber, E. Navickas, G. Friedbacher, H. Hutter, J. Fleig, *ChemElectroChem* 2 (2015) 1487–1494.

[18] I. Yasuda, K. Ogasawara, M. Hishinuma, T. Kawada, M. Dokiya, *Solid State Ionics* 86-88 (1996) 1197–1201.

[19] E.S. Raj, A. Atkinson, J.A. Kilner, *Solid State Ionics* 180 (2009) 952–955.

[20] R.B. Bird, W.E. Stewart, E.N. Lightfoot, *Transport Phenomena, second ed.*, John Wiley & Sons, Inc., (2007).

[21] The Japan Society of Mechanical Engineers, *JSME Data Book: Heat Transfer 5th Edition*, pp. 39, Maruzen (2009). (in Japanese)

[22] The Japan Society of Mechanical Engineers, *JSME Textbook Series, Heat Transfer*, pp. 45, Maruzen (2005). (in Japanese)

[23] G. Knöner, K. Relmann, R. Röwer, U. Södervall, H-E. Schaefer, *PNAS* 100, 7 (2003) 3870–3873.

[24] K.C. Wincewicz, J.S. Cooper, *J. Power Sources* 140 (2005) 280–296.

[25] S.P. Jiang, J.G. Love, L. Apateanu, *Solid State Ionics* 160 (2003) 15–26.

[26] K. Sasaki, J.-P. Wurth, R. Gschwend, M. Gödickemeier, L.J. Gauckler, *J. Electrochem. Soc.* 143 (2) (1996) 530–543.

[27] T.M. Huber, E. Navickas, K. Sasaki, B. Yildiz, H. Tuller, G. Friedbacher, H. Hutter, J. Fleig, *J. Electrochem. Soc.* 164 (7) (2017) F809–F814.

[28] M. Juhl, S. Primdahl, C. Manon, M. Mogensen, *J. Power Sources* 61 (1996) 173–181.

[29] E.P. Murray, T. Tsai, S.A. Barnett, *Solid State Ionics* 110 (1998) 235–243.

[30] K. Miyoshi, H. Iwai, M. Kishimoto, M. Saito, H. Yoshida, *J. Power Sources* 326

(2016) 331–340.

[31] J. Crank, *The Mathematics of Diffusion*, Oxford University Press, Oxford, 1975.

[32] R.A. De Souza, J.A. Kilner, J.F. Walker, *Mater. Lett.* 43 (2000) 43–52.

[33] S. Fearn, J.C.H. Rossiny, J.A. Kilner, J.R.G. Evans, *Solid State Ionics* 211 (2012) 51–57.

[34] Y-L. Huang, C. Pellegrinelli, E.D. Wachsman, *ACS Catal.* 6 (2016) 6025–6032.

[35] L. Wang, R. Merkle, Y.A. Mastrikov, E.A. Kotomin, J. Maier, *J. Mater. Res.* 27, 15 (2012) 2000–2008.

[36] J.R. Wilson, A.T. Duong, M. Gameiro, H-Y. Chen, K. Thornton, D.R. Mumm, S.A. Barrnet, *Electrochem. Commun.* 11 (2009) 1052–1056.

Chapter 5

Analysis method of oxide ion flux at cathode/electrolyte interface through oxygen isotope labeling

5.1 Introduction

In Chapter 4, active sites of LSM/ScSZ cathode were identified in microstructure scale based on the ^{18}O diffusion into LSM induced by overpotential. However, the quantitative discussion of the reaction rate or oxide ion flux incorporated to the cathode is difficult only from the information in LSM because most flux is directly incorporated from a zirconia surface (YSZ, ScSZ) near the TPB (Fig. 4-1, TPB path). As shown in Chapter 4, the fast ^{18}O diffusion inside ScSZ resulted in a uniform ^{18}O concentration in the cathode microstructure scale, which is difficult to analyze by diffusion equation.

In this chapter, the oxygen isotope exchange experiment is conducted at 973 K, 100 ℃ lower than in Chapter 4, to suppress the ^{18}O diffusion in a zirconia phase, and the ^{18}O diffusion profile in YSZ electrolyte is analyzed. Based on the results, quantitative oxide ion flux incorporated from the cathode/electrolyte interface is estimated.

5.2 Experimental section

In this experiment, a YSZ-electrolyte supported cell with a Ni/YSZ anode and LSM/YSZ (LSM:YSZ = 50:50 wt%) cathode was used. The cell geometry and fabrication process are the same as in Chapter 4, and only ScSZ in the cathode was changed to YSZ.

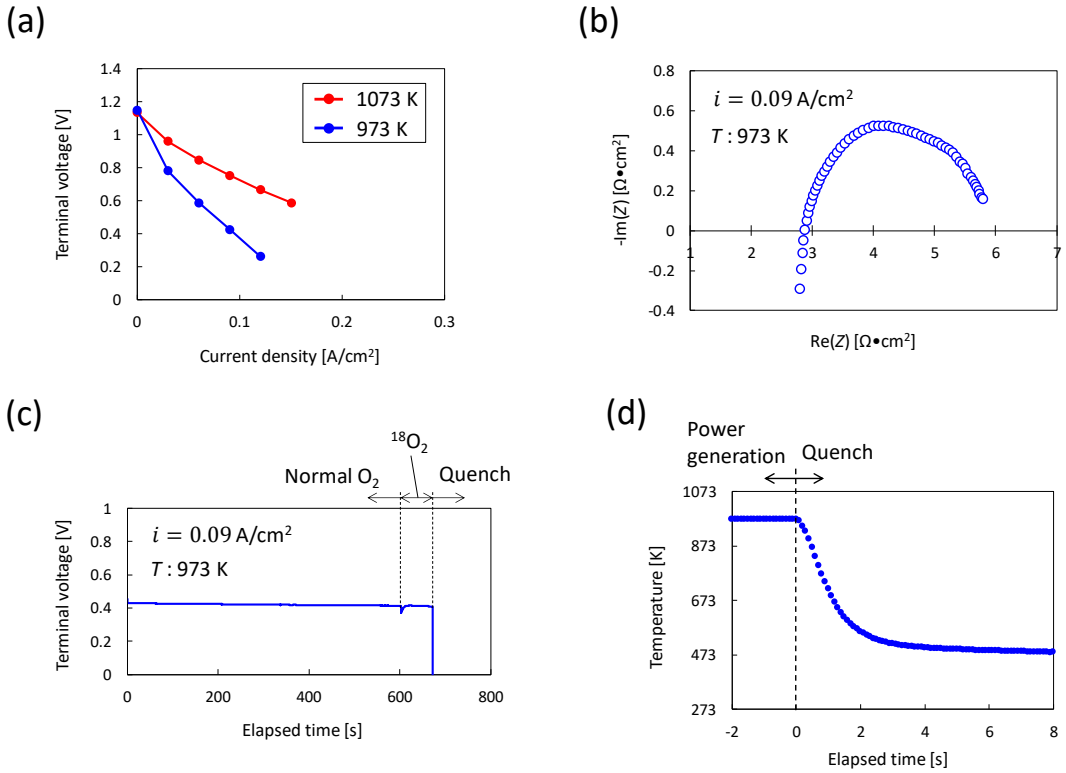

Figure 5-1. (a) Initial performance of the cell used in the isotope exchange at 1073 and 973 K. Humidified mixture of 50% H_2 – 50% Ar and pure oxygen were supplied as a fuel and oxidant, respectively. (b) Impedance spectra at 0.09 A/cm^2 measured between anode working and cathode working. (c) Terminal voltage versus elapsed time with a constant current density of 0.09 A/cm^2. (d) Temperature change of the cell during quenching measured by the thermocouple attached in anode reference (Fig. 4-3(a)).

Here, the electrode area covered by an Ag current collector was about 46.7 % ($S_{\mathrm{Ag}}/S_{\mathrm{CW}} = 0.467$ in Fig. 4-3(a)) .The experimental procedure is almost the same as in Chapter 4. Initially, the cell was operated in a mixture of 50% H_2 and 50% Ar, which was humidified by a bubbler, for the anode side and in 100% normal O_2 for the cathode side at 973 K for 10 min under a constant current density of 0.09 A/cm^2. Then, the normal O_2 was switched to $^{18}O_2$ (>97.5%), and the cell was operated for 70 sec. Finally, the cell was abruptly quenched to a room temperature by the helium impinging jet. The initial performance of the cell at 1073 and 973 K, impedance spectra at 0.09 A/cm^2 measured between anode

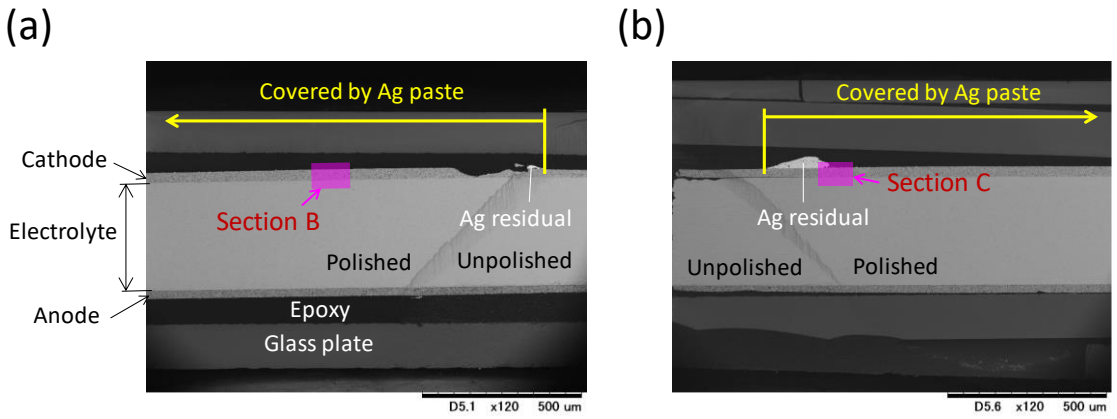

Figure 5-2. SEM images of the polished cross section of the cell. The position of sections B and C are shown in (a) and (b), respectively. Most part of Ag paste was peeled off from the cathode surface during the quench process. The sample is infiltrated with an epoxy resin and sandwiched with two glass plates for the polishing process.

working and cathode working, the terminal voltage with time until quenching, and temperature change of the cell during quenching are shown in Figures 5-1(a)–(d), respectively. The cell showed an almost stable terminal voltage of about 0.42 V at 0.09 A/cm^2 until quenching reaction as shown in Fig. 5-1(c).

The ^{18}O distribution in a cross section of the quenched cathode was obtained by NanoSIMS 50L (CAMECA), as is the case in Chapter 4. Here, SIMS images at the interface between the cathode and electrolyte were taken from both reference (Section A) and working (Section B and C) electrodes. The position of section A is the same as in Fig. 4-3(a), which represents OCV (non-biased) condition. Both sections B and C are placed directly under the contact area of the Ag paste current collector of cathode working (biased condition). As shown in Figures 5-2(a) and (b), section B is inside the area covered by Ag paste while section C is near the edge of the paste.

5.3 Results and discussion

5.3.1 Secondary ion mappings

Figures 5-3 and 5-4 show the secondary ion mappings of the interface between the LSM/YSZ cathode and YSZ electrolyte at OCV (Section A) and biased (Sections B and C) conditions, respectively. Among these, Figs. 5-3(a), 5-4(a), and 5-4(c) show phase mappings of LSM and YSZ based on the intensity of $Mn^{16}O^-$ and $Zr^{16}O^-$, and Figs. 5-3(b), 5-4(b), and 5-4(d) show ^{18}O concentration ($= c_{18O}$) mappings represented by $I(^{18}O^-)/[I(^{16}O^-) + I(^{18}O^-)]$. Here, $I(^{16}O^-)$ and $I(^{18}O^-)$ indicate the SIMS signal intensity of

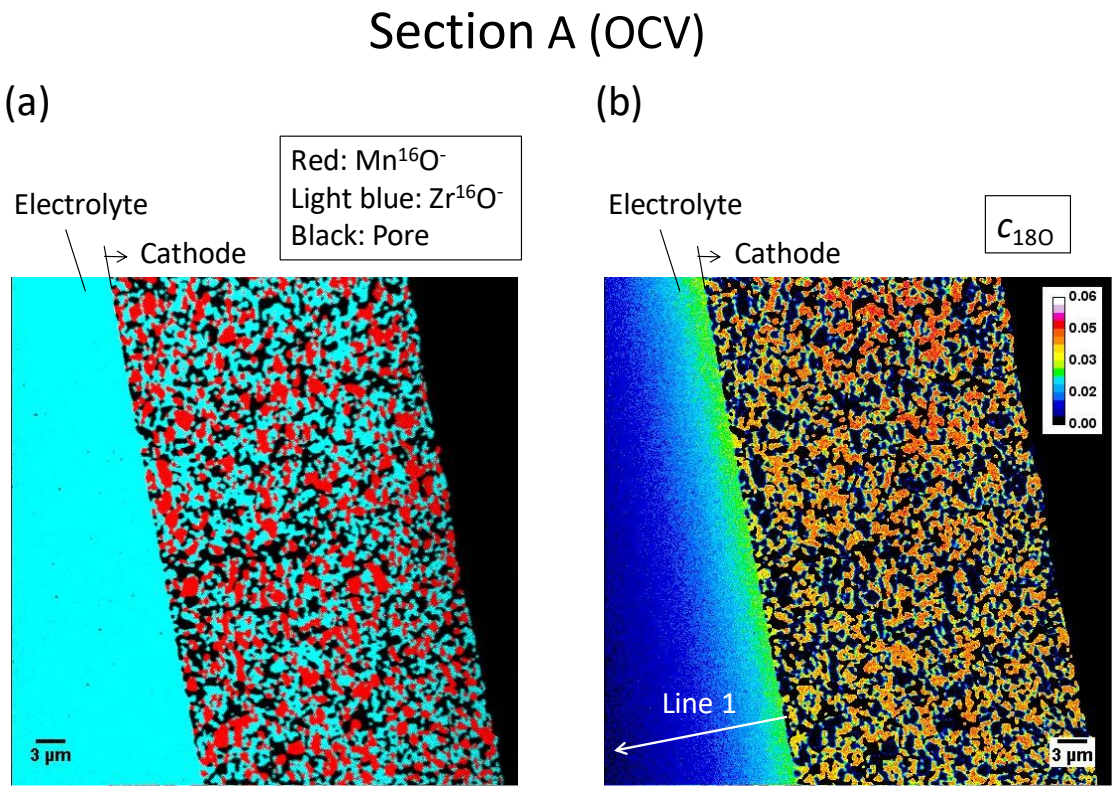

Figure 5-3. Secondary ion mappings of the interface between the LSM/YSZ cathode and YSZ electrolyte at OCV condition obtained from section A (cathode reference). (a) Phase mapping of each material. Red and light blue represent $Mn^{16}O^-$ (LSM) and $Zr^{16}O^-$ (YSZ), respectively. The black regions show the pore phases. (b) Oxygen isotope concentration ($= c_{18O}$) mapping represented by $I(^{18}O^-)/[I(^{16}O^-) + I(^{18}O^-)]$.

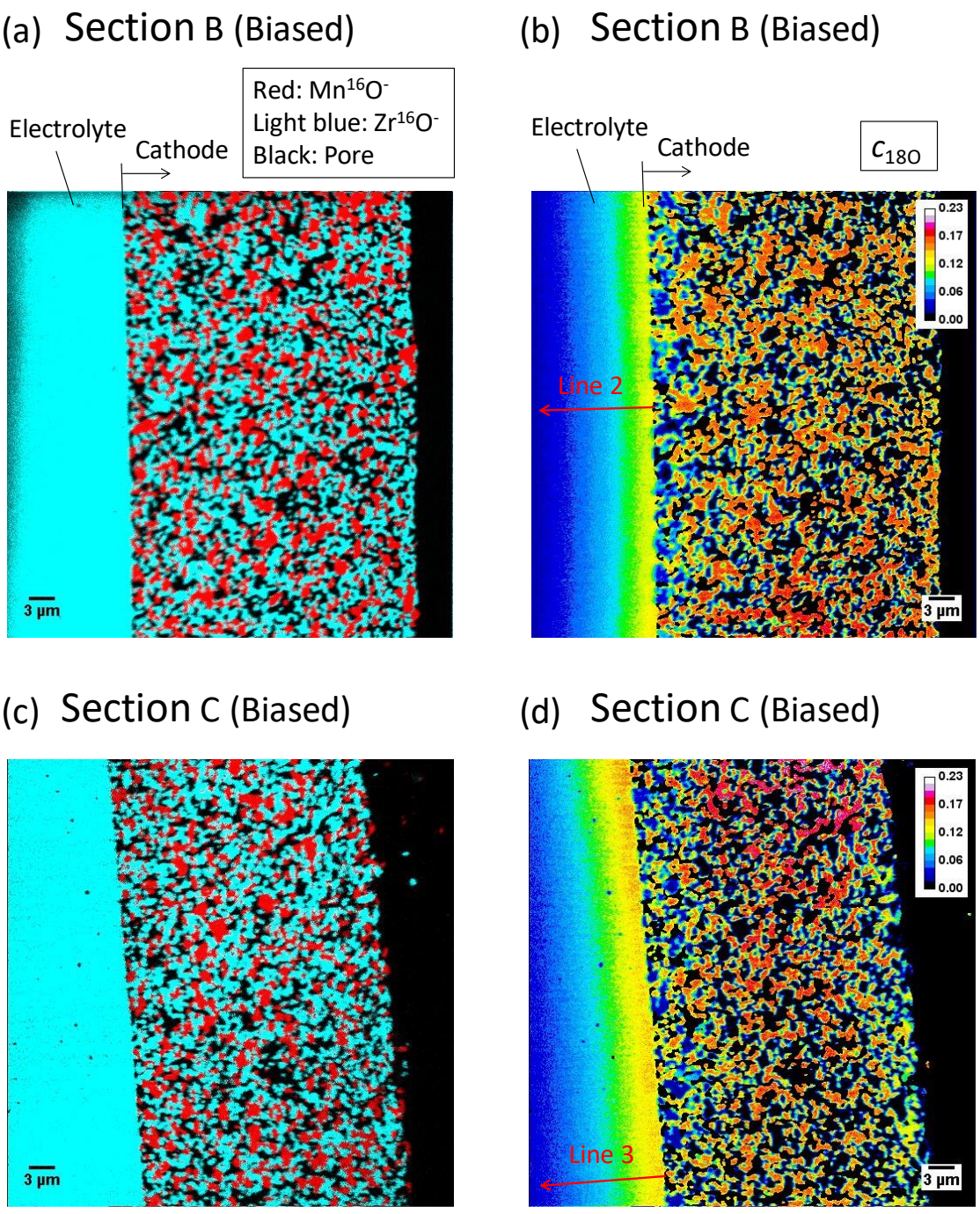

Figure 5-4. Secondary ion mappings of the interface between the LSM/YSZ cathode and YSZ electrolyte at biased condition obtained from sections B (a,b) and C (c,d) in Fig. 5-2. (a,c) Phase mapping of each material. Red and light blue represent $Mn^{16}O^-$ (LSM) and $Zr^{16}O^-$ (YSZ), respectively. The black regions show the pore phases. (b,d) Oxygen isotope concentration ($= c_{18O}$) mapping represented by $I(^{18}O^-)/[I(^{16}O^-) + I(^{18}O^-)]$.

each ion. Prior to the calculation of c_{18O} image, binarization processing is performed on the $^{16}O^-$ image to remove all signal from pore phases. As shown in Fig. 5-3(b), $c_{18O} \approx 0.04$ of YSZ phases in cathode part is higher than that in the electrolyte (maximum

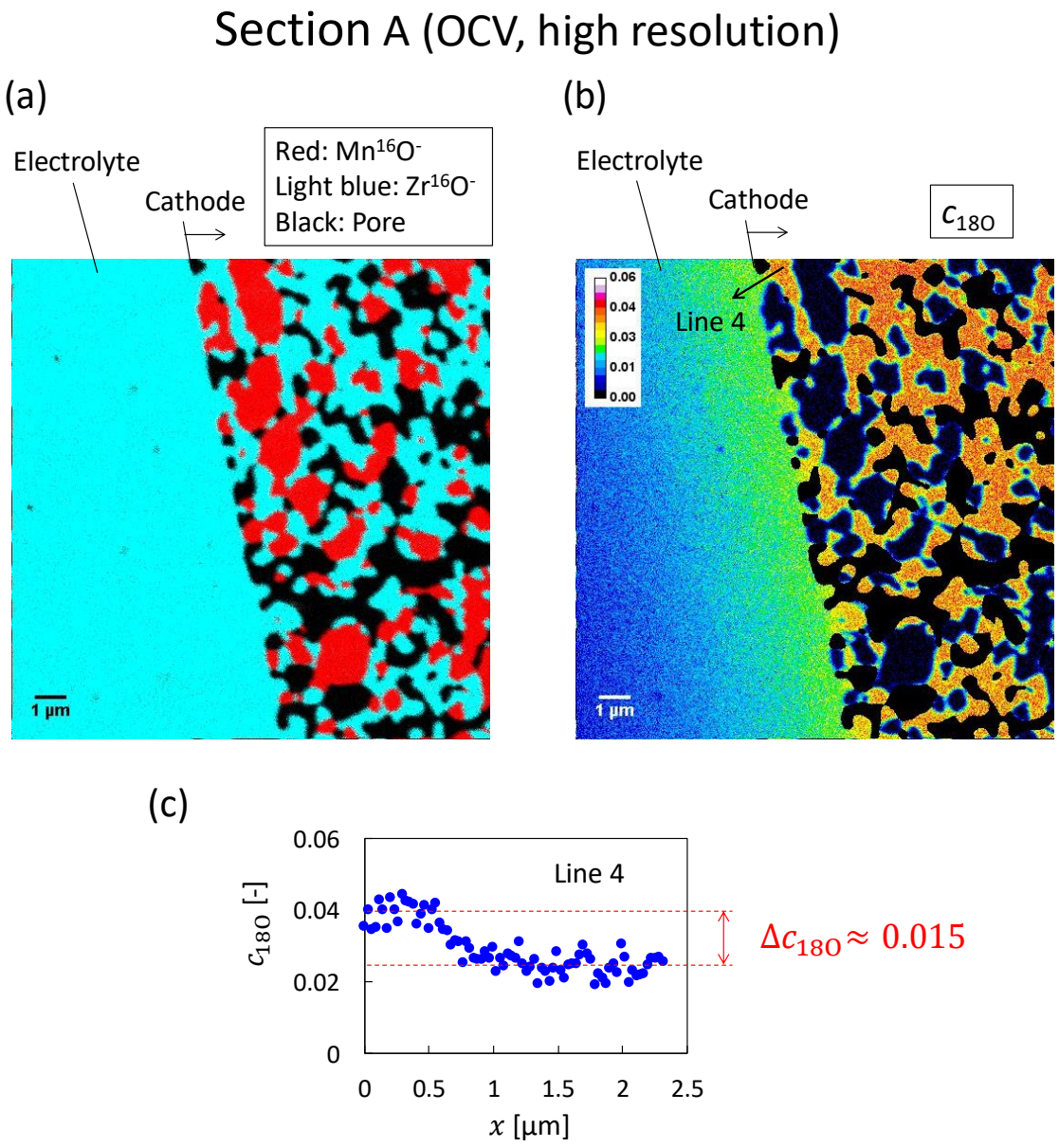

Figure 5-5. High-resolution secondary ion mappings of the interface between the LSM/YSZ cathode and YSZ electrolyte at OCV condition in section A (cathode reference). (a) Phase and (b) ^{18}O concentration (c_{18O}) mappings are shown. c_{18O} profile in Line 4 is also shown in (c).

$c_{18O} \approx 0.025$ at the surface) at OCV condition. This is because the surface to volume ratio of YSZ phase in cathode part is much larger than that in electrolyte part. At biased condition, c_{18O} in YSZ phase is around 0.12–0.16 at cathode or electrolyte surface,

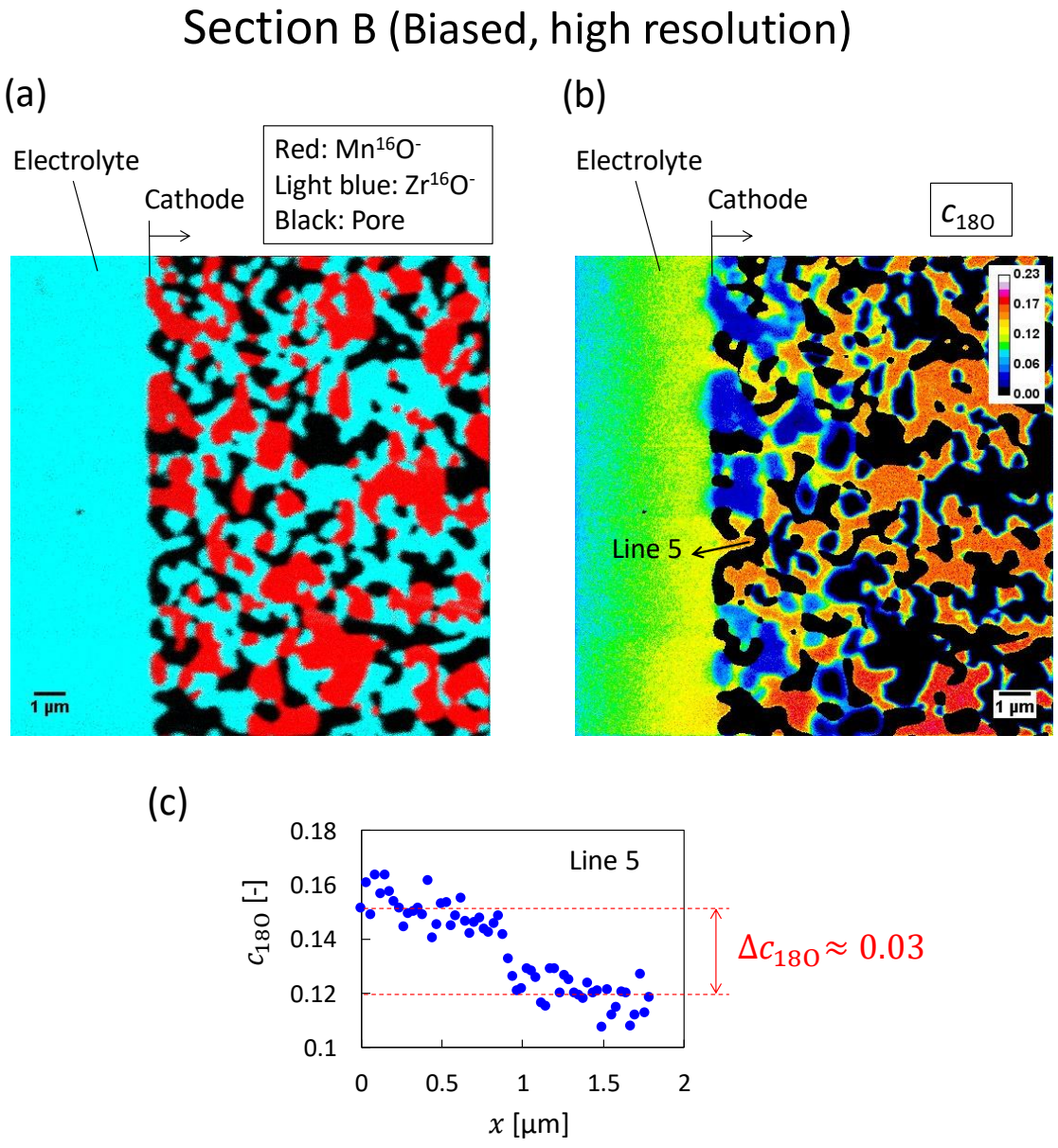

Figure 5-6. High-resolution secondary ion mappings of the interface between the LSM/YSZ cathode and YSZ electrolyte at biased condition in section B (cathode working). (a) Phase and (b) ^{18}O concentration (c_{18O}) mappings are shown. c_{18O} profile in Line 5 is also shown in (c).

which is higher than that at OCV condition because of additionally-incorporated ^{18}O by the electrochemical reaction. Both in OCV and biased conditions, c_{18O} in the electrolyte gradually decrease from cathode/electrolyte interface to anode side.

Figures 5-5 and 5-6 show the high-resolution secondary ion mappings at section A (OCV) and B (biased), respectively. As is the case in Chapter 4, ^{18}O diffusion to LSM bulk was only observed at the region near the cathode/electrolyte interface under biased condition. In addition, c_{18O} in the electrolyte is uniform near the cathode/electrolyte interface at OCV while inhomogeneous at biased condition, which may come from the non-uniform oxide ion flux incorporated from the interface.

5.3.2 ^{18}O diffusion profile analysis in YSZ electrolyte

c_{18O} line profiles inside YSZ electrolyte denoted by Line 1 in Fig. 5-3 (OCV) and Line 2 and 3 in Fig. 5-4 (biased) are shown in Figure 5-7. In this study, polycrystalline YSZ (8mol%Y_2O_3-ZrO_2) was used as an electrolyte. In all cases, typical monotonically decreasing diffusion profiles are observed, which can be analyzed by 1-dimensional diffusion in a semi-infinite media. As shown in Fig. 5-7, the analytical solution of diffusion equation (Eq. (4.8)) is well fitted to each profile, which gives oxygen tracer diffusion coefficient D^* and surface exchange coefficient k^*. The D^* and k^* obtained here and other references [1,2] are summarized in Table 5-1. At OCV, obtained $D^* = 9.70 \times 10^{-13}$ m^2/s and $k^* = 2.45 \times 10^{-9}$ m/s are relatively close to those of polycrystalline YSZ (9.1mol%Y_2O_3) by Naito et al. [1], and within the range of summarized data sets by Knöner et al. (single crystal, polycrystalline) [2].

When the current is applied, D^* increased by a factor of only 1.2 (section B) to 1.5 (section C) compared to that of OCV while k^* was enhanced by one order of magnitude,

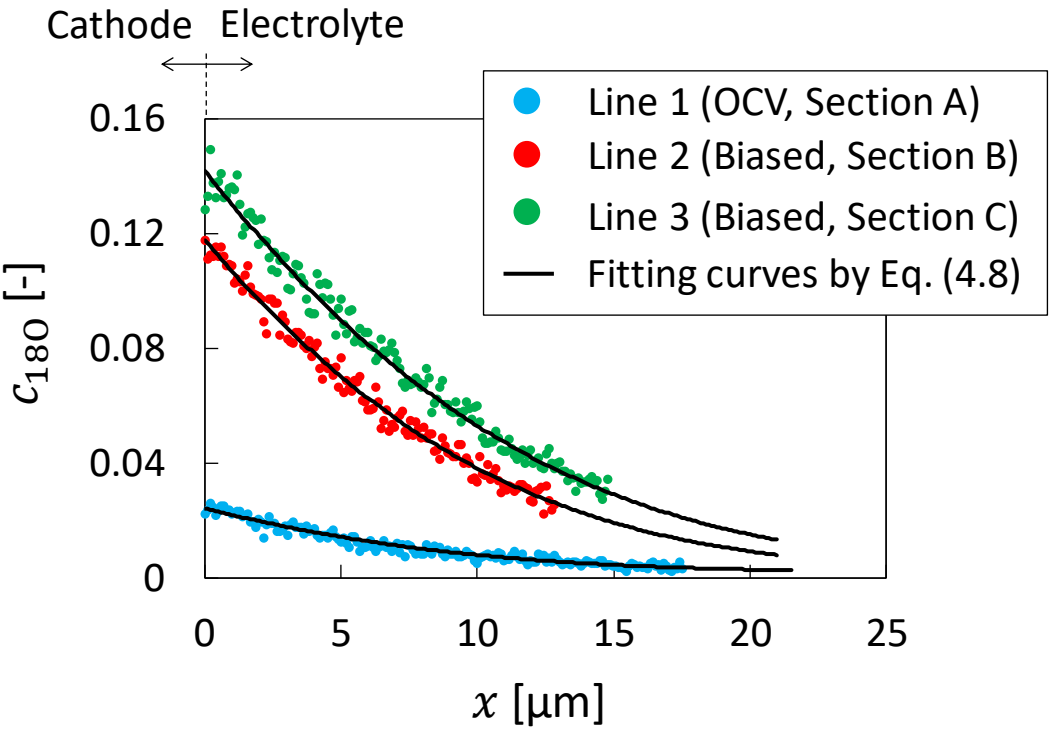

Figure 5-7. c_{18O} line profiles inside YSZ electrolyte denoted by Line 1 in Fig. 5-3 (OCV) and Line 2 and 3 in Fig. 5-4 (biased). Positive direction in position x corresponds to each arrow direction in Figs. 5-3 and 5-4. Analytical solution of diffusion equation (Eq. (4.8)) is fitted to each profile.

as shown in Table 5-1. The weak enhancement of D^* means that the enhancement of ^{18}O diffusion in YSZ bulk by the current is small. In a YSZ, oxide ion moves through vacancy diffusion mechanism [3]. In a fuel cell operation, when one oxide ion is incorporated to an electrolyte form a cathode, one oxide ion is emitted to an anode accompanied by a generation of oxygen vacancy in the electrolyte. Subsequently the generated oxygen vacancy moves from anode to cathode side. Therefore, incorporated ^{18}O itself does not move along the electrochemical potential gradient of oxide ion, $\nabla\tilde{\mu}_{O^{2-}}$ (see Appendix B), but moves along the ^{18}O concentration gradient ∇c_{18O}.

On the other hand, the one order enhancement of apparent k^* indicates that ^{18}O flux

Table 5-1. D^* and k^* of YSZ electrolyte at 973 K obtained in this study and other references. All literature values were measured at non-biased condition.

Measurement	Sample	D^* [m^2/s]	k^* [m/s]
Section A (OCV)	8mol%Y_2O_3-ZrO_2 Polycrystalline (with LSM/YSZ cathode)	9.70×10^{-13}	2.45×10^{-9}
Section B (Biased)		1.15×10^{-12}	1.50×10^{-8}
Section C (Biased)		1.45×10^{-12}	2.08×10^{-8}
Naito et al. [1]	9.1mol%Y_2O_3-ZrO_2 Polycrystalline	4.0×10^{-13}	1.4×10^{-9}
Knöner et al. [2]	2.8–16mol%Y_2O_3-ZrO_2 Single crystal, Polycrystalline	2.1×10^{-13} – 4.0×10^{-12}	2.0×10^{-11} – 2.8×10^{-8}

incorporated from the cathode/electrolyte interface to the electrolyte is greatly increased by applying the current. The detail of the ^{18}O flux is quantitatively discussed in the next section.

5.3.3 Oxide ion flux incorporated from the cathode/electrolyte interface

As shown in Figure 5-8(a), three kinds of ^{18}O fluxes, $J_{18O}^{ex(C/E)}$, $J_{18O}^{c(C/E)}$, and $J_{18O}^{ion(C/E)}$ contribute to a total ^{18}O flux at the cathode/electrolyte interface. $J_{18O}^{ex(C/E)}$ is a ^{18}O flux by a $^{16}O/^{18}O$ exchange at a free electrolyte surface and $J_{18O}^{ion(C/E)}$ is an isotope oxide ion ($^{18}O^{2-}$) flux by an electrochemical reaction at a LSM/YSZ/gas TPB on the electrolyte surface. In addition, c_{18O} of YSZ phase in the cathode is generally higher than that of the electrolyte due to the higher surface to volume ratio of YSZ phase in the cathode, as mentioned previously (section 5.3.1). $J_{18O}^{c(C/E)}$ is a ^{18}O flux by the c_{18O} difference of YSZ phase between cathode and electrolyte part. Here $J_{18O}^{ex(C/E)}$ and $J_{18O}^{c(C/E)}$ flow at both OCV and biased conditions while $J_{18O}^{ion(C/E)}$ exists only at biased. Therefore, the total ^{18}O flux incorporated from the cathode/electrolyte interface to the electrolyte at OCV and biased conditions, $J_{18O}^{OCV(C/E)}$ and $J_{18O}^{Biased(C/E)}$ are described as follows.

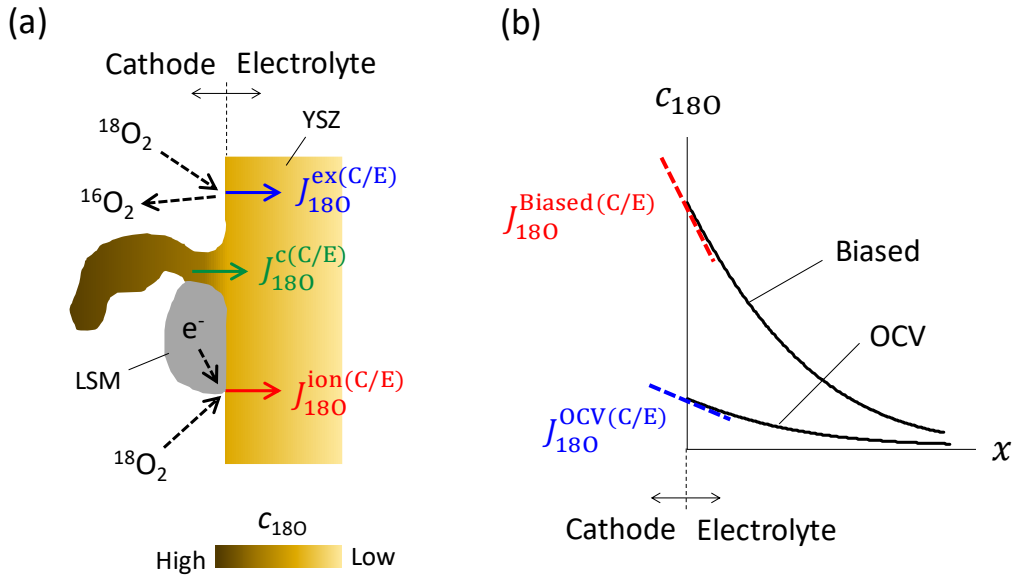

Figure 5-8. (a) Three kinds of ^{18}O fluxes incorporated from the cathode/electrolyte interface to the electrolyte. $J_{18O}^{ex(C/E)}$ and $J_{18O}^{c(C/E)}$ flow at both OCV and biased conditions while $J_{18O}^{ion(C/E)}$ exists only at biased. (b) The relationship between c_{18O} profile and total ^{18}O flux incorporated from the cathode/electrolyte interface to the electrolyte

$$J_{18O}^{OCV(C/E)} = J_{18O}^{ex(C/E)} + J_{18O}^{c(C/E)} \tag{5.1}$$

$$J_{18O}^{Biased(C/E)} = J_{18O}^{ex(C/E)} + J_{18O}^{c(C/E)} + J_{18O}^{ion(C/E)} \tag{5.2}$$

As shown in Figure 5-8(b), $J_{18O}^{OCV(C/E)}$ and $J_{18O}^{Biased(C/E)}$ [mol/(m^2•s)] corresponds to a c_{18O} gradient at cathode/electrolyte interface ($x = 0$), which can be described as follows.

$$J_{18O}^{OCV(C/E)} = -C_O^{YSZ} D_{OCV}^{*} \left[\left. \frac{\partial c_{18O}}{\partial x} \right|_{x=0} \right]^{OCV} \tag{5.3}$$

$$J_{18O}^{Biased(C/E)} = -C_O^{YSZ} D_{Biased}^{*} \left[\left. \frac{\partial c_{18O}}{\partial x} \right|_{x=0} \right]^{Biased} \tag{5.4}$$

Here D_{OCV}^{*} and D_{Biased}^{*} [m^2/s] represents the oxygen tracer diffusion coefficient at OCV and biased condition, respectively. C_O^{YSZ} [mol/m^3] is an absolute concentration of

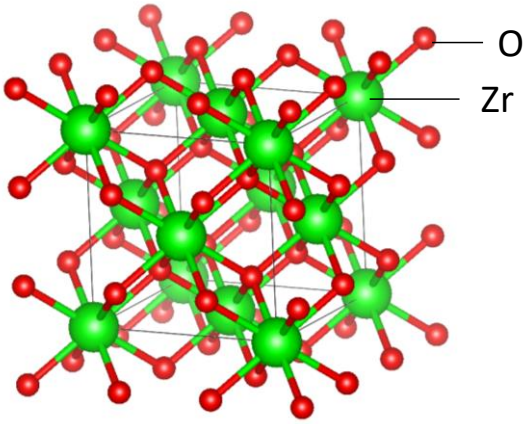

YSZ unit cell

- 8.3mol%Y_2O_3-ZrO_2
- Fluorite structure
- Lattice constant: 5.135 Å
- Zr site: 4, O site: 8
- Zr : Y : O : V_O = 10 : 2 : 23 : 1
- $C_O^{YSZ} = 9.41 \times 10^4$ mol/m³

Figure 5-9. Fluorite structure of zirconia and information of YSZ unit cell to calculate C_O^{YSZ}. Lattice constant is refereed from Hayashi et al [4]. V_O represents an oxygen vacancy in the lattice. The illustration of the structure was created using the VESTA package of Momma and Izumi [5].

total oxygen atom in a YSZ bulk, which is calculated based on the lattice structure as shown in Figure 5-9. The calculated $J_{18O}^{Biased(C/E)}$ is one order of magnitude larger than $J_{18O}^{OCV(C/E)}$ as summarized in Table 5-2.

At OCV, $J_{18O}^{OCV(C/E)}$ is also described by the surface exchange coefficient k_{OCV}^* [m/s] as follows:

$$J_{18O}^{OCV(C/E)} = J_{18O}^{ex(C/E)} + J_{18O}^{c(C/E)} = C_O^{YSZ} k_{OCV}^* \left[c_{18O}^{gas} - c_{18O}\big|_{x=0} \right]^{OCV} \tag{5.5}$$

where c_{18O}^{gas} is a relative ^{18}O concentration in gas phase (= 0.975) In the above expression, it seems to be difficult to separate the contribution from $J_{18O}^{ex(C/E)}$ and $J_{18O}^{c(C/E)}$ precisely. Therefore, in order to calculate $J_{18O}^{ion(C/E)}$ in Eq. (5.2), $J_{18O}^{ex(C/E)} + J_{18O}^{c(C/E)}$ at biased condition is roughly estimated below.

Both in OCV and biased condition, surface exchange coefficient on free YSZ surface, which determines $J_{18O}^{ex(C/E)}$, should be the same. In addition, $J_{18O}^{c(C/E)}$ at OCV is not more than 2.18 × 10^{-4} mol/(m^2•s) from Eq. (5.5) and Table 5-2. As shown in Fig. 5-8(a), the driving force of $J_{18O}^{c(C/E)}$ is the difference of c_{18O} (Δc_{18O}) between cathode and

Table 5-2. ^{18}O flux incorporated from the cathode/electrolyte interface to the electrolyte estimated by diffusion profiles. Total $^{18}O^{2-}$ flux at given current density is also shown.

Flux	Value [mol/(m²•s)]
$J_{18O}^{OCV(C/E)}$	2.18×10^{-4}
$J_{18O}^{Biased(C/E)}$	1.21×10^{-3} (Section B) 1.63×10^{-3} (Section C)
$J_{18O}^{ion(C/E)}$	1.01×10^{-3} (Section B) 1.43×10^{-3} (Section C)
$J_{18O}^{ion(all)}$	4.58×10^{-3} ($i = 0.09$ A/cm², $c_{18O}^{gas} = 0.975$)

electrolyte part. From c_{18O} line profiles in Figs. 5-5(c) and 5-6(c), Δc_{18O} at OCV (≈ 0.015) and biased condition (≈ 0.03) is the same order of magnitude. Therefore, $J_{18O}^{c(C/E)}$ at biased condition is also estimated to be less than or equal to 10^{-4} order of magnitude. Because $J_{18O}^{Biased(C/E)}$ is 10^{-3} order of magnitude, rough estimation of $J_{18O}^{ex(C/E)} + J_{18O}^{c(C/E)}$ at biased condition (10^{-4} order of magnitude) does not strongly affect $J_{18O}^{ion(C/E)}$.

Based on the above discussion, sum of $J_{18O}^{ex(C/E)}$ and $J_{18O}^{c(C/E)}$ at biased condition was approximately estimated using k_{OCV}^{*} as follows.

$$\left[J_{18O}^{ex(C/E)} + J_{18O}^{c(C/E)} \right]^{Biased} = C_O^{YSZ} k_{OCV}^{*} \left[c_{18O}^{gas} - c_{18O}\big|_{x=0} \right]^{Biased} \tag{5.6}$$

Substitution of Eqs. (5.4) and (5.6) into Eq. (5.2) gives $J_{18O}^{ion(C/E)}$, which are summarized in Table 5-2. The total $^{18}O^{2-}$ flux incorporated from whole cathode $J_{18O}^{ion(all)}$ at given current density i [A/m²] is also shown in this table.

$$J_{18O}^{ion(all)} = c_{18O}^{gas} \frac{i}{2F} \tag{5.7}$$

Under the assumption that whole cathode area contributes to the electrochemical reaction equivalently, the results in Table 5-2 indicate that 22% (section B) ~ 31% (section C) of

the overall electrochemical reaction (oxide ion incorporations to YSZ phase) occurs at the cathode/electrolyte interface, while the remaining 69~78% of those proceeds inside the porous cathode.

In 3-dimensional numerical simulation of LSM/YSZ porous cathode (LSM:YSZ = 50:50 wt%) based on the actual microstructure by Miyoshi et al [6], charge transfer current distribution in the cathode thickness direction was calculated at 850 ℃. In their result, 22.5% of the overall electrochemical reaction occurs at the region within 1.25 μm from the cathode/electrolyte interface, which is relatively close to the scale of one LSM particle on the electrolyte as shown in Fig. 5-6.

5.4 Summary

Oxygen isotope exchange and quench experiment was conducted at 973 K using the electrolyte-supported cell under fuel cell operation condition. From the analysis of ^{18}O diffusion profiles in YSZ electrolyte, it was disclosed that by applying a current, oxygen tracer diffusion coefficient D^* increased by a factor of only 1.2–1.5 while surface exchange coefficient k^* was enhanced by one order of magnitude. The greatly enhanced k^* comes from oxide ion flux incorporated from the cathode/electrolyte interface to the electrolyte. Based on the ^{18}O profiles, quantitative oxide ion flux incorporated from the cathode/electrolyte interface was estimated. The results indicated that 22~31% of the overall electrochemical reaction occurs at the cathode/electrolyte interface, while the remaining 69~78% of those proceeds inside the porous cathode.

References

[1] H. Naito, N. Sakai, T. Otake, H. Yugami, H. Yokokawa, *Solid State Ionics* 135 (2000) 669–673.

[2] G. Knöner, K. Reimann, R. Röwer, U. Södervall, H-E. Schaefer, *PNAS* 100 (7) (2003) 3870–3873.

[3] 田川博章，固体酸化物燃料電池と地球環境，アグネ承風社 (1998). (in Japanese)

[4] H. Hayashi, T. Saitou, N. Maruyama, H. Inaba, K. Kawamura, M. Mori, *Solid State Ionics* 176 (2005) 613–619.

[5] K. Momma, F. Izumi, *J. Appl. Crystallogr.* 41 (2008) 653–658.

[6] K. Miyoshi, T. Miyamae, H. Iwai, M. Saito, M. Kishimoto, H. Yoshida, *J. Power Sources* 315 (2016) 63–69.

Chapter 6

Conclusions

6.1 Key findings and contributions

In this thesis, toward construction of the detailed reaction kinetics and dynamics on SOFC porous electrodes, analytical reaction model was constructed and active sites imaging was conducted for more accurate understanding and description of species transport phenomena coupled with electrochemical reactions proceeding inside SOFC. The key findings and contributions from the study are summarized below.

- The analytical model for hydrogen oxidation at anode, species territory adsorption model, was newly proposed. Based on the model, explicit expressions of the current density with respect to oxygen activity and the anode overpotential with respect to current density could be obtained. The latter could combine the overpotentials at low- and high-current-density regions to unique expression, which were conventionally expressed independently.
- Based on the model, the current density asymptotes the limiting value as the oxygen coverage around the TPB approaches unity. The theoretical limitation of current density given by the model is determined by the rate constants of surface reactions and the coverage of adsorbed hydrogen on Ni.
- From referenced DFT-database and careful fitting process between the analytical and experimental results, all thermodynamic and kinetic parameters for the species territory

adsorption model were determined. This made it possible to estimate effective anode thickness based on the model, which tends to increase with temperature in six kinds of Ni/YSZ anodes used in this study and references.

- The proposed model can predict more precise dependence of anode overpotential on steam partial pressure than that by Butler-Volmer equation with empirical exchange current density when the same Ni-patterned anode experiment is selected as a basic data.
- The power generation equipment with a nozzle for direct helium gas impinging jet to the cell was newly constructed to quench an SOFC reaction for active sites imaging of porous electrodes. By using the equipment, the temperature of YSZ electrolyte could be decreased from 830 to 150 ^{o}C within 1.5 sec., which was in good agreement with analytical results based on the average Nusselt number of impinging jet heat transfer.
- By using the developed quench apparatus and oxygen isotope labeling, active sites in LSM/ScSZ porous cathode were first visualized in microstructure scale. The obtained ^{18}O mapping showed that the reaction sites near the cathode/electrolyte interface are more electrochemically active than those at other regions.
- Quantitative estimation of oxide ion flux incorporated from the cathode/electrolyte interface to the electrolyte indicates that 22~31% of the overall electrochemical reaction occurs at the interface, while the remaining 69~78% of those proceeds inside the porous cathode.

6.2 Future perspective

Future perspective to extend this study are suggested and summarized as follows.

- The introduction of the species territory adsorption model into numerical simulation

instead of Butler-Volmer equation can give more accurate prediction of the polarization behavior of Ni/YSZ anode. Based on numerically-solved local oxygen chemical potential, the model can give local charge transfer current density.

- The information of effective anode thickness predicted by the model is useful to design two-layered anode (Ni/YSZ as an active layer and porous metal as a current collecting layer), which can reduce ohmic resistance of a tubular SOFC in the longitudinal direction while enough anode reaction sites remain.
- The sensitivity analysis of the model indicates that anode overpotential can be drastically reduced by changing the adsorption state of oxygen on oxide ion conductor near the TPB, which can be new guideline to develop and design anode materials.
- The quench technique can be applied to visualize active sites of fuel electrode (e.g. Ni/YSZ), where the species territory adsorption model was assumed in this study. The adsorbed hydrogen, oxygen, or water around the Ni/YSZ/gas TPB in quenched anode can be detected through surface analysis, e.g. X-ray photoelectron spectroscopy (XPS). In addition, oxygen migration in the YSZ bulk near the TPB can be tracked by oxygen isotope labeling in the case of electrolysis reaction because oxygen incorporation sites can be easily imaged in this method.
- The effect of cathode materials, operating temperature, gas compositions, and current density on active sites distribution can be investigated by developed quench and oxygen isotope labeling method. In addition, the electrochemical impedance or overpotential should be linked to the imaged active sites distribution.
- The changes of active sites distribution and cathode degradations such as chromium poisoning, secondary phase formation, or segregation of strontium component can be tracked simultaneously during long-term operation, which can give valuable

information to further understand and improve SOFC stability.

- The correlation between oxide ion flux incorporated from a cathode/electrolyte interface to an electrolyte and various parameters and factors, e.g., electrochemical impedance, cathode composition or microstructure, and operating temperature, can be investigated.
- In order to suppress a cathode degradation by electrochemically-enhanced chromium poisoning especially at the region near the cathode/electrolyte interface, the reaction should proceed uniformly in the entire cathode. Active sites imaging can give useful information to design a cathode material, composition, or structure to realize uniform reaction distribution in the entire cathode.

Appendix A

Derivation of coverage formulas

In this Appendix, the detailed derivation of coverages in Areas 1 and 2, $\theta_{i(k)}$ [Eqs. (2.21)–(2.28)], are given. From Eqs. (2.13)–(2.16), $\theta_{\mathrm{H}(1)}$, $\theta_{\mathrm{H_2O}(1)}$, $\theta_{\mathrm{H_2O}(2)}$, and $\theta_{\mathrm{O}(2)}$ are expressed using $\theta_{V(1)}$ or $\theta_{V(2)}$, as follows:

$$\theta_{\mathrm{H}(1)} = \sqrt{K_{\mathrm{H}} P_{\mathrm{H_2}}}\,\theta_{V(1)} \tag{A.1}$$

$$\theta_{\mathrm{H_2O}(1)} = K_{\mathrm{H_2O}} P_{\mathrm{H_2O}} \theta_{V(1)} \tag{A.2}$$

$$\theta_{\mathrm{H_2O}(2)} = K'_{\mathrm{H_2O}} P_{\mathrm{H_2O}} \theta_{V(2)} \tag{A.3}$$

$$\theta_{\mathrm{O}(2)} = K_{\mathrm{O}} a_{\mathrm{O}} \theta_{V(2)} \tag{A.4}$$

From Eqs. (2.18) and (2.19) and above expressions, $\theta_{\mathrm{H}(2)}$ and $\theta_{\mathrm{O}(1)}$ are expressed using $\theta_{V(1)}$ or $\theta_{V(2)}$, as follows:

$$\theta_{\mathrm{H}(2)} = K_{\mathrm{H(ex12)}} \frac{\theta_{\mathrm{H}(1)}}{\theta_{V(1)}} \theta_{V(2)} = K_{\mathrm{H(ex12)}} \sqrt{K_{\mathrm{H}} P_{\mathrm{H_2}}}\,\theta_{V(2)} \tag{A.5}$$

$$\theta_{\mathrm{O}(1)} = K_{\mathrm{O(ex12)}} \frac{\theta_{\mathrm{O}(2)}}{\theta_{V(2)}} \theta_{V(1)} = K_{\mathrm{O(ex12)}} K_{\mathrm{O}} a_{\mathrm{O}} \theta_{V(1)} \tag{A.6}$$

Substitution of Eqs. (A.1), (A.2), and (A.6) into Eq. (2.11) gives following equation:

$$\left(1 + \sqrt{K_{\mathrm{H}} P_{\mathrm{H_2}}} + K_{\mathrm{O(ex12)}} K_{\mathrm{O}} a_{\mathrm{O}} + K_{\mathrm{H_2O}} P_{\mathrm{H_2O}}\right) \theta_{V(1)} = 1 \tag{A.7}$$

From Eq. (A.7), $\theta_{V(1)}$ is derived as shown in Eq. (2.21). By substituting Eq. (2.21) into Eqs. (A.1), (A.2), and (A.6), Eqs. (2.22)–(2.24) are derived.

In the same way, substitution of Eqs. (A.3)–(A.5) into Eq. (2.12) gives following equation:

$$\left(1+K_{\mathrm{H(ex12)}}\sqrt{K_{\mathrm{H}}P_{\mathrm{H_2}}}+K_{\mathrm{O}}a_{\mathrm{O}}+K'_{\mathrm{H_2O}}P_{\mathrm{H_2O}}\right)\theta_{V(2)}=1 \tag{A.8}$$

From Eq. (A.8), $\theta_{V(2)}$ is derived as shown in Eq. (2.25). By substituting Eq. (2.25) into Eqs. (A.3)–(A.5), Eqs. (2.26)–(2.28) are derived.

Appendix B

Oxygen transport and reaction described by chemical potential

B.1 Introduction

In Chapter 2, the relationship between anode potential and oxygen activity (Eq. (2.47)) is used. This expression is originated from a concept of chemical potential, which has been often introduced in solid state chemistry [1]. In the case of electrochemical devices such as SOFCs, both ion/electron transports in solids and chemical reactions at electrodes are described by using chemical potentials [2]. Several numerical studies have expressed overpotentials and ion/electron fluxes in SOFC electrodes using chemical potentials [3,4]. In this Appendix, equations for particle transport in solid written by chemical potentials are explained, typical chemical potential distributions in an SOFC are presented, and the derivation of Eq. (2.47) are shown.

B.2 Equation for particle transport in solid

As shown in Figure B-1, it is assumed that each particle (neutral atom, ion) in an ordered crystal lattice in a solid receives a periodic potential energy with a barrier of E_{act}~$10-100$ kJ/mol. If a thermally-vibrated atom has an energy higher than E_{act}, the atom can jump a potential barrier and move to a next lattice position. This probability p is generally described by using Boltzmann factor as follows.

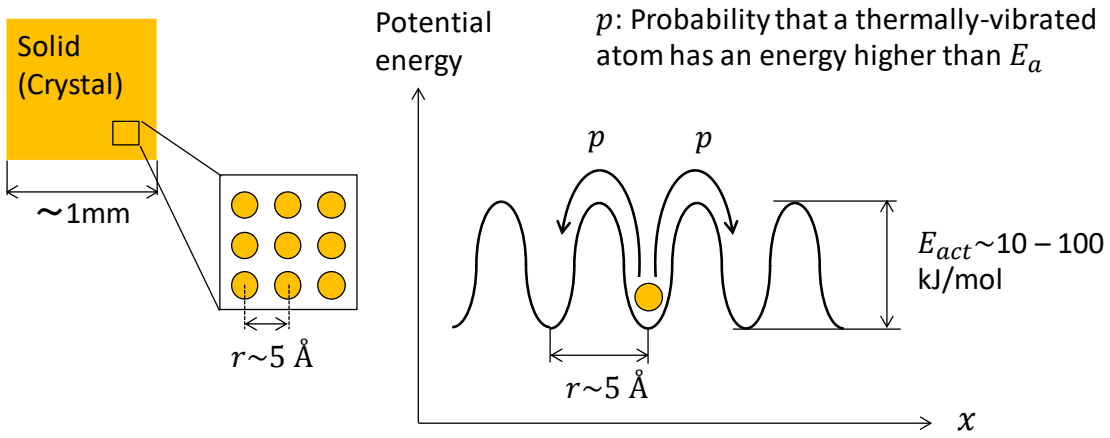

Figure B-1. Potential energy of each particle (neutral atom, ion) in an ordered crystal lattice in a solid.

$$p = \exp\left(-\frac{E_{act}}{RT}\right) \tag{B.1}$$

The mean-square displacement of each particle per sec. R^2_{av} [m^2/s] is described by lattice constant r [m], vibrational frequency of atom ν_0 [/s], and p as follows [2].

$$R_{\mathrm{av}}^{\ 2} = r^2 \nu_0 p \tag{B.2}$$

The diffusion of particle in solid is assumed to occur equally in all 6 directions, which gives self-diffusion coefficient D [m^2/s].

$$D = \frac{R_{\mathrm{av}}^{\ 2}}{6} = \frac{r^2 \nu_0}{6} \exp\left(-\frac{E_{act}}{RT}\right) \tag{B.3}$$

The tracer diffusion coefficient D^* discussed in Chapter 4 is generally smaller than D especially for oxygen diffusion in oxide through vacancy-diffusion mechanism. This is because an oxygen can jump to a next lattice position only when the next site is a vacancy, thus the diffusion is not isotropic. The relationship between D^* and D is expressed by using correlation factor f ($0 < f < 1$) as follows [2,5].

$$D^* = fD \tag{B.4}$$

When particles in solid are under a potential gradient, such as chemical potential

(including concentration) gradient, electric field, magnetic field, or temperature gradient, the potential energy distribution changes as shown in Figure B-2. Here, only chemical potential and electric field is considered as an external field, and sum of those is called an electrochemical potential $\tilde{\mu}_i(x)$. In this situation, diffused particle flux from left to right direction j_{LR} [mol/(m^2•s)] is below:

$$j_{\mathrm{LR}} = \left(\frac{1}{r}\right)^2 \frac{cr^3\nu_0}{6} \exp\left(-\frac{E_{act} - \Delta E/2}{RT}\right) \tag{B.5}$$

where c is a concentration of diffused particle [mol/m^3] and ΔE is a potential difference between two lattice positions generated by the potential gradient (Fig. B-2). Considering the order of number of atoms in solid $\sim 10^7$/cm, $\Delta E \sim E_{act}/10^7 \ll E_{act}$ can be assumed. Using this approximation, j_{LR} is rewritten as follows.

$$j_{\mathrm{LR}} = \frac{cr\nu_0}{6} \exp\left(-\frac{E_{act}}{RT}\right) \cdot \left(1 + \frac{\Delta E/2}{RT}\right) \tag{B.6}$$

In the same manner, diffused particle flux from right to left direction j_{RL} [mol/(m^2•s)] is obtained as follows.

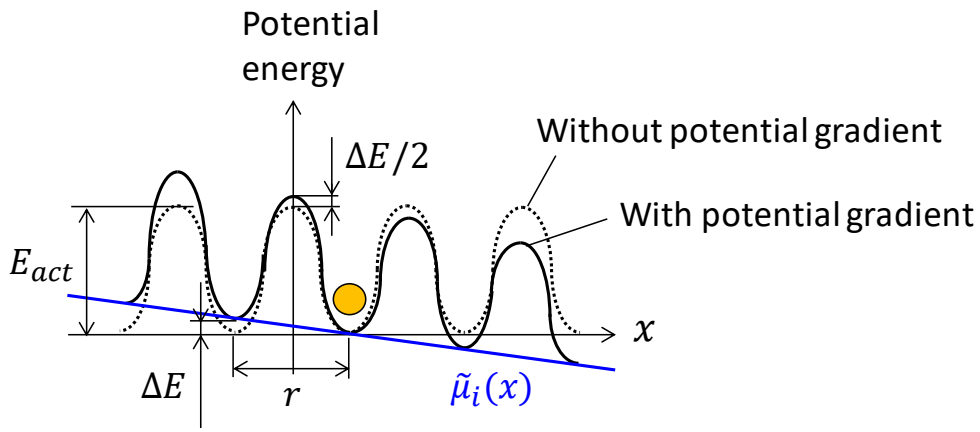

Figure B-2. Potential energy of each particle (neutral atom, ion) in an ordered crystal lattice in a solid with and without potential gradient. $\tilde{\mu}_i(x)$ is an electrochemical potential.

$$j_{\mathrm{RL}} = \frac{cr\nu_0}{6}\exp\left(-\frac{E_{act}}{RT}\right)\cdot\left(1-\frac{\Delta E/2}{RT}\right) \tag{B.7}$$

Finally, net flux of diffused particle from left to right j [mol/(m^2•s)] is below.

$$j = j_{\mathrm{LR}} - j_{\mathrm{LR}} = \frac{cr\nu_0}{6RT}\exp\left(-\frac{E_{act}}{RT}\right)\cdot\Delta E = -\frac{cD}{RT}\cdot\frac{\partial\tilde{\mu}_i}{\partial x} \tag{B.8}$$

Here, Eq. (B.3) and following relationship are used.

$$\Delta E = -\left(\frac{\partial\tilde{\mu}_i}{\partial x}\right)r \tag{B.9}$$

Eq. (B.8) is a general form of a basic equation for particle transport in solid.

B.3 Fick's first law and equation for ion conduction

Electrochemical potential of species i, $\tilde{\mu}_i$, consists of chemical potential μ_i and electric field $Z_iF\phi$ below:

$$\begin{aligned}\tilde{\mu}_i(x) &= \mu_i(x) + Z_iF\phi(x)\\ &= \mu_i^{\circ} + RT\ln a_i(x) + Z_iF\phi(x)\\ &= \mu_i^{\circ} + RT\ln\gamma_i(x)c_i(x) + Z_iF\phi(x)\end{aligned} \tag{B.10}$$

where Z_i is a valence, F a Faraday constant [C/mol], ϕ an electro-static potential [J/C], μ_i° a chemical potential at standard condition [J/mol], a_i an activity ($=\gamma_i c_i$), γ_i an activity coefficient ($0 \le \gamma_i \le 1$), and c_i a concentration [mol/m^3]. Substitution of Eq. (B.10) into Eq. (B.8) gives:

$$j_i = -\frac{c_iD_i}{RT}\left(RT\frac{\partial\ln\gamma_i}{\partial x} + RT\frac{\partial\ln c_i}{\partial x} + Z_iF\frac{\partial\phi}{\partial x}\right) \tag{B.11}$$

The first, second, and third term on the right side in the above expression is a contribution of activity coefficient gradient, concentration gradient, and electrical potential gradient, respectively.

In the case of neutral atom ($Z_i = 0$) or $\nabla\phi = 0$, Eq. (B.11) is reduced to following expression.

$$j_i = -c_i D_i \left(\frac{\partial \ln \gamma_i}{\partial x} + \frac{\partial \ln c_i}{\partial x} \right) = -D_i \left(1 + \frac{\partial \ln \gamma_i}{\partial \ln c_i} \right) \cdot \frac{\partial c_i}{\partial x} \tag{B.12}$$

Here, $(1 + \partial \ln \gamma_i / \partial \ln c_i)$ is called a thermodynamic factor. If species i behaves as an ideal solution in a solid, γ_i becomes unity and Eq. (B.12) corresponds Fick's first law.

$$j_i = -D_i \frac{\partial c_i}{\partial x} \tag{B.13}$$

In the case of ion ($Z_i \neq 0$) and $\nabla \mu_i = 0$, Eq. (B.11) becomes below.

$$j_i = -\frac{Z_i F c_i D_i}{RT} \cdot \frac{\partial \phi}{\partial x} \tag{B.14}$$

Using the definition of current density $i_i = Z_i F j_i$ [A/m^2] and Ohm's law, $i_i = \sigma_i(-\partial \phi / \partial x)$, following Nernst-Einstein equation is derived.

$$\sigma_i = \frac{Z_i^2 F^2 c_i D_i}{RT} \tag{B.15}$$

Here σ_i is an ionic conductivity [S/m]. Finally, basic equation for ion conduction can be obtained as follows.

$$i_i = -\frac{\sigma_i}{Z_i F} \cdot \frac{\partial \tilde{\mu}_i}{\partial x} \tag{B.16}$$

As shown here, both Fick's first law and basic equation for ion conduction are derived from the same equation (B.11).

B.4 Chemical potential distribution in SOFC

In this section, typical chemical and electrochemical potential distributions in an SOFC are explained. Here, a single cell consisting of YSZ electrolyte, Pt porous cathode, and Ni porous anode is assumed as shown in Figure B-3. In this figure, the number 1–8 represents the position of electrode top surfaces or electrode/electrolyte interface. In this cell, electrochemical reaction sites are limited to Pt/YSZ/gas TPB (position 2, 6) for

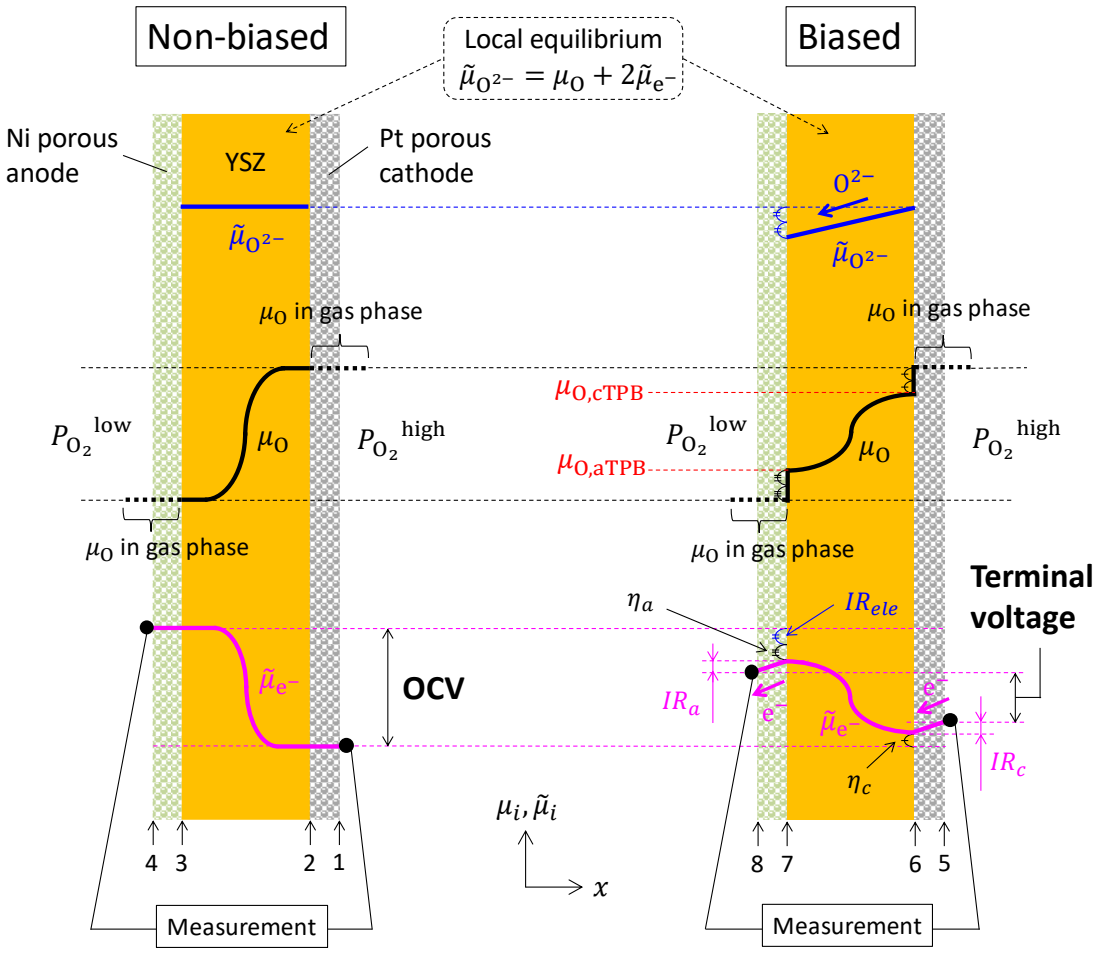

Figure B-3. Typical chemical and electrochemical potential distributions (μ_i, $\tilde{\mu}_i$) with respect to thickness direction x of an SOFC consisting of YSZ electrolyte, Pt porous cathode, and Ni porous anode. Both non-biased and biased conditions are shown. The number 1–8 represents the position of electrode top surface or electrode/electrolyte interface.

cathode and Ni/YSZ/gas TPB (position 3, 7) for anode. The cathode side is exposed to high oxygen partial pressure $P_{O_2}{}^{high}$ (~0.21–1 atm) while the anode side to low oxygen partial pressure $P_{O_2}{}^{low}$ (~10^{-20} atm in humidified hydrogen). Fig. B-3 shows the distributions of chemical potential of oxygen μ_O and electrochemical potentials of oxide ion $\tilde{\mu}_{O^{2-}}$ and electron $\tilde{\mu}_{e^-}$ with respect to the thickness direction x at both non-biased and biased conditions.

In addition to oxide ion, electron also exists as a minor career in YSZ. From Eq. (B.16), the equations for oxide ion and electron conduction in YSZ are described as follows:

$$i_{O^{2-}} = \frac{\sigma_{O^{2-}}}{2F} \cdot \frac{\partial \tilde{\mu}_{O^{2-}}}{\partial x} \tag{B.17}$$

$$i_{e^-} = \frac{\sigma_{e^-}}{F} \cdot \frac{\partial \tilde{\mu}_{e^-}}{\partial x} \tag{B.18}$$

where $\sigma_{O^{2-}}$ and σ_{e^-} shows an ionic and electronic conductivity of YSZ, respectively. In the non-biased condition, μ_O (equivalent to oxygen partial pressure) in YSZ continuously decreases from the cathode to anode side as shown in Fig. B-3. In a steady state ($i_{O^{2-}}$ and i_{e^-} is independent of x), $\nabla\tilde{\mu}_{O^{2-}}$ is constant based on Eq. (B.17) because $\sigma_{O^{2-}}$ is independent of μ_O. On the other hand, $\nabla\tilde{\mu}_{e^-}$ is not constant because σ_{e^-} in YSZ depends on μ_O [6]. In addition, local equilibrium between O^{2-}, O, and e^- ($O^{2-} \leftrightarrow O + 2e^-$) is assumed in any position of YSZ [3], giving following relationship.

$$\tilde{\mu}_{O^{2-}} = \mu_O + 2\tilde{\mu}_{e^-} \tag{B.19}$$

In non-biased condition, there is no oxide ionic flow and $\nabla\tilde{\mu}_{O^{2-}}$ is zero. As a result, $\tilde{\mu}_{e^-}$ continuously increases from the cathode to anode side and its profile has an upside-down curve of μ_O, as shown in Fig. B-3. The $\tilde{\mu}_{e^-}$ of Pt and Ni, which are actually detected in electrochemical measurement, can be assumed to be the same as those of YSZ at electrode/electrolyte interface at non-biased condition (position 2 and 3). The difference of $\tilde{\mu}_{e^-}$ between anode and cathode ($\tilde{\mu}_{e^-}(4) - \tilde{\mu}_{e^-}(1)$) detected here is an OCV.

The origin of OCV can be also qualitatively interpreted based on the phenomenological description. An oxygen vacancy formation in YSZ is described as follows:

$$O_O^{\times} \leftrightarrow V_O^{\bullet\bullet} + 2e^- + \frac{1}{2}O_2 \tag{B.20}$$

where $O_O^{\times}$ and $V_O^{\cdot\cdot}$ represent O^{2-} and oxygen vacancy in the YSZ bulk, respectively. The equilibrium constant K_e of reaction (B.20) is below.

$$K_e = \left[V_O^{\bullet\bullet}\right] c_{e^-}{}^2 \cdot P_{O_2}{}^{1/2} \tag{B.21}$$

In YSZ, vacancy concentration $[V_O^{\cdot\cdot}]$ is determined by the additive amount of yttrium and is independent of P_{O_2}. Therefore, electron concentration in YSZ c_e is proportional to ${P_{O_2}}^{-1/4}$. At anode side (${P_{O_2}}^{low}$), more electrons are stored compared to cathode side (${P_{O_2}}^{high}$), resulting in the higher $\tilde{\mu}_{e^-}$.

In the biased condition, $\tilde{\mu}_{O^{2-}}$ linearly decreases from cathode to anode side accompanied by an O^{2-} flow, and the decrement of $\tilde{\mu}_{O^{2-}}$ corresponds IR loss of electrolyte (IR_{ele}). At the cathode/electrolyte interface, μ_O drastically decreases from $\mu_O(5)$, which corresponds to ${P_{O_2}}^{high}$, to $\mu_{O,cTPB}$, and the difference $\mu_O(5) - \mu_{O,cTPB}$ is equivalent to cathode overpotential η_c. Here $\mu_O(k)$ (k = 1–8) denotes μ_O in position k. In the same manner, the difference $\mu_{O,aTPB} - \mu_O(8)$ corresponds to anode overpotential η_a. In addition, $\tilde{\mu}_{e^-}$ of Pt and Ni linearly decreases from position 5 to 6 (Pt) and 7 to 8 (Ni), which come from IR losses in cathode layer (IR_c) and anode layer (IR_a), respectively. As a result, terminal voltage corresponding to $\tilde{\mu}_{e^-}(8) - \tilde{\mu}_{e^-}(5)$ is smaller than OCV, as shown in Fig. B-3. The calculation method of precise μ_O profile inside YSZ electrolyte is given by Choudhury and Patterson [7]

B.5 Overpotentials described by oxygen activity

The oxygen activity of YSZ near the anode TPB, a_O, introduced in Chapters 2 and 3 corresponds to $\mu_{O,aTPB}$ in Fig. B-3. From Fig. B-3,

$$\mu_{O,aTPB} - \mu_O(8) = 2F\eta_a \tag{B.22}$$

Here gas phase P_{O_2} is assumed be constant at non-biased and biased condition in both anode and cathode sides, that is, $\mu_O(1) = \mu_O(5)$ and $\mu_O(4) = \mu_O(8)$. As a result,

$$\begin{aligned}\mu_{O,aTPB} &= \mu_O(4) + 2F\eta_a \\ &= \mu_O(1) - 2F \cdot OCV + 2F\eta_a\end{aligned} \tag{B.23}$$

μ_O is rewritten by a_O as follows:

$$\mu_O^\circ + RT \ln a_{O,aTPB} = \mu_O^\circ + RT \ln a_O(1) + 2F\left(\eta_a - OCV\right) \tag{B.24}$$

where $a_{O,aTPB}$ and $a_O(1)$ represents an oxygen activity of YSZ at anode TPB and of gas phase in positon 1, respectively. From Eq. (B.24), following relationship is obtained.

$$\eta_a - OCV = \frac{RT}{2F} \ln\left[\frac{a_{O,aTPB}}{a_O(1)}\right] \tag{B.25}$$

Replacing OCV with V_{R-R} and $a_O(1)$ with $a_{O(CR)}$ gives Eq. (2.47) in Chapter 2.

In the same manner, η_c can be also described by $a_{O,cTPB}$, an oxygen activity of YSZ at cathode TPB. From Fig. B-3,

$$\mu_O(1) - \mu_{O,cTPB} = 2F\eta_c \tag{B.26}$$

μ_O is rewritten by a_O as follows:

$$\mu_O^\circ + RT \ln a_O(1) - \left\{\mu_O^\circ + RT \ln a_{O,cTPB}\right\} = 2F\eta_c \tag{B.27}$$

This gives following expression.

$$\eta_c = \frac{RT}{2F} \ln\left[\frac{a_O(1)}{a_{O,cTPB}}\right] \tag{B.28}$$

As shown in Eqs. (B.25) and (B.28), both anode and cathode overpotentials are related to oxygen activities near the reaction sites [8,9].

References

[1] H. Yokokawa, *Materia Japan* 35 (9) (1996) 1025–1030. (in Japanese)

[2] 水田進，脇原將孝（編），固体電気化学，実験法入門，講談社サイエンティフィク (2001). (in Japanese)

[3] N. Shikazono, D. Kanno, K. Matsuzaki, H. Teshima, S. Sumino, N. Kasagi, *J. Electrochem. Soc.* 157 (5) (2010) B665–B672.

[4] K. Matsuzaki, N. Shikazono, N. Kasagi, *J. Power Sources* 196 (2011) 3073–3082.

[5] H. Mehrer, *Diffusion in Solids*, Springer, Maruzen (2012). (in Japanese)

[6] 田川博章，固体酸化物燃料電池と地球環境，アグネ承風社 (1998). (in Japanese)

[7] N.S. Choudhury, J.W. Patterson, *J. Electrochem. Soc.* 118 (9) (1971) 1398–1403.

[8] M. Ihara, T. Kusano, C. Yokoyama, *J. Electrochem. Soc.* 148, 3 (2001) A209–A219.

[9] H. Fukunaga, M. Koyama, N. Takahashi, C. Wen, K. Yamada, *Solid State Ionics* 132 (2000) 279–285.

Appendix C

IV curves and fitting results of impedance spectra

The I-V curves of power generation experiment at 1073 K using YSZ electrolyte-supported single cell with Ni/YSZ anode and LSM/ScSZ cathode are summarized in Figure C-1, which were mentioned in Chapter 3, section 3.2. In addition, impedance spectra, fitting curves, and obtained R_{ohm}, R_1, and R_2 are shown in Figure C-2 for $(P_{H_2}, P_{H_2O}) = (0.97,0.03)$ atm, in Figure C-3 for $(P_{H_2}, P_{H_2O}) = (0.07,0.03)$ atm, in Figure C-4 for $(P_{H_2}, P_{H_2O}) = (0.02,0.03)$ atm, and in Figure C-5 for $(P_{H_2}, P_{H_2O}) = (0.015,0.01)$ atm.

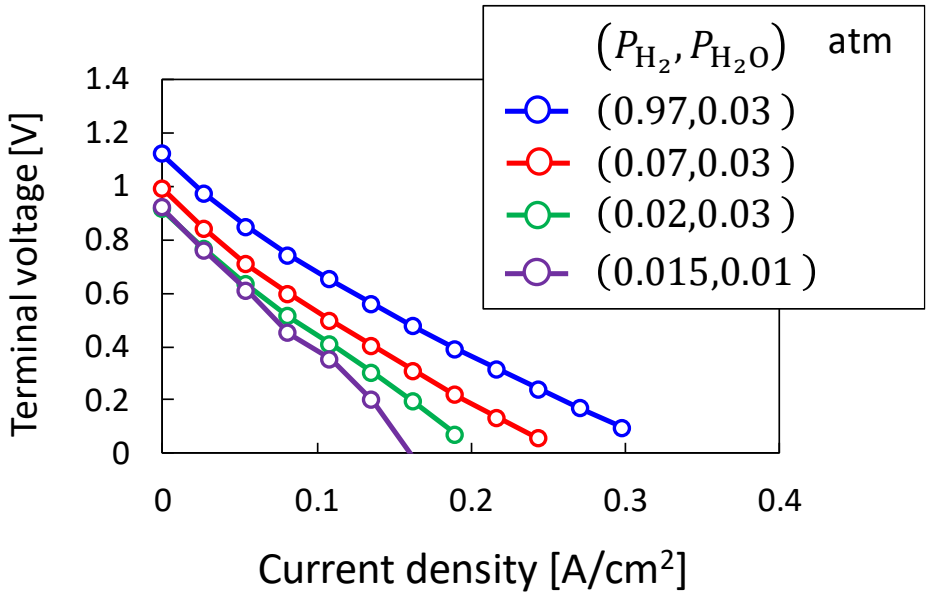

Figure C-1. I-V curves of YSZ electrolyte-supported single cell with Ni/YSZ anode and LSM/ScSZ cathode at 1073 K under different four fuel compositions on anode side. At cathode side, pure oxygen is supplied.

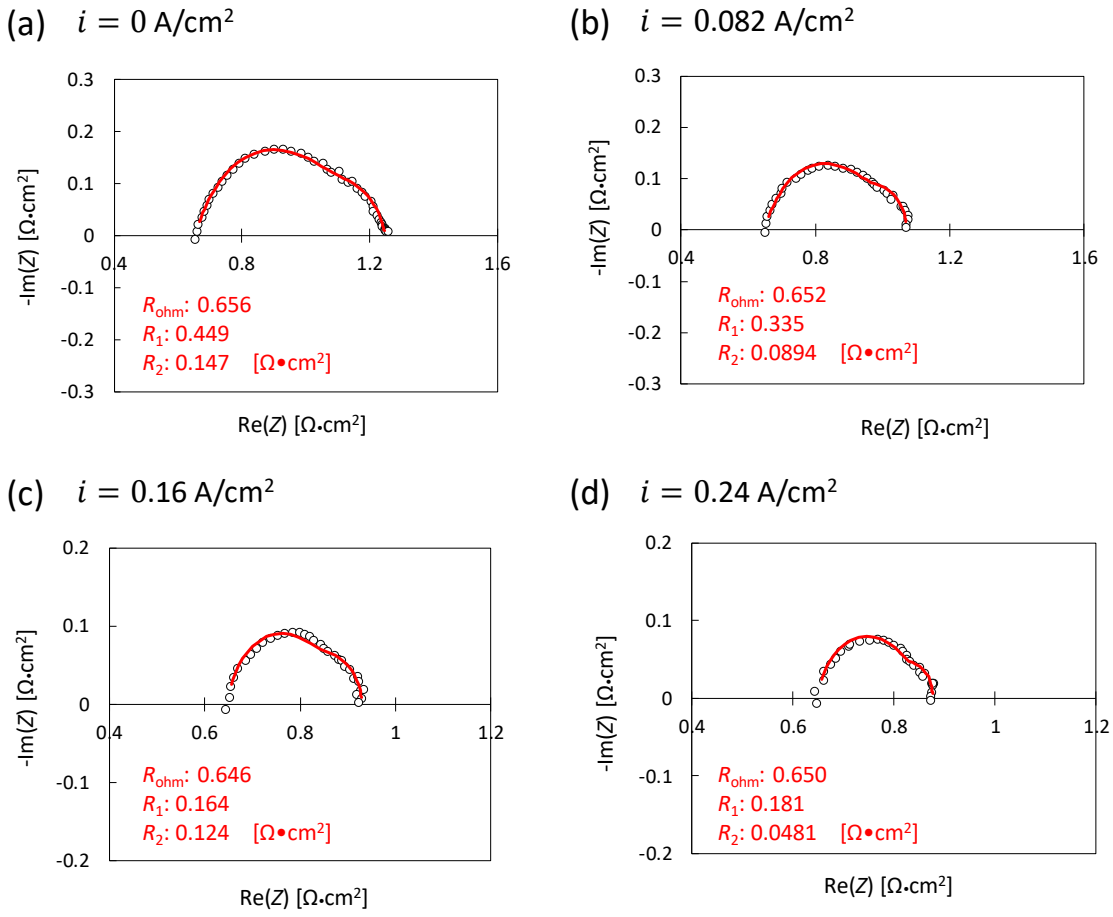

Figure C-2. Impedance spectra and fitting curves of Ni/YSZ anode at a direct current of (a) 0 A/cm^2, (b) 0.082 A/cm^2, (c) 0.16 A/cm^2, and (d) 0.24 A/cm^2 under $(P_{H_2}, P_{H_2O}) = (0.97, 0.03)$ atm. The obtained fitted values R_{ohm}, R_1, and R_2 are also shown. The equivalent circuit for the fitting process is shown in Figure 3-4(b) in Chapter 3.

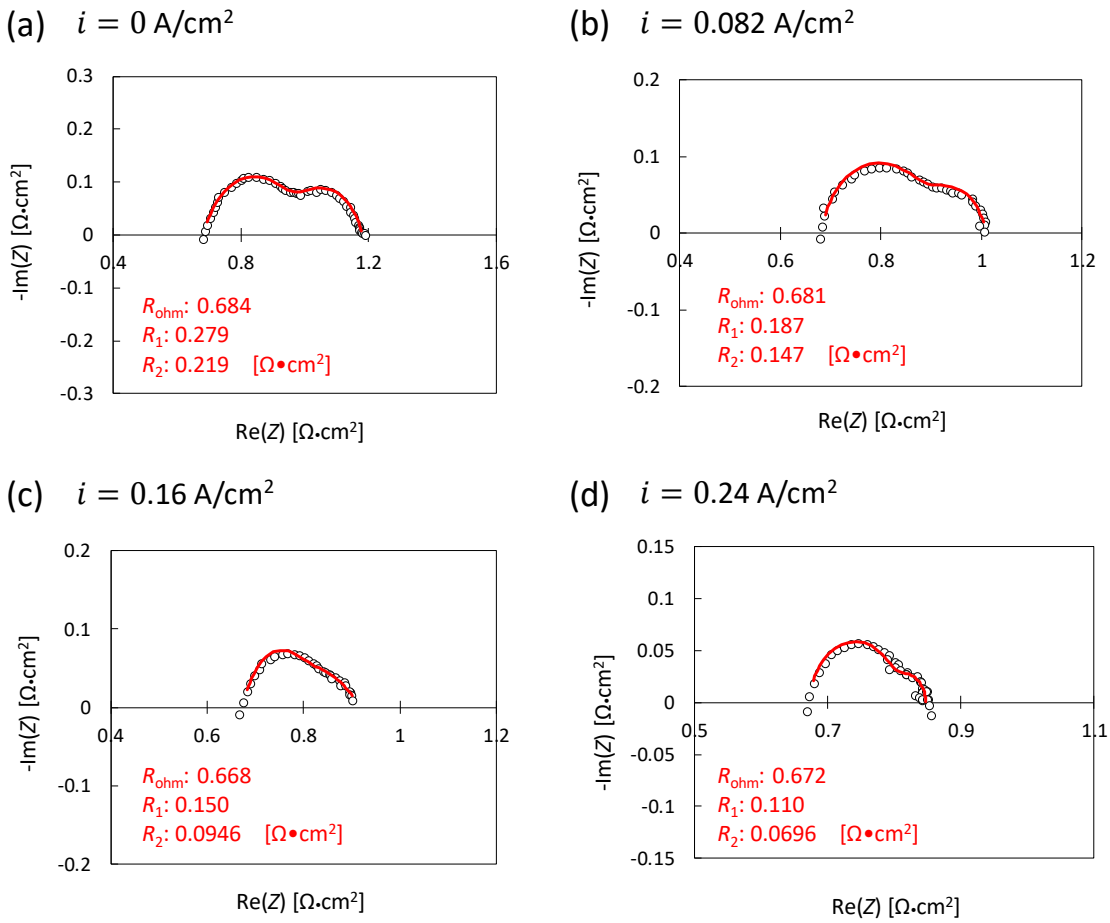

Figure C-3. Impedance spectra and fitting curves of Ni/YSZ anode at a direct current of (a) 0 A/cm^2, (b) 0.082 A/cm^2, (c) 0.16 A/cm^2, and (d) 0.24 A/cm^2 under $\left(P_{H_2}, P_{H_2O}\right) = (0.07, 0.03)$ atm. The obtained fitted values R_{ohm}, R_1, and R_2 are also shown. The equivalent circuit for the fitting process is shown in Figure 3-4(b) in Chapter 3.

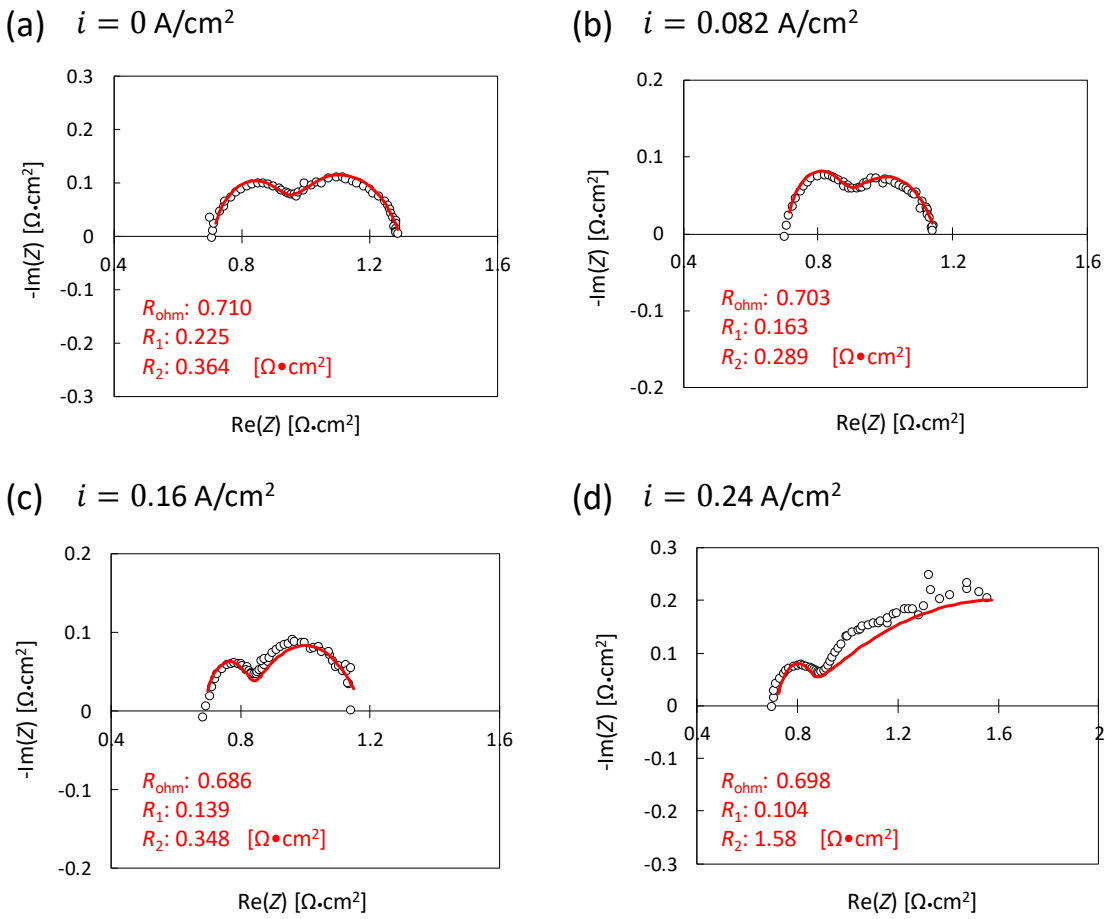

Figure C-4. Impedance spectra and fitting curves of Ni/YSZ anode at a direct current of (a) 0 A/cm^2, (b) 0.082 A/cm^2, (c) 0.16 A/cm^2, and (d) 0.24 A/cm^2 under $\left(P_{H_2}, P_{H_2O}\right) = (0.02,0.03)$ atm. The obtained fitted values R_{ohm}, R_1, and R_2 are also shown. The equivalent circuit for the fitting process is shown in Figure 3-4(b) in Chapter 3.

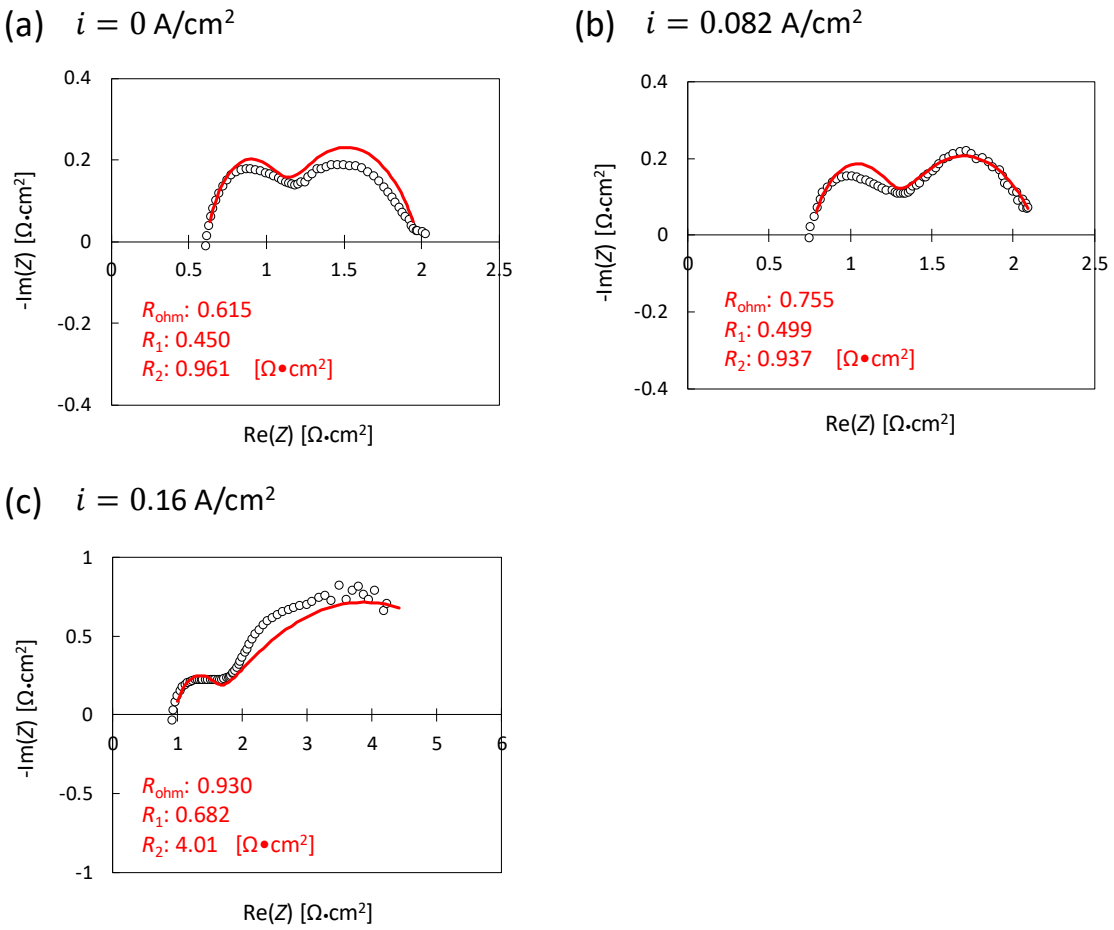

Figure C-5. Impedance spectra and fitting curves of Ni/YSZ anode at a direct current of (a) 0 A/cm^2, (b) 0.082 A/cm^2, and (c) 0.16 A/cm^2 under $\left(P_{H_2}, P_{H_2O}\right) = (0.015, 0.01)$ atm. The obtained fitted values R_{ohm}, R_1, and R_2 are also shown. The equivalent circuit for the fitting process is shown in Figure 3-4(b) in Chapter 3.

Appendix D

Thermal design of quench system

D.1 Detailed structure of quench nozzle

In this Appendix, the detailed thermal design of the developed quench system in Chapter 4 is presented. Figure D-1 shows the detailed structure of the helium nozzle covered by the water cooling jacket and heat insulator. Inside the stainless tube with an inner diameter of $D_1 = 6$ mm and outer diameter of $D_2 = 8$ mm, other two stainless tubes for supply of cooling water (outer diameter $D_{\mathrm{W,O}} = 3.5$ mm, wall thickness = 0.5 mm) and for helium nozzle (outer diameter $D_{\mathrm{He,O}} = 2$ mm, wall thickness = 0.5 mm) are inserted. The tube is covered by the heat insulator made of a ceramic fiber (3M$^{\mathrm{TM}}$, NEXTEL$^{\mathrm{TM}}$) with an outer diameter of $D_3 = 10$ mm. This cooling unit is set inside a mullite tube with an inner diameter of $D_4 = 16$ mm and outer diameter of $D_5 = 21$ mm. The mullite tube is fixed with a SOFC single cell using a glass seal.

D.2 Assumed temperature distribution

Figure D-2 shows a schematic of an assumed temperature distribution of in a radial direction of the cooling tube. Here, Q is a heat flux from a tubular electric furnace (Asahi Rika Seisakusho Co., Ltd., ARF-50KC, Power output: 700 W). For simplicity in heat calculation, the helium nozzle tube is not considered and the coaxial structure of two tubes with the outer diameter of $D_{\mathrm{W,O}}$ and D_2 are assumed in Fig. D-2, which are actually

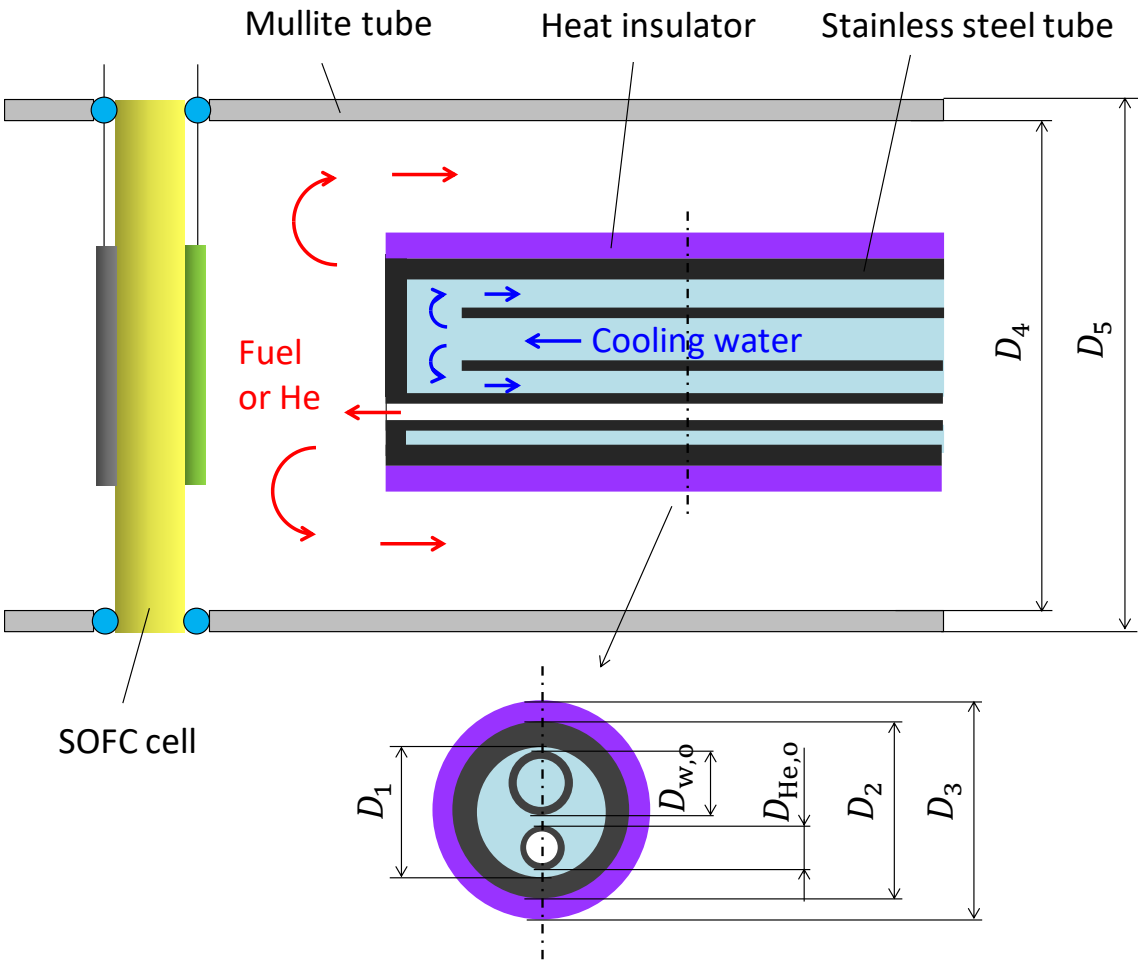

Figure D-1. Detailed structure of the helium nozzle covered by the water cooling jacket and heat insulator. The cooling unit is set inside a mullite tube, which is fixed with a SOFC single cell using a glass seal.

eccentric as shown in Fig. D-1. The flow rate of cooling water and hydrogen gas are assumed to be 0.9 L/min and 0.2 L/min, respectively. Each position in the radial direction is numbered by 0 to 5 in Fig. D-2, and the temperature and radius of each position are denoted by T_i and r_i $(i = 0{\sim}5)$, respectively. T_{34} is a temperature of a middle position between wall 3 and 4. In the experiment, an inside of the nozzle should be kept at around room temperature while the SOFC cell is operated at 1073 K. Therefore, the requirement of the thermal design is $T_1 < 100℃$ and $T_{34} \approx 800℃$.

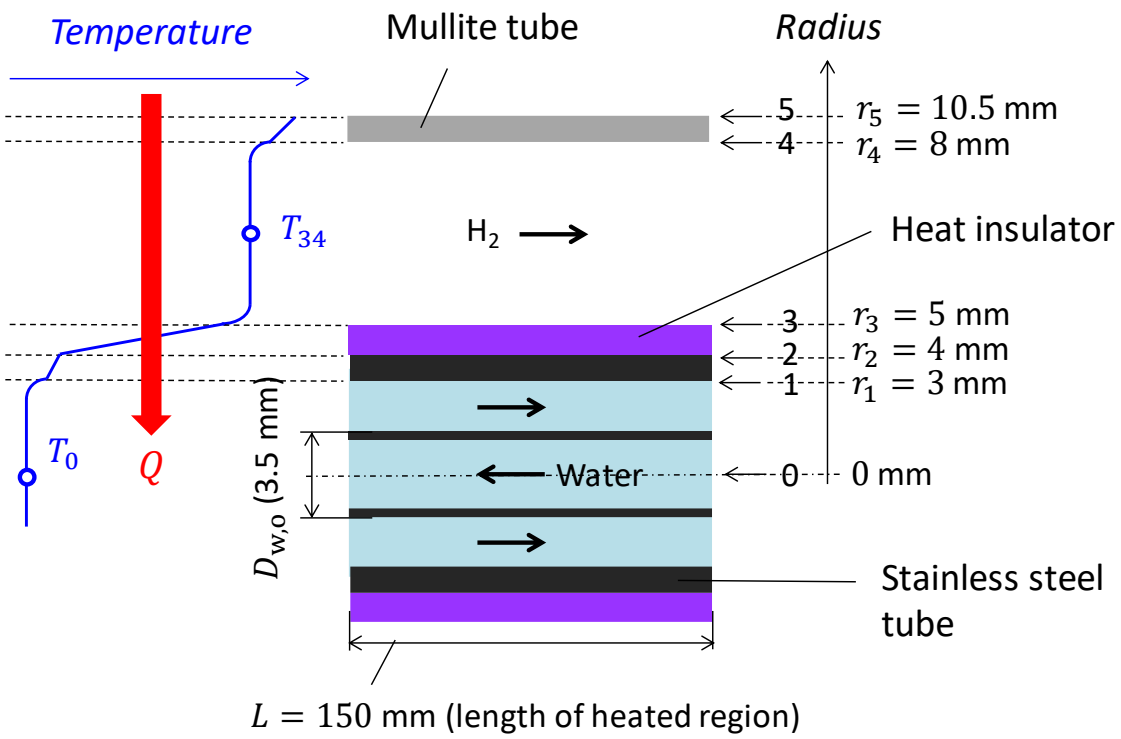

Figure D-2. Assumed temperature distribution of in a radial direction of the cooling tube. Q is a heat flux from a tubular electric furnace.

D.3 Heat transfer calculation

In order to calculate temperature of each position (T_0~T_5), heat resistance of each position needs to be calculated. Nusselt number near the wall 1 cooled by water (Nu_1) is given as follows, which is for turbulence heat transfer in concentric annulus [1].

$$\frac{Nu_1}{Nu(D_h)} = 1 - 0.14\left(\frac{D_{W,O}}{D_1}\right)^{0.6} \tag{D.1}$$

Here, $D_h = D_1 - D_{W,O}$ is a hydraulic diameter and $Nu(D_h)$ is a Nusselt number of a tube flow with a diameter of D_h, which is calculated by Gnielinski's expression [2].

$$Nu(D_h) = \frac{(f/2)\left[Re(D_h) - 1000\right]Pr}{1 + 12.7\sqrt{f/2}\left(Pr^{2/3} - 1\right)} \tag{D.2}$$

where Pr is a Prandtl number of water and $Re(D_h)$ is a Reynolds number based on the representative length D_h. Friction factor in the pipe f is calculated by Blasius equation as follows [2]:

$$f = \frac{0.079}{Re^{0.25}} \tag{D.3}$$

As a result, $Nu_1 = 17.9$ and heat transfer coefficient in the wall 1, $h_1 = 4.39 \times 10^3$ W/(m^2•K) are obtained. The heat resistance near the wall 1, R_1 is expressed as follows:

$$R_1 = \frac{1}{2\pi L} \cdot \frac{1}{r_1 h_1} \tag{D.4}$$

where L is a length of heated region (= 150 mm).

Nusselt number near the wall 3 (Nu_3) or 4 (Nu_4) ($Nu_3 = Nu_4$) is given by Stephan as follows, which is for laminar heat transfer in concentric annulus [1].

$$Nu_3 = \left[3.66 + 1.2\left(\frac{D_3}{D_4}\right)^{0.5} + \left\{1 + 0.14\left(\frac{D_3}{D_4}\right)^{1/3}\right\} \frac{0.19\left(RePr\frac{D_{h4}}{L}\right)^{0.8}}{1 + 0.117\left(RePr\frac{D_{h4}}{L}\right)^{0.467}} \right] \left(\frac{Pr}{Pr_w}\right)^{0.11} \tag{D.5}$$

Here, $D_{h4} = D_4 - D_3$ is a hydraulic diameter, Re is a Reynolds number based on the representative length D_{h4}, Pr is a Prandtl number of hydrogen at 800 ℃, and Pr_w is a Prandtl number of hydrogen at wall temperature ($Pr = Pr_w$ is assumed). As a result, $Nu_3 = Nu_4 = 4.61$ and heat transfer coefficient in the wall 3 or 4, $h_3 = h_4 = 3.97 \times 10^2$ W/(m^2•K) are obtained. The heat resistances near the wall 3 and 4, R_3 and R_4 are expressed as follows.

$$R_3 = \frac{1}{2\pi L} \cdot \frac{1}{r_3 h_3} \tag{D.6}$$

$$R_4 = \frac{1}{2\pi L} \cdot \frac{1}{r_4 h_4} \tag{D.7}$$

The heat resistances by heat conduction from wall 1 to 2, 2 to 3, and 4 to 5 are denoted by R_{12}, R_{23}, and R_{45}, respectively. These are expressed as follows.

$$R_{12} = \frac{1}{2\pi L k_{\mathrm{s}}} \ln\left(\frac{r_2}{r_1}\right) \tag{D.8}$$

$$R_{23} = \frac{1}{2\pi L k_{\mathrm{i}}} \ln\left(\frac{r_3}{r_2}\right) \tag{D.9}$$

$$R_{45} = \frac{1}{2\pi L k_{\mathrm{m}}} \ln\left(\frac{r_5}{r_4}\right) \tag{D.10}$$

Here k_{s}, k_{i}, and k_{m} is a thermal conductivity of a stainless steel ($k_{\mathrm{s}} = 16.7$ W/(m•K)), heat insulator made of a ceramic fiber ($k_{\mathrm{i}} = 0.1$ W/(m•K)), and mullite ($k_{\mathrm{m}} = 3.4$ W/(m•K)), respectively.

As shown in Figure D-3, linear temperature profile is assumed for cooling water flowing in the stainless tube to roughly estimate water temperature T_0. The energy balance of the water is described as follows:

$$\rho C_{\mathrm{p}} u_x \frac{\pi D_1^{\,2}}{4} \cdot \frac{\partial T}{\partial x} = \rho C_{\mathrm{p}} u_x \frac{\pi D_1^{\,2}}{4} \cdot \frac{T_0 - T_{\mathrm{in}}}{L} = q\pi D_1 \tag{D.11}$$

where ρ and C_{p} is a density and specific heat of water at room temperature, u_x is a flow velocity, q is a heat flux from the tubular electric furnace ($q = Q/(\pi D_1 L)$), and T_{in} is an inlet temperature of cooling water ($T_{\mathrm{in}} = 25$℃). Here, total heat flux Q should be lower than 350 W (half of maximum output of the electric furnace, 700 W). In this calculation, $Q = 260$ W is assumed and T_0 is determined as follows.

$$T_0 = \frac{4qL}{\rho C_{\mathrm{p}} u_x D_1} + T_{\mathrm{in}} = 29.2\,^{\circ}\mathrm{C} \tag{D.12}$$

Finally, $T_1 \sim T_5$ are determined as follows.

$$T_1 = T_0 + QR_1 = 50.1\,^{\circ}\mathrm{C} \tag{D.13}$$

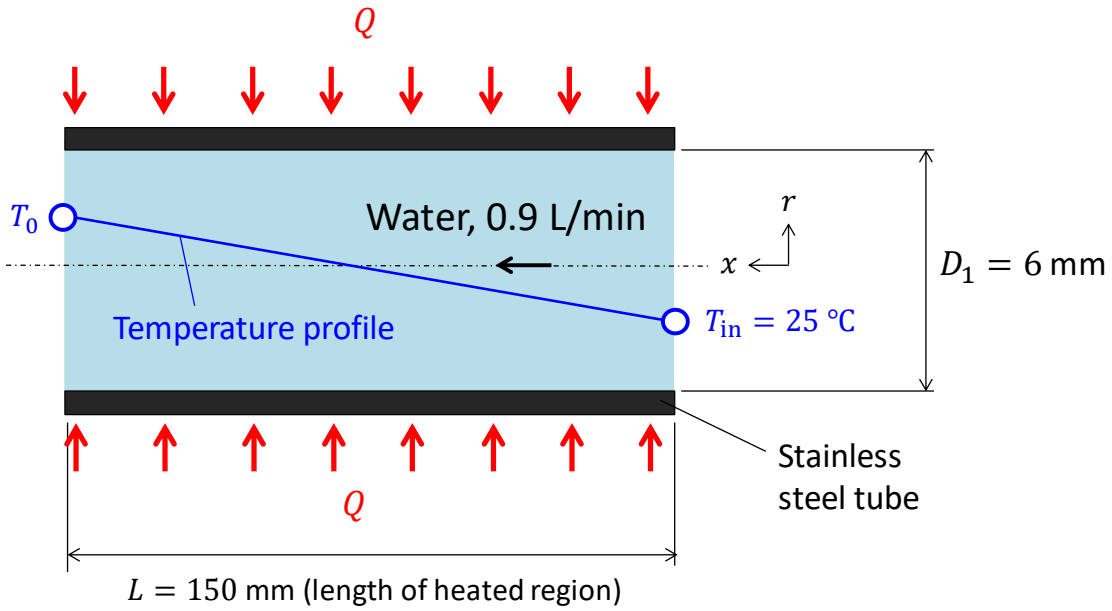

Figure D-3. Assumed linear temperature profile of cooling water. Q is a heat flux from a tubular electric furnace.

$$T_2 = T_1 + QR_{12} = 54.9^{\circ}\mathrm{C} \tag{D.14}$$

$$T_3 = T_2 + QR_{23} = 670^{\circ}\mathrm{C} \tag{D.15}$$

$$T_{34} = T_3 + QR_3 = 809^{\circ}\mathrm{C} \tag{D.16}$$

$$T_4 = T_3 + QR_4 = 896^{\circ}\mathrm{C} \tag{D.17}$$

$$T_5 = T_4 + QR_{45} = 918^{\circ}\mathrm{C} \tag{D.18}$$

These results fulfill the requirement of the thermal design: $T_1 < 100$℃ and $T_{34} \approx 800$℃.

Figure D-4 shows a drawing of the helium nozzle combined with water-cooling jacket used in this study. In this figure, flow directions of helium and water are also shown. The total pressure drop of helium (10 L/min) and water (0.9 L/min) lines are estimated to be 62.7 kPa and 28.9 kPa, respectively.

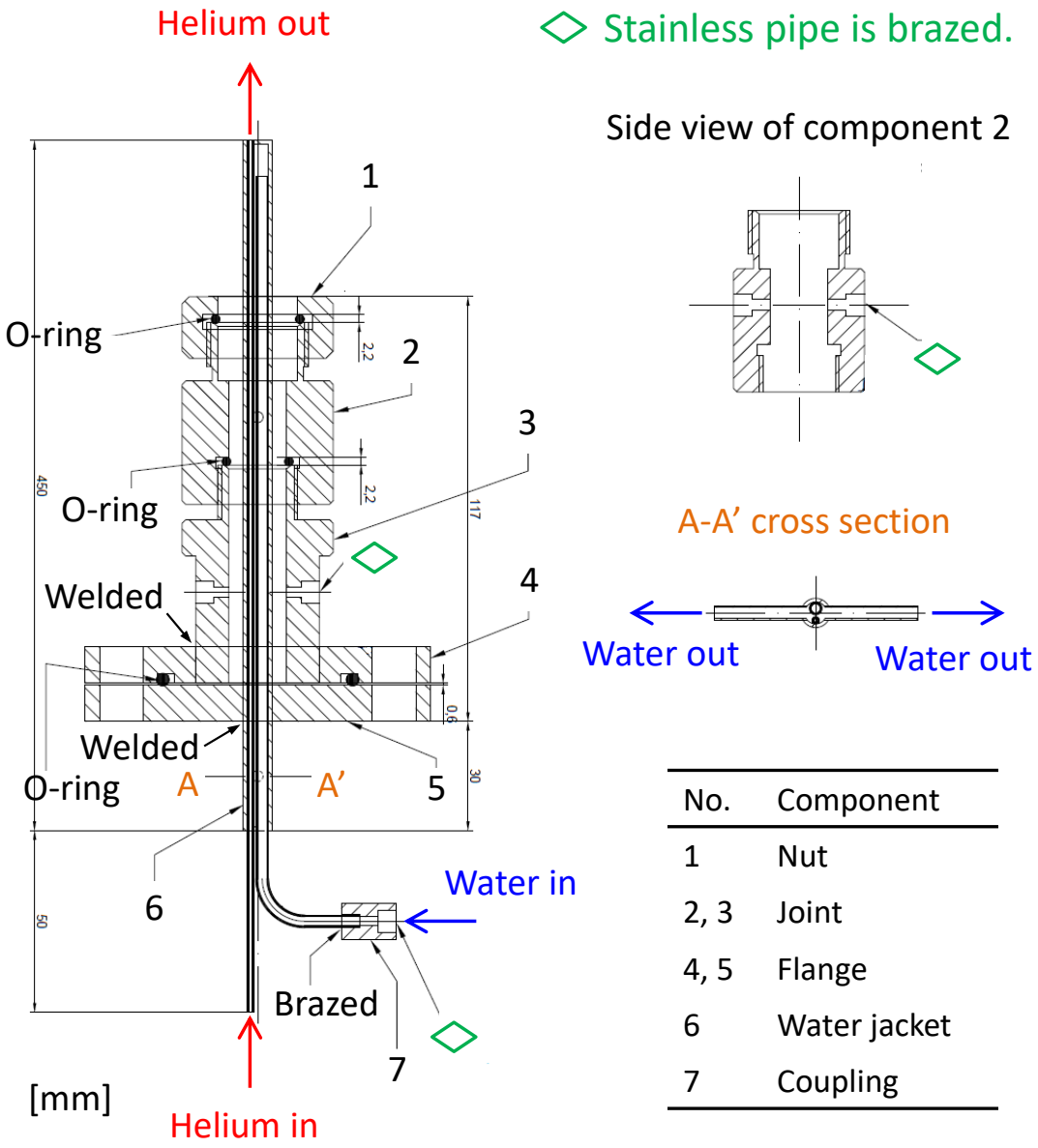

No.	Component
1	Nut
2, 3	Joint
4, 5	Flange
6	Water jacket
7	Coupling

Figure D-4. A drawing of the helium nozzle combined with water-cooling jacket. Flow directions of helium and water are shown.

References

[1] Verein Deutscher Ingenieure (Ed.), *VDI Heat Atlas, 4th Edition*, Springer (1984), Japan Management Association. (in Japanese)

[2] The Japan Society of Mechanical Engineers, *JSME Data Book: Heat Transfer 5th Edition*, pp. 45, Maruzen (2009). (in Japanese)

Appendix E

Oxygen tracer diffusion coefficient and surface exchange coefficient of LSM

Oxygen tracer diffusion coefficient D^* and surface exchange coefficient k^* of LSM particles were determined by fitting Eq. (4.8) to line profiles of ^{18}O concentration c_{18O} in Chapter 4, section 4.3. All measured points, examples of fitted graph, and obtained D^* and k^* values are shown in Appendix E. All measured points in section A (OCV) and C (biased, directly under the contact area of the current collector) are shown in Figure E-1(a) and (b), respectively. Examples of fitting results are shown in Figure E-2, and all D^* and k^* values obtained here are summarized in Table E-1 for section A and in Table E-2 for section C. In Table E-1 and E-2, distance d of each point (LSM/gas interface at each measured line profile) from electrolyte/cathode interface is also shown.

(a) Section A

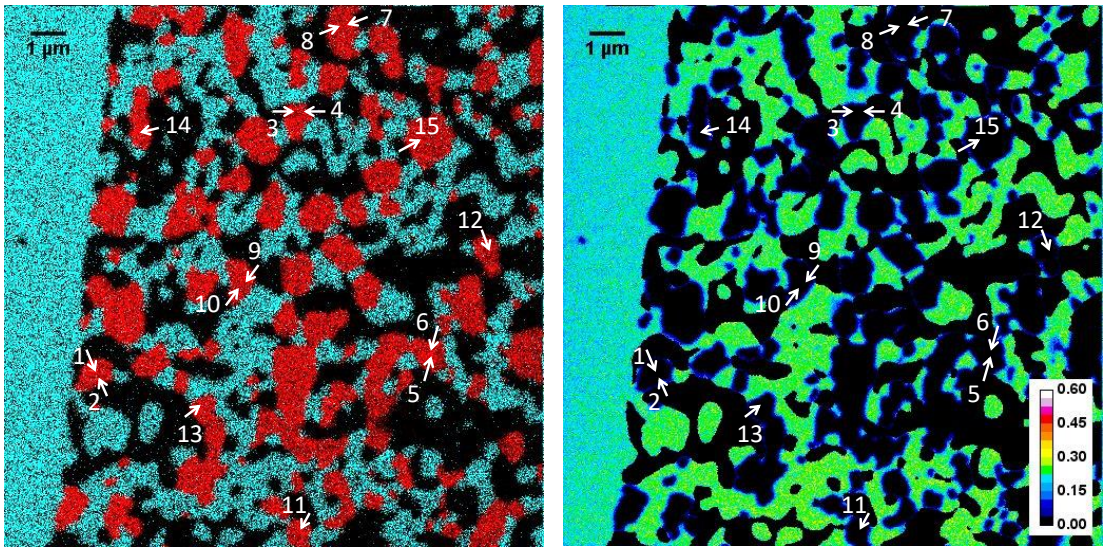

(b) Section C

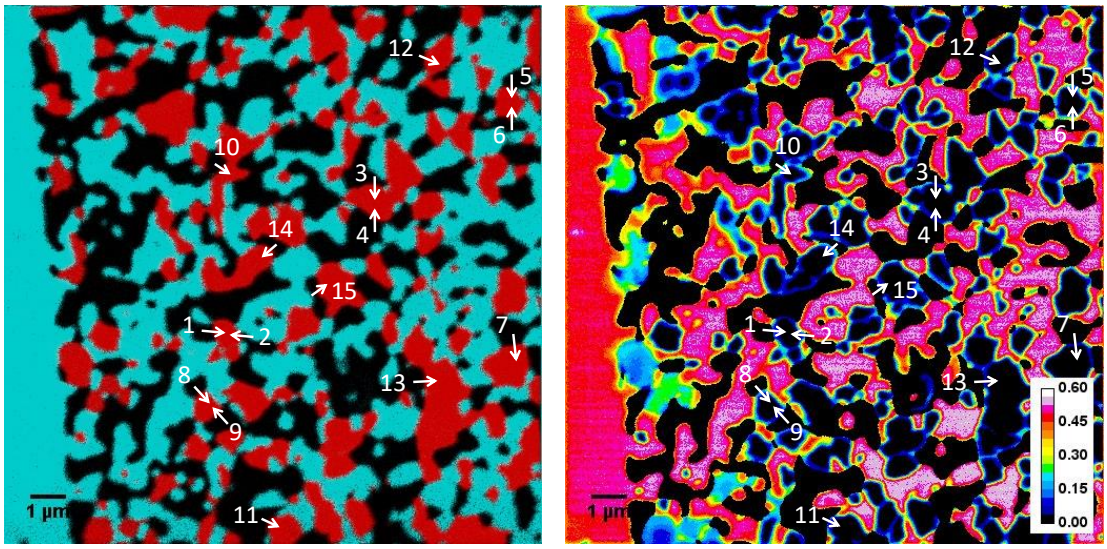

Figure E-1. All measured points of c_{18O} line profiles to determine oxygen tracer diffusion coefficient D^* and surface exchange coefficient k^* for (a) section A (OCV) and (b) section C (biased, directly under the contact area of the current collector).

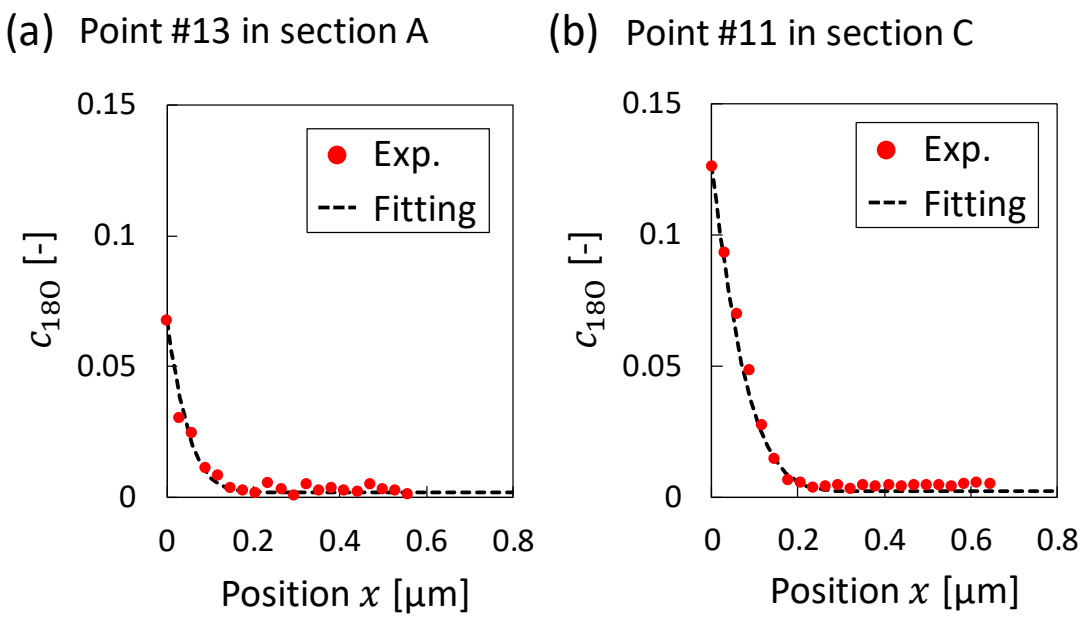

Figure E-2. Fitting results of diffusion equation [Eq. (4.8)] to ^{18}O concentration profile c_{180} at (a) Point #13 in Section A (OCV, Fig. E-1(a)) and (b) Point #11 in Section C (biased, Fig. E-1(b)). Positive direction in position x corresponds to each arrow direction in Fig. E-1.

Table E-1. All fitted D^* and k^* of LSM at point #1-15 in section A (OCV, Fig. E-1(a)). Distance of each point from electrolyte/cathode interface (d) is also shown.

Point #	D^* [cm^2/s]	k^* [cm/s]	d [μm]
1	6.70×10^{-14}	5.50×10^{-10}	0.424
2	5.00×10^{-14}	4.40×10^{-10}	0.693
3	2.00×10^{-13}	1.30×10^{-9}	4.977
4	7.00×10^{-14}	7.00×10^{-10}	5.762
5	9.00×10^{-14}	4.80×10^{-10}	9.676
6	7.00×10^{-14}	4.33×10^{-10}	10.0039
7	9.50×10^{-14}	9.30×10^{-10}	6.63
8	1.50×10^{-13}	1.10×10^{-9}	5.822
9	1.50×10^{-13}	1.10×10^{-9}	4.7
10	1.80×10^{-13}	1.30×10^{-9}	4.199
11	5.50×10^{-14}	8.70×10^{-10}	6.858
12	8.80×10^{-14}	1.85×10^{-9}	10.739
13	1.30×10^{-13}	1.65×10^{-9}	3.458
14	1.85×10^{-13}	2.40×10^{-9}	1.452
15	2.30×10^{-13}	2.40×10^{-9}	8.412

Table E-2. All fitted D^* and k^* of LSM at point #1-15 in section C (biased, Fig. E-1(b)). Distance of each point from electrolyte/cathode interface (d) is also shown.

Point #	D^* [cm^2/s]	k^* [cm/s]	d [μm]
1	5.50×10^{-13}	6.20×10^{-9}	4.367
2	3.50×10^{-13}	4.80×10^{-9}	5.089
3	2.70×10^{-13}	3.00×10^{-9}	9.131
4	3.70×10^{-13}	3.20×10^{-9}	9.045
5	3.00×10^{-13}	1.50×10^{-8}	12.909
6	2.40×10^{-13}	1.25×10^{-8}	12.821
7	1.00×10^{-13}	1.35×10^{-9}	12.633
8	2.70×10^{-13}	6.50×10^{-9}	3.786
9	2.60×10^{-13}	2.60×10^{-9}	4.289
10	2.20×10^{-13}	8.00×10^{-9}	5.016
11	3.00×10^{-13}	5.05×10^{-9}	5.361
12	4.40×10^{-13}	4.00×10^{-9}	10.795
13	3.80×10^{-13}	2.90×10^{-9}	10.184
14	2.50×10^{-13}	7.20×10^{-9}	6.299
15	5.60×10^{-13}	6.30×10^{-9}	7.42

Acknowledgements

First of all, my greatest appreciation goes to my supervisor, Professor Katsunori Hanamura, a respectable scientist and engineer in mechanical and thermal engineering. His continuous encouragements, valuable ideas, essential comments, and abundant knowledge has greatly helped my research go well. Many of ideas in this thesis were born from the fruitful discussions with him, and his critical insights often illuminated the new research directions. It's my great pleasure to continue the research activities with him for 6 years from undergraduate to Ph.D. course.

I would like to express my gratitude to members of my committee, Professor Isao Satoh, Professor Shuichiro Hirai, Professor Ichiro Yamanaka, and Associate Professor Kazuyoshi Fushinobu for spending precious time to evaluate the thesis and giving valuable comments, which were truly helpful to improve the quality of the thesis.

My deep thanks also go to the faculty members and staff of Hanamura laboratory. I want to thank Assistant Professor Hirotatsu Watanabe for his critical comments and fruitful discussions. His active attitude toward researches is a good example for me as a young researcher. I also thank Assistant Professor Masamichi Nakagawa for his valuable comments in seminars. I want to show my special thanks to Ms. Hiroe Shikata, a secretary of the laboratory, for her works in office procedure, which was indispensable for our research and daily activities.

I would like to show my appreciation to the faculty members and staffs of Hirai-Sasabe laboratory. I thank Professor Shuichiro Hirai for his valuable comments in the joint seminars and daily life. His attitude and vision in research always reminds me the

importance of research background, value, and role in society. I thank Project Associate Professor Suguru Uemura for his kind and continuous help in research and daily activities. I thank Associate Professor Takashi Sasabe, Project Professor Toshihiko Yoshida, and all the other current and former staffs. My special thanks goes to Project Associate Professor Yuki Kameya for his great help and many valuable advices about my future career.

The days at Georgia Institute of Technology as a visiting researcher was also an irreplaceable experience for me. I specially thank Professor Meilin Liu, my supervisor in Atlanta. His abundant ideas and knowledge of material science and practical attitude in research made my stay so productive. I would like to express my thanks to Dr. Dongchang Chen, Dr. Samson Yuxiu Lai, and all the other members in Liu group.

The connection with many researchers in SOFC field is of great value and importance. I thank Professor Manabu Ihara in Tokyo Tech for giving precise knowledge in solid state electrochemistry and discussing with me many times. I also thank the members of Ihara laboratory for the support in fuel cell preparation. I thank Associate Professor Tomofumi Tada in Tokyo Tech for telling me fundamentals of first principle calculation. I thank Professor Michihisa Koyama in Kyushu University, Associate Professor Hiroshi Iwai in Kyoto University, and Professor Naoki Shikazono in The University of Tokyo, for discussing with me many times.

I got many technical supports in experiments. I thank staffs in Ookayama Materials Analysis Division, especially Mr. Jun Koki for the support in sample preparation for secondary ion mass spectroscopy (SIMS). I thank staffs in the factory of Tokyo Tech. My special thanks goes to Dr. Miyuki Takeuchi in The University of Tokyo for the great support in SIMS measurement.

I received generous supports in financial and research environment. I thank

Academy for Co-creative Education of Environmental and Energy Science (ACEEES), a leading graduate school in Tokyo Tech, and its staffs for financial support and giving many valuable opportunities including the stay in Georgia Tech. I thank the Japan Society for the Promotion of Science (JSPS) for financial support.

Most memories in the graduate school are brought back with many lab-mates. I would like to express my deep gratitude to all the current and former members of Tanso Center (Hanamura and Hirai-Sasabe laboratories), with whom I greatly enjoyed the research and daily activities. Special thanks go to two former Ph.D. students in Hanamura laboratory, Dr. Ryoko Chijiiwa (Sanui) and Dr. Naphatsorn Vongsoasup. We shared the long time as lab-mates and encouraged and stimulated each other, which are important memories for me. I also specially thank Mr. Masaru Kanie and Ms. Merika Chanthanumataporn in Hanamura laboratory for spending a long time on the SOFC research together. It's my great fortune and pleasure to share the time with all the members in Tanso Center.

The last words of appreciation go to my family. I would like to express the deepest gratitude from the bottom of my heart to my parents and sister for their continuous, kind, and warm encouragements and supports throughout my long Ph.D. life.

Tsuyoshi Nagasawa

Ookayama, Tokyo

March 2018

Publications

Journals (reviewed)

Related to the thesis

1. Tsuyoshi Nagasawa, Katsunori Hanamura, “Power generation characteristics of a SOFC with a Ni/YSZ anode incorporating a $SrZr_{0.95}Y_{0.05}O_{3-\alpha}$ proton conductor”, *Journal of Thermal Science and Technology* 10 (1) (2015) 15-00112. (Chapter 3)
2. Tsuyoshi Nagasawa, Katsunori Hanamura, “Theoretical analysis of hydrogen oxidation reaction in solid oxide fuel cell anode based on species territory adsorption model”, *Journal of Power Sources* 290 (2015) 168–182. (Chapter 2)
3. Tsuyoshi Nagasawa, Katsunori Hanamura, “Prediction of overpotential and effective thickness of Ni/YSZ anode for solid oxide fuel cell by improved species territory adsorption model”, *Journal of Power Sources* 353 (2017) 115–122. (Chapter 3)
4. Tsuyoshi Nagasawa, Katsunori Hanamura, “Microstructure-scaled active sites imaging of a solid oxide fuel cell composite cathode”, *Journal of Power Sources* 367 (2017) 57–62. (Chapter 4)

Others

5. Masaru Kanie, Warit Ua-Amnueychai, Merika Chanthanumataporn, Keiji Asada, Tsuyoshi Nagasawa, Katsunori Hanamura, “Surface reaction controlling hydrogen permeation through lanthanum-doped ceria membrane with asymmetric structure”, *Mechanical Engineering Letters* 1 (2015) 15-00359.
6. Tsuyoshi Nagasawa, Dongchang Chen, Samson Yuxiu Lai, Meilin Liu, Katsunori

Hanamura, “In situ Raman spectroscopic analysis of the coking resistance mechanism on $SrZr_{0.95}Y_{0.05}O_{3-x}$ surface for solid oxide fuel cell anodes”, *Journal of Power Sources* 324 (2016) 282–287.

International Conference Proceedings (reviewed)

Related to the thesis

1. Tsuyoshi Nagasawa, Katsunori Hanamura, “Reaction Characteristics around Triple Phase Boundary in Anode including Proton Conductor for Solid Oxide Fuel Cell”, *ECS Transactions* 64 (2) (2014) 117–134.
2. Tsuyoshi Nagasawa, Katsunori Hanamura, “Overpotential and Interfacial Conductivity of Ni/YSZ Anode Based on Species Territory Adsorption Model in SOFCs”, *ECS Transactions* 68 (1) (2015) 1315–1322.
3. Tsuyoshi Nagasawa, Katsunori Hanamura, “Particle-scaled Visualization of Active Sites in LSM/ScSZ Composite Cathode of SOFC through Oxygen Isotope Labeling”, *ECS Transactions* 78 (1) (2017) 855–859.
4. Tsuyoshi Nagasawa, Katsunori Hanamura, “Quenching of chemical species transport in SOFC by He impinging jet for visualization of oxide ion path in composite electrodes”, *Extended Abstracts of the Ninth JSME-KSME Thermal and Fluid Engineering Conference* (2017) TFEC9-1072.

Others

5. Merika Chanthanumataporn, Tsuyoshi Nagasawa, Masaru Kanie, Katsunori Hanamura, “A Proton-Conducting Solid Oxide Fuel Cell with an Yttrium and Tin Co-Doped Barium Zirconate Electrolyte”, The 27th International Symposium on Transport

Phenomena, *ISTP27 Proceedings* (2016) pp.27.

6. Hirotatsu Watanabe, Masaru Kanie, Merika Chanthanumataporn, Tsuyoshi Nagasawa, Katsunori Hanamura, “Experimental and Detailed Kinetic Modeling Study of Carbon Deposition on Ni/YSZ Anode in SOFC”, *ECS Transactions* 78 (1) (2017) 1107–1114.